

Carbon in flux:
Measuring the climate sensitivity of
terrestrial greenhouse gas uptake

Thesis by
Hannah Dion-Kirschner

In Partial Fulfillment of the Requirements for
the degree of
Doctor of Philosophy in Geobiology

The Caltech logo is displayed in a bold, orange, sans-serif font. The letters are thick and closely spaced, with a slight shadow effect behind them.

CALIFORNIA INSTITUTE OF TECHNOLOGY
Pasadena, California

2025
(Defended 8 May 2025)

© 2025

Hannah Dion-Kirschner
ORCID: 0000-0001-5978-5250

ACKNOWLEDGEMENTS

I feel fortunate beyond words to have been surrounded by an incredible community in both my work life and my personal life during my time at Caltech. I owe a debt of gratitude to countless people (and a few pets) for their tangible and intangible contributions to the pages that follow.

To my advisors and committee members: Alex, I have learned so much from you about how to think and problem-solve. In our conversations you always help me discover new dimensions or approaches to a problem that I hadn't yet considered. Your unwaveringly thoughtful and rigorous approach to science is a model I hope I can emulate in my research career. Woody, enthusiasm is a precious resource during a Ph.D. and I am fortunate to count you as a reliable source. Thank you for acting as my tour guide to the geobiology literature and for supporting me to follow my curiosity. John, having access to your wealth of technical knowledge (and your trove of analytical tools) is the stuff most geochemists can only dream of. Thank you for supporting me with your time, ideas, and resources, and for your advocacy when things didn't go to plan. Victoria, I didn't see myself as a biologist when I came to Caltech and here I am about to join a biology lab! Thank you for welcoming me as an Orphan lab hanger-on and for helping to foster my appreciation for the microscopic things in life. I owe further thanks to the many other professors at Caltech who have helped me make sense of my data, learn new techniques, and grow as a scientist, including George Rossman, Mike Lamb, John Grotzinger, Dianne Newman, Christian Frankenberg, and Xiaojing (Ruby) Fu.

To the numerous formative teachers and mentors I have been blessed with throughout my life, including Jamie McFarlin, Maggie Osburn, Yarrow Axford, Neal Blair, Patricia Beddows, Gail Williams, Jon Boen, Jena Gardner, Olga Sanchez, Kristi Crago, Dietrich Hemann, Jon Balcerak, Jean Biebel, Elaina Meier, Casey Twanow, Keith Hartmann, Wendy Prostek, Dorothy Johnson, Melissa Kirkish, Christine Srok, and Bruce Warren: Thank you for opening doors for me, awakening my sense of wonder, and teaching me how to learn. A special thanks goes to Leah Witus, whose first-year seminar offering at Northwestern introduced me to environmental chemistry and set me on this path.

To the countless outstanding staff scientists who make Caltech what it is, including Michael Mathuri, Fenfang Wu, Stephanie Connon, John Magyar, Nathan Dalleska, Dave VanderVelde, Nathan

Siladke, Jonathan Treffkorn, and Nami Kitchen; and, at Northwestern (now USGS), Andy Masterson: Thank you for teaching me how to think with my hands. I owe so many data points to each of you!

To the Caltech staff who truly make everything possible, including (but certainly not limited to!) Julie Lee, Jen Shechet, Kacey Gibson, Sandi Parra, Andrea Valenzuela, Emi Vasquez, Grace Ames, Julia Zuckerman, Leticia Calderon, Mona Eadington, Kristy Nguyen, and Mark Garcia: Thank you for supporting my work, my life as a student here, and the vibrancy of the GPS community.

To the brilliant mentees who I've been so privileged to work with during my time at Caltech, including Celia Kong-Johnson, Sarah Vierling, Avani Athavale, Jocelyn Rodriguez, and the many bright K-12 students who I've had the pleasure of meeting: Thank you for your boundless enthusiasm and for helping me remember why I'm here.

To my labmates, including Shae Silverman, Makayla Betts, Elliott Mueller, Yeonsoo Park, Madison Dunitz, Guannan Dong, Alex Phillips, Tristan Caro, Selva Marroquin, Eryn Eitel, Elise Wilkes, Gabriella Weiss, Elle Chimiak, Hemani Kalucha, Josh Anadu, Noam Lotem, Calvin Rusley, Forrest McCann, Avi Flamholz, Bryn Stewart, Yutian Ke, Sarah Zeichner, Renee Wang, and Usha Lingappa; and to my adoptive labmates in the Eiler and Orphan labs and the CZI collaboration, including Simon Andren, Tim Csernica, Amy Hofmann, Elizabeth Heiny, Rebecca Wipfler, James Mullahoo, Aditi Narayanan, Philip Woods, Serg Parra, Hannah Way, Magdi Mayr, Dan Utter, Justus Fink, Jeremy Schreier, Emily Geyman, Justin Nghiem, Kieran Dunne, Yinon Bar-On, Harrison Martin, and Renato Braghieri: When people ask me what I think of Caltech, the first thing I mention is the amazing community I have found here among my peers and how much I learn from all of you. Many of my best memories from the last six years center on times I've spent among labmates both on campus and off. Thank you all for your support, advice, and friendship, and for making my work life so rich and interesting.

The data for Chapter 2 was collected at three field sites in California. For access to these sites, I am grateful to the Mother Lode and Barstow field offices of the Bureau of Land Management, including Lis Lucas and Chris Otahal; and especially to the White Buffalo Land Trust including Ann Close, Aarushi Jhatro, and Jesse Smith for your hospitality and unwavering support. These field sites are

located on the ancestral lands of the Chumash, Sierra Miwok, and Serrano peoples, who had no say in my access to their lands, but I am grateful for their longtime stewardship and care of these beautiful landscapes. I am also grateful for the river channels, hillslopes, oaks, pines, cacti, sagebrushes, and all the other neighbors that kept me company and helped me find my way on each return visit.

Collecting the field data was a heavy lift, and would have been genuinely impossible without many field partners who generously contributed their time and energy, including Noam Lotem, Elin Larsson, John Magyar, James Mullahoo, Richard Horak, Josh Anadu, Eran Funaro, Tristan Caro, Katie Huy, Hemani Kalucha, Celia Kong-Johnson, Jarek Kwiecinski, Pippa Richter, Alejandro Cabrero-Cortez, and, incredibly, my dad and my husband (I'll get to you two later!). Here I have to give special acknowledgement to Rebecca Wipfler, who has joined me for no fewer than nine trips, carried countless carloads of gear, administered wilderness first aid, accompanied me on last-minute errands to Harbor Freight, supported me through many ups and downs, and stood by me as the most loyal friend and field partner I could ever ask for. Rebecca, I owe you a lifetime supply of snacks.

I am grateful to the people, activities, organizations, and places that helped ground me in my non-working hours. To the members of OcTech, thank you for helping me reconnect with the joy of making music in community. To Polina, Ronak, Rebecca, and Tristan, thank you for giving me a reason to set aside time for play and fun. To Kitty Cahalan and Mitch Aiken at the CTLO, Liz Jackman and Courtney Reddix at the Caltech Y, and all the current and past members of GO-Outdoors, thank you for greatly enriching my time at Caltech by helping connect me with the wider Pasadena community. To the Los Angeles and King County Libraries, the City of Pasadena, and the LA County Department of Parks and Recreation, thank you for caring for the books and landscapes that give my mind and body places to explore and rest. To Wendy, Jamie, Dr. Shankwiler, Divina, Amanda, Kanika, Heather, Erin, and Romero, thank you for your care of my growth and wellbeing. To Nadia and Brittany, thank you for your unrelenting love and support even during these months when I've been hard to reach, and for always reminding me what matters.

To Maud, Lucy, and Ruby, thank you for being the best (and worst) work-from-home company.

To my family: my husband, siblings, parents, grandparents, and in-laws. Thank you all for the bounty of love and support you have provided me during my Ph.D. and throughout my life. Because of all

of you, I wake up knowing that I have firm ground to stand on no matter what the day will bring. Particular and infinite thanks go to my most beloved staff scientist, field partner, data science consultant, beta tester, and steadfast companion. Nick, with you there's no day I can't get through and no problem I can't solve. I love you.

ABSTRACT

The greenhouse gases carbon dioxide and methane exert a major control on Earth's climate, and their accumulation in the atmosphere is tempered by biological uptake. These biological uptake processes—photosynthesis and methanotrophy—are key contributors to the carbon-climate system, but their sensitivity to ongoing environmental change remains uncertain. In this thesis, I investigate how the ecophysiology of methanotrophy and photosynthesis dictate their response to perturbations in atmospheric composition, temperature, and other environmental variables. In Chapter 1, I present the first comprehensive compilation of kinetic measurements of methanotrophy in soils, and use this dataset to explore how kinetic properties may provide additional constraints to improve global models of the soil methane sink. Chapter 2 is a study of soil methane uptake rates in California dryland ecosystems and their relationship to local climate, ecology, and edaphic properties. This study reveals unique characteristics of dry climate regions that contradict typical assumptions about soil methane cycling. In Chapter 3, I present a novel method for position-specific carbon isotope analysis of submilligram glucose samples by Orbitrap mass spectrometry, and an application of this method to glucose standards isolated from C₃ and C₄ plants. In Chapter 4, I apply this new method to cellulose-derived glucose from tree-ring samples. Measurements of trees grown in climate chambers show how ¹³C-PSIA can disentangle changes in temperature, soil moisture, and tree carbon allocation. Finally, in two appendices, I describe methodological progress toward field-portable measurements of sedimentary porewater methane and the kinetics of soil methane uptake. Taken together, this work makes progress toward a more nuanced understanding of biological greenhouse gas uptake processes and their sensitivity to climate change.

PUBLISHED CONTENT AND CONTRIBUTIONS

Dion-Kirschner, H., Nguyen, N. H., Frankenber, C., & Fischer, W. W. (2024). Evaluating the contribution of methanotrophy kinetics to uncertainty in the soil methane sink. *Environmental Research Letters*, 19(6), 064059. <https://doi.org/10.1088/1748-9326/ad4c7a>

HDK jointly conceived the project with WWF, compiled and analyzed the data, performed simulations with assistance from NHN and CF, and wrote the paper.

TABLE OF CONTENTS

Acknowledgements.....	iii
Abstract	vii
Published Content and Contributions.....	viii
Table of Contents.....	ix
List of Figures and Tables.....	x
Introduction: Challenges and opportunities for understanding terrestrial greenhouse gas sinks.....	1
Chapter 1: Evaluating the contribution of methanotrophy kinetics to uncertainty in the soil methane sink.....	10
Chapter 2: Trends in dryland soil methane uptake highlight knowledge gaps in soil methane modeling.....	32
Chapter 3: Position-specific carbon isotope analysis of glucose at natural isotope abundance by Orbitrap Mass Spectrometry	79
Chapter 4: Position-specific ¹³ C analysis of cellulose by Orbitrap uncovers species-specific environmental and physiological signals in tree rings.....	107
Appendix I: Porewater methane concentration measurements by portable spectroscopy analyzer: Method and proof-of-concept measurements.....	140
Appendix II: Towards field-based measurements of methanotrophy kinetics: Justification and method development	151

LIST OF FIGURES AND TABLES

<i>Number</i>		<i>Page</i>
1.1	Global map visualizing distribution of methanotrophy kinetic observations.	14
1.2	Boxplot of compiled Michaelis-Menten kinetic measurements from natural soil samples.	17
1.3	Crossplot of compiled Michaelis-Menten kinetic measurements from natural soil samples.	18
1.4	Comparison of calculated soil methane sink size for linear and Michaelis-Menten kinetics across a range of atmospheric CH ₄ mixing ratios and quartiles of kinetic data.	20
1.5	Sensitivity of the modeled methane sink size to the kinetic parameters of methanotrophy.	21
1.6	The combined effects of kinetic variability, globally averaged near-surface air temperature increases, and atmospheric methane concentrations from Shared Socioeconomic Pathway projections on the calculated soil methane sink size for 2100.	23
ST1.1	Default input values for soil methane sink calculations.	29
ST1.2	Kinetic constant data summary by ecosystem.	29
SF1.7	The combined effects of kinetic variability, globally averaged near-surface air temperature increases, and atmospheric methane concentrations from Shared Socioeconomic Pathway projections on the calculated soil methane sink size for 2100, showing uncertainty for each data point.	30
2.1	Map of California Köppen-Geiger climate regions (Beck <i>et al</i> 2023, Esri 2024) showing the locations of the three field sites described in this study and photos of field sites.	38
T2.1	Field site geospatial, climatic, edaphic, and ecological properties.	39
2.2	Soil temperature, air temperature, and volumetric water content (VWC) data as derived from ERA5 reanalysis data and measured during timepoint measurements at sampling locations.	48
2.3	Net soil methane uptake measured for each time point and field location.	49
2.4	Correlogram showing the Spearman correlation of methane flux with measured soil and climate variables.	53
2.5	Trends in soil methane uptake distributions by vegetation type.	56
2.6	Analyses of soil microbial community composition, as assessed by 16S rRNA sequencing, and its relationship to site and soil methane uptake rates.	58
2.7	Comparison of modeled and measured soil methane uptake rates for coastal, desert, and foothills sites.	61
ST2.1	Parameters used for modified DLEM model of soil methane fluxes.	76
S2.8	Model results for Foothills site under low and high K_M and V_{max} values, demonstrating the sensitivity to kinetic constants used as model parameters.	77

3.1	Schematic illustrating method steps for glucose sample preparation and method verification.	82
T3.1	Instrument settings for Orbitrap position-specific carbon isotope analysis of glucose.	84
3.2	Metrics of measurement stability and sensitivity.	89
3.3	Orbitrap mass spectrum of gluconate, annotated with the molecular structure and atomic position makeup of 4 fragment ions and the molecular ion.	91
3.4	Cumulative precision of fragment ^{13}R values as ions are counted during an acquisition, assessed as the relative standard error of ^{13}R values.	92
3.5	Metrics of measurement accuracy.	96
3.6	Measuring and comparing glucose standards MC4 and SC3 (as gluconate) via ESI-Orbitrap.	101
ST3.2	Summary of all ions in the mass spectrum of gluconate when analyzed under the conditions described in Table 3.1.	105
S3.7	Matrix of equations used to calculate the $\delta^{13}\text{C}$ of five intramolecular positions,	106
S3.8	Measurement accuracy as a function of relative differences in sample-standard concentration, assessed by repeat measurements of GlcnA against itself ($\delta^{13}\text{C}_{\text{GlcNA}}$ of GlcnA, accurate value = 0‰).	106
T4.1	Summary of experimental conditions, tree species, and sample number for climate chamber experiment.	112
4.1	Measurement accuracy for all five measured ions across a range of relative TIC differences, assessed by repeat measurements of SC3 against itself ($\delta^{13}\text{C}_{\text{SC3}}$ of SC3, accurate value = 0‰).	119
4.2	Comparison of molecular-average $\delta^{13}\text{C}$ values as measured by EA-IRMS (x-axis) and Orbitrap (y-axis).	124
4.3	Position-specific $\delta^{13}\text{C}_{\text{GlcNA}}$ values measured for <i>F. sylvatica</i> and <i>L. decidua</i> tree-ring cellulose samples, plotted by climate chamber treatment.	130
4.4	Position-specific $\delta^{13}\text{C}_{\text{GlcNA}}$ values measured for <i>F. sylvatica</i> and <i>L. decidua</i> tree-ring cellulose samples.	131
S4.5	$\delta^{13}\text{C}_{\text{VPDB}}$ of α -cellulose standard and glucose product of hydrolysis by EA-IRMS, showing no discernable offset between the reactant and product.	138
ST4.2	$\delta^{13}\text{C}_{\text{VPDB}}$ of cellulose samples and the product of sample hydrolysis by EA-IRMS, showing a systematic enrichment of glucose relative to sample cellulose.	138
S4.5	$\delta^{13}\text{C}_{\text{VPDB}}$ of cellulose samples and the product of sample hydrolysis by EA-IRMS, showing a systematic enrichment of glucose relative to sample cellulose.	138
S4.6	Measured $\Delta\delta^{13}\text{C}$ of post-hydrolysis glucose product vs. pre-hydrolysis sample cellulose, showing a weak but significant correlation between hydrolysis yield and isotopic offset.	138
S4.7	Estimated $\delta^{13}\text{C}_{\text{VPDB}}$ of climate chamber tree-ring samples, calculated based on $\delta^{13}\text{C}_{\text{VPDB}}$ values of a glucose standard from the same product number (but different batch) as standard SC3.	139
5.1	Measured concentration of methane (in ppm) across 20 injections of a 2% methane standard at known volume.	145

5.2	Porewater methane concentrations from sampling campaign 1 measured by field-portable cavity ringdown spectroscopy and by gas chromatography-flame ionization detection.	146
5.3	Porewater methane concentrations from sampling campaign 2 measured by field-portable cavity ringdown spectroscopy (CRDS).	147
5.4	Comparison of porewater methane concentrations measured by field-portable cavity ringdown spectroscopy (CRDS) during campaigns 1 (orange) and 2.	148
6.1	Components of kinetics measurement system.	153
6.2	Example of one kinetic measurement series, showing $p\text{CH}_4$ values measured by the CRDS analyzer following each of five methane injections into the chamber headspace.	155
6.3	Measured methane loss rate (in ppm min^{-1}) from the chamber-analyzer system when no soil sample was present, plotted against the methane gradient between the chamber interior and the ambient atmosphere ($\Delta p\text{CH}_4$, ppm).	156
6.4	Kinetic characterization of three soil samples.	158

*Introduction*CHALLENGES AND OPPORTUNITIES FOR UNDERSTANDING
TERRESTRIAL GREENHOUSE GAS SINKS

Two atmospheric carbon species—carbon dioxide and methane—exert primary control on Earth’s climate system (NOAA Global Monitoring Laboratory 2024). These molecules are also common metabolites subject to major biological fluxes. As a result, while over \$3 billion was spent last year on engineered solutions to remove these species from the atmosphere (Global CCS Institute 2024), the terrestrial biosphere is contributing substantially to atmospheric carbon removal of its own accord. Roughly 36,000 Tg of fossil carbon dioxide (CO₂) are emitted to the atmosphere each year, while ~33% of that amount is removed from the atmosphere through photosynthesis to become new plant biomass (Friedlingstein *et al* 2025). Photosynthetic carbon dioxide uptake dwarfs the global capacity for engineered carbon capture, which in 2024 was only 51 Tg (Global CCS Institute 2024). Meanwhile, human activity adds ~359 Tg of methane to the atmosphere each year (equivalent to >10,000 Tg CO₂), and ~31 Tg are consumed annually by soil-dwelling bacteria, which oxidize methane to obtain energy and build biomass in a metabolic process called methanotrophy (Saunois *et al* 2020). Photosynthesis and methanotrophy are the largest biological sinks for carbon dioxide and methane, respectively, and thus play a major role in shaping Earth’s climate.

Despite their importance to the greenhouse gas budget, estimated global photosynthetic and methanotrophic uptake rates are highly uncertain. State-of-the-art models of the land carbon dioxide sink produce estimates that vary by >4-fold for a given year (Friedlingstein *et al* 2020). Similarly, bottom-up estimates of global methane uptake by soils also vary by a factor of >4 (Saunois *et al* 2020). The uncertainty in estimates of these greenhouse gas sinks presents a challenge for accurately predicting ongoing changes in climate and the carbon budget.

While some of the uncertainty in predictions of global carbon sinks results from extreme events that are difficult to project and model, such as fire (Burton *et al* 2024), models of photosynthetic and methanotrophic carbon uptake are also hindered by incomplete understanding of more fundamental processes. For example, the effect of increasing atmospheric carbon dioxide abundance (pCO₂) on

photosynthetic uptake rates is not well-constrained by measurements (Frank *et al* 2015, Walker *et al* 2021). This response, called the “carbon fertilization effect,” is a key parameter in carbon cycle models, but its strength, climate sensitivity, and effect on land carbon stocks is a subject of ongoing debate (Bar-On *et al* 2025, Brienen *et al* 2015, Chen *et al* 2022, Li 2024, Yu *et al* 2022).

In comparison to the terrestrial carbon dioxide sink, soil methanotrophy is yet more poorly understood. In large part this stems from methane’s shorter history of observations: by 1949, scientists had already compiled a 79-year record (albeit discontinuous) of atmospheric carbon dioxide measurements (Callendar 1949), while methane had only been identified as a component of Earth’s atmosphere the year before (Migeotte 1948). Today, fundamental relationships of soil methane uptake with environmental parameters like temperature and soil moisture are still not well-constrained; these relationships are often modeled based on weak correlations drawn from sparse datasets (Murguia-Flores 2018). Model parameterizations are built based on regionally-biased or scant datasets because biomes other than forests are heavily underrepresented in the literature. For example, a 2024 metaanalysis identified only 190 published time series measurements of soil methane flux across all global dryland environments, most from arid regions of China (Song *et al* 2024), despite the fact that drylands comprise roughly 40% of global land area (Právělie 2016).

Because the terrestrial carbon dioxide and methane are sensitive to processes that span many spatial scales—from the water content of soil pore space to the chemical composition of the atmosphere—building more accurate models will require scientific advances across many subfields. Current challenges range from assembling terrestrial methane model ensembles (Saunois *et al* 2024) to tracking specific tree metabolite pools (O’Sullivan *et al* 2022). In this thesis, I combine methodological and analytical advances with strategic sampling of understudied biomes, with the goal of contributing to a more nuanced understanding of how biological greenhouse gas uptake processes respond (and feed back) to ongoing planetary change.

Chapter 1: Methanotrophy kinetics contribute to uncertainty in the soil methane sink

In Chapter 1, I investigate the sensitivity of the soil methane sink to atmospheric methane concentrations using the lens of Michaelis-Menten kinetics. I present the first comprehensive

compilation of methanotrophy kinetic measurements ($n = 542$), which reveals extreme variability in the measured kinetic properties of soil methane uptake. Although K_M and V_{max} values both span more than six orders of magnitude in environmental samples, the kinetic parameters show a clear power-law correlation across these ($r^2 = 0.44$). I discuss possible physiological, evolutionary, and environmental explanations for this correlation. Using an idealized calculation of the soil methane sink, I explore the effect of kinetic variability on projected methane uptake. While the choice of linear vs. Michaelis-Menten kinetic model produces only minor differences in modeled methanotrophy rates, the modeled rate is highly sensitive to the choice of kinetic parameters; however, accounting for the correlation I observe between parameters constrains the calculated sink size by up to 96%. This finding exemplifies how ecophysiological trends provide novel constraints that can improve the accuracy of global biogeochemical models.

Chapter 2: Trends in dryland soil methane uptake highlight knowledge gaps in soil methane modeling

In Chapter 2, I further explore how soil methane uptake rates respond to environmental conditions through measurements of understudied dryland ecosystems. I pair 275 measurements of soil methane uptake rates across three California sites with soil physical, chemical, and biological analyses at each measurement location. These measurements reveal very weak seasonality and climate sensitivity of methanotrophy across all sites, which contrasts starkly with observations from temperate, tropical, and boreal regions. While methanotrophy is typically assumed to be diffusion-limited, the tenuous correlation of net methane flux with soil moisture suggests that both methanotrophy and methanogenesis in these dryland soils may be limited by low soil moisture. I additionally show a strong stratification of methane flux rates according to local vegetation type, but no corresponding association with microbial community composition, which hints at control of methane cycling by carbon inputs from vegetation. I additionally present a comparison of measured methane fluxes with modeled values. Modeled fluxes are simulated using a simple model modified from a previous work, which represents a common approach to parameterizing soil methane cycling. With no variable tuning, the model produces reasonable, if elevated, average methane flux estimates for two out of three sites. However, the modeled results strongly overestimate the amplitude of seasonal signals.

These findings highlight unique characteristics of methane cycling in dryland soils that may require modelers to rethink the parameterization of soil biogeochemical models.

Chapter 3: Position-specific carbon isotope analysis of glucose at natural isotope abundance by Orbitrap Mass Spectrometry

In Chapter 3, I report on a new method I have developed for position-specific isotope analysis (PSIA) of submilligram glucose samples. This method was developed to enable PSIA of tree-ring cellulose, as applied in Chapter 4. However, it can accommodate glucose from a wide range of natural samples, and isotopic measurements of glucose can provide useful insights for environmental, biomedical, and food research. In this chapter, I establish the metrics of performance for glucose ^{13}C -PSIA by Electrospray-Ionization (ESI)-Orbitrap: I demonstrate that the method is sufficiently sensitive and precise to distinguish position-specific signals in natural glucose from C3 and C4 plants, and recovers accurate $\delta^{13}\text{C}$ values at five unique intramolecular sites in the glucose molecule. I also show a strong linear response of measured $\delta^{13}\text{C}$ ratios to relative differences in sample and standard signal intensity that provides further insight into best practices for isotopic analysis by Orbitrap. The method overcomes the limitations of existing methods for PSIA by NMR, including large sample size requirements (>100 mg) and high sensitivity to contaminants. In addition to laying the groundwork for the tree-ring measurements in Chapter 4, the work in Chapter 3 paves the way for more detailed study of sugar metabolism and provenance in plants and other natural systems.

Chapter 4: Position-specific ^{13}C analysis of cellulose by Orbitrap uncovers species-specific environmental and physiological signals in tree rings

In Chapter 4, I apply the method described in Chapter 3 to tree-ring samples, with the goal of using PSIA to disentangle climate and physiological signals recorded in the $\delta^{13}\text{C}$ of cellulose. I report position-specific $\delta^{13}\text{C}$ values measured for 23 samples of gymnosperm and angiosperm trees grown under varied soil moisture, humidity, and temperature. Using only 33 μg of cellulose per sample, I achieve average precision of 1.8‰, measure intramolecular $\delta^{13}\text{C}$ differences up to 21.7‰, and accurately match values obtained by traditional compound-specific isotope analysis (CSIA). These measurements reveal that signals of temperature and soil moisture are recorded by the C-3 atomic

position with greater sensitivity than by molecular-average $\delta^{13}\text{C}$ measurements, highlighting the value of PSIA for more sensitively reconstructing paleoclimate from tree-ring records. The $\delta^{13}\text{C}$ values of most intramolecular positions are uncorrelated with one another across the sample set, indicating that each position records unique signals that cannot be independently interpreted via CSIA. Species-specific trends at positions C-4–C-6 provide evidence for different carbon allocation and climate adaptation strategies between gymnosperm and angiosperm samples. Taken together, these results demonstrate the wealth of information available through PSIA of tree-ring cellulose that cannot be accessed by traditional compound-specific measurements. Because trees' carbon allocation in response to climate is a key source of uncertainty in models of the land carbon sink (O'Sullivan et al., 2022), the ability to reconstruct carbon allocation in trees through time will support more accurate carbon cycle models. More broadly, this chapter underlines the utility of innovative new methods for providing needed mechanistic insights into biological greenhouse gas uptake processes.

Appendices

Finally, I include two appendices that describe additional new methods I have developed in the course of my research. Appendix I describes a method for measurements of porewater methane using a field-portable analyzer. I demonstrate an application of this method to two sediment cores recovered from Mono Lake, and a comparison to values measured by a more standard methane quantification method. Appendix II outlines a method for field-based characterization of methanotrophy kinetics in soil samples, and describes why an improvement in kinetic measurement techniques would substantially contribute to our understanding of soil methane cycling.

Summary and outlook

The work I present here attempts to close gaps in our ability to understand and predict biological greenhouse gas uptake. Modeling the global carbon cycle is a generational challenge for today's researchers (and yesterday's, and tomorrow's), and no single approach is sufficient to resolve the remaining uncertainties. Nevertheless, these chapters make inroads in better understanding key mechanisms: the environmental sensitivities of soil methane uptake and tree carbon allocation.

Chapters 1 and 2 inform a clearer understanding of how soil methane fluxes behave under changing atmospheric composition and in understudied environments. Together, they show how ecological and physiological properties can offer unexpected constraints for global models. In Chapters 3 and 4, I demonstrate a novel method that holds great promise in resolving trees' contributions to terrestrial carbon pools under climate perturbations in the past and present. These chapters highlight how innovative approaches can help disentangle interacting variables in environmental samples. While my thesis work offers new insights into carbon metabolism in plants and soils, upscaling this type of process understanding for application in planetary-scale models represents a critical hurdle still facing biogeochemists—and one that I plan to confront in my postdoctoral research. Ultimately, through new methods and analyses this work sets a path for a more nuanced understanding of the terrestrial carbon cycle, which I look forward to following in years ahead.

References

- Bar-On Y M, Li X, O'Sullivan M, Wigneron J-P, Sitch S, Ciais P, Frankenberg C and Fischer W W 2025 Recent gains in global terrestrial carbon stocks are mostly stored in nonliving pools *Science* **387** 1291–5
- Brienen R J W, Phillips O L, Feldpausch T R, Gloor E, Baker T R, Lloyd J, Lopez-Gonzalez G, Monteagudo-Mendoza A, Malhi Y, Lewis S L, Vásquez Martínez R, Alexiades M, Álvarez Dávila E, Alvarez-Loayza P, Andrade A, Aragão L E O C, Araujo-Murakami A, Arets E J M M, Arroyo L, Aymard C. G A, Bánki O S, Baraloto C, Barroso J, Bonal D, Boot R G A, Camargo J L C, Castilho C V, Chama V, Chao K J, Chave J, Comiskey J A, Cornejo Valverde F, da Costa L, de Oliveira E A, Di Fiore A, Erwin T L, Fauset S, Forsthofer M, Galbraith D R, Grahame E S, Groot N, Hérault B, Higuchi N, Honorio Coronado E N, Keeling H, Killeen T J, Laurance W F, Laurance S, Licona J, Magnussen W E, Marimon B S, Marimon-Junior B H, Mendoza C, Neill D A, Nogueira E M, Núñez P, Pallqui Camacho N C, Parada A, Pardo-Molina G, Peacock J, Peña-Claros M, Pickavance G C, Pitman N C A, Poorter L, Prieto A, Quesada C A, Ramírez F, Ramírez-Angulo H, Restrepo Z, Roopsind A, Rudas A, Salomão R P, Schwarz M, Silva N, Silva-Espejo J E, Silveira M, Stropp J, Talbot J, ter Steege H, Teran-Aguilar J, Terborgh J, Thomas-Caesar R, Toledo M, Torello-Raventos M, Umetsu R K, van der Heijden G M F, van der Hout P, Guimarães Vieira I C, Vieira S A, Vilanova E, Vos V A and Zagt R J 2015 Long-term decline of the Amazon carbon sink *Nature* **519** 344–8
- Burton C A, Kelley D I, Burke E, Mathison C, Jones C D, Betts R A, Robertson E, Teixeira J C M, Cardoso M and Anderson L O 2024 Fire weakens land carbon sinks before 1.5 °C *Nat. Geosci.* **17** 1108–14
- Callendar G S 1949 Can Carbon Dioxide Influence Climate? *Weather* **4** 310–4

- Chen C, Riley W J, Prentice I C and Keenan T F 2022 CO₂ fertilization of terrestrial photosynthesis inferred from site to global scales *Proceedings of the National Academy of Sciences* **119** e2115627119
- Frank D C, Poulter B, Saurer M, Esper J, Huntingford C, Helle G, Treydte K, Zimmermann N E, Schleser G H, Ahlström A, Ciais P, Friedlingstein P, Levis S, Lomas M, Sitch S, Viovy N, Andreu-Hayles L, Bednarz Z, Berninger F, Boettger T, D'Alessandro C M, Daux V, Filot M, Grabner M, Gutierrez E, Haupt M, Hilasvuori E, Jungner H, Kalela-Brundin M, Krapiec M, Leuenberger M, Loader N J, Marah H, Masson-Delmotte V, Pazdur A, Pawelczyk S, Pierre M, Planells O, Pukiene R, Reynolds-Henne C E, Rinne K T, Saracino A, Sonninen E, Stievenard M, Switsur V R, Szczepanek M, Szychowska-Krapiec E, Todaro L, Waterhouse J S and Weigl M 2015 Water-use efficiency and transpiration across European forests during the Anthropocene *Nature Clim Change* **5** 579–83
- Friedlingstein P, O'Sullivan M, Jones M W, Andrew R M, Hauck J, Landschützer P, Le Quéré C, Li H, Luijckx I T, Olsen A, Peters G P, Peters W, Pongratz J, Schwingshackl C, Sitch S, Canadell J G, Ciais P, Jackson R B, Alin S R, Arneeth A, Arora V, Bates N R, Becker M, Bellouin N, Berghoff C F, Bittig H C, Bopp L, Cadule P, Campbell K, Chamberlain M A, Chandra N, Chevallier F, Chini L P, Colligan T, Decayeux J, Djeutchouang L M, Dou X, Duran Rojas C, Enyo K, Evans W, Fay A R, Feely R A, Ford D J, Foster A, Gasser T, Gehlen M, Gkritzalis T, Grassi G, Gregor L, Gruber N, Gürses Ö, Harris I, Hefner M, Heinke J, Hurtt G C, Iida Y, Ilyina T, Jacobson A R, Jain A K, Jarníková T, Jersild A, Jiang F, Jin Z, Kato E, Keeling R F, Klein Goldewijk K, Knauer J, Korsbakken J I, Lan X, Lauvset S K, Lefèvre N, Liu Z, Liu J, Ma L, Maksyutov S, Marland G, Mayot N, McGuire P C, Metzl N, Monacci N M, Morgan E J, Nakaoka S-I, Neill C, Niwa Y, Nützel T, Olivier L, Ono T, Palmer P I, Pierrot D, Qin Z, Resplandy L, Roobaert A, Rosan T M, Rödenbeck C, Schwinger J, Smallman T L, Smith S M, Sospedra-Alfonso R, et al 2025 Global Carbon Budget 2024 *Earth System Science Data* **17** 965–1039
- Friedlingstein P, O'Sullivan M, Jones M W, Andrew R M, Hauck J, Olsen A, Peters G P, Peters W, Pongratz J, Sitch S, Le Quéré C, Canadell J G, Ciais P, Jackson R B, Alin S, Aragão L E O C, Arneeth A, Arora V, Bates N R, Becker M, Benoit-Cattin A, Bittig H C, Bopp L, Bultan S, Chandra N, Chevallier F, Chini L P, Evans W, Florentie L, Forster P M, Gasser T, Gehlen M, Gilfillan D, Gkritzalis T, Gregor L, Gruber N, Harris I, Hartung K, Haverd V, Houghton R A, Ilyina T, Jain A K, Joetzjer E, Kadono K, Kato E, Kitidis V, Korsbakken J I, Landschützer P, Lefèvre N, Lenton A, Lienert S, Liu Z, Lombardozzi D, Marland G, Metzl N, Munro D R, Nabel J E M S, Nakaoka S-I, Niwa Y, O'Brien K, Ono T, Palmer P I, Pierrot D, Poulter B, Resplandy L, Robertson E, Rödenbeck C, Schwinger J, Séférian R, Skjelvan I, Smith A J P, Sutton A J, Tanhua T, Tans P P, Tian H, Tilbrook B, van der Werf G, Vuichard N, Walker A P, Wanninkhof R, Watson A J, Willis D, Wiltshire A J, Yuan W, Yue X and Zaehle S 2020 Global Carbon Budget 2020 *Earth System Science Data* **12** 3269–340
- Global CCS Institute 2024 *The Global Status of CCS: 2024* (Australia) Online: <https://www.globalccsinstitute.com/wp-content/uploads/2024/11/Global-Status-Report-6-November.pdf>

- Li Y 2024 Climate feedback from plant physiological responses to increasing atmospheric CO in Earth system models *New Phytologist* **244** 2176–82
- Migeotte M V 1948 Spectroscopic Evidence of Methane in the Earth's Atmosphere *Phys. Rev.* **73** 519–20
- Murguia-Flores F M 2018 *Modelling the global atmospheric methane uptake by soils in the past, present and future* (Bristol: University of Bristol)
- NOAA Global Monitoring Laboratory 2024 Annual Greenhouse Gas Index (AGGI) - NOAA Global Monitoring Laboratory Online: <https://gml.noaa.gov/aggi/aggi.html>
- O'Sullivan M, Friedlingstein P, Sitch S, Anthoni P, Arneth A, Arora V K, Bastrikov V, Delire C, Goll D S, Jain A, Kato E, Kennedy D, Knauer J, Lienert S, Lombardozzi D, McGuire P C, Melton J R, Nabel J E M S, Pongratz J, Poulter B, Séférian R, Tian H, Vuichard N, Walker A P, Yuan W, Yue X and Zaehle S 2022 Process-oriented analysis of dominant sources of uncertainty in the land carbon sink *Nat Commun* **13** 4781
- Práválie R 2016 Drylands extent and environmental issues. A global approach *Earth-Science Reviews* **161** 259–78
- Sauniois M, Martinez A, Poulter B, Zhang Z, Raymond P, Regnier P, Canadell J G, Jackson R B, Patra P K, Bousquet P, Ciais P, Dlugokencky E J, Lan X, Allen G H, Bastviken D, Beerling D J, Belikov D A, Blake D R, Castaldi S, Crippa M, Deemer B R, Dennison F, Etiope G, Gedney N, Höglund-Isaksson L, Holgerson M A, Hopcroft P O, Hugelius G, Ito A, Jain A K, Janardan R, Johnson M S, Kleinen T, Krummel P, Lauerwald R, Li T, Liu X, McDonald K C, Melton J R, Mühle J, Müller J, Murguia-Flores F, Niwa Y, Noce S, Pan S, Parker R J, Peng C, Ramonet M, Riley W J, Rocher-Ros G, Rosentreter J A, Sasakawa M, Segers A, Smith S J, Stanley E H, Thanwerdas J, Tian H, Tsuruta A, Tubiello F N, Weber T S, Van Der Werf G, Worthy D E, Xi Y, Yoshida Y, Zhang W, Zheng B, Zhu Q, Zhu Q and Zhuang Q 2024 Global Methane Budget 2000–2020 Online: <https://essd.copernicus.org/preprints/essd-2024-115/>
- Sauniois M, Stavert A R, Poulter B, Bousquet P, Canadell J G, Jackson R B, Raymond P A, Dlugokencky E J, Houweling S, Patra P K, Ciais P, Arora V K, Bastviken D, Bergamaschi P, Blake D R, Brailsford G, Bruhwiler L, Carlson K M, Carrol M, Castaldi S, Chandra N, Crevoisier C, Crill P M, Covey K, Curry C L, Etiope G, Frankenberg C, Gedney N, Hegglin M I, Höglund-Isaksson L, Hugelius G, Ishizawa M, Ito A, Janssens-Maenhout G, Jensen K M, Joos F, Kleinen T, Krummel P B, Langenfelds R L, Laruelle G G, Liu L, Machida T, Maksyutov S, McDonald K C, McNorton J, Miller P A, Melton J R, Morino I, Müller J, Murguia-Flores F, Naik V, Niwa Y, Noce S, O'Doherty S, Parker R J, Peng C, Peng S, Peters G P, Prigent C, Prinn R, Ramonet M, Regnier P, Riley W J, Rosentreter J A, Segers A, Simpson I J, Shi H, Smith S J, Steele L P, Thornton B F, Tian H, Tohjima Y, Tubiello F N, Tsuruta A, Viovy N, Voulgarakis A, Weber T S, van Weele M, van der Werf G R, Weiss R F, Worthy D, Wunch D, Yin Y, Yoshida Y, Zhang W, Zhang Z, Zhao Y, Zheng B, Zhu Q, Zhu Q and Zhuang Q 2020 The Global Methane Budget 2000–2017 *Earth Syst. Sci. Data* **12** 1561–623

- Song H, Peng C, Zhu Q, Chen Z, Blanchet J-P, Liu Q, Li T, Li P and Liu Z 2024 Quantification and uncertainty of global upland soil methane sinks: Processes, controls, model limitations, and improvements *Earth-Science Reviews* **252** 104758
- Walker A P, De Kauwe M G, Bastos A, Belmecheri S, Georgiou K, Keeling R F, McMahon S M, Medlyn B E, Moore D J P, Norby R J, Zaehle S, Anderson-Teixeira K J, Battipaglia G, Brienen R J W, Cabugao K G, Cailleret M, Campbell E, Canadell J G, Ciais P, Craig M E, Ellsworth D S, Farquhar G D, Faticchi S, Fisher J B, Frank D C, Graven H, Gu L, Haverd V, Heilman K, Heimann M, Hungate B A, Iversen C M, Joos F, Jiang M, Keenan T F, Knauer J, Körner C, Leshyk V O, Leuzinger S, Liu Y, MacBean N, Malhi Y, McVicar T R, Penuelas J, Pongratz J, Powell A S, Riutta T, Sabot M E B, Schleucher J, Sitch S, Smith W K, Sulman B, Taylor B, Terrer C, Torn M S, Treseder K K, Trugman A T, Trumbore S E, van Mantgem P J, Voelker S L, Whelan M E and Zuidema P A 2021 Integrating the evidence for a terrestrial carbon sink caused by increasing atmospheric CO₂ *New Phytologist* **229** 2413–45
- Yu K, Ciais P, Seneviratne S I, Liu Z, Chen H Y H, Barichivich J, Allen C D, Yang H, Huang Y and Ballantyne A P 2022 Field-based tree mortality constraint reduces estimates of model-projected forest carbon sinks *Nat Commun* **13** 2094

Chapter 1

EVALUATING THE CONTRIBUTION OF METHANOTROPHY KINETICS TO UNCERTAINTY IN THE SOIL METHANE SINK

Dion-Kirschner, H., Nguyen, N. H., Frankenberg, C., & Fischer, W. W. (2024). Evaluating the contribution of methanotrophy kinetics to uncertainty in the soil methane sink. *Environmental Research Letters*, 19(6), 064059. <https://doi.org/10.1088/1748-9326/ad4c7a>

1.1) Abstract

The oxidation of atmospheric methane by soil microbes is an important natural sink for a potent greenhouse gas. However, estimates of the current and future soil methane sink are highly uncertain. Here we assessed the extent to which methanotrophy enzyme kinetics contribute to uncertainty in projections of the soil methane sink. We generated a comprehensive compilation of methanotrophy kinetic data from modern environments and assessed the patterns in kinetic parameters present in natural samples. Our compiled data enabled us to quantify the global soil methane sink through two idealized calculations comparing first-order and Michaelis-Menten models of kinetics. We show that these two kinetic models diverge only under high atmospheric CH₄ scenarios, where first-order rate constants slightly overestimate the soil methane sink size, but produce similar predictions at modern atmospheric concentrations. Our compilation also shows that the kinetics of methanotrophy in natural soil samples is highly variable—both the V_{max} (oxidation rate at saturation) and K_M (half-saturation constant) in natural samples span over six orders of magnitude. However, accounting for the correlation we observe between V_{max} and K_M reduces the range of calculated uptake rates by as much as 96%. Additionally, our results indicate that variation in enzyme kinetics introduces a similar magnitude of variation in the calculated soil methane sink as temperature sensitivity. Systematic sampling of methanotroph kinetic parameters at multiple spatial scales should therefore be a key objective for closing the budget on the global soil methane sink.

1.2) Introduction

Aerobic microbial methane oxidation, or methanotrophy, is the only known Earth surface process that removes methane from the atmosphere. Today, methanotrophy is thought to account for roughly 5% of the total sink for atmospheric methane (Saunio *et al* 2020). However, estimates of the soil methane sink size span a wide range: for example, in the range of bottom-up estimates reported by Saunio *et al.* (2020) of 11-49 Tg CH₄ yr⁻¹, the low and high estimates differ by almost a factor of five. Minimizing the uncertainty in estimates of the global methane cycle, including the soil methane sink, is crucial to accurately projecting and effectively managing ongoing climate change.

Several sources contribute to the uncertainty in estimates of the soil methane sink. Estimates based on upscaled field data rely on observations from specific locations at specific times, and these datasets may not fully capture the large spatial and temporal heterogeneity that is characteristic of biogeochemical processes in soils (Lacroix *et al* 2023, Nunan *et al* 2020). Bottom-up estimates also hinge on correlations between methane flux and environmental variables such as climate or soil properties, but these correlations are often relatively weak. For example, a statistical model considering ecosystem type, soil texture, and climatic zone explained at best only 29% of the variation in observed methane flux (Dutaur and Verchot 2007). Process-based models estimate global methane fluxes by defining mathematical relationships between methane flux and environmental conditions based on theoretical considerations or field-based observations, but these mathematical definitions are similarly hampered by limited mechanistic understanding and small datasets (Murguia-Flores *et al* 2018). In order to improve ongoing modeling efforts, it therefore is important to identify which processes contribute the most to uncertainty in the modeled soil methane sink.

Many existing models of the soil methane sink employ linear rate constants to calculate methane uptake rate as a function of atmospheric methane concentration (Curry 2007, Murguia-Flores *et al* 2018, Ridgwell *et al* 1999). The rate constants among three canonical models vary by a factor of ~50 (Murguia-Flores *et al* 2018). While these models calculate soil methane uptake rate as a linear function of methane availability, many experimental studies have found that methanotrophy in natural soils follows Michaelis-Menten kinetics (e.g., Bender & Conrad, 1992, 1993). Accordingly, a subset of soil methane sink models implement Michaelis-Menten kinetics (Shu *et al* 2020). The

Michaelis-Menten model supports quantitative descriptions of cellular and ecosystem-level processes wherein the rate is sensitive to the concentration of available substrate, but reaches some theoretical maximum when the enzyme or community is saturated with substrate (Alvarez-Ramirez *et al* 2019, Liu 2007). In contrast to Michaelis-Menten kinetics, first-order rate constants allow for infinitely large oxidation rates as the concentration of substrate (e.g., methane) increases.

Previous work has shown that methanotrophs have variable kinetic properties. Methanotrophs from environments with substantial local methane sources, such as wetlands or landfills, are known to have a lower apparent affinity to methane than methanotrophs with reliable access to only atmospheric methane (Knief and Dunfield 2005). Studies commonly divide methanotrophs into two classes according to their kinetic properties: low-affinity and high-affinity methanotrophs, where only the high-affinity populations are capable of oxidizing methane at atmospheric abundance. The effect of kinetic variability at the enzymatic and the population level on the soil methane sink has not yet been assessed.

Here, we assessed the potential for variation in methanotrophy kinetics to contribute to uncertainty in soil methane sink estimates. We first characterized the variability in kinetic parameters observed in natural soil samples through a comprehensive literature compilation. We then performed an idealized calculation informed by our literature review to test the sensitivity of the modeled methane sink size under different scenarios. We compared the calculated sink size under Michaelis-Menten and linear kinetics models to assess whether the assumption of first-order kinetics substantially affects model outputs. We also quantified the sensitivity of the calculated sink size to the range of kinetic properties observed in natural soils. Finally, we calculated the sink size under future changes in methane concentration (via kinetic parameters) and temperature (via Q_{10} values). Our results highlight important considerations for future observations and models of the soil methane sink.

1.3) Methods

1.3.1) Literature compilation

To evaluate the range of methanotrophy kinetics in Earth surface environments, we generated a comprehensive compilation of published Michaelis-Menten kinetic data for methanotrophy in natural soils (Dion-Kirschner et al., 2024). The equation to describe Michaelis-Menten kinetics is:

$$V = V_{max} \frac{[S]}{K_M + [S]} \quad (1.1)$$

where V is the reaction rate, V_{max} is the maximum reaction rate observed at saturation, $[S]$ is the concentration of substrate (in this case methane), and K_M is the substrate concentration where $\frac{1}{2} V_{max}$ is attained. K_M values are often discussed in terms of affinity, where low K_M values indicate high affinity for methane and vice versa.

We extracted 542 observations of V_{max} and/or K_M values (Section 1.8.1, Dion-Kirschner et al., 2024). At least 1 observation was reported for 5 continents, but the vast majority of these (441) were from Europe and North America, exhibiting strong regional bias (Figure 1.1). Observations spanned diverse environments including forest, grassland, peat, and shrubland vegetation, although no data were available for desert or high-latitude sites. Treatment of the soil samples before and during the kinetic incubations varied among studies, as did the units for reported K_M and V_{max} values (Section 1.8.1, Dion-Kirschner et al., 2024). To standardize the dataset for analysis, we converted all K_M values to the mixing ratio of methane in the headspace in units of ppbv and all V_{max} values to $\text{nmol CH}_4 \text{ hour}^{-1} \text{ g soil}^{-1}$ (Section 1.8.1).

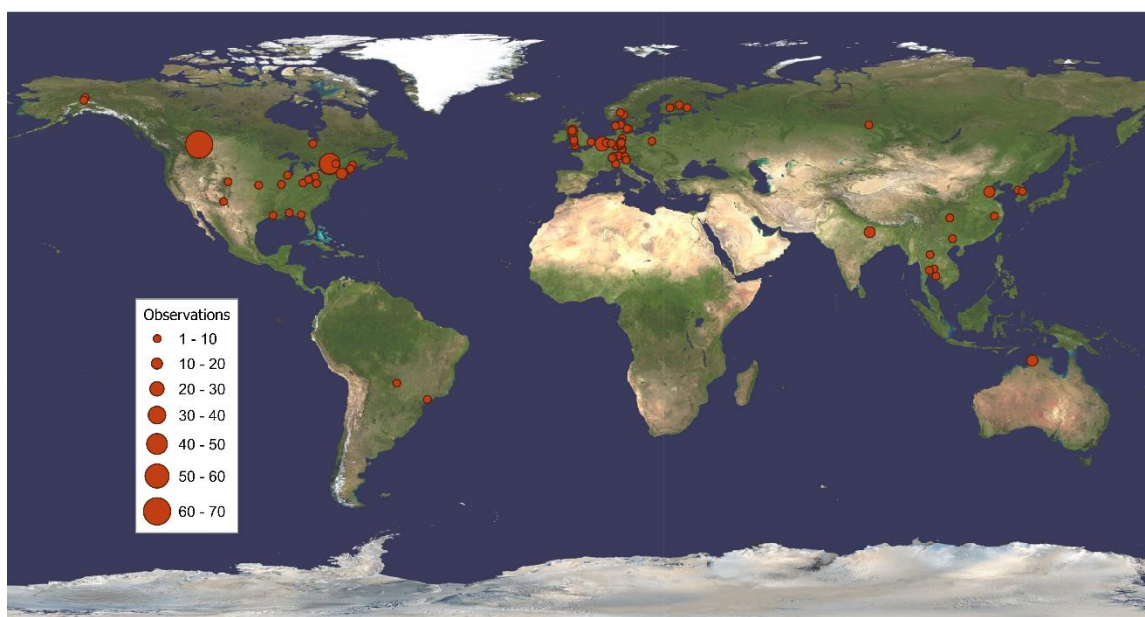


Figure 1.1: Global map visualizing distribution of methanotrophy kinetic observations. Point size is proportional to the number of observations at a given location. Basemap courtesy of NASA.

1.3.2) Soil methane sink calculations

We used data from our literature compilation to inform an idealized calculation of the soil methane sink size. Our calculation is based on a soil layer of constant thickness covering a fixed percentage of Earth's surface area. In contrast to studies with spatially resolved models (e.g., Curry 2007, Murguia-Flores *et al* 2018, Ridgwell *et al* 1999, Shu *et al* 2020), we did not implement diffusion limitation within the simulated soil layer for two reasons: First, an accurate model of methane diffusion in soils must account for *in situ* methane production within anoxic microsites and/or below the water table, mechanisms that are beyond the scope of this work. Second, and more importantly, we are not using this calculation to produce an accurate value for the soil methane sink size, but rather to test the sensitivity of the calculated sink size to kinetic parameters.

We selected the following parameters for our calculation: 1) We assumed an average soil bulk density of 1.41 g/cm^3 (Sequeira *et al* 2014). 2) We used MODIS data to estimate the total area of Earth's land surface where methanotrophs contribute to atmospheric methane drawdown (Friedl *et al* 2019). We included all land area from ecosystem types in our dataset without persistent local sources of methane: forest, shrubland, grassland/meadow, and cropland (Section 1.8.2). 3) To select

default K_M and V_{max} values for the model, we selected the median values for each ecosystem, and weighted them by the global extent of the respective ecosystem to calculate global median values.

4) We specified the average thickness of the soil layer where methanotrophy may occur as 5.36 cm [4.96, 6.30]. We calibrated this value for soil depth to produce a calculated sink size at the modern methane mixing ratio (1850 ppbv) of 40 Tg yr⁻¹ (range: 37-47 Tg yr⁻¹), matching the average and uncertainty for top-down models in 2017 (Saunio *et al* 2020). Process-based models of methanotrophy have chosen soil depths ranging from 1 to 10 cm (Curry, 2007, 2009; Ridgwell *et al.*, 1999 and references therein), while a recent global model allows the depth of methanotrophic soils to vary as a function of methane diffusion and uptake rates (Murguía-Flores *et al* 2018). Although methanotrophy may certainly occur at a wider range of depths in natural soils, our calibrated value for soil depth partially accounts for the fact that our calculation does not otherwise account for limitations on vertical transport. Values for each parameter are summarized in Supplementary Table 1.1.

1.4) Results and discussion

1.4.1) Compiled K_M and V_{max} values support physiological or evolutionary adaptation of methanotrophs

In this dataset, K_M and V_{max} values each varied over several orders of magnitude: K_M from 10^{3.2} to 10^{9.4} ppbv and V_{max} from 10^{-2.7} to 10^{4.9} nmol CH₄ g dry soil⁻¹ h⁻¹ (Figure 1.2). All but 1 of 413 K_M values exceeded modern atmospheric methane abundance, and the maximum K_M value exceeded atmospheric abundance by 6 orders of magnitude. These high K_M values indicate that soil methanotrophy at ambient methane concentration is generally slow, but that rising methane availability can stimulate large increases in rate. Both K_M and V_{max} values related to the environmental source of the sample. Most low-affinity, high- V_{max} measurements were from landfill or compost soil samples (categorized here as “waste”). These samples come from environments where methanotroph communities experience persistently high local methane concentrations. Meanwhile, most high-affinity, low- V_{max} measurements came from forest and grassland sites. These findings align with previous laboratory experiments showing that the methane concentration available to an enrichment culture can affect the kinetics displayed by that culture, with lower

methane concentrations corresponding with higher-affinity kinetics (Dunfield *et al* 1999, Dunfield and Conrad 2000).

However, substantial variation was also evident within each ecosystem type (Figure 1.2). For example, K_M values spanned 7 orders of magnitude within the full dataset, up to 4 orders of magnitude in ecosystems with limited local methane sources (e.g., grasslands), and up to 6 orders of magnitude in ecosystems with substantial local methane sources (e.g., peat bogs). Similarly, the range of V_{max} values within individual ecosystems spanned up to 6 orders of magnitude, an equivalent range to the full dataset. Within-ecosystem variability may partially be explained by variability in local methane concentrations that is not captured by ecosystem type. Additionally, recent work has shown that the kinetics of methanotrophy can also change within a single strain: some methanotroph strains harbor two distinct types of the particulate methane monooxygenase enzyme used to mediate methane oxidation, each with distinct kinetic properties (Baani and Liesack 2008, Tikhonova *et al* 2021). These findings suggest that a single methanotroph community in a single environment may express distinct kinetic properties under different conditions, for reasons that are not yet understood.

The studies included in our data compilation employed varied sample handling strategies before and during kinetic analyses (Section 1.8.1). These methodological differences could partially account for differences in observed K_M and V_{max} values between studies. A Mann-Whitney U-test showed a statistically significant difference between the K_M and V_{max} values of samples that underwent preincubation, but no significant difference due to amendments. Samples that underwent preincubation were also dominantly from waste sites (82%), unlike samples that did not receive preincubation treatment (23%), making it impossible to conclude whether preincubation caused the observed difference. Other aspects of sample treatment including soil moisture adjustments were not reported with sufficient consistency to perform statistical tests. We suggest that the effect of sample handling on kinetic measurements is a worthwhile topic for future investigation.

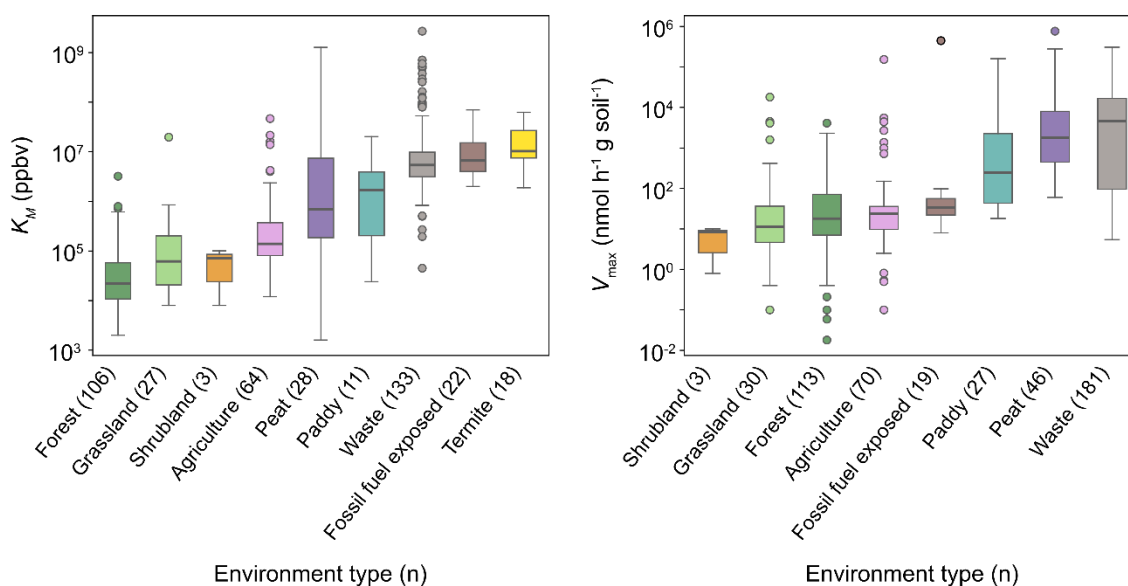


Figure 1.2: Compiled Michaelis-Menten kinetic measurements from natural soil samples (Dion-Kirschner *et al* 2024) sorted by environment type. Categories are ordered from low to high median values, which are indicated by heavy gray lines. For termite mounds, only K_M values were available in the literature.

Across the wide range of K_M and V_{max} values in our compiled dataset, we found that the two parameters were positively correlated when \log_{10} -transformed, demonstrated by a standardized major axis (SMA) regression ($r^2 = 0.44$, slope = $10^{-2.94}$ nmol g soil⁻¹ h⁻¹ ppbv⁻¹) (Figure 1.3). This correlation is not an inherent property of the methods for deriving or measuring K_M and V_{max} values. Few similar compilations of kinetic data are available to investigate the prevalence of this trend; however, a study of the kinetics of nitrification did not reveal a correlation between K_M and V_{max} values (Kits *et al* 2017), indicating that this trend is not ubiquitous in biological systems. A study that investigated *in vitro* k_{cat} and K_M values across several thousand enzymes showed a weak correlation between these two parameters ($r^2 = 0.09$) (Bar-Even *et al* 2011). Because V_{max} is a function of k_{cat} and the concentration of active sites, a similarly weak correlation between K_M and V_{max} values might be expected across diverse enzyme classes. The study noted stronger correlations in enzyme classes with simple catalytic mechanisms and particularly low correlations for many monooxygenase enzymes.

The correlation we observed between methanotrophy kinetic parameters may reflect physiological or evolutionary processes through which methanotrophs adapt to the availability of methane in their ecological niches. A low K_M value suggests a high affinity for methane, an advantageous trait in

environments where methanotrophs subsist on primarily atmospheric methane, like forests and grasslands. Conversely, a high V_{max} value paired with a higher K_M value implies rapid methane oxidation at elevated methane levels, enabling faster methane turnover and possibly faster growth in methane-rich environments such as landfills or peatlands. If methanotrophs have adapted their enzymatic properties according to substrate availability, they are not alone among biological systems. For instance, the oxygen reductase enzyme families involved in aerobic respiration demonstrate a tradeoff between oxygen affinity and proton pumping capacity (Han *et al* 2011). Methanotrophy may offer another example where ecological niche partitioning drives enzymatic adaptations. This possible evolutionary mechanism, alongside the grouping of variability in kinetic parameters by ecosystem type in our dataset, supports that ecosystem type may be a useful constraint for predicting methanotrophy kinetics.

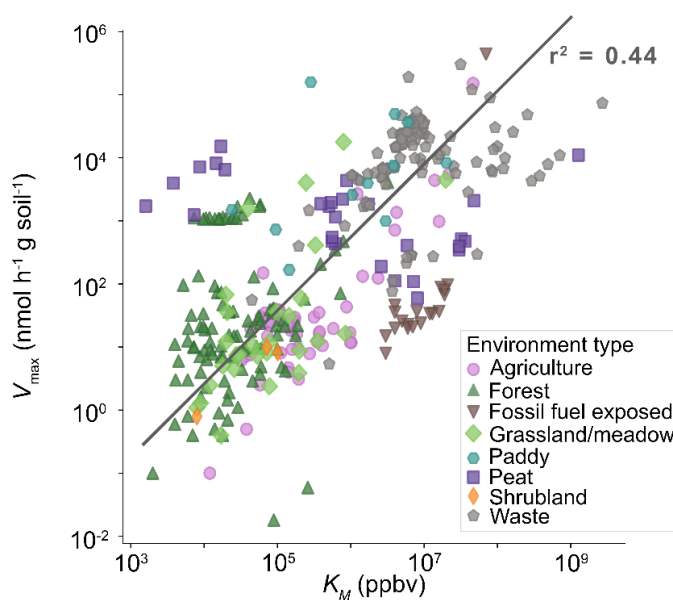


Figure 1.3: Compiled Michaelis-Menten kinetic measurements from natural soil samples (Dion-Kirschner *et al.*, 2024). Point shape and color correspond to the environment where the measured soil sample was obtained. Dark gray line represents a standardized major axis regression performed on the \log_{10} -transformed K_M and V_{max} data using the Python package `plyr2` ($r^2 = 0.44$).

Previous studies have found that laboratory cultures can develop a higher affinity for methane under extended incubation with low methane availability (Dunfield *et al* 1999, Dunfield and Conrad 2000). These changes could result from a change in the expression of methane monooxygenase enzymes with distinct kinetic properties (Baani and Liesack 2008, Tikhonova *et al* 2021). In enrichment cultures, kinetic changes could also reflect the selective enrichment of taxa with higher methane

affinity. However, in these culture studies, the decrease in K_M was accompanied by a decrease in V_{max} values only under starvation conditions (Dunfield and Conrad 2000), and not when samples were methane-replete (Dunfield *et al* 1999). Dunfield and Conrad suggested that concomitant decreases in K_M and V_{max} may have resulted from limitation in a cosubstrate, such as NADH. This provides an additional explanation for the correlation between K_M and V_{max} in natural samples: methanotrophs may frequently be limited for substrates other than methane. It may be that physiological adaptations, evolutionary adaptations, and cosubstrate limitation all contribute to the correlation evident in this compiled dataset.

1.4.2) Comparing Michaelis-Menten kinetics to linear rate constants

We calibrated our idealized calculation to yield a methanotrophy sink of 40 Tg yr⁻¹ [37, 47] at 1850 ppbv methane. By calibrating our parameters to produce a realistic methane sink size under a modern methane mixing ratio, we were able to test the effect of different kinetic models and kinetic parameter values on the calculated soil methane sink size relative to a reasonable baseline. To test the importance of the choice of kinetic model, we quantified the effect of implementing Michaelis-Menten versus linear kinetics on the calculated soil methane sink size. We identified the first quartile, median, and third quartile K_M and V_{max} values for each ecosystem (Figure 1.2), and calculated area-weighted average kinetic parameters for each quartile. For each set of K_M and V_{max} values, we calculated the corresponding first-order rate constants by solving Equation 1.1 for $[S] = 1850$ and dividing the result by $[S]$.

Both kinetic models agreed closely at modern and historical pCH₄ values (Figure 1.4). This results from the fact that most K_M values substantially exceed the atmospheric abundance of methane: Michaelis-Menten kinetics produce a near-linear response when $[S]$ is much smaller than K_M . The soil methane sink size calculated from the two models diverged most at high pCH₄ and low values of K_M . At 4000 ppbv methane, linear kinetics using 1st quartile kinetic values yielded a sink of 75 Tg yr⁻¹, while Michaelis-Menten kinetics yielded a sink of 70 Tg yr⁻¹, a 1.1-fold difference. As pCH₄ reached closer values to K_M , the linear and Michaelis-Menten models reached a 1.2-fold difference of 22 Tg yr⁻¹ at 8000 ppbv. Our findings indicate that under very high-emissions projections such as SSP 3-7.0 (Kleinen *et al* 2021), a linear rate constant may overestimate the size of the soil methane

sink. However, in all cases, results of the two kinetic models overlapped when accounting for the uncertainty in the modern methane sink size used to calibrate our calculation. The difference between the two kinetic models was greatest for the lowest K_M values, where Michaelis-Menten kinetics produce a saturation effect at lower values of $p\text{CH}_4$. Therefore, models focusing on the methane sink in forest environments, where K_M and V_{max} values are typically low (Figure 1.2), may derive a benefit from implementing Michaelis-Menten kinetics. Generally, however, differences between the calculated soil methane sink size were far more pronounced between quartiles of kinetic values than between linear and Michaelis-Menten kinetic models. As a result, the selection of kinetic parameters may be more important to accurate modeling results than the choice of kinetic model.

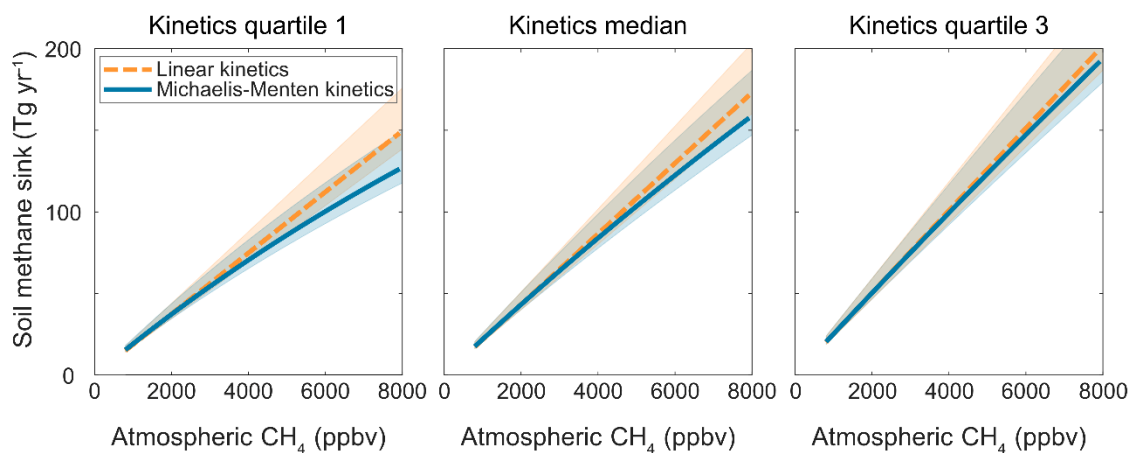


Figure 1.4. Comparison of calculated soil methane sink size for linear and Michaelis-Menten kinetics across a range of atmospheric CH_4 mixing ratios and quartiles of kinetic data. Shaded regions represent calculated results across the range of soil depth values [4.96 cm, 6.30 cm] calibrated to match uncertainty in the soil methane sink [37 Tg yr^{-1} , 47 Tg yr^{-1}] under the modern methane mixing ratio, as described in Section 1.3.2.

1.4.3) Quantifying the effect of kinetic variability

We found that the soil methane sink size calculated under the Michaelis-Menten model was highly sensitive to the K_M and V_{max} values used as model inputs. We first calculated the sink size across all combinations of K_M and V_{max} values between the 1st and 3rd quartiles for the ecosystem types without persistent local methane sources. K_M values ranged from 18,000 to 141,000 ppbv and V_{max} values from 0.71 to 3.83 $\text{nmol g soil}^{-1} \text{ hour}^{-1}$. Within this range of kinetic parameters, the calculated soil

methane sink varied from 11 [10, 12] to 410 [378, 481] Tg year⁻¹, a 37-fold difference between the minimum and maximum values (Figure 1.5).

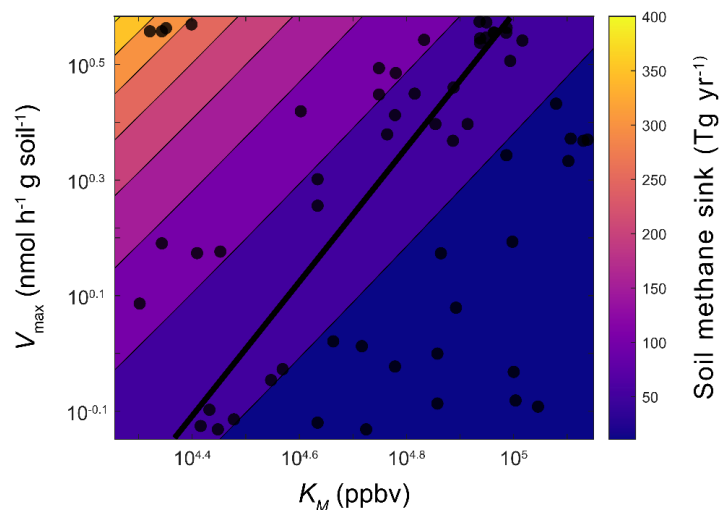


Figure 1.5. Sensitivity of the modeled methane sink size to the kinetic parameters of methanotrophy. Black points are the kinetic measurements from natural soil samples that fall within the interquartile range of the data compilation, shown in greater detail in Figure 1.3. Black solid line is a standardized major axis regression on the log₁₀-transformed K_M and V_{max} values.

We also tested whether the correlation between K_M and V_{max} values constrained the possible range for the soil methane sink strength. As noted in section 2.4.1, the K_M and V_{max} values from natural samples covaried (r^2 for log-transformed data = 0.44). We first calculated the soil methane sink size using K_M and V_{max} values that were limited to ordered pairs from natural samples, including only pairs where both K_M and V_{max} values were between the 1st and 3rd quartile values from low-methane ecosystems. The calculated soil methane sink values ranged from 15 [14, 18] to 415 [384, 488] Tg year⁻¹, a 28-fold difference between minimum and maximum values. We also calculated the soil methane sink size when pairs of K_M and V_{max} values all fell within the 95% confidence interval of the SMA regression slope ($10^{-2.97}$ - $10^{-2.91}$). This calculation yielded a sink size ranging from 52 [48, 61] to 76 [70, 89] Tg year⁻¹, a 1.5-fold difference between minimum and maximum predicted sink sizes—much smaller than the 37-fold difference where the correlation was not accounted for. This finding suggests that the correlation between K_M and V_{max} values can lend certainty to estimates of the soil methane sink, and that a deeper understanding of the controls on methanotroph kinetics can support more accurate models.

1.4.4) Comparing kinetic and temperature sensitivity of the soil methane sink

Finally, we compared the sensitivity of our calculated methane sink size to atmospheric methane (via kinetics) versus its sensitivity to global temperature. To assess the temperature sensitivity of soil methanotrophy, we used a temperature coefficient, or Q_{10} . Q_{10} values are commonly used to express the rate of biological reactions as an exponential function of temperature, including for methanotrophy (e.g., Segers 1998). Only 14 studies in our compiled dataset reported Q_{10} values, of which 8 measured exclusively landfill samples, making it difficult to predict expected Q_{10} values for soils globally. For this reason, we elected to use a previously published Q_{10} value of 1.95 (Murguía-Flores *et al* 2018). This value was calculated from a compilation of global methanotrophy rates and was used in a recent process-based model of methanotrophy; additionally, it fell within the range of observations from low-methane environments in our compiled dataset (Dion-Kirschner *et al.*, 2024). We used this Q_{10} value to calculate the estimated soil methane sink size for 5 Shared Socioeconomic Pathways (SSPs) based on the predicted atmospheric methane concentration (McBride *et al* 2021, Riahi *et al* 2017) and global mean near-surface air temperature increase (Tebaldi *et al* 2021) for each SSP. The methane concentration and temperature data we used as inputs were globally averaged projected values for 2100. We performed this calculation by modifying Equation 1.1 as follows:

$$V = \left(V_{max} \frac{[S]}{K_M + [S]} \right) Q_{10}^{\frac{\Delta T}{10}} \quad (1.2)$$

where ΔT is the projected near-surface air temperature increase (Tebaldi *et al* 2021). Although methanotrophy is located in the soil, where temperatures are often offset from air temperatures, the projected changes in air and soil temperatures are expected to be similar in magnitude (e.g., Soong *et al* 2020).

Our calculations yielded increased soil methane sink values in proportion to both temperature and atmospheric methane concentration, as has been found in previous work (Oh *et al* 2020) (Figure 1.6). The combined kinetic and temperature response to the SSPs resulted in a 2.8-fold increase in the soil methane sink strength from SSP1-1.9 to SSP5-8.5, while the kinetic response alone produced a 1.8-fold increase, indicating that kinetics may be of equal or greater importance to future changes in the soil methane sink than the temperature response. The variation in soil methanotrophy kinetics produced variability in the predicted soil methane sink size across all five SSPs. Further, the

variability under each SSP between quartiles of kinetic data was of a similar magnitude to the uncertainty introduced by the 90% confidence interval of CMIP6 temperature projections. Calculations based on bootstrapped 90% confidence intervals on kinetic median values produced a similar range of variability as the range between quartiles, but bootstrapping calculations were limited by the sparsity of shrubland data (Figure 1.7). In total, these results support that the uncertainty in methanotrophy kinetics may be an important contributor to uncertainty in models of the soil methane sink.

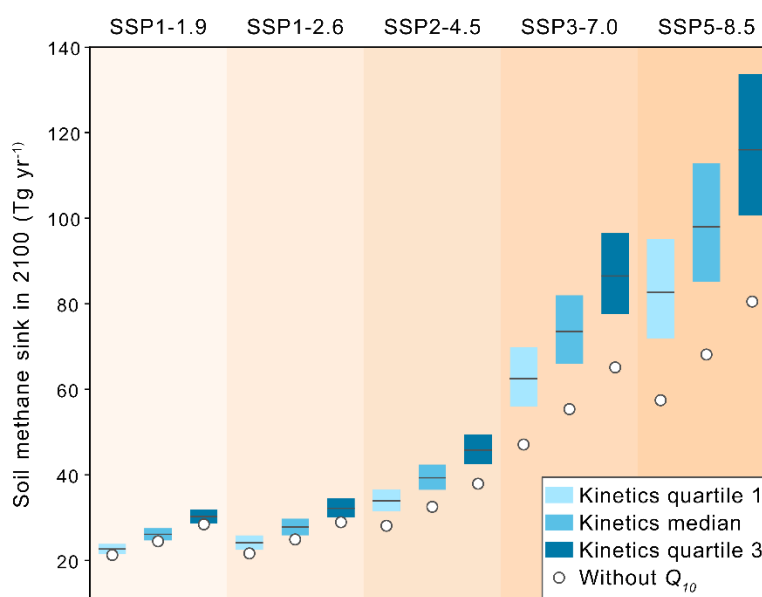


Figure 1.6. The combined effects of kinetic variability, globally averaged near-surface air temperature increases, and atmospheric methane concentrations from Shared Socioeconomic Pathway projections on the calculated soil methane sink size for 2100. Bars represent uncertainty ranges and lines represent average values for projected global mean near-surface air temperatures from CMIP6 (Tebaldi *et al* 2021). Open circles indicate the effect of atmospheric methane increases in the absence of temperature sensitivity.

1.5) Summary and recommendations

This work provides the first comprehensive compilation of methanotrophy kinetics, lending support to modeling efforts for the soil methane sink which are often data-limited (Murguia-Flores *et al* 2018). The compiled dataset revealed a correlation between methanotrophy K_M and V_{max} values in natural samples, which could result from physiological and/or evolutionary adaptations according to ambient methane mixing ratios, or from cosubstrate limitation. In an idealized calculation of the soil methane sink based on our compiled kinetic data, our results indicated that linear and Michaelis-

Menten kinetics closely replicate the modeled soil methane sink size over a modest range of CH₄ mixing ratios. In extreme scenarios, linear kinetics overestimate the size of the sink. This overestimation is especially important in environments where high-affinity methanotrophy dominates, such as forests and grasslands. Nevertheless, the choice of kinetic parameters had a larger effect on the calculated soil methane sink size than the choice of kinetic model. Additionally, the correlation between K_M and V_{max} values substantially constrained the range of possible values for the calculated soil methane sink, indicating that a clearer understanding of the mechanisms driving methanotrophy kinetics can reduce modeling uncertainty. Our calculations comparing the effects of future atmospheric methane concentrations and temperature indicated that kinetic variability may introduce a significant source of uncertainty into models of the soil methane sink.

The values reported here are spatially and temporally unresolved, and were calculated using globally averaged parameters rather than a process-based model. By taking this simplified approach, we were able to efficiently test a wide range of input parameters and understand their impact on the outcomes. While a process-based model may amplify or dampen the magnitude of the trends we observe here due to interactions between variables, our results illustrate that methanotrophy kinetics are likely to exert a significant effect on the projected soil methane sink size. This finding highlights the potential value of thoughtfully implementing methanotrophy kinetics in future process-based models. Accordingly, we make several recommendations for ongoing work that can build on our findings.

We recommend that researchers prioritize further kinetic measurements of natural soils, focusing on environments that are underrepresented in our data compilation (e.g., high and low latitudes and sparsely vegetated environments). Our findings also indicate the importance of ongoing experimental work to better determine controls on the kinetics exhibited by methanotroph populations, including the effect of sample preparation methods. More complete datasets and improved mechanistic understanding will support modelers in selecting appropriate kinetic parameters for their models. The choice of linear versus Michaelis-Menten kinetics may be less consequential than the selection of accurate kinetic parameters or rate constants, and modelers may consider assigning different kinetic parameters for different ecosystems. Overall, our results highlight the value in better understanding the mechanisms underlying microbial methane oxidation

kinetics, and indicate that a stronger understanding will improve the accuracy of process-based models of the methane cycle.

1.6) Acknowledgments

This project was supported by the Resnick Sustainability Institute at Caltech and the Center for Environmental-Microbial Interactions at Caltech. We express our gratitude to Benjamin Poulter, Xiaojing (Ruby) Fu, Adrian Moure, Avi Flamholz, Joshua Goldford, and Tapio Schneider for helpful discussions of early results, to Joshua Anadu for assistance with data visualization, to three anonymous reviewers for insightful suggestions for improving this work, and to Christopher Cappa and three reviewers for constructive feedback on an earlier version of the manuscript.

1.7) References

- Alvarez-Ramirez J, Meraz M and Jaime Vernon-Carter E 2019 A theoretical derivation of the monod equation with a kinetics sense *Biochemical Engineering Journal* 150 107305
- Baani M and Liesack W 2008 Two isozymes of particulate methane monooxygenase with different methane oxidation kinetics are found in *Methylocystis* sp. strain SC2 *Proceedings of the National Academy of Sciences* 105 10203–8
- Bar-Even A, Noor E, Savir Y, Liebermeister W, Davidi D, Tawfik D S and Milo R 2011 The Moderately Efficient Enzyme: Evolutionary and Physicochemical Trends Shaping Enzyme Parameters *Biochemistry* 50 4402–10
- Bender M and Conrad R 1992 Kinetics of CH₄ oxidation in oxic soils exposed to ambient air or high CH₄ mixing ratios *FEMS Microbiology Ecology* 10 261–9
- Bender M and Conrad R 1993 Kinetics of methane oxidation in oxic soils *Chemosphere* 26 687–96
- Curry C L 2007 Modeling the soil consumption of atmospheric methane at the global scale *Global Biogeochemical Cycles* 21 Online: <https://agupubs.onlinelibrary.wiley.com/doi/abs/10.1029/2006GB002818>
- Curry C L 2009 The consumption of atmospheric methane by soil in a simulated future climate *Biogeosciences* 6 2355–67
- Dion-Kirschner H, Nguyen N, Frankenberg C and Fischer W 2024 A comprehensive compilation of Michaelis-Menten kinetic observations of methanotrophy Online: <https://zenodo.org/records/11225342>
- Dunfield P F and Conrad R 2000 Starvation Alters the Apparent Half-Saturation Constant for Methane in the Type II Methanotroph *Methylocystis* Strain LR1 *Appl. Environ. Microbiol.* 66 4136–8

- Dunfield P F, Liesack W, Henckel T, Knowles R and Conrad R 1999 High-Affinity Methane Oxidation by a Soil Enrichment Culture Containing a Type II Methanotroph *Appl. Environ. Microbiol.* 65 1009–14
- Dutaur L and Verchot L V 2007 A global inventory of the soil CH₄ sink *Global Biogeochemical Cycles* 21 Online: <https://agupubs.onlinelibrary.wiley.com/doi/abs/10.1029/2006GB002734>
- Han H, Hemp J, Pace L A, Ouyang H, Ganesan K, Roh J H, Daldal F, Blanke S R and Gennis R B 2011 Adaptation of aerobic respiration to low O₂ environments *Proceedings of the National Academy of Sciences* 108 14109–14
- Kits K D, Sedlacek C J, Lebedeva E V, Han P, Bulaev A, Pjevac P, Daebeler A, Romano S, Albertsen M, Stein L Y, Daims H and Wagner M 2017 Kinetic analysis of a complete nitrifier reveals an oligotrophic lifestyle *Nature* 549 269–72
- Kleinen T, Gromov S, Steil B and Brovkin V 2021 Atmospheric methane underestimated in future climate projections *Environ. Res. Lett.* 16 094006
- Knief C and Dunfield P F 2005 Response and adaptation of different methanotrophic bacteria to low methane mixing ratios *Environmental Microbiology* 7 1307–17
- Lacroix E M, Aeppli M, Boye K, Brodie E, Fendorf S, Keiluweit M, Naughton H R, Noël V and Sihi D 2023 Consider the Anoxic Microsite: Acknowledging and Appreciating Spatiotemporal Redox Heterogeneity in Soils and Sediments *ACS Earth Space Chem.* 7 1592–609
- Liu Y 2007 Overview of some theoretical approaches for derivation of the Monod equation *Appl Microbiol Biotechnol* 73 1241–50
- McBride L A, Hope A P, Canty T P, Bennett B F, Tribett W R and Salawitch R J 2021 Comparison of CMIP6 historical climate simulations and future projected warming to an empirical model of global climate *Earth System Dynamics* 12 545–79
- Murguía-Flores F, Arndt S, Ganesan A L, Murray-Tortarolo G and Hornibrook E R C 2018 Soil Methanotrophy Model (MeMo v1.0): a process-based model to quantify global uptake of atmospheric methane by soil *Geoscientific Model Development* 11 2009–32
- Nunan N, Schmidt H and Raynaud X 2020 The ecology of heterogeneity: soil bacterial communities and C dynamics *Philosophical Transactions of the Royal Society B: Biological Sciences* 375 20190249
- Oh Y, Zhuang Q, Liu L, Welp L R, Lau M C Y, Onstott T C, Medvigy D, Bruhwiler L, Dlugokencky E J, Hugelius G, D'Imperio L and Elberling B 2020 Reduced net methane emissions due to microbial methane oxidation in a warmer Arctic *Nature Climate Change* 10 317–21
- Riahi K, van Vuuren D P, Kriegler E, Edmonds J, O'Neill B C, Fujimori S, Bauer N, Calvin K, Dellink R, Fricko O, Lutz W, Popp A, Cuaresma J C, Kc S, Leimbach M, Jiang L, Kram T, Rao S, Emmerling J, Ebi K, Hasegawa T, Havlik P, Humpenöder F, Da Silva L A, Smith S, Stehfest E, Bosetti V, Eom J, Gernaat D, Masui T, Rogelj J, Strefler J, Drouet L, Krey V, Luderer G, Harmsen M, Takahashi K, Baumstark L, Doelman J C, Kainuma M, Klimont Z,

- Marangoni G, Lotze-Campen H, Obersteiner M, Tabeau A and Tavoni M 2017 The Shared Socioeconomic Pathways and their energy, land use, and greenhouse gas emissions implications: An overview *Global Environmental Change* 42 153–68
- Ridgwell A J, Marshall S J and Gregson K 1999 Consumption of atmospheric methane by soils: A process-based model *Global Biogeochemical Cycles* 13 59–70
- Sauniois M, Stavert A R, Poulter B, Bousquet P, Canadell J G, Jackson R B, Raymond P A, Dlugokencky E J, Houweling S, Patra P K, Ciais P, Arora V K, Bastviken D, Bergamaschi P, Blake D R, Brailsford G, Bruhwiler L, Carlson K M, Carrol M, Castaldi S, Chandra N, Crevoisier C, Crill P M, Covey K, Curry C L, Etiope G, Frankenberg C, Gedney N, Hegglin M I, Höglund-Isaksson L, Hugelius G, Ishizawa M, Ito A, Janssens-Maenhout G, Jensen K M, Joos F, Kleinen T, Krummel P B, Langenfelds R L, Laruelle G G, Liu L, Machida T, Maksyutov S, McDonald K C, McNorton J, Miller P A, Melton J R, Morino I, Müller J, Murguía-Flores F, Naik V, Niwa Y, Noce S, O’Doherty S, Parker R J, Peng C, Peng S, Peters G P, Prigent C, Prinn R, Ramonet M, Regnier P, Riley W J, Rosentretter J A, Segers A, Simpson I J, Shi H, Smith S J, Steele L P, Thornton B F, Tian H, Tohjima Y, Tubiello F N, Tsuruta A, Viovy N, Voulgarakis A, Weber T S, van Weele M, van der Werf G R, Weiss R F, Worthy D, Wunch D, Yin Y, Yoshida Y, Zhang W, Zhang Z, Zhao Y, Zheng B, Zhu Q, Zhu Q and Zhuang Q 2020 The Global Methane Budget 2000–2017 *Earth Syst. Sci. Data* 12 1561–623
- Segers R 1998 Methane production and methane consumption: a review of processes underlying wetland methane fluxes *Biogeochemistry* 41 23–51
- Sequeira C H, Wills S A, Seybold C A and West L T 2014 Predicting soil bulk density for incomplete databases *Geoderma* 213 64–73
- Shu S, Jain A K and Khashgi H S 2020 Investigating Wetland and Nonwetland Soil Methane Emissions and Sinks Across the Contiguous United States Using a Land Surface Model *Global Biogeochemical Cycles* 34 e2019GB006251
- Soong J L, Phillips C L, Ledna C, Koven C D and Torn M S 2020 CMIP5 Models Predict Rapid and Deep Soil Warming Over the 21st Century *Journal of Geophysical Research: Biogeosciences* 125 e2019JG005266
- Tebaldi C, Debeire K, Eyring V, Fischer E, Fyfe J, Friedlingstein P, Knutti R, Lowe J, O’Neill B, Sanderson B, van Vuuren D, Riahi K, Meinshausen M, Nicholls Z, Tokarska K B, Hurtt G, Kriegler E, Lamarque J-F, Meehl G, Moss R, Bauer S E, Boucher O, Brovkin V, Byun Y-H, Dix M, Gualdi S, Guo H, John J G, Kharin S, Kim Y, Koshiro T, Ma L, Olivié D, Panickal S, Qiao F, Rong X, Rosenbloom N, Schupfner M, Séférian R, Sellar A, Semmler T, Shi X, Song Z, Steger C, Stouffer R, Swart N, Tachiiri K, Tang Q, Tatebe H, Voldoire A, Volodin E, Wyser K, Xin X, Yang S, Yu Y and Ziehn T 2021 Climate model projections from the Scenario Model Intercomparison Project (ScenarioMIP) of CMIP6 Earth System Dynamics 12 253–93
- Tikhonova E N, Grouzdev D S, Avtukh A N and Kravchenko I K 2021 *Methylocystis silviterrae* sp.nov., a high-affinity methanotrophic bacterium isolated from the boreal forest soil *International Journal of Systematic and Evolutionary Microbiology* 71 005166

1.8) Supplementary information

1.8.1) Detailed methods for data compilation

We identified relevant publications using a Google Scholar search with the search terms “soil AND kinetic AND Michaelis-Menten OR Monod OR Vmax AND intitle:methane OR intitle:ch4.” Out of 909 results for these search terms, 67 publications dating from between 1987 and 2023 met our requirements for reporting V_{\max} and/or K_M values for natural soils (Dion-Kirschner et al., 2024). These 67 publications yielded 542 individual observations of V_{\max} and/or K_M values, predominantly from Europe and North America. Land uses in the compiled data included crop land, rice paddies, landfills, and fossil fuel extraction sites. Only 36 of 542 observations were from the tropics (7%), and 18 from latitudes > 60 degrees (3%).

Studies in our compiled dataset used variable approaches to measure and calculate sample V_{\max} and K_M values. Broadly, kinetic values were measured by exposing soil samples to a range of methane concentrations, then taking headspace samples to measure the rate of methane decrease over a period of hours to days. Sample treatment before and during kinetic measurements varied among studies. In 17 of 67 studies, samples were preincubated in the lab for days or longer at high methane concentration; in 10, soil samples were amended with nitrogen species, potassium, or biochar (Dion-Kirschner et al., 2024). The treatment of sample water content also varied, where some samples were adjusted to specific water content values or slurried with water, while others were maintained at their original soil moisture values. Instances of preincubation, sample amendment, and adjustment to specific moisture levels are noted in Dion-Kirschner et al., 2024. As there is no established standard protocol for soil methanotrophy kinetic measurements, we did not attempt to correct or account for different treatments among studies. Section 2.4.1 of the main text contains further discussion of sample treatment variability.

We performed unit conversions as needed to harmonize the dataset for analysis. When K_M was reported as aqueous methane concentration, we assumed that $[\text{CH}_4]_{\text{aqueous}}$ was in equilibrium with headspace $p\text{CH}_4$ according to Henry’s Law to convert to units of ppbv. Since the most common unit

for V_{\max} values was $\text{nmol CH}_4 \text{ hour}^{-1} \text{ g soil}^{-1}$, we converted all other units to match. We used reported values for soil bulk density as needed to convert from soil volume to mass. Soil bulk density values are reported in Dion-Kirschner et al., 2024.

1.8.2) Detailed methods for soil methane sink calculations

Our selected value for soil bulk density was based on the mean value from a National Resource Conservation Service database of over 20,000 samples (Sequeira *et al* 2014). To estimate the total land surface area hosting methanotrophs contributing to atmospheric methane drawdown, we excluded permanent wetlands, water bodies, and urban and built-up land where drawdown of atmospheric methane is expected to be negligible. Additionally, we excluded areas of permanent snow and ice and barren or sparsely vegetated land: although some evidence exists for methanotrophy in these landscapes (Dion-Kirschner *et al* 2023; Mosier *et al* 1997; Sommerfeld *et al* 1993; Striegl *et al* 1992), no kinetic data was available.

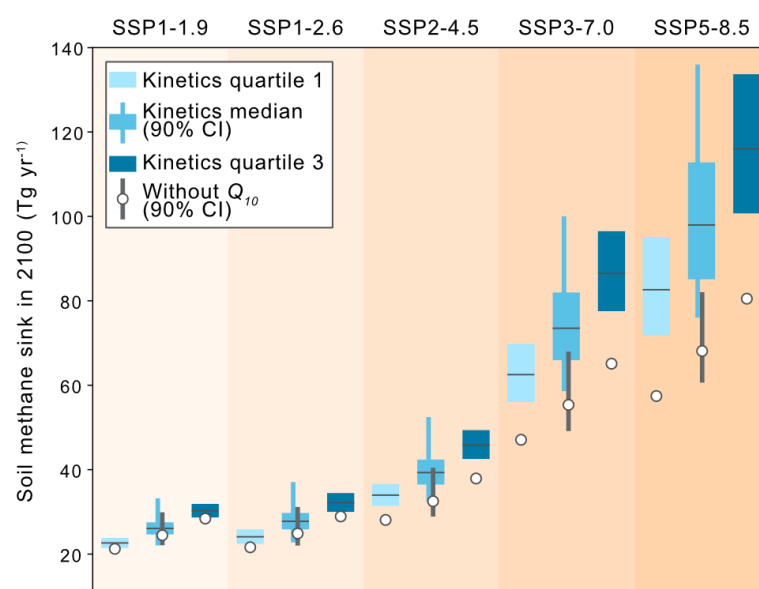
Supplementary Table 1.1 Default input values for soil methane sink calculations.

Parameter	Input value	Source
K_M	67,000 ppbv	Ecosystem-weighted median value from low-flux ecosystems in literature compilation
V_{\max}	$1.30 \text{ nmol CH}_4 \text{ g dry soil}^{-1} \text{ h}^{-1}$	Ecosystem-weighted median value from low-flux environments in literature compilation
$V_{\max, \text{ global}}$	$1.43 \text{ ppbv CH}_4 \text{ d}^{-1}$	$\frac{V_{\max} * 24 \text{ h d}^{-1} * 16.04 * 10^{-9} \text{ g CH}_4 \text{ nmol}^{-1} * \rho_b * Z * A}{10^{12} * 2.8611 \text{ g CH}_4 \text{ ppb}^{-1}}$
ρ_b (bulk soil density)	1.41 g cm^{-3}	Sequeira <i>et al</i> 2014
Z (thickness of soil methanotrophic zone)	5.36 [4.96, 6.30] cm	Calibrated to average and uncertainty of 2017 top-down estimates from Sauniois <i>et al</i> 2020
A (Earth's surface area hosting methanotrophy)	$107.806 \times 10^{16} \text{ cm}^2$	MODIS (Friedl <i>et al</i> 2019)

Supplementary Table 1.2. Kinetic constant data summary by ecosystem.

Ecosystem or land use (n)	K_M mean (ppm)	K_M range	V_{\max} mean (nmol dry soil ⁻¹ h ⁻¹)	V_{\max} range
Agriculture (70)	1918	12-46,700	243	0-15,300
Forest (113)	92	2-3,210	26	0-410

Fossil fuel exposed soil (24)	11,690	2,000-70,000	2356	1-44,500
Grassland/meadow (30)	847	8-19700	97	0-1,803
Rice paddy (27)	3,667	24-20200	1056	2-16,000
Peat (46)	52,960	2-1,272,000	3,796	0-76,300
Shrubland (3)	60	8-101	1	0-1
Termite mounds (18)	17,540	1,883-62,499	N.D.	N.D.
Waste (211)	58,279	45-2,700,000	1313	1-30,729



Supplementary Figure 1.7. The combined effects of kinetic variability, globally averaged near-surface air temperature increases, and atmospheric methane concentrations from Shared Socioeconomic Pathway projections on the calculated soil methane sink size for 2100. Bars represent uncertainty ranges and horizontal gray lines represent average values for projected global mean near-surface air temperatures from CMIP6 (Tebaldi et al 2021). Open circles indicate the effect of atmospheric methane increases in the absence of temperature sensitivity. Vertical blue and gray lines indicate the range of soil methane sink values calculated for the 90% confidence interval on median kinetic parameters assessed by bootstrapping. Note that bootstrapping results are biased by the inadequate number of data points in the shrubland ecosystem ($n = 3$, see Dion-Kirschner et al., 2024).

1.8.3) Supplementary material references

Dion-Kirschner H, Nguyen N, Frankenberg C and Fischer W 2024 A comprehensive compilation of Michaelis-Menten kinetic observations of methanotrophy Online: <https://zenodo.org/records/11225342>

Friedl M and Sulla-Menashe D 2022 (NASA EOSDIS Land Processes Distributed Active Archive Center) <https://doi.org/10.5067/MODIS/MCD12Q1.061>

- Mosier A R, Delgado J A, Cochran V L, Valentine D W and Parton W J 1997 Impact of agriculture on soil consumption of atmospheric CH₄ and a comparison of CH₄ and N₂O flux in subarctic, temperate and tropical grasslands
- Saunois M, Stavert A R, Poulter B, Bousquet P, Canadell J G, Jackson R B, Raymond P A, Dlugokencky E J, Houweling S, Patra P K, Ciais P, Arora V K, Bastviken D, Bergamaschi P, Blake D R, Brailsford G, Bruhwiler L, Carlson K M, Carrol M, Castaldi S, Chandra N, Crevoisier C, Crill P M, Covey K, Curry C L, Etiope G, Frankenberg C, Gedney N, Hegglin M I, Höglund-Isaksson L, Hugelius G, Ishizawa M, Ito A, Janssens-Maenhout G, Jensen K M, Joos F, Kleinen T, Krummel P B, Langenfelds R L, Laruelle G G, Liu L, Machida T, Maksyutov S, McDonald K C, McNorton J, Miller P A, Melton J R, Morino I, Müller J, Murguía-Flores F, Naik V, Niwa Y, Noce S, O'Doherty S, Parker R J, Peng C, Peng S, Peters G P, Prigent C, Prinn R, Ramonet M, Regnier P, Riley W J, Rosentreter J A, Segers A, Simpson I J, Shi H, Smith S J, Steele L P, Thornton B F, Tian H, Tohjima Y, Tubiello F N, Tsuruta A, Viovy N, Voulgarakis A, Weber T S, van Weele M, van der Werf G R, Weiss R F, Worthy D, Wunch D, Yin Y, Yoshida Y, Zhang W, Zhang Z, Zhao Y, Zheng B, Zhu Q, Zhu Q and Zhuang Q 2020 The Global Methane Budget 2000–2017 *Earth Syst. Sci. Data* 12 1561–623
- Sequeira C H, Wills S A, Seybold C A and West L T 2014 Predicting soil bulk density for incomplete databases *Geoderma* 213 64–73
- Sommerfeld R A, Mosier A R and Musselman R C 1993 CO₂, CH₄ and N₂O flux through a Wyoming snowpack and implications for global budgets *Nature* 361 140–2
- Striegl R G, McConnaughey T A, Thorstenson D C, Weeks E P and Woodward J C 1992 Consumption of atmospheric methane by desert soils *Nature* 357 145–7
- Tebaldi C, Debeire K, Eyring V, Fischer E, Fyfe J, Friedlingstein P, Knutti R, Lowe J, O'Neill B, Sanderson B, van Vuuren D, Riahi K, Meinshausen M, Nicholls Z, Tokarska K B, Hurtt G, Kriegler E, Lamarque J-F, Meehl G, Moss R, Bauer S E, Boucher O, Brovkin V, Byun Y-H, Dix M, Gualdi S, Guo H, John J G, Kharin S, Kim Y, Koshiro T, Ma L, Olivié D, Panickal S, Qiao F, Rong X, Rosenbloom N, Schupfner M, Séférian R, Sellar A, Semmler T, Shi X, Song Z, Steger C, Stouffer R, Swart N, Tachiiri K, Tang Q, Tatebe H, Voldoire A, Volodin E, Wyser K, Xin X, Yang S, Yu Y and Ziehn T 2021 Climate model projections from the Scenario Model Intercomparison Project (ScenarioMIP) of CMIP6 Earth System Dynamics 12 253–93

*Chapter 2***TRENDS IN DRYLAND SOIL METHANE UPTAKE HIGHLIGHT
KNOWLEDGE GAPS IN SOIL METHANE MODELING**

Hannah Dion-Kirschner, Katie R. Huy, Elin Larsson, John S. Magyar, Avi Flamholz, Bryn Stewart, and Woodward W. Fischer

2.1) Abstract

Despite the importance of the soil methane sink to global methane cycling, modeled global methanotrophy rates are still highly uncertain. This is especially true for dryland ecosystems, which cover over 40% of Earth's surface, but are drastically underrepresented in soil methane flux datasets. Here, we present 275 new field measurements of soil methane fluxes from three California dryland sites, paired with soil physical, chemical, and biological analyses. We compare these observations to predictions from a simple model that incorporates common model parameterizations of soil methane fluxes. While prior studies have often identified strong climate sensitivity of soil methane fluxes—especially in response to soil moisture—we find that methane uptake's seasonality and its correlation with soil temperature and moisture are weak or absent at these dryland sites. Our findings suggest that both methanogenesis and methanotrophy in dryland soils may be moisture-limited, muting seasonal and climatic signals. Methane uptake is most significantly stratified by vegetation type; we hypothesize that this relationship is mediated by soil organic carbon inputs. Comparing our measured and modeled results, we find that the model recapitulates average uptake rates within an order of magnitude at two out of three field sites, even when no parameters are tuned to match observations; tuning parameters would allow an exact match of average modeled uptake rates. However, the model fails to reproduce the observed lack of seasonal trends. We attribute these mismatches to three key factors: inaccurate parameterization of climate sensitivity, omission of influential variables like vegetation type, and mismatches between the spatial and temporal scales of models and observations. Our findings highlight the need for further investigation of the climate and ecological sensitivity of dryland methane fluxes, and indicate potential avenues to improve methane cycle models for a widespread climate type.

2.2) Introduction

Methane is responsible for ~31% of anthropogenic climate warming (Forster *et al* 2021), but only one Earth surface process is known to drive meaningful atmospheric methane removal: the aerobic oxidation of methane by soil microbes. This process, called methanotrophy, is thought to draw down ~35 Tg of methane from the atmosphere annually, accounting for ~5% of the sink for atmospheric methane, while atmospheric chemical reactions make up the other ~95% (Saunio *et al* 2020). Although methanotrophy is thus a minority contributor to total methane drawdown, it is a biological process and occurs on Earth's surface; because of these traits, methanotrophy has an outside chance of being usefully leveraged through human land management (e.g., He *et al* 2024) and bioengineering efforts (e.g., He *et al* 2023) to support climate stability. It is therefore essential to understand what conditions are favorable to soil methanotroph activity and how activity might respond to ongoing environmental change.

Despite numerous studies of aerobic microbial methane uptake in culture and in the environment, we still have limited ability to accurately predict soil methane uptake rates as a function of environmental variables. Laboratory studies of methanotroph cultures or soil samples have often produced strong, predictable relationships of methane uptake rate with fundamental variables like temperature, methane concentration, and soil moisture (King and Adamsen 1992, Czepiel *et al* 1995, Bender and Conrad 1993). However, in recent metaanalysis studies focused on forest ecosystems—where the soil methane sink has been most thoroughly studied—regression models were able to explain only 34–77% of the variability in observed methane uptake rates (Yu *et al* 2017, Gatica *et al* 2020, Feng *et al* 2023). These forest methane uptake regression models incorporated numerous climatic, edaphic, and/or anthropogenic variables as parameters. However, statistical relationships between individual variables and observed *in situ* methane uptake—including those variables that have been shown to strongly control methane uptake in lab experiments—were often weak or absent.

Yet less predictive power has been demonstrated by ANOVA or regression models constructed from measurements of other, less-studied biomes (Dutaur and Verchot 2007, Yu *et al* 2017). This stems in part from a lack of data. Drylands, in particular, are poorly represented in soil methane

flux datasets. A recent review recovered only 21 peer-reviewed publications containing a total of 190 published time series measurements of soil methane uptake rates from dryland environments around the globe (Song *et al* 2024). In contrast, a recent meta-analysis of forest soil methane uptake included 772 studies (Feng *et al* 2023). Because of this data sparsity, although drylands are estimated to account for over 40% of global land area (Prävālie 2016) and to support methanotrophy at rates near the global average (Song *et al* 2024), the accuracy of methane uptake rates simulated for drylands in global biogeochemical models cannot readily be determined.

The poor ability of these regression models to predict the measured variability in methane uptake rates propagates into global process-based biogeochemical models. Because it remains unclear how to accurately parameterize methane fluxes, bottom-up estimates of soil methane uptake have a large uncertainty range (Saunois *et al* 2020). Recent analyses point out that most model simulations of the soil methane sink do not accurately match global or regional-scale observations (Xu *et al* 2016 and references therein). We highlight three possible reasons for this mismatch between models and observations: first, although laboratory experiments have demonstrated the importance of variables like temperature and soil moisture, the model representations of how these variables drive differences in methane flux may not be adequate, especially for understudied environments. Along this line, a review of 40 terrestrial methane models suggests that models could be improved by better simulating the dynamics of methane fluxes in response to soil moisture (Xu *et al* 2016). Second, there may be additional variables important for controlling methane fluxes that are not yet considered in most models. For example, field studies have shown that methane flux is sensitive to soil texture, nitrogen content, copper content, microbial community composition, land use, and/or topography, in addition to moisture and temperature (Boeckx *et al* 1997, Castaldi *et al* 2006, Courtois *et al* 2018, D'Imperio *et al* 2017, Hartmann *et al* 2011, Ho *et al* 2016, Kaiser *et al* 2018, Smith *et al* 2000). Finally, because models and measurements often represent very different temporal and spatial scales, comparing these different scales may lead to disagreement between data types.

Here, we studied rates of methane uptake in California dryland soils, with two aims: first, to contribute more measurements of an understudied climate type; and second, to assess whether

common soil methane modeling approaches can adequately simulate trends in dryland methane uptake. We collected 275 observations of soil methane fluxes from natural dryland soils, and performed physical, chemical, and biological characterization of the soil at each measurement site. We additionally constructed a simple model to predict methane flux based on the environmental variables most commonly included in global models, and compared the model results to our field measurements. Through this analysis, we compared the observed trends in methane uptake rate to common model representations. We used our comparison of measured and modeled methane uptake as a lens to investigate potential sources of model-data disagreement in terrestrial methane cycle simulations for dryland environments.

2.3) Methods

2.3.1) Selection of relevant study variables

We focused our measurements and primary analysis on net soil-atmosphere methane flux and the variables that are most widely used to parameterize this flux in global models: temperature and soil volumetric water content (VWC). These variables were universally used to model methane production and/or consumption in 19 process-based biogeochemical models described in a recent review (Xu *et al* 2016). We also identified soil organic carbon (SOC) content as a model-relevant variable, as it is directly or indirectly related to methane production in many but not all recent models. To this point, we have measured SOC in a subset of soil samples (1-2 timepoints per measurement site); for model input data, we estimated organic carbon content from values reported in SoilGrids (Poggio *et al* 2021), discussed further in Section 2.3.11.

To identify additional controlling parameters that might improve model accuracy, we measured a number of other soil properties that have been indicated as determinants for methanotroph activity in natural soils. Soil properties previously indicated as relevant include nitrogen content, pH, texture, copper content, and microbial community properties (Benstead and King 2001, Boeckx *et al* 1997, D'Imperio *et al* 2023, Hartmann *et al* 2011, Ho *et al* 2016, Semrau *et al* 2010). As a result, we selected a subset of samples for which we analyzed total and available nitrogen content, pH, particle size distribution, copper abundance (as well as the abundance of additional biorelevant

elements: iron, zinc, manganese, and phosphorus), and microbial community composition as assessed by 16S rRNA sequencing. The methods for soil property analyses are described in section 2.3.5.

2.3.2) Field site description

Three field sites were selected for this study to capture a range of climate characteristics, biomes, and land use types typical of California arid and dry-summer landscapes (Figure 2.1), which we expected to produce relevant differences in temperature, soil water content, and other soil properties. All sites meet the definition for drylands, with aridity index of < 0.65 (Mirzabaev *et al* 2019). Mean summer high temperatures among the three sites between 2006–2020 ranged from 22.6–39.8 °C and winter lows from 2.6–6.1 °C (NOAA National Centers for Environmental Information, 2021). Mean annual precipitation ranged from 8.4–80.7 mm, falling primarily in the winter months.

In order to capture seasonal and interannual variation in soil microbial activity, we visited each site seasonally (spring, summer, autumn, and winter) for two years, with all field work occurring between 11/2021 and 4/2024. During each site visit, we measured soil-atmosphere methane fluxes at between 11 and 15 unique measurement locations, which were selected to capture the range of vegetation, land use, and topography across the landscape. We revisited the same locations for each timepoint: all measurements for a single measurement location occurred within a radius of ≤ 8 meters, maintaining consistent topographic context and vegetation while avoiding areas disturbed by previous sampling. All measurements were performed during daylight hours. Timepoint measurements are absent for some sites and seasons due to extreme weather events that prevented access to field sites (flooding, landslides, and/or high temperatures that caused instrument failure). In particular, no winter timepoints were collected at the coastal site due to landslides that precluded vehicle access to the area.

The coastal site was located at Jalama Canyon Ranch, Lompoc, Santa Barbara County (34.57, -120.45, 340 m a.s.l.). Jalama Canyon ranch is located near Point Conception, CA; from at least the early 20th century it was a small conventionally-managed ranch with pasture areas subject to

continual grazing, and since 2019 it has been regeneratively managed (Terra Genesis International 2020). This site is located in a warm dry-summer climate zone and the Southern California Coast USDA ecoregion section. This site has an average JJA high temperature of 22.6 °C and an average DJF low temperature of 6.1 °C, and receives a mean annual precipitation of 324 mm (NOAA National Centers for Environmental Information, 2021). Soils are sandy or silt loams. We performed measurements at 12 locations within the coastal field site, spanning the range of vegetation and land use present on the landscape: coastal sage scrub (n = 3), oak woodland (n = 2), riparian (n = 1), cattle pasture (annual brome grassland, n = 4), vineyard (n = 1), and marginal land (n = 1).

The desert site was located at Afton Canyon, San Bernardino County (35.03, -116.36, 440 m a.s.l.). Afton Canyon is located in a hot desert climate zone and the Mojave Desert USDA ecoregion section, and the Mojave River intermittently flows aboveground through the canyon. The average JJA high temperature measured at the nearest long-term weather station at Barstow Daggett Airport (584.8 m a.s.l.) is 39.8 °C, the average DJF low temperature is 2.6 °C, and the mean annual precipitation is 83.6 mm. We performed measurements at 12 locations within the desert site, spanning the wide range of topography across the landscape: riverbank (n = 2), river floodplain (n = 2), wash (n = 4), and hillslope (n = 4). After sieving to 2 mm, soil textures were determined as sandy loam or sand (see Section 2.3.5), but gravel dominated the soils by volume at hillslope and wash sites. Vegetation, where present, was dominated by riparian plants along the river channel and sparse desert scrub vegetation away from the channel. However, much of the study area was unvegetated, due in part to geomorphological disturbances of the floodplain, washes, and hillslopes occurring with each rain event (James Danoff-Burg and Luis Ramirez 2024).

The foothills site was located at Hunter Valley, Mariposa, Mariposa County (37.64, -120.25, 480 m a.s.l.). This site is located in a hot dry-summer climate zone and the Sierra Nevada Foothills USDA ecoregion section. Mariposa is located along a strong climate gradient between California's Central Valley and the Sierra Nevada, and the nearest weather stations where long-term data are available from NOAA are substantially downslope in Merced and upslope in Yosemite Valley (46.9 m a.s.l. and 1538.3 m a.s.l, respectively). At these weather stations, average JJA high

temperatures range from 26.4–34.7 °C, average DJF low temperatures from -3.3–2.9 °C, and mean annual precipitation from 297–807 mm (NOAA National Centers for Environmental Information, 2021). Soil at this site is silt loam. We performed measurements at 15 locations within the foothills field site. Six of the measurement locations fell within a Bureau of Land Management (BLM) grazing allotment, intermittently accessed by cattle and characterized by non-native annual brome grassland vegetation (Menke *et al* 2011). The other nine measurement locations were excluded from grazing, and hosted the California endemic foothill pine woodland vegetation alliance (Klein *et al* 2007).

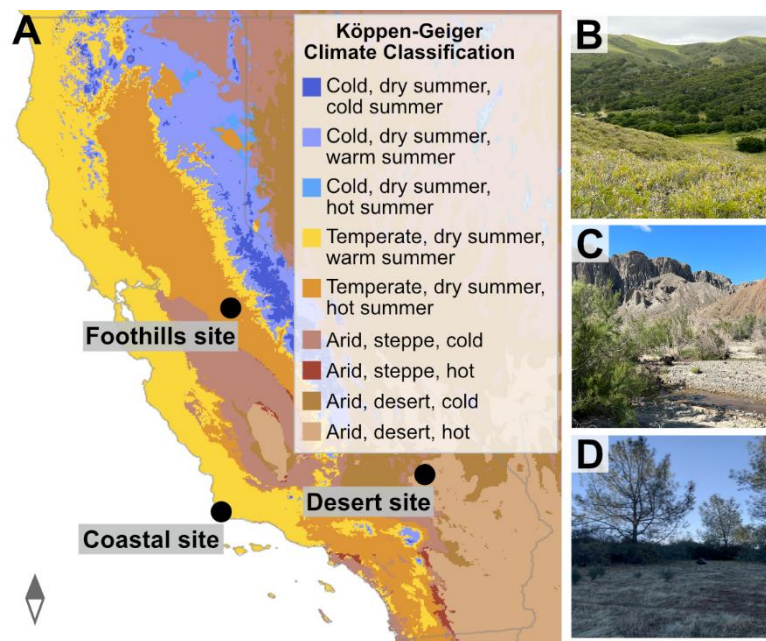


Figure 2.1: A. Map of California Köppen-Geiger climate regions (Beck *et al* 2023, Esri 2024) showing the locations of the three field sites described in this study. B. Photo of coastal site, showing coastal sage scrub (foreground), pasture (middle distance), and oak woodland (background) vegetation types. C. Photo of desert site, showing riparian (foreground) and unvegetated hillslope (background) measurement locations. D. Photo of foothills site, showing pine woodland vegetation.

Table 2.1: Field site geospatial, climatic, edaphic, and ecological properties.

*Temperature and precipitation data for the foothills site were retrieved from the two nearest weather stations where long-term weather data is available through NOAA. This site is located along a steep climate gradient between the two stations, so the values for both climate stations are provided. See section 2.3.2 for further details.

Site	Coordinates	Elevation (m asl)	Average DJF low temp (° C)	Average JJA high temp (° C)	Mean annual precipitation (cm)	Climate zone	USDA ecoregion section	Soil type	Land cover/land use type
Coastal	34.57, -120.45	340	6.1	22.6	32.4	Warm dry- summer	Southern California Coast	Silt loam, sandy loam	Pasture, coastal sage scrub, oak woodland, riparian
Desert	35.03, -116.36	440	2.6	39.8	8.36	Hot desert	Mojave Desert	Gravel, sand, sandy loam	Riparian, desert scrub, unvegetated/ barren
Foothills	37.64, -120.25	480	-3.3–2.9*	26.4–34.7*	297–807*	Hot dry- summer	Sierra Nevada Foothills	Silt loam	Pasture, pine woodland

2.3.3) Methane flux measurements

From 11/2021 to 1/2023, soil-atmosphere methane fluxes were measured using a Picarro GasScouter G4302 mobile gas concentration analyzer (Picarro, Santa Clara, CA) with a custom-built flow-through soil gas flux chamber. The chamber had an internal volume of 8.2 L and a footprint of 0.0307 m². Reflective tape was applied to the chamber's external surfaces and the G4302 analyzer was covered in a reflective tarp to prevent overheating in the sun. Prior to each measurement, the chamber was inserted 1-2 cm deep into the soil until it was solidly embedded on all sides, and was equipped with a Neoprene skirt to improve the seal. Due to instrument malfunctions, in 4/2023, methane exchange rates were measured using a Picarro G2401-mc analyzer and the home-built chamber described above. During each 10-minute chamber enclosure time, the analyzer operated with a sample flow rate of 2 slpm (standard liters per minute) and measured headspace methane concentration with a frequency of ~1.2 Hz. Air temperature during the enclosures was measured using a thermocouple probe mounted inside the chamber and connected to an Omega HH506A data logger (DwyerOmega, Michigan City, IN). Soil temperature was measured with a 10-inch penetration thermocouple probe and the same logger. Pressure inside the chamber was assumed constant and in equilibrium with local atmospheric pressure due to equivalent inflow and outflow rates. Outlier values resulting from instrument artefacts were removed by identifying points that

deviated from the detrended average methane concentration by greater than three times the interquartile range. Up to 60 seconds at the beginning of the measurement were dropped from analysis as deadband time to allow the signal to stabilize, and net soil-atmosphere methane flux was then calculated as the slope of a linear regression between time and methane concentration, correcting for temperature inside the chamber. For measurements where the 95% confidence interval of the slope included 0, the net flux was set to 0. The difficulty of simulating a precise methane flux in a porous medium makes it challenging to assess measurement accuracy; however, a negative control test using autoclave-sterilized sand produced no measured methane flux.

From 5/2023 to 4/2024, fluxes were measured using a LI-COR LI-7810 trace gas analyzer and 8200-01S portable soil gas flux chamber (LI-COR, Lincoln, NE). The 8200-01S chamber had a volume of 4.2 L and a footprint of 0.0318 m², almost identical to the footprint of the lab-built chamber used with the Picarro instruments. In sunny weather, the LI-7810 was covered with a reflective tarp to prevent overheating. Prior to each measurement, the chamber collar was installed at the measurement location to a minimum of 2 cm depth until it was solidly embedded. The internal depth from the top of the collar to the soil surface was measured and averaged over four points to track differences in internal volume. The chamber was set to automatically perform five chamber enclosures of two minutes each, while the LI-7810 analyzer maintained a sample flow rate of 0.25 slpm and measured methane headspace concentration with a frequency of 1 Hz. Air temperature during enclosures was automatically monitored by a thermistor onboard the 8200-01S chamber. In between enclosures, the chamber lifted to equilibrate the headspace with the atmosphere for 30 seconds. Soil temperature during enclosures was measured using the thermocouple probe described above. Constant pressure was maintained by the chamber in equilibrium with local atmospheric pressure. The net soil-atmosphere methane flux was calculated from headspace methane concentration measurements using SoilFluxPro version 5.3.1 (LI-COR Biosciences Inc.). Like for data collected with the custom-built chamber, methane flux measured with the LI-COR chamber and analyzer was calculated as the slope of a linear regression between time and methane concentration, using a 25-second deadband time and correcting for temperature inside the chamber. Reported flux values are the average of the five 2-minute enclosures. For measurements where the 95% confidence interval of the mean flux

value included 0, the net flux was set to 0. The accuracy of flux measurements made with the 8200-01S chamber design has previously been demonstrated (Xu *et al* 2006).

In a Mann-Whitney U-test, no statistically significant difference was detected between methane flux values recovered between any combination of chamber and analyzer, despite confounding factors such as weather variability ($p = 0.12\text{--}0.25$).

2.3.4) Field sample collection

At every flux measurement location, soil samples were collected from within the measurement footprint for physical, chemical, and biological characterization. Soil samples for physical and chemical analyses were collected with a trowel to a depth of 0–10 cm with a typical hole diameter of ~15 cm. Soil samples for bulk density and volumetric water content (VWC) measurements were collected by inserting a cylindrical metal can or ring of known volume (diameter ~5 cm) horizontally into the soil to maintain constant volume and avoid compression. Samples for bulk density and VWC could not be collected at 19% of sample locations where soil was too hard to insert the sampling tool. In a Mann-Whitney U-test, no statistically significant difference was detected between methane fluxes for samples where bulk density samples could or could not be collected ($p = 0.21$). All samples were stored at $-20\text{ }^{\circ}\text{C}$ until laboratory analysis.

At each measurement location, two samples were collected for DNA extraction and analysis: one sample of surface soil (< 1 cm depth) and one sample of soil from 0–10 cm, immediately subsampled from the collected bulk soil sample. The DNA samples were collected with an isopropanol-cleaned spatula. Soil was directly sampled into PowerBead lysis tubes from the DNeasy PowerSoil Pro kit, prepared with 800 μL of LifeGuard soil preservation solution to stabilize the samples at room temperature (Qiagen, Hilden, Germany), such that the soil sample filled $\frac{1}{3}$ of the tube depth (~0.5–0.8 g soil). DNA samples were stored at room temperature and DNA was extracted within 30 days of sample collection.

2.3.5) Laboratory soil characterization

Soil bulk density and volumetric water content (VWC) were determined for every measurement location and timepoint. Soil samples for bulk density and volumetric water content were weighed, oven-dried at 105 °C for a minimum of 24 hours, and reweighed.

Additional soil properties—total organic carbon (TOC), total nitrogen (TN), particle size distribution, select elemental composition, and nitrogen speciation—were determined at 1–3 timepoints for each measurement location. Samples for these additional measurements were oven-dried at 50 °C to constant weight and sieved to 2 mm, breaking apart aggregates as needed and removing visible roots > 1 cm.

To compare these additional soil properties to methane fluxes over time, rather than just at the time of sample collection, we tested the assumption that TOC, TN, particle size distribution, and elemental composition were relatively invariant on the timescale of 1–2 years and spatial scale of < 10 m (the time and spatial distances between replicate sampling). We performed measurements of these variables for two to three replicate samples collected from seven measurement locations spanning all three field sites.

Inorganic carbon was removed from samples for TOC and TN by decarbonation, incubating samples in 1 N HCl for 10 minutes under sonication for 3 rounds or until the sample ceased to produce bubbles on HCl addition. Samples were rinsed with deionized water, freeze dried, weighed to ~20 µg carbon in duplicate, and encapsulated in tin for elemental analysis (EA) (Thermo Fischer Scientific, Waltham, MA, USA). The organic carbon and total nitrogen content of each sample was calculated in comparison to an 11-point calibration produced using authentic alanine and serine standards. TOC and total N values are reported as the average of two duplicate measurements.

Samples were prepared for particle size analysis by decarbonation of ~100 mg of soil in 1 N HCl at 60 °C overnight. Decarbonation was followed by removal of organic material in 30% H₂O₂ at 70 °C for 30 mins and subsequently at room temperature overnight. After rinsing, samples were suspended in deionized water with 2% sodium hexametaphosphate added as a dispersant and sample particle size distribution was measured by laser diffraction using the Mastersizer 3000E (Malvern Panalytical, Malvern, England).

Soil pH was determined by combining soil samples with MilliQ water at a ratio of 1:1 w/w and letting stand for ≥ 10 minutes, then measuring with a Beckman Coulter $\Phi 350$ pH meter and probe (Beckman Coulter, Brea, CA, USA). For consistency, the probe was submerged into the supernatant for each measurement, avoiding the underlying soil.

Soil elemental composition (Fe, Cu, Zn, Mn, and P) and nitrogen speciation (NH_4^+ and NO_3^- content) measurements were made at the Oregon State University Soil Health Lab. Samples for elemental composition measurements were extracted in an Anton Paar microwave digestion system (Anton Paar GmbH, Graz, Austria), and the digest was diluted, filtered, and measured on an Agilent 5110 ICP-OES (Agilent, Santa Clara, CA, USA). For nitrogen species determination, samples were extracted in 2 M KCl. Nitrogen as NO_3^- was measured using Griess reagents on a VWR V-1200 spectrophotometer (Avantor, Radnor, PA, USA) and nitrogen as NH_4^+ was measured on a Lachat QuikChem 8500 Series 2 flow injection analyzer (Hach, Loveland, CO, USA). The detection limit for nitrogen species was 0.2 ppm. For soil samples where nitrogen species were below detection limit, the abundance was set to 0.

2.3.6) Soil DNA extraction

After LifeGuard preservative was removed from soil samples by centrifugation, DNA was extracted using the Qiagen DNeasy PowerSoil Pro kit following manufacturer instructions. The 515f and 926r primer pairs with Illumina adapters were used to amplify the V4 to V5 region of the 16S rRNA gene by polymerase chain reaction (PCR) (Parada *et al* 2016). PCR for each sample was performed in duplicate in 15 μL reaction volumes with the Q5 Hot Start High-Fidelity 2x Master Mix (New England Biolabs, Ipswich, MA, USA), using an annealing temperature of 54 $^\circ\text{C}$ for 30–35 cycles. PCR product duplicates were pooled and barcoded with Illumina NexteraXT index 2 primers (Illumina, San Diego, CA, USA). Barcoded samples were sent to Laragen (Culver City, CA, USA) for sequencing on Illumina's MiSeq platform.

DNA samples for the first five of 24 field sampling trips were lysed in LifeGuard preservative rather than in the Qiagen-provided lysis buffer. Sequencing data analysis indicated substantially lower yield in these samples, so they were excluded from further analysis.

2.3.7) 16S sequence data processing

Amplicon sequence variants (ASVs) were obtained from 16S rRNA sequencing data using the dada2 R package version 1.28 following the developer's recommendations (Callahan *et al* 2016). Reads were trimmed to 230 and 200 bp for forward and reverse reads, respectively, excluding reads with more than two expected errors. Reads were denoised using the pool = 'pseudo' flag to increase the sensitivity to rare ASVs. Forward and reverse reads of denoised data were then merged and chimeras were removed using default settings. Taxonomic assignment of ASVs used the IdTaxa function from the R package DECIPHER version 2.28.0 (Murali *et al* 2018) and the SILVA 138.2 database. 84 ASVs were identified as contaminants based on their presence in negative DNA extraction controls and removed using the 'prevalence' method of the R package decontam version 1.20.0 (Davis *et al* 2018) with a threshold of 0.3.

2.3.8) Soil microbial community analysis

To visualize differences in soil microbial community structure among field sites, we used non-metric multidimensional scaling (NMDS) analysis using the R package vegan version 2.6-8 (Jari Oksanen *et al* 2024). To prepare ASV count data for NMDS analysis, a variance-stabilizing transformation (VST) was applied using the R package DESeq2 version 1.40.2. After VST, taxa in the bottom five percentile of abundance NMDS plots were generated from normalized and cleaned data using the vegan metaMDS function with the Bray-Curtis dissimilarity metric.

To assess whether differences in soil microbial community structure were associated with different soil methane uptake rates, we performed lasso regression using the LassoCV function from the Python library scikit-learn. VST-normalized counts were used for lasso regression analysis at the family and ASV level. The model L1 penalty parameter (α) was tuned by three-fold cross-validation. Model performance was assessed by in-sample and cross-validated r^2 values.

2.3.9) Statistical analysis of uptake rates and soil properties

To test for significant differences between sites, seasons, and conditions, we applied Welch's t-test using the function `ttest_ind` and the Mann-Whitney U-test using the function `mannwhitneyu`, both

from the Python library SciPy. The appropriate test was determined based on whether data conformed to expectations for a normal distribution (e.g., temperature data was normally distributed, while methane fluxes were not). P-values were adjusted to account for multiple hypothesis testing using the Benjamini-Hochberg False Discovery Rate correction with the `multipletests` function from the Python module `statsmodels`. For comparisons of properties across seasons where multiple data points were available at the same measurement location, paired t-tests were applied using the SciPy function `ttest_rel`. Linear regression and multiple regression, where described, were performed using the ordinary least squares method with the `statsmodels` OLS function.

Correlations reported in Section 2.4.4 were calculated using the Spearman methods with the `corr` function in the `pandas` Python library. P values for correlations were calculated using the SciPy function `spearmanr` and again adjusted using the Benjamini-Hochberg correction. Significance was assessed relative to a threshold of 0.05.

2.3.10) Model and comparison to data

To assess the performance of existing model frameworks for predicting dryland methane fluxes, we compared our flux measurements to a simple model for soil methane uptake. We constructed this model to incorporate the most common parameters used across existing methane models: soil temperature, water content, and organic carbon content (Xu *et al* 2016), as discussed in section 2.3.1. Our parameterization of methane production and consumption in response to these variables is modified from the process-based dynamic land ecosystem model (DLEM) as described in Tian *et al* (2010). The processes simulated are soil methane production, methane oxidation, and diffusive and ebullitive methane flux between soil and atmosphere:

$$F_{CH_4} = F_D + F_E - (F_{air\ oxidation} * H) [=] g/(m^2*s) \quad (\text{Equation 2.1})$$

where F_{CH_4} is net methane flux, F_D is flux due to diffusion, F_E is ebullitive flux, $F_{air\ oxidation}$ is methanotrophic uptake in the gas phase, and H is the height of the domain. Methane production is modeled as $f_{prod}(T, VWC)$ and oxidation as $f_{oxid}(T, VWC)$.

The model was run using the COMSOL Multiphysics software version 5.3 (COMSOL, Burlington, MA, USA) with a dynamically adjusted timestep. Full model details, including all equations, parameters, and boundary conditions, are included in Section 2.8.

We made minor modifications to the DLEM in order to better match the conditions of our field measurements, the data availability for the study sites, and the current state of knowledge for methane uptake kinetics. First, because we used our model results to compare to methane flux measurements by small-volume chambers, we omitted the DLEM terms for plant-mediated transport and oxidation. We expect this omission to minimally affect our results because during most chamber enclosures, the chamber contained little or no plant material. Second, we did not include a pH dependence of methanotrophy in our simplified model, as the overall effect of pH on soil methane uptake is not well-characterized and may be minimal (Born *et al* 1990, Dunfield *et al* 1993); additionally, methanotrophs have demonstrated wide variability in pH-tolerance among environments (Saari *et al* 2004), so a generalized pH dependence is not likely to be representative. Finally, unlike Tian *et al* (2010), we did not tune the kinetic parameters V_{max} or K_M of methanotrophy to match measured methane fluxes: here, rather than building the most accurate possible model, we instead aimed to assess how well an existing model framework fits measured values. Thus, rather than using the tuned kinetic parameters reported by Tian *et al*, we used the median V_{max} and K_M values for low-methane ecosystems (including shrublands and grasslands) from a recent compilation of methanotrophy kinetic measurements (Dion-Kirschner *et al* 2024). Lacking a similar compilation for the kinetics of methanogenesis, we maintained the tuned kinetic parameters reported by Tian *et al*.

2.3.11) Model input data

Existing models rely on time-continuous soil temperature and VWC data, while our measurements were limited to point-in-time measurements during seasonal field visits. Accordingly, we retrieved time series for hourly temperature and soil moisture from ERA5 reanalysis data (Hersbach *et al* 2023). The ERA5 dataset provides globally gridded estimates of climate variables by integrating satellite and *in situ* observations into a numerical weather prediction system using data assimilation. Temperature data were retrieved for air temperature at 2 m above the ground surface and for the soil

horizons 0-7, 7-28, and 28-100 cm, and VWC for 0-7 and 28-100 cm. VWC values for the 7-28 cm horizon were not available in ERA5 data, so were calculated as an interpolation of values from the over- and underlying soil layers. Because ERA5 data is limited to a resolution of 0.25°, soil temperature and moisture values were retrieved as the average of values across the grid cell containing each field site (coastal, desert, and foothills).

Soil carbon content is represented in the model by Tian *et al* (and many similar models) as dissolved organic carbon (DOC). In practice, soil DOC is an operationally defined class of water-extractable organic carbon separated from bulk soil by centrifugation and/or filtration (Jones and Willett 2006, Sullivan *et al* 2013). We estimated site-averaged values for soil DOC content using soil organic carbon (SOC) values retrieved from SoilGrids 2.0 (Poggio *et al* 2021). Soil organic carbon (SOC) values within the bounds of each field site were retrieved and recorded for each site as the mean and standard deviation of values reported across all grid cells within the site bounds. Approximate soil DOC content was estimated from SOC by assuming that 0.23% of SOC is DOC, the average value obtained from a global meta-analysis (Guo *et al* 2020).

2.4) Results and discussion

2.4.1) Site climate data

In a comparison of *in situ* measurements and ERA5 estimates of local climate data, air and soil temperature values measured at the time and location of each measurement generally corresponded closely with the values reported in ERA5 data (Figure 2.2). VWC values from ERA5 in soil level 1 (0–7 cm) matched measured values well at the desert field site, but were typically higher than values we measured at the coastal and foothills field sites. This offset may result from the range of topography integrated in the ERA5 grid cell, where local topographic lows could contribute to higher estimated soil VWC relative to the actual measurement locations visited for this study. Nevertheless, relative trends in VWC as recorded by ERA5 and field-measured data are generally in agreement.

Comparing ERA5 data with timepoint measurements demonstrates that seasonal timepoints at each site effectively captured the typical seasonal range in air and soil temperatures (Figure 2.2). Because

of the offset in VWC values at coastal and foothills sites, it is difficult to assess whether the full range of expected seasonality in VWC was captured by the field measurements there, but clear seasonal trends are apparent, with highest values of soil moisture in the spring and summer at the coastal site, and in the fall and winter at the foothills site. Meanwhile, at the desert site, predicted highs in VWC from ERA5 data were not captured during our seasonal timepoint measurements. In all, the timepoint measurements of methane uptake performed at coastal and foothill sites are expected to effectively capture seasonal shifts in temperature and soil moisture; at the desert site, seasonal changes in temperature are well-captured, while seasonal changes in soil moisture may not be fully represented.

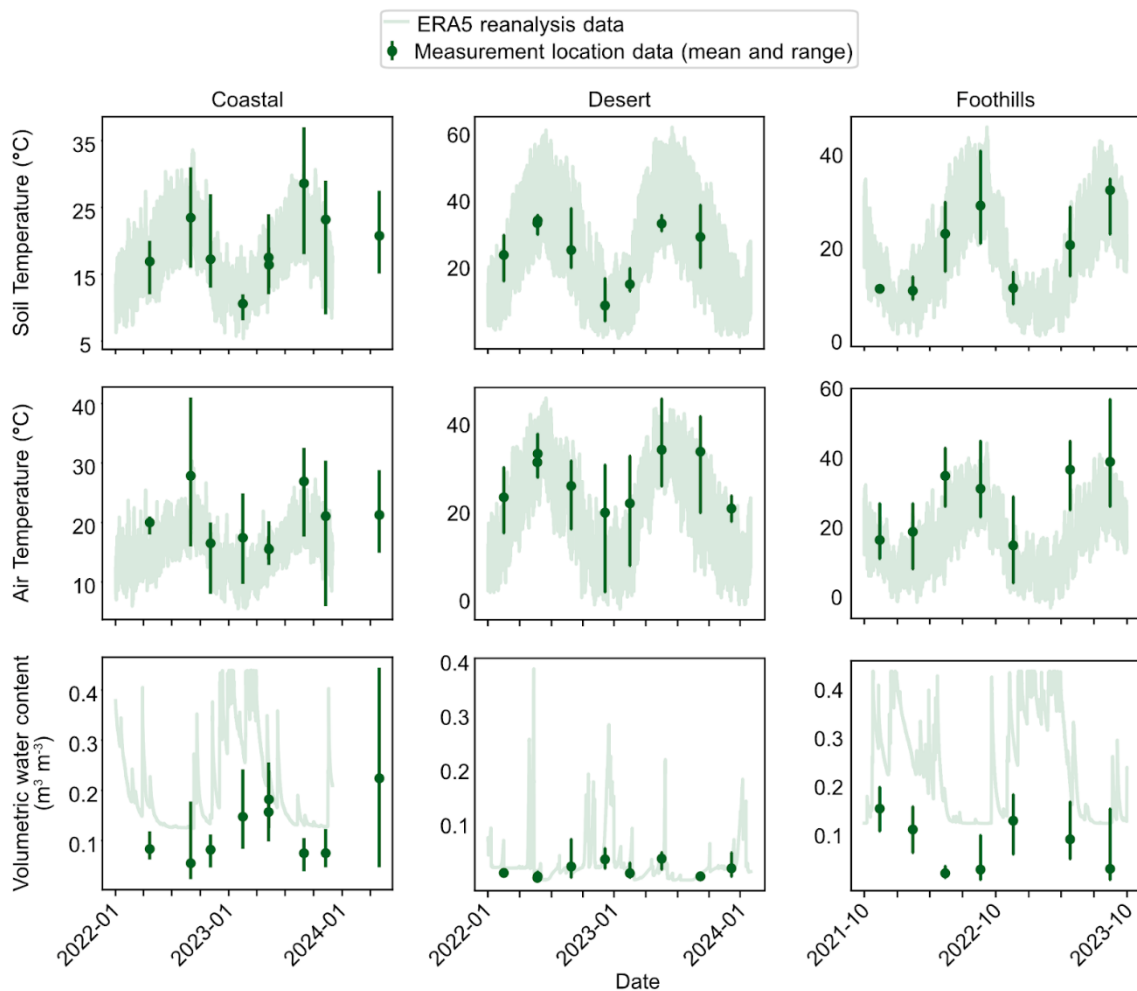


Figure 2.2: Soil temperature, air temperature, and volumetric water content (VWC) data as derived from ERA5 reanalysis data (pale green lines; Hersbach *et al* 2023). Soil data from ERA5 are reported for level 1, 0–7 cm, which corresponds most closely to the 0–10 cm horizon measured in this study. Measurement location data are superimposed on ERA5 data as dark green points

(indicating the mean value measured at a given site and day) and vertical lines (indicating the range of values among measurement locations for that site and day).

2.4.2) Trends in California dryland methane uptake

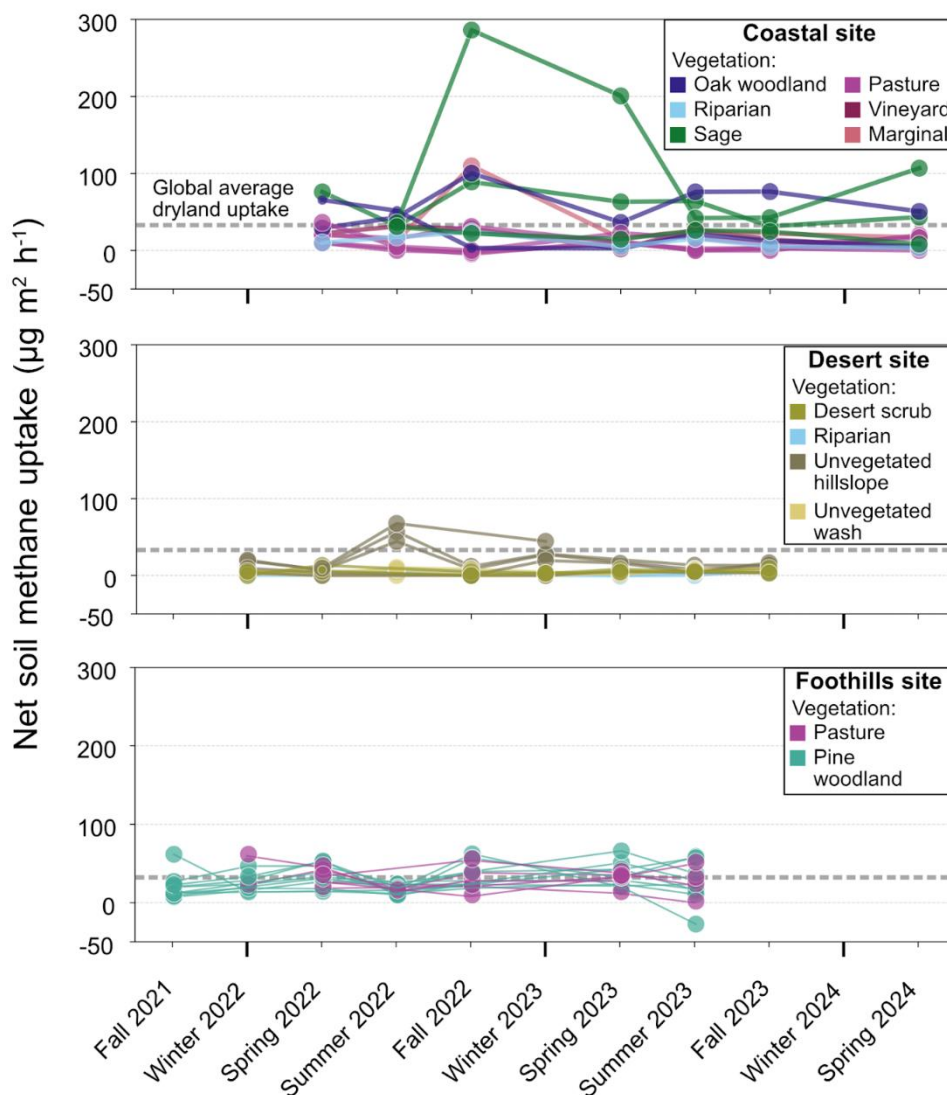


Figure 2.3: Net soil methane uptake measured for each time point and field location. Positive values indicate a higher rate of atmospheric methane uptake from air into soil; negative values indicate net soil methane efflux. Colors represent landscape features (vegetation type and/or topography). Dashed line indicates the global average uptake rate for drylands from Song *et al* (2024) ($34 \pm 23 \mu\text{g m}^{-2} \text{h}^{-1}$).

Across all sites and seasons, the average observed soil methane uptake was $21.4 \pm 28 \mu\text{g m}^{-2} \text{h}^{-1}$ ($n = 275$). This value is lower than, but within error of, the average value of global dryland observations of $34 \pm 23 \mu\text{g m}^{-2} \text{h}^{-1}$ (Song *et al* 2024); it more closely aligns with the estimated global methane

uptake in desert and shrubland from a canonical early model, which produced a value of $20.8 \mu\text{g m}^{-2} \text{h}^{-1}$ (Curry 2007).

Of 275 measured flux values, 91% were significantly different from 0 and only 2% indicated net methane efflux from the soil to the atmosphere (Figure 2.3). This finding is consistent with the common expectation that methane consumption dominates soil methane cycling in oxic soils (Dutaur and Verchot 2007; Saunio *et al* 2020). Net methane efflux was observed at least once at all three sites: two instances at the coastal site in fall 2022, two at the desert site in fall 2023, and one at the foothills site in summer 2023. Efflux ranged from $0.5 \mu\text{g m}^{-2} \text{h}^{-1}$ in the desert riparian zone to $29.2 \mu\text{g m}^{-2} \text{h}^{-1}$ in the foothills pine woodland. Among the five measurements where efflux was observed, it averaged $7.4 \pm 11.0 \mu\text{g m}^{-2} \text{h}^{-1}$. None of these locations were observed to be water-saturated in the surface soil, with VWC ranging from 4.6–7.9% in the top 10 cm. Instead, local methane production may have derived from anoxic microsites formed by heterogeneous organic carbon and porewater distribution within dominantly oxic soils (Lacroix *et al* 2023).

2.4.3) Seasonality in methane uptake rates is muted and varies among sites

Despite strong seasonal trends among measurement timepoints in temperature and VWC (Figure 2.2), the seasonality in observed methane fluxes at each site was weak or absent (Figure 2.3). In paired t-tests comparing matching measurement locations within each site between seasons, most comparisons produced p-values indicating no significant seasonal difference in methane flux. At the coastal and desert sites, no seasonal differences in methane uptake were statistically significant ($p = 0.09$ – 0.33). This is despite significant differences in VWC and temperature at both sites across most seasonal comparisons, and in contrast to previous studies that have found soil moisture to be a dominant driver of seasonal methane uptake trends using similar measurement methods (Zhao *et al* 2019, Shrestha *et al* 2012). Further, no statistically significant correlation between methane flux and temperature or VWC (via linear or multiple regression) was observed for either site across or within seasons. It is possible that the larger shifts in VWC at the desert site estimated in ERA5 data, which were not captured by our measurement timepoints, create seasonal signals in methane fluxes not captured by our measurements. Nevertheless, despite distinct seasonality in temperature and soil

moisture across our measurement timepoints, these environmental variables did not drive any significant seasonal signals in measured methane uptake at desert and coastal sites.

In contrast to the lack of seasonality we observe at the coastal site, substantial seasonal trends in soil-atmosphere methane fluxes have commonly been observed in previous studies of grassland and pasture environments (Shrestha *et al* 2012, Täumer *et al* 2022). Seasonal trends at desert sites are less consistent; one study found limited variability in methane uptake during two growing seasons, but a significant correlation with temperature in a semiarid region of northern China (Hou *et al* 2012), while another found significant seasonal trends and a strong influence of precipitation events in the Mojave Desert (Striegl *et al* 1992).

At the foothills site, spring methane flux measurements were distinct from all other seasons by pairwise comparison of measurement locations ($p = 0.0001\text{--}0.0497$). This difference was driven by a small but systematic springtime increase in methane uptake rate across pine woodland measurement locations (Figure 2.3). While the highest average air temperatures at pine woodlands locations were observed in the spring ($p < 0.01$), no statistically significant correlation between methane flux and temperature or VWC (via linear or multiple regression) was observed for either vegetation type at the foothills site across or within seasons. Thus, temperature may drive seasonal signals in methane uptake at pine woodland measurement locations, but it is not a dominant control on absolute methane uptake rates.

The relative temporal variability in measured fluxes was fairly consistent among locations. The coefficient of variation (CV) of fluxes across all time points was $56 \pm 32\%$ among locations at the foothills site, $83 \pm 19\%$ at the desert site, and $86 \pm 36\%$ at the coastal site. The lower CV at the foothills site ($p \leq 0.02$) contrasted with the higher CV in temperature at that site relative to other sites ($p < 0.01$) and higher CV in VWC than at the coastal site ($p = 0.01$), suggesting that the amplitude of climate variability did not determine the amplitude of methane flux variability.

2.4.4) Methane uptake rates correlate poorly with climatic variables

Because the three sites experience unique regional climates and host unique biomes (Section 2.3.2), we assessed how these distinctions affected trends in methane uptake. For inter-site comparisons, we considered only timepoints in spring through fall, since no wintertime measurements were possible at the coastal site. Among sites, measured methane fluxes were the highest on average at the coastal site (-30.6 ± 42.9), intermediate at the foothills site (-26.1 ± 16.3), and lowest at the desert site (-7.9 ± 11.8). Higher average methane uptake fluxes at the coastal site were driven by measurement locations with sage vegetation ($n=3$, discussed further in Section 2.4.5); excluding sage locations produced a lower site average value of -20.1 ± 23.8 . Uptake rates at the desert site were statistically distinct from the other two sites ($p < 0.0001$), while the coastal and foothills sites were not significantly different from one another ($p = 0.08$). This overlap in uptake rates between coastal and foothill sites was observed despite statistically significant differences in VWC and temperature ($p = 0.008$ – 0.012).

To more fully assess the relationship of soil and climate variables with methane uptake rates, we calculated the Spearman correlation of these variables with measured methane uptake (Figure 2.4) at each site and across all three sites. We assessed the relationship between variables on the basis of Spearman rather than Pearson correlation to accommodate the potential for nonlinear relationships and extreme outliers. Among air and soil temperature, VWC, and bulk density—properties measured at every methane flux measurement location—little or no correlation was observed with methane flux ($r^2 < 0.14$) (Figure 2.4A). VWC and bulk density were not significantly correlated with flux at any individual site, but correlated weakly with flux across all sample sites. This likely results from systematically lower VWC, higher bulk density, and lower methane uptake rates at the desert site ($p < 0.0001$ for all), and may not indicate mechanistic control of VWC or bulk density on uptake rates across sites. In contrast, VWC is often reported to control net methane uptake rates (Dijkstra *et al* 2011, Shrestha *et al* 2012, Zhao *et al* 2019), including in dryland environments (Dijkstra *et al* 2011; Hou *et al*, 2012) and under experimental soil wetting (Castro *et al* 1994). Previous findings on the temperature sensitivity of net soil methane uptake are more equivocal, in part because both methanogenesis and methanotrophy are typically stimulated by increased temperature (Feng *et al* 2020 and references therein).

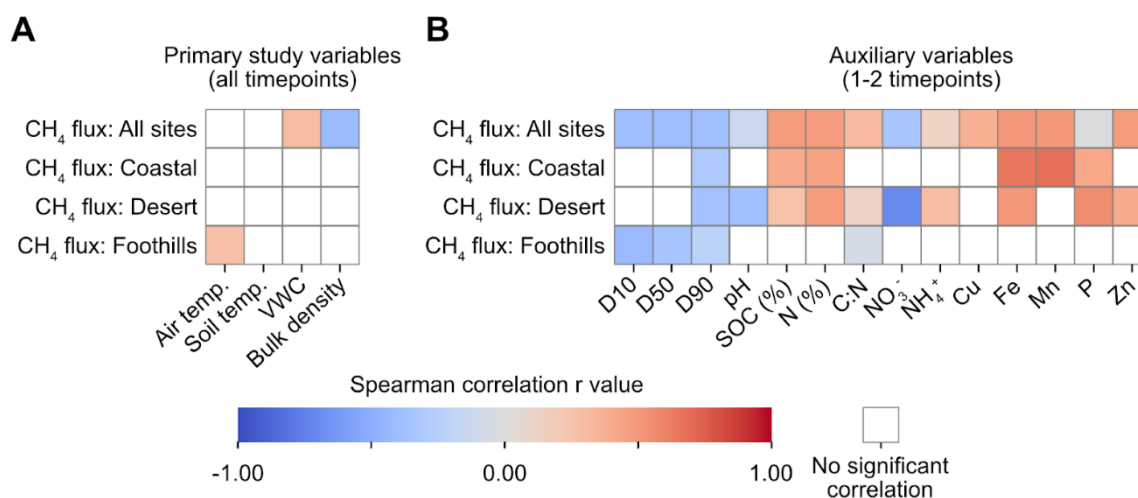


Figure 2.4: Correlogram showing the Spearman correlation of methane flux with measured soil and climate variables. Correlation is shown across all sites (top row) and at each individual site (bottom three rows). Color indicates the r value of correlation; boxes are colorless where no statistically significant correlation between variables exists. A: Correlation of net methane uptake rate with primary study variables, which were measured for every timepoint and measurement location. VWC, volumetric water content. B: Correlation of net methane uptake with auxiliary study variables (soil physical and chemical properties), which were measured for only one to two timepoints per measurement location. D_n , the n th percentile of soil particle diameter; SOC, soil organic carbon content; C:N, SOC to total N ratio.

Some stronger correlations were evident among additional physical and chemical characteristics measured on one to two timepoint samples per measurement location (Section 2.3.5; Figure 2.4B). Among individual sites, the foothills site had the fewest significant correlates with any measured soil or climate properties, correlating weakly with air temperature, particle size, and C:N (the mass ratio of SOC to total N). At the coastal site, iron (Fe) and manganese (Mn) abundance were the strongest correlates of methane uptake (Fe: $r^2 = 0.43$, $p = 0.02$, $n = 13$; Mn: $r^2 = 0.47$, $p = 0.0001$, $n = 13$). Previous studies have shown that iron and manganese decrease soil methane efflux, especially in saturated soils, by providing alternative electron acceptors that outcompete methanogenesis and by stimulating anaerobic oxidation of methane (AOM) (Miller *et al* 2015, Zhang *et al* 2023, Zhang *et al* 2024). While AOM is unlikely to occur in the unsaturated soils we study here, the correlation of iron and manganese with net methane uptake at the coastal site may reflect the effects of these alternate electron acceptors in limiting methanogenesis, rather than enhancing aerobic methanotrophy.

At the desert site, nitrate (NO₃⁻) was the strongest correlate of net methane uptake ($r^2 = 0.50$, $p < 0.0001$, $n = 13$). Close ties between methane and nitrogen cycling have long been recognized (Bédard and Knowles 1989), although these typically relate to ammonium (NH₄⁺) metabolism, while here,

no significant correlation between ammonium concentration and methane uptake was identified. Fewer studies have investigated the effects of nitrate on soil methane uptake, and the existing work has found evidence for both stimulatory and inhibitory effects with an unknown mechanism (Wang and Ineson 2003, Reay and Nedwell 2004, Jang *et al* 2011). Hillslope measurement locations at the desert site all had below-average nitrate values, and these locations also had significantly higher methane uptake rates than other desert measurement locations ($p < 0.001$), so without additional measurements and experiments, it is difficult to attribute the observed relationship to nitrate abundance versus topography or some other confounding factor.

All auxiliary variables had a significant correlation with net methane uptake rate when all sites were considered together; however, only D90 (the 90th percentile of soil particle diameter) correlated with fluxes at each site individually as well as across all three sites. Soil texture has previously been identified as a relevant control on soil methane uptake in some field studies, which is typically attributed to the effect of particle size on soil permeability and thus methane and oxygen diffusion (Dalal *et al* 2008). Under this framework, higher methane uptake would be expected in soils with higher sand content, and thus higher D90. Instead, here we find a small but systematic correlation between lower soil methane uptake and increased D90 ($r^2 = 0.16$, $p < 0.0001$, $n = 46$). It is possible that at these dryland sites, methanotrophy is moisture-limited, consistent with the weak positive correlation of uptake with VWC ($r^2 = 0.10$, $p = 0.002$). A positive correlation between methane uptake and soil moisture has similarly been shown in laboratory experiments when soil water content is low (Czepiel *et al.*, 1995). In this case, higher soil particle size might lead to lower soil moisture retention, inhibiting microbial activity including methanotrophy. This explanation is consistent with a weak positive relationship between D90 and measured VWC (r^2 of log-log regression = 0.25, $p < 0.0001$). Since VWC measurements were based on timepoint samples, D90 may be a better proxy for long-term VWC, indicating that in California dryland environments, methanotrophy rates may be limited by low soil moisture. Supporting this possibility, soil moisture-related enhancement of methane uptake rates has been shown previously in dryland environments (Striegl *et al* 1992; Dijkstra *et al.*, 2011).

The hypothesis of moisture limitation of methanotrophy in dryland soils further provides an explanation for the poor correlation of VWC with net soil methane uptake. An analogy can be drawn to the case of temperature, where field studies often find a weak relationship of temperature with net methane flux: this is attributed to the positive correlation of both methanotrophy and methanogenesis with temperature (Feng *et al* 2020 and references therein). Similarly, if both methanotrophy and methanogenesis are stimulated by increased soil moisture in dry soils, the matching trends in gross methane production and consumption will produce a muted signal of net moisture sensitivity.

2.4.5) Influence of vegetation and soil microbiome on methane uptake rates

When measured methane uptake rates are grouped by the dominant vegetation alliance at the measurement location, significant distinctions emerge. Analysis of fluxes by vegetation was limited to vegetation alliances that were present at more than one measurement location. Desert vegetation types were not statistically distinct from one another ($p > 0.05$), and riparian locations at both the desert and coastal sites produced similarly low uptake rates (Figure 2.5). Pasture sites, characterized by intermediate uptake rates, were statistically different from all other vegetation types ($p < 0.02$). Pine and oak woodlands were statistically indistinct from one another ($p = 0.17$). Coastal sage scrub, the vegetation type with the highest mean and maximum methane uptake rates, was significantly different from all other vegetation types except for oak woodlands ($p \leq 0.001$). This finding is consistent with previous studies that find land cover or land use type an important determinant of soil methane uptake (Dutaur and Verchot 2007).

As the distribution of vegetation types is closely tied to local soil properties and microclimate (e.g., Gough *et al* 2000, Dodd *et al* 2002, D’Odorico *et al* 2013, Metzger *et al* 2017), many possible factors could explain distinct uptake rates across vegetation types. First, different vegetation types may be associated with particular values of relevant soil or climatic parameters that correlate with uptake rate. For example, pasture and pine woodland measurement locations yield distinct methane uptake rates; pasture locations also have higher bulk density than pine woodland locations ($p = 0.0001$), which correlates with lower uptake rates (Figure 2.4). Similarly, at the coastal site, iron and manganese were found to be the strongest correlates of uptake rates, and are also more abundant in coastal sage scrub sites than other vegetation types ($p \leq 0.02$). In many such cases, it is difficult to

determine which variable is the true driver of differences in methane uptake rate: vegetation or soil/climatic properties.

However, in the case of soil organic carbon content (SOC), significant differences between vegetation types closely mirror the observed differences in flux: desert scrub, riparian, and unvegetated measurement locations have significantly lower SOC than other vegetation types, and SOC at pine woodland locations is significantly lower than coastal sage scrub locations ($p \leq 0.03$). Given that vegetation is known to profoundly affect SOC content and distribution (Jobbágy and Jackson 2000), vegetation control on SOC is a likely contributor to the trends observed here.

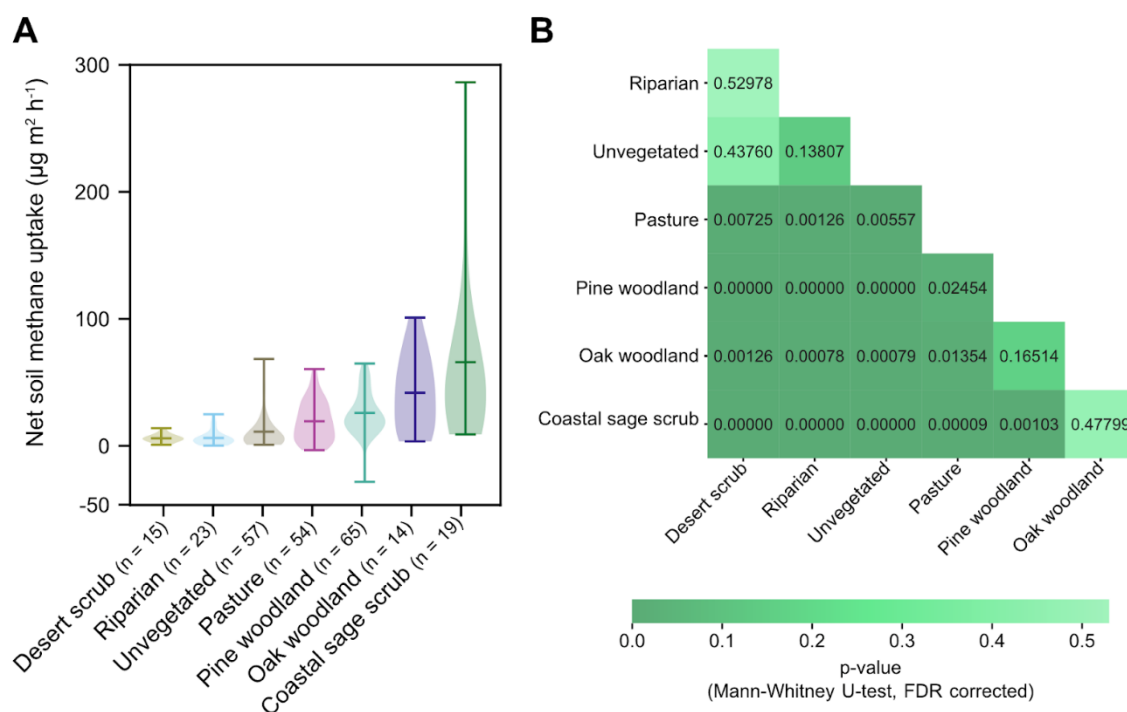


Figure 2.5: A. Violin plots of soil methane uptake distributions by vegetation type. For each vegetation type, the central line shows the mean value, and top and bottom lines show the minimum and maximum value. B. P-values produced by Mann-Whitney U-tests in pairwise comparison of vegetation types, adjusted for multiple hypothesis testing via a Benjamini-Hochberg false discovery rate (FDR) correction and rounded to five significant figures.

To further investigate the effects of ecological differences on soil methane cycling at these field sites, we compared soil microbial community composition among sites and its relationship to methane uptake rate. We assessed microbial community composition on the basis of 16S rRNA sequence abundance data (Section 2.3.8). Of 20 most abundant taxonomic families present at each site, they

dominantly belonged to the *Actinomycetota*, *Alphaproteobacteria*, and *Planctomycetes* orders (Figure 2.6A), and all three sites shared 9 of 20 families at greatest relative abundance. Among these shared most abundant families was *Beijerinckiaceae*, the family that contains upland soil cluster alpha (USC- α), an uncultivated group of taxa that has been associated with high-affinity methane uptake in soils (Knief *et al* 2003, Pratscher *et al* 2018). However, of known methylotrophic taxa in *Beijerinckiaceae*, only one ASV—*Methylobacterium soli*—was found at >1% abundance in more than five samples. Meanwhile, commonly known methanotrophic taxa including *Methylomonas*, *Methylobacter*, *Methyломicrobium*, *Methylococcus*, and *Methylocaldum* (Knief *et al* 2003) were universally not detected, occurring at $\leq 1\%$ across all samples.

Non-metric multidimensional scaling (NMDS) analysis, which uses dimensionality reduction to summarize differences in microbial community structure, indicated a systematic difference in the microbial community at desert sites relative to coastal and foothills sites (Figure 2.6B). When net methane flux was superimposed on NMDS results, no clear relationship between Bray-Curtis distance and net methane flux was evident, outside the systematically low fluxes measured at the desert site. Additionally, lasso regression indicated that the abundance of microbial taxa (at both ASV and family levels) was weakly correlated or uncorrelated with microbial community structure as assessed by 16S. For lasso regression of VST-stabilized ASV abundances with methane uptake across all sites, the cross-validation (CV) r^2 was at best 0.11 when flux outliers were omitted (flux values more than 2.5 standard deviations from the dataset average), and predicted methane uptake rates were poorly correlated with measured values (Figure 2.6C). Predictive ability did not improve at the family level (CV $r^2 = 0.10$). Lasso regressions of abundance data with flux at individual field sites produced no significant correlations (CV $r^2 \leq 0.03$). This suggests that any significant predictive ability achieved by lasso regression across all three sites likely results from distinct microbial community composition and lower net methane uptake at the desert site. Further, it seems likely that the influence of vegetation type on net uptake rates does not result from the enrichment or depletion of specific microbial taxa in association with vegetation. Thus, although microbial metabolic activity is a key parameter in controlling soil methane flux, large-scale taxonomic structure (as assessed by 16S sequencing) appears to be a poor proxy for metabolic activity at these sites. This finding is consistent with previous work that has found a decoupling of function and taxonomy across a wide

range of Earth surface environments (Louca *et al* 2016, 2018) and in laboratory-assembled communities (Goldford *et al* 2018). Net soil-atmosphere methane flux has previously been found to correspond to the abundance of the *pmoA* gene (Sabrekov *et al* 2020, Xu *et al* 2023), so the lack of correspondence between methane uptake rates and taxon abundance may indicate that *pmoA* transcription has no clear relationship with taxonomy in these samples.

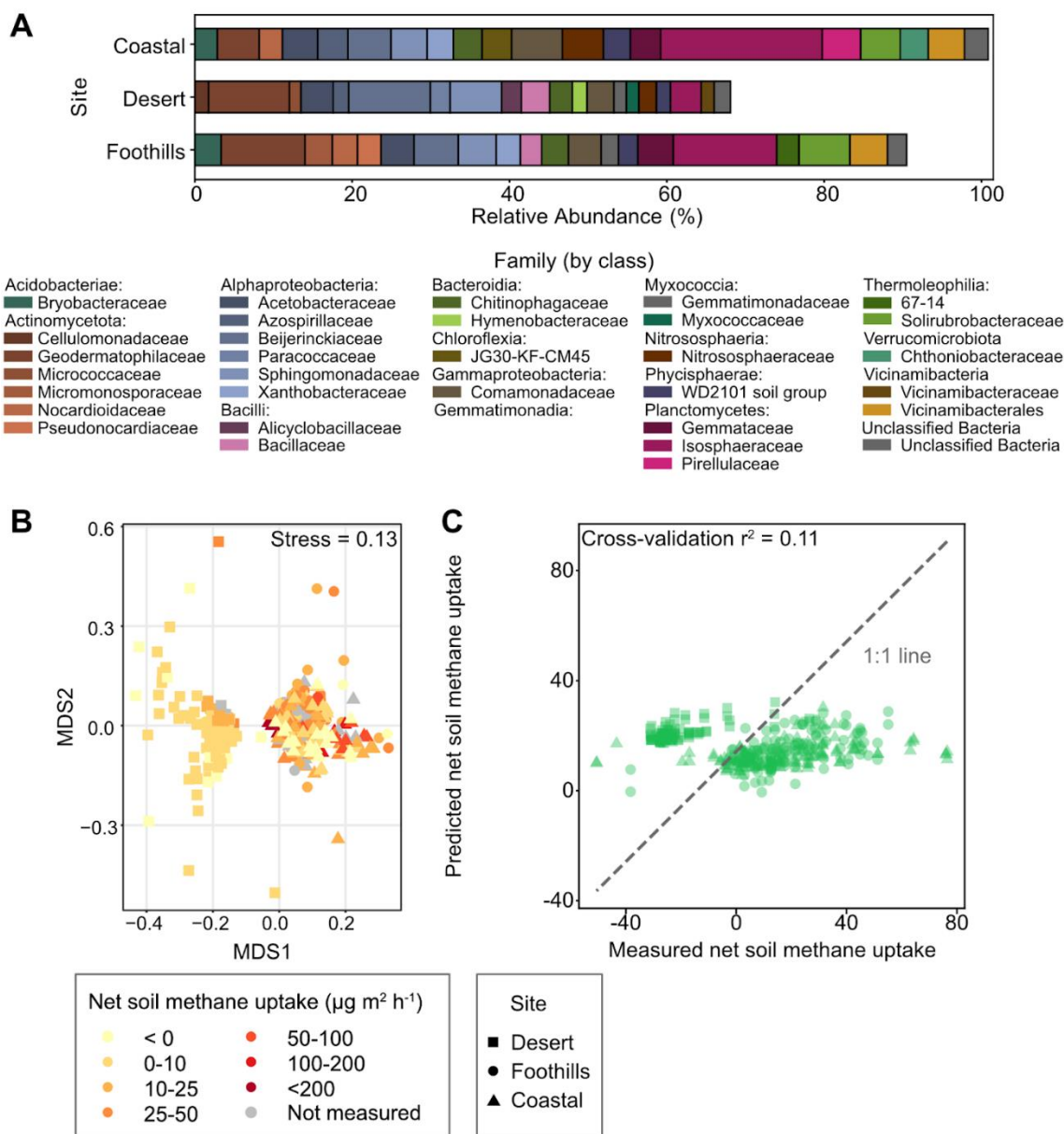


Figure 2.6: Analyses of soil microbial community composition, as assessed by 16S rRNA sequencing, and its relationship to site and soil methane uptake rates. A. Relative abundance of the top 20 taxonomic families at each site. Families are grouped and colored by taxonomic class. B. Non-metric multidimensional scaling (NMDS) analysis of amplicon sequence variant (ASV) data

after variance-stabilizing transformation (VST) (stress = 0.13). MDS1 substantially separates desert samples (squares) from foothills (circle) and coastal (triangle) samples. Points are colored by net soil methane uptake rate; gray indicates samples for which net soil methane uptake measurements were not acquired due to instrument malfunction. C. Lasso regression of VST-stabilized ASV data versus net soil methane uptake rate across all sites, excluding outliers where uptake was more than 2.5 standard deviations away from the dataset mean. Point shape indicates measurement site. The regression has weak predictive power for soil methane uptake rates, and the cross-validation r^2 is 0.11.

2.4.6) Comparison to a simple soil methane flux model

To assess how common model formulations perform in predicting soil methane fluxes at our dryland field sites, we implemented a simplified version of the DLEM model (Tian *et al* 2010) for each field site (Section 2.3.10) and compared modeled and measured methane fluxes. At the coastal site, the model predicts high rates of soil methane efflux through most of the year (Figure 2.7A), with an average value of over $-19,000 \mu\text{g methane m}^{-2} \text{h}^{-1}$ between January 2022 and January 2024. Modeled periods of maximum efflux correspond with high values of VWC as estimated in ERA5 data (Hersbach *et al* 2023) (Figure 2.2). Because the coastal site is situated adjacent to riverine and estuarine areas, robust methane efflux is likely at some locations within the ERA5 grid cell that contains this site. However, even considering the possibility for spatial heterogeneity, the modeled efflux is certain to overestimate the true rate: it is 3–44 times higher than the average methane efflux measured for saturated soil and sediment types at FLUXNET sites (Delwiche *et al* 2021) (Delwiche *et al.*, 2021). As model output is highly sensitive to kinetic parameters (Supplementary Figure 2.8), this may indicate that the tuned kinetic parameters for methanogenesis reported by Tian *et al* (2010) are inaccurate for this site. Meanwhile, periods where the coastal site model predicts net methane uptake, the modeled uptake rate is $112 \pm 36 \mu\text{g m}^{-2} \text{h}^{-1}$. This modeled rate exceeds the average measured uptake rate ($31 \pm 43 \mu\text{g m}^{-2} \text{h}^{-1}$) by ~ 3.6 -fold.

In contrast to the coastal site, modeled methane fluxes at the desert and foothills sites agree more closely with measured rates (Figure 2.7B–C). At the desert site, modeled methane uptake averages $48 \pm 26 \mu\text{g m}^{-2} \text{h}^{-1}$ (1σ), 6-fold higher than the measured value of $8.1 \pm 12 \mu\text{g m}^{-2} \text{h}^{-1}$. Meanwhile, at the foothills site, modeled uptake is $96 \pm 60 \mu\text{g m}^{-2} \text{h}^{-1}$, 3.8-fold higher than measured rates of $25 \pm 17 \mu\text{g m}^{-2} \text{h}^{-1}$. Given the sensitivity of model outputs to kinetic parameters, an adjustment of K_M and V_{max} of methanotrophy could enable the model to accurately reproduce average values while remaining well within natural variability of methanotrophy kinetics (Dion-Kirschner *et al* 2024). Additionally, because of high soil pH at the desert site (9 ± 0.4) and low-growing vegetation at the

foothills site, reintroducing pH limitation and plant methane transport to the model could lower modeled uptake rates, bringing them closer in line with measured values.

Across all three sites, the model produces much larger seasonal trends in methane fluxes than what was observed in measured values. Modeled seasonality is a function of temperature and VWC variability, while in our dataset temperature did not correlate with measured methane fluxes across field sites, and VWC correlated only weakly (Figure 2.4). In the case of the desert site, this may be due partly to the temporal mismatch between seasonal measurements and transient periods of increased VWC. However, the consistency in overestimation of seasonal trends across all field sites indicates that the modeled sensitivity of methane uptake to temperature and soil moisture may be inflated for these dryland sites, possibly a function of moisture limitation for both methanotrophy and methanogenesis.

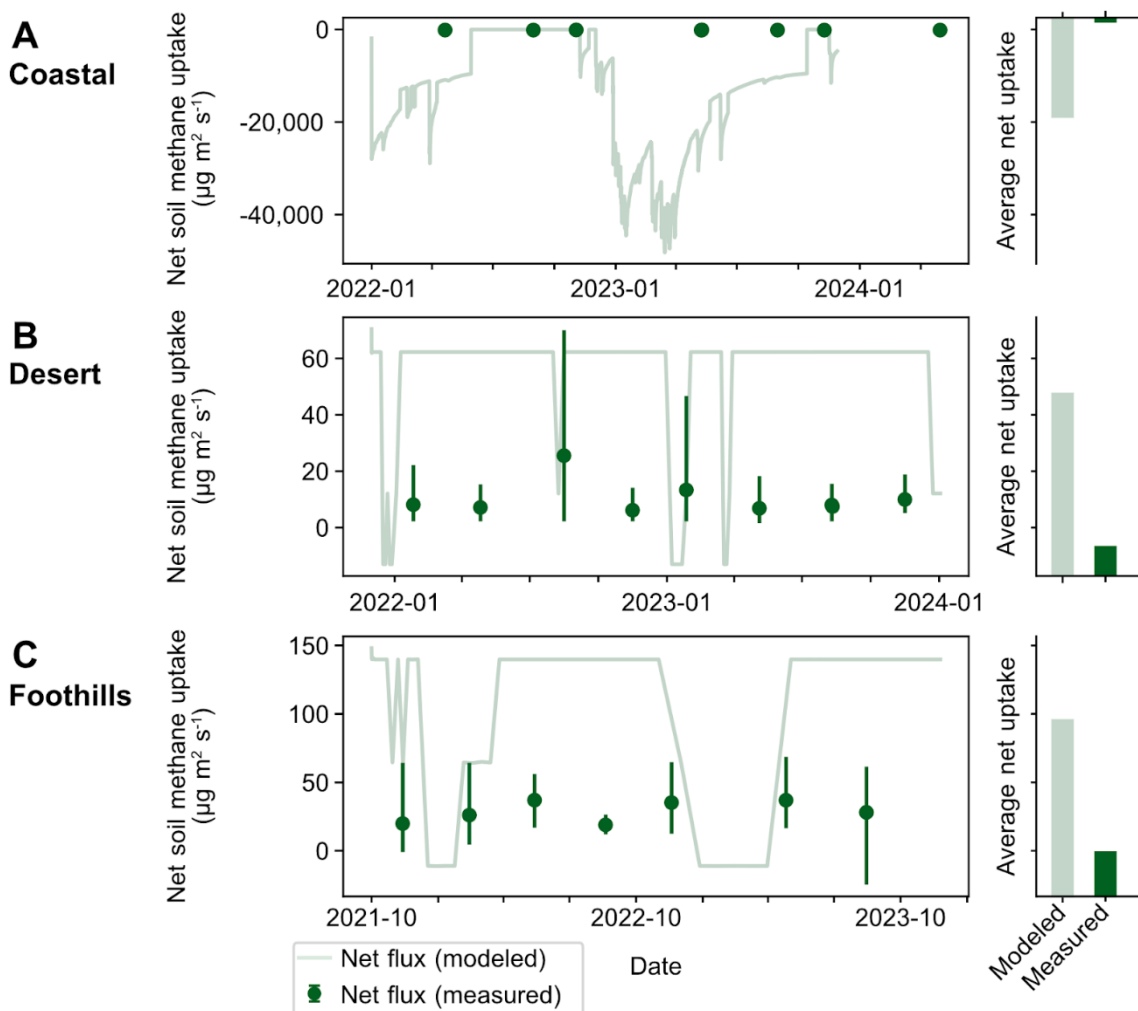


Figure 2.7: Comparison of modeled (pale green lines) and measured (dark green points) soil methane uptake rates for coastal (A), desert (B), and foothills (C) sites. Dark green points show the mean value measured at a given field site and day, and dark green lines span the range of measured values. Bar charts at right show the average value from modeled (pale green) and measured (dark green) uptake rates.

2.4.7) Possible sources of data-model gaps

Where modeled methane flux diverges from measured values, several explanations are possible. Broadly, possible explanations for model-data gaps can be delineated into three categories: 1) the model mechanics may be sufficient, but parameterization inaccurate; 2) the model mechanics may be insufficient, excluding important controlling parameters (or including unimportant ones); and/or 3) a mismatch in the temporal and spatial scales of modeled and measured values may prevent meaningful comparison between the two. In Section 2.4.6, we have described how explanation 1

might be relevant for this study, given that adjusting the kinetic parameters may adequately match average modeled methane uptake with average measured values.

Meanwhile, explanation 3 may contribute to the large disagreement in the direction and magnitude of methane fluxes at the coastal site, because of the topographic variety represented in the ERA5 grid cell. While, as in this work, many studies of soil-atmosphere methane fluxes are performed as point-in-time measurements using a small portable chamber, this measurement strategy may not always accurately capture the true spatial and temporal dynamics of methane cycling. Previous studies have shown that estimates of ecosystem methane exchange based on chamber measurements often disagree with estimates from larger-scale measurements like eddy covariance (Hill and Vargas 2022, Clement *et al* 1995). These larger-scale measurements with time-continuous data collection may be a more appropriate basis to compare field-collected data to modeled uptake rates.

On the other hand, the limited spatial resolution of ERA5 data prevents the model from capturing the substantial spatial variability in methane flux rates that we have observed across a single site on a single day—even though this meter- and hour-scale variability is the main source of variance in this study. While it is possible that these differences among measurement locations may average out to match modeled values in a grid cell, they may also point to mechanisms that are inadequately represented in models and could lead to bias. This aligns with explanation 2 for model-data mismatch: the omission of potentially important variables from existing models may prevent models from accurately predicting naturally existing variability.

In this study, we found that many previously identified controls on soil methane uptake rate were weak, insignificant, or inconclusive correlates of uptake rates: these include soil nitrogen and metal content, pH, and microbial community structure. However, in our dataset, the observed methane uptake rates, both within and among sites, were significantly stratified by vegetation type (Figure 2.5). As discussed in section 2.4.5, the control of vegetation type on methane uptake rates may be a function of vegetation soil carbon inputs. Plant exudates could include methanogenic substrates (Girkin *et al* 2018, Waldo *et al* 2019), inhibitory compounds affecting methanogens and/or methanotrophs, and/or substrates supporting facultative methanotroph activity (Dedysh *et al* 2005). Especially given previous findings that soil soluble organic carbon content (reported as DOC)

correlates with methane uptake in a dryland environment (Sullivan *et al* 2013), a systematic study of soil methane cycling in response to plant carbon inputs could reveal additional mechanisms that might improve model accuracy.

2.5) Summary and recommendations

Our measurements of methane uptake in dryland soils present several important considerations for modeling efforts. First, we find that despite large ranges in temperature and VWC, seasonal signals are weak or absent at each site. We further find that correlations between temperature, VWC, and soil methane uptake are weak or absent. This contrasts starkly with many previous studies showing that soil methane fluxes are strongly dependent on moisture. Here, the lack of a clear relationship with VWC suggests that both methanotrophy and methanogenesis may be moisture-limited: as a result, spikes in soil moisture may stimulate both gross methane production and consumption, creating a muted response of net flux to moisture. The resulting climate-insensitivity of net methane fluxes at these dryland sites drives disagreement in seasonal patterns between measured and modeled soil uptake rates.

Additionally, while many physical and chemical variables are uncorrelated or weakly correlated with methane uptake across the three dryland sites, we find a strong stratification of methane fluxes by vegetation type. The relationship between vegetation type and methane uptake does not evidently correspond with any differences in the soil microbial community, but seems at least partially mediated by plant inputs of soil organic carbon (SOC). While most global biogeochemical models assign differential soil carbon cycling properties by plant functional type, the specific relationship of vegetation types with methane uptake should be more closely investigated to improve model accuracy.

The simple model we implement here overestimates both methane uptake in unsaturated soils and methane production in saturated soils. The model-data disagreement we observe in time-averaged methane fluxes is likely to be resolved by parameter tuning. Meanwhile, the model overestimates seasonal trends and cannot capture small-scale spatial variability in fluxes. These areas of mismatch can likely be attributed to all three explanations we advance here: inadequate parameterization of

existing relationships (e.g., climate sensitivity), omission of additional important parameters (e.g., vegetation type), and mismatch in temporal and spatial scales. Based on these findings, we recommend more systematic study of methane fluxes in dryland environments, focusing on the key mechanisms of temperature and soil moisture sensitivity and the role of vegetation type. In particular, additional measurements may reveal the specific plant litter or exudate components that drive differences in methane cycling, enabling better modeling of the soil methane sink according to plant functional type. Finally, while we acknowledge the financial and logistical challenges of long-term methane flux monitoring, our findings highlight the value of high temporal resolution and large spatial scale *in situ* measurements in comparing measured and modeled soil methane fluxes. Taken together, our results reveal unique characteristics of dryland soils that merit focused efforts to improve model parameterization for these important earth surface environments.

2.6) Acknowledgements

This project was supported by the Resnick Sustainability Institute at Caltech. Access was provided to the desert and foothills field sites by the Bureau of Land Management Barstow and Mother Lode field offices, respectively, with particular help from Lis Lucas and Chris Otahal. Access to the coastal field site was provided by the White Buffalo Land Trust, and special thanks go out to Ann Close, Aarushi Jhatro, Jesse Smith, and Darien Rubow for their help and hospitality. Many field partners made this work possible: Rebecca Wipfler, Nicholas Koranda, Bradley Kirschner, Noam Lotem, James Mullahoo, Richard Horak, Josh Anadu, Eran Funaro, Tristan Caro, Katie Huy, Hemani Kalucha, Celia Kong-Johnson, Jarek Kwiecinski, Pippa Richter, and Alejandro Cabrero-Cortez. Stephanie Connon and Dan Utter helped substantially with DNA sample preparation and 16S sequence analyses. Renato Braghiere helped retrieve ERA5 data and Xiaojing (Ruby) Fu's guidance on soil modeling was instrumental.

2.7) References

Beck H E, McVicar T R, Vergopolan N, Berg A, Lutsko N J, Dufour A, Zeng Z, Jiang X, van Dijk A I J M and Miralles D G 2023 High-resolution (1 km) Köppen-Geiger maps for 1901–2099 based on constrained CMIP6 projections *Sci Data* **10** 724

- Bédard C and Knowles R 1989 Physiology, biochemistry, and specific inhibitors of CH₄, NH₄⁺, and CO oxidation by methanotrophs and nitrifiers. *Microbiology and Molecular Biology Reviews* **53** 68–84
- Bender M and Conrad R 1993 Kinetics of methane oxidation in oxic soils *Chemosphere* **26** 687–96
- Benstead J and King G M 2001 The effect of soil acidification on atmospheric methane uptake by a Maine forest soil *FEMS Microbiol Ecol* **34** 207–12
- Boeckx P, Van Cleemput O and Villaralvo I 1997 Methane oxidation in soils with different textures and land use *Nutrient Cycling in Agroecosystems* **49** 91–5
- Born M, Dörr H and Levin I 1990 Methane consumption in aerated soils of the temperate zone *Tellus B* **42** 2–8
- Callahan B J, McMurdie P J, Rosen M J, Han A W, Johnson A J A and Holmes S P 2016 DADA2: High-resolution sample inference from Illumina amplicon data *Nat Methods* **13** 581–3
- Castaldi S, Ermice A and Strumia S 2006 Fluxes of N₂O and CH₄ from soils of savannas and seasonally-dry ecosystems *Journal of Biogeography* **33** 401–15
- Castro M S, Melillo J M, Steudler P A and Chapman J W 1994 Soil moisture as a predictor of methane uptake by temperate forest soils *Can. J. For. Res.* **24** 1805–10
- Clement R J, Verma S B and Verry E S 1995 Relating chamber measurements to eddy correlation measurements of methane flux *Journal of Geophysical Research: Atmospheres* **100** 21047–56
- Courtois E A, Stahl C, Van den Berge J, Bréchet L, Van Langenhove L, Richter A, Urbina I, Soong J L, Peñuelas J and Janssens I A 2018 Spatial Variation of Soil CO₂, CH₄ and N₂O Fluxes Across Topographical Positions in Tropical Forests of the Guiana Shield *Ecosystems* **21** 1445–58
- Curry C L 2007 Modeling the soil consumption of atmospheric methane at the global scale *Global Biogeochemical Cycles* **21** Online: <https://agupubs.onlinelibrary.wiley.com/doi/abs/10.1029/2006GB002818>
- Czepiel P M, Crill P M and Harriss R C 1995 Environmental factors influencing the variability of methane oxidation in temperate zone soils *Journal of Geophysical Research: Atmospheres* **100** 9359–64
- Dalal R C, Allen D E, Livesley S J and Richards G 2008 Magnitude and biophysical regulators of methane emission and consumption in the Australian agricultural, forest, and submerged landscapes: a review *Plant Soil* **309** 43–76

- Davis N M, Proctor D M, Holmes S P and Relman D A Simple statistical identification and removal of contaminant sequences in marker-gene and metagenomics data
- Dedysh S N, Knief C and Dunfield P F 2005 *Methylocella* Species Are Facultatively Methanotrophic *JB* **187** 4665–70
- Delwiche K B, Knox S H, Malhotra A, Fluet-Chouinard E, McNicol G, Feron S, Ouyang Z, Papale D, Trotta C, Canfora E, Cheah Y-W, Christianson D, Alberto M C R, Alekseychik P, Aurela M, Baldocchi D, Bansal S, Billesbach D P, Bohrer G, Bracho R, Buchmann N, Campbell D I, Celis G, Chen J, Chen W, Chu H, Dalmagro H J, Dengel S, Desai A R, Detto M, Dolman H, Eichelmann E, Euskirchen E, Famulari D, Fuchs K, Goeckede M, Gogo S, Gondwe M J, Goodrich J P, Gottschalk P, Graham S L, Heimann M, Helbig M, Helfter C, Hemes K S, Hirano T, Hollinger D, Hörtnagl L, Iwata H, Jacotot A, Jurasinski G, Kang M, Kasak K, King J, Klatt J, Koebsch F, Krauss K W, Lai D Y F, Lohila A, Mammarella I, Belelli Marchesini L, Manca G, Matthes J H, Maximov T, Merbold L, Mitra B, Morin T H, Nemitz E, Nilsson M B, Niu S, Oechel W C, Oikawa P Y, Ono K, Peichl M, Peltola O, Reba M L, Richardson A D, Riley W, Runkle B R K, Ryu Y, Sachs T, Sakabe A, Sanchez C R, Schuur E A, Schäfer K V R, Sonnentag O, Sparks J P, Stuart-Haëntjens E, Sturtevant C, Sullivan R C, Szutu D J, Thom J E, Torn M S, Tuittila E-S, Turner J, Ueyama M, Valach A C, Vargas R, et al 2021 FLUXNET-CH₄: a global, multi-ecosystem dataset and analysis of methane seasonality from freshwater wetlands *Earth System Science Data* **13** 3607–89
- Dijkstra F A, Morgan J A, Fischer J C von and Follett R F 2011 Elevated CO₂ and warming effects on CH₄ uptake in a semiarid grassland below optimum soil moisture *Journal of Geophysical Research: Biogeosciences* **116** Online: <https://agupubs.onlinelibrary.wiley.com/doi/abs/10.1029/2010JG001288>
- D’Imperio L, Li B-B, Tiedje J M, Oh Y, Christiansen J R, Kepfer-Rojas S, Westergaard-Nielsen A, Brandt K K, Holm P E, Wang P, Ambus P and Elberling B 2023 Spatial controls of methane uptake in upland soils across climatic and geological regions in Greenland *Commun Earth Environ* **4** 1–10
- D’Imperio L, Nielsen C S, Westergaard-Nielsen A, Michelsen A and Elberling B 2017 Methane oxidation in contrasting soil types: responses to experimental warming with implication for landscape-integrated CH₄ budget *Global Change Biology* **23** 966–76
- Dion-Kirschner H, Nguyen N H, Frankenberg C and Fischer W W 2024 Evaluating the contribution of methanotrophy kinetics to uncertainty in the soil methane sink *Environ. Res. Lett.* **19** 064059
- Dodd M B, Lauenroth W K, Burke I C and Chapman P L 2002 Associations between vegetation patterns and soil texture in the shortgrass steppe *Plant Ecology* **158** 127–37

- D'Odorico P, He Y, Collins S, De Wekker S F J, Engel V and Fuentes J D 2013 Vegetation–microclimate feedbacks in woodland–grassland ecotones *Global Ecology and Biogeography* **22** 364–79
- Duc N T, Crill P and Bastviken D 2010 Implications of temperature and sediment characteristics on methane formation and oxidation in lake sediments *Biogeochemistry* **100** 185–96
- Dunfield P, Knowles R, Dumont R and Moore T 1993 Methane production and consumption in temperate and subarctic peat soils: Response to temperature and pH *Soil Biology and Biochemistry* **25** 321–6
- Dutaur L and Verchot L V 2007 A global inventory of the soil CH₄ sink *Global Biogeochemical Cycles* **21** Online: <https://agupubs.onlinelibrary.wiley.com/doi/abs/10.1029/2006GB002734>
- Esri 2024 Koppen-Geiger Climate Classification Online: <https://www.arcgis.com/home/item.html?id=1e468410784c4b9a81f43af7f0f9b133>
- Feng H, Guo J, Han M, Wang W, Peng C, Jin J, Song X and Yu S 2020 A review of the mechanisms and controlling factors of methane dynamics in forest ecosystems *Forest Ecology and Management* **455** 117702
- Feng H, Guo J, Peng C, Ma X, Kneeshaw D, Chen H, Liu Q, Liu M, Hu C and Wang W 2023 Global estimates of forest soil methane flux identify a temperate and tropical forest methane sink *Geoderma* **429** 116239
- Forster, P., T. Storelvmo, K. Armour, W. Collins, J.-L. Dufresne, D. Frame, D.J. Lunt, T. Mauritsen, M.D. Palmer, M. Watanabe, M. Wild, and H. Zhang, 2021: The Earth's Energy Budget, Climate Feedbacks, and Climate Sensitivity. In *Climate Change 2021: The Physical Science Basis. Contribution of Working Group I to the Sixth Assessment Report of the Intergovernmental Panel on Climate Change* [Masson-Delmotte, V., P. Zhai, A. Pirani, S.L. Connors, C. Péan, S. Berger, N. Caud, Y. Chen, L. Goldfarb, M.I. Gomis, M. Huang, K. Leitzell, E. Lonnoy, J.B.R. Matthews, T.K. Maycock, T. Waterfield, O. Yelekçi, R. Yu, and B. Zhou (eds.)]. Cambridge University Press, Cambridge, United Kingdom and New York, NY, USA, pp. 923–1054, doi: 10.1017/9781009157896.009.
- Gatica G, Fernández M E, Juliarena M P and Gyenge J 2020 Environmental and anthropogenic drivers of soil methane fluxes in forests: Global patterns and among-biomes differences *Global Change Biology* **26** 6604–15
- Girkin N T, Turner B L, Ostle N, Craigon J and Sjögersten S 2018 Root exudate analogues accelerate CO₂ and CH₄ production in tropical peat *Soil Biology and Biochemistry* **117** 48–55

- Goldford J E, Lu N, Bajić D, Estrela S, Tikhonov M, Sanchez-Gorostiaga A, Segrè D, Mehta P and Sanchez A 2018 Emergent simplicity in microbial community assembly *Science* **361** 469–74
- Gough L, Shaver G R, Carroll J, Royer D L and Laundre J A 2000 Vascular plant species richness in Alaskan arctic tundra: the importance of soil pH *Journal of Ecology* **88** 54–66
- Guo Z, Wang Y, Wan Z, Zuo Y, He L, Li D, Yuan F, Wang N, Liu J, Song Y, Song C and Xu X 2020 Soil dissolved organic carbon in terrestrial ecosystems: Global budget, spatial distribution and controls ed T Hickler *Global Ecol. Biogeogr.* **29** 2159–75
- H. Hersbach, B. Bell, P. Berrisford, G. Biavati, Horányi, A, Muñoz Sabater, J., J. Nicolas, C. Peubey, R. Radu, I. Rozum, D. Schepers, A. Simmons, C. Soci, D. Dee, and J-N Thépaut 2023 ERA5 hourly data on single levels from 1940 to present.
- Hartmann A A, Buchmann N and Niklaus P A 2011 A study of soil methane sink regulation in two grasslands exposed to drought and N fertilization *Plant Soil* **342** 265–75
- He L, Groom J D, Wilson E H, Fernandez J, Konopka M C, Beck D A C and Lidstrom M E 2023 A methanotrophic bacterium to enable methane removal for climate mitigation *Proceedings of the National Academy of Sciences* **120** e2310046120
- He T, Ding W, Cheng X, Cai Y, Zhang Y, Xia H, Wang X, Zhang J, Zhang K and Zhang Q 2024 Meta-analysis shows the impacts of ecological restoration on greenhouse gas emissions *Nat Commun* **15** 2668
- Hill A C and Vargas R 2022 Methane and Carbon Dioxide Fluxes in a Temperate Tidal Salt Marsh: Comparisons Between Plot and Ecosystem Measurements *Journal of Geophysical Research: Biogeosciences* **127** e2022JG006943
- Ho A, Lüke C, Reim A and Frenzel P 2016 Resilience of (seed bank) aerobic methanotrophs and methanotrophic activity to desiccation and heat stress *Soil Biology and Biochemistry* **101** 130–8
- Hou L-Y, Wang Z-P, Wang J-M, Wang B, Zhou S-B and Li L-H 2012 Growing season in situ uptake of atmospheric methane by desert soils in a semiarid region of northern China *Geoderma* **189–190** 415–22
- James Danoff-Burg and Luis Ramirez 2024 *Afton Canyon Bioblitz 2024 Report*
- Jang I, Lee S, Zoh K-D and Kang H 2011 Methane concentrations and methanotrophic community structure influence the response of soil methane oxidation to nitrogen content in a temperate forest *Soil Biology and Biochemistry* **43** 620–7

- Jari Oksanen, F. Guillaume Blanchet, Michaeli Friendly, Roeland Kindt, Pierre Legendre, Dan McGlinn, Peter R. Minchin, R. B. O'Hara, Gavin L. Simpson, Peter Solymos, M. Henry H. Stevens, Eduard Szoecs, and Helene Wagner 2024 Vegan: Community Ecology Package Online: <https://CRAN.R-project.org/package=vegan>
- Jobbágy E G and Jackson R B 2000 The Vertical Distribution of Soil Organic Carbon and Its Relation to Climate and Vegetation *Ecological Applications* **10** 423–36
- Jones D L and Willett V B 2006 Experimental evaluation of methods to quantify dissolved organic nitrogen (DON) and dissolved organic carbon (DOC) in soil *Soil Biology and Biochemistry* **38** 991–9
- Kaiser K, McGlynn B and Dore J 2018 Landscape Analysis of Soil Methane Flux Across Complex Terrain *Biogeosciences* Online: https://scholarworks.boisestate.edu/geo_facpubs/412
- King G M and Adamsen A P S 1992 Effects of Temperature on Methane Consumption in a Forest Soil and in Pure Cultures of the Methanotroph *Methylobacterium rubrum* *Appl. Environ. Microbiol.* **58** 2758–63
- Klein A, Crawford J, Evens J, Keeler-Wolf T and Hickson D 2007 *Classification of the Vegetation Alliances and Associations of the Northern Sierra Nevada Foothills, California Volume 1 of 2 – Introduction, Methods, and Results* (California Department of Fish and Game)
- Knief C, Lipski A and Dunfield P F 2003 Diversity and Activity of Methanotrophic Bacteria in Different Upland Soils *AEM* **69** 6703–14
- Lacroix E M, Aeppli M, Boye K, Brodie E, Fendorf S, Keiluweit M, Naughton H R, Noël V and Sihi D 2023 Consider the Anoxic Microsite: Acknowledging and Appreciating Spatiotemporal Redox Heterogeneity in Soils and Sediments *ACS Earth Space Chem.* **7** 1592–609
- Louca S, Parfrey L W and Doebeli M 2016 Decoupling function and taxonomy in the global ocean microbiome *Science* **353** 1272–7
- Louca S, Polz M F, Mazel F, Albright M B N, Huber J A, O'Connor M I, Ackermann M, Hahn A S, Srivastava D S, Crowe S A, Doebeli M and Parfrey L W 2018 Function and functional redundancy in microbial systems *Nat Ecol Evol* **2** 936–43
- Menke J, Reyes E and Johnson D 2011 *Northern Sierra Nevada foothills vegetation project: vegetation mapping report*. (California Department of Fish and Game)
- Metzger J C, Wutzler T, Dalla Valle N, Filipzik J, Grauer C, Lehmann R, Roggenbuck M, Schelhorn D, Weckmüller J, Küsel K, Totsche K U, Trumbore S and Hildebrandt A 2017 Vegetation

- impacts soil water content patterns by shaping canopy water fluxes and soil properties *Hydrological Processes* **31** 3783–95
- Miller K E, Lai C-T, Friedman E S, Angenent L T and Lipson D A 2015 Methane suppression by iron and humic acids in soils of the Arctic Coastal Plain *Soil Biology and Biochemistry* **83** 176–83
- Mirzabaev, A., J. Wu, J. Evans, F. García-Oliva, I.A.G. Hussein, M.H. Iqbal, J. Kimutai, T. Knowles, F. Meza, D. Nedjraoui, F. Tena, M. Türkeş, R.J. Vázquez, M. Weltz, 2019: Desertification. In: *Climate Change and Land: an IPCC special report on climate change, desertification, land degradation, sustainable land management, food security, and greenhouse gas fluxes in terrestrial ecosystems* [P.R. Shukla, J. Skea, E. Calvo Buendia, V. Masson-Delmotte, H.-O. Pörtner, D.C. Roberts, P. Zhai, R. Slade, S. Connors, R. van Diemen, M. Ferrat, E. Haughey, S. Luz, S. Neogi, M. Pathak, J. Petzold, J. Portugal Pereira, P. Vyas, E. Huntley, K. Kissick, M. Belkacemi, J. Malley, (eds.)]. <https://doi.org/10.1017/9781009157988.005>
- Murali A, Bhargava A and Wright E S 2018 IDTAXA: a novel approach for accurate taxonomic classification of microbiome sequences *Microbiome* **6** 140
- Murguía-Flores F M 2018 *Modelling the global atmospheric methane uptake by soils in the past, present and future* (Bristol: University of Bristol)
- NOAA National Centers for Environmental Information. (2021). *Monthly Climate Normals for 1991–2020: Temperature and Precipitation*. <https://www.ncei.noaa.gov/products/us-climate-normals>
- Parada A E, Needham D M and Fuhrman J A 2016 Every base matters: assessing small subunit rRNA primers for marine microbiomes with mock communities, time series and global field samples *Environmental Microbiology* **18** 1403–14
- Poggio L, de Sousa L M, Batjes N H, Heuvelink G B M, Kempen B, Ribeiro E and Rossiter D 2021 SoilGrids 2.0: producing soil information for the globe with quantified spatial uncertainty *SOIL* **7** 217–40
- Pratscher J, Vollmers J, Wiegand S, Dumont M G and Kaster A-K 2018 Unravelling the Identity, Metabolic Potential and Global Biogeography of the Atmospheric Methane-Oxidizing Upland Soil Cluster α *Environmental Microbiology* **20** 1016–29
- Právělie R 2016 Drylands extent and environmental issues. A global approach *Earth-Science Reviews* **161** 259–78
- Reay D S and Nedwell D B 2004 Methane oxidation in temperate soils: effects of inorganic N *Soil Biology and Biochemistry* **36** 2059–65

- Saari A, Rinnan R and Martikainen P J 2004 Methane oxidation in boreal forest soils: kinetics and sensitivity to pH and ammonium *Soil Biology and Biochemistry* **36** 1037–46
- Sabrekov A F, Semenov M V, Terent'eva I E, Litti Yu V, Il'yasov D V and Glagolev M V 2020 The link between Soil Methane Oxidation Rate and Abundance of Methanotrophs Estimated by Quantitative PCR *Microbiology* **89** 182–91
- Saunio M, Stavert A R, Poulter B, Bousquet P, Canadell J G, Jackson R B, Raymond P A, Dlugokencky E J, Houweling S, Patra P K, Ciais P, Arora V K, Bastviken D, Bergamaschi P, Blake D R, Brailsford G, Bruhwiler L, Carlson K M, Carrol M, Castaldi S, Chandra N, Crevoisier C, Crill P M, Covey K, Curry C L, Etiope G, Frankenberg C, Gedney N, Hegglin M I, Höglund-Isaksson L, Hugelius G, Ishizawa M, Ito A, Janssens-Maenhout G, Jensen K M, Joos F, Kleinen T, Krummel P B, Langenfelds R L, Laruelle G G, Liu L, Machida T, Maksyutov S, McDonald K C, McNorton J, Miller P A, Melton J R, Morino I, Müller J, Murguía-Flores F, Naik V, Niwa Y, Noce S, O'Doherty S, Parker R J, Peng C, Peng S, Peters G P, Prigent C, Prinn R, Ramonet M, Regnier P, Riley W J, Rosentreter J A, Segers A, Simpson I J, Shi H, Smith S J, Steele L P, Thornton B F, Tian H, Tohjima Y, Tubiello F N, Tsuruta A, Viovy N, Voulgarakis A, Weber T S, van Weele M, van der Werf G R, Weiss R F, Worthy D, Wunch D, Yin Y, Yoshida Y, Zhang W, Zhang Z, Zhao Y, Zheng B, Zhu Q, Zhu Q and Zhuang Q 2020 The Global Methane Budget 2000–2017 *Earth Syst. Sci. Data* **12** 1561–623
- Semrau J D, DiSpirito A A and Yoon S 2010 Methanotrophs and copper *FEMS Microbiol Rev* **34** 496–531
- Shrestha P M, Kammann C, Lenhart K, Dam B and Liesack W 2012 Linking activity, composition and seasonal dynamics of atmospheric methane oxidizers in a meadow soil *The ISME Journal* **6** 1115–26
- Smith K A, Dobbie K E, Ball B C, Bakken L R, Sitaula B K, Hansen S, Brumme R, Borken W, Christensen S, Priemé A, Fowler D, Macdonald J A, Skiba U, Klemmedtsson L, Kasimir-Klemmedtsson A, Degórska A and Orlanski P 2000 Oxidation of atmospheric methane in Northern European soils, comparison with other ecosystems, and uncertainties in the global terrestrial sink *Global Change Biology* **6** 791–803
- Song H, Peng C, Zhu Q, Chen Z, Blanchet J-P, Liu Q, Li T, Li P and Liu Z 2024 Quantification and uncertainty of global upland soil methane sinks: Processes, controls, model limitations, and improvements *Earth-Science Reviews* **252** 104758
- Striegl R G, McConnaughey T A, Thorstenson D C, Weeks E P and Woodward J C 1992 Consumption of atmospheric methane by desert soils *Nature* **357** 145–7
- Sullivan B W, Selmants P C and Hart S C 2013 Does dissolved organic carbon regulate biological methane oxidation in semiarid soils? *Global Change Biology* **19** 2149–57

- Täumer J, Marhan S, Groß V, Jensen C, Kuss A W, Kolb S and Urich T 2022 Linking transcriptional dynamics of CH₄-cycling grassland soil microbiomes to seasonal gas fluxes *The ISME Journal* **16** 1788–97
- Terra Genesis International 2020 *Jalama Canyon Ranch Concept Design Report* (Ithaca, New York)
- Tian H, Xu X, Liu M, Ren W, Zhang C, Chen G and Lu C 2010 Spatial and temporal patterns of CH₄ and N₂O fluxes in terrestrial ecosystems of North America during 1979–2008: application of a global biogeochemistry model *Biogeosciences* **7** 2673–94
- Waldo N B, Hunt B K, Fadely E C, Moran J J and Neumann R B 2019 Plant root exudates increase methane emissions through direct and indirect pathways *Biogeochemistry* **145** 213–34
- Wang Z-P and Ineson P 2003 Methane oxidation in a temperate coniferous forest soil: effects of inorganic N *Soil Biology and Biochemistry* **35** 427–33
- Xu H, Duan P and Li D 2023 Topography-dependent mechanisms underlying the impacts of nitrogen addition on soil methane uptake in a subtropical karst forest *Applied Soil Ecology* **190** 104992
- Xu L, Furtaw M D, Madsen R A, Garcia R L, Anderson D J and McDermitt D K 2006 On maintaining pressure equilibrium between a soil CO₂ flux chamber and the ambient air *Journal of Geophysical Research: Atmospheres* **111** Online: <https://onlinelibrary.wiley.com/doi/abs/10.1029/2005JD006435>
- Xu X, Yuan F, Hanson P J, Wullschleger S D, Thornton P E, Riley W J, Song X, Graham D E, Song C and Tian H 2016 Reviews and syntheses: Four decades of modeling methane cycling in terrestrial ecosystems *Biogeosciences* **13** 3735–55
- Yu L, Huang Y, Zhang W, Li T and Sun W 2017 Methane uptake in global forest and grassland soils from 1981 to 2010 *Science of The Total Environment* **607–608** 1163–72
- Zhang K, Gan R, Li Y, Chen W, Ma D, Chen J and Luo H 2024 Effects of anaerobic oxidation of methane (AOM) driven by iron and manganese oxides on methane emissions in constructed wetlands and underlying mechanisms *Chemical Engineering Journal* **495** 153539
- Zhang Y, Huang M, Yu K, Xie Y, Wang Y, Wu J, Zheng F, Wu S, Li S, Sardans J, Peñuelas J and Zou J 2023 Decreased CH₄ emissions associated with methanogenic and methanotrophic communities and their interactions following Fe(III) fertiliser application in rice paddies *Geoderma* **431** 116375
- Zhao J-F, Peng S-S, Chen M-P, Wang G-Z, Cui Y-B, Liao L-G, Feng J-G, Zhu B, Liu W-J, Yang L-Y and Tan Z-H 2019 Tropical forest soils serve as substantial and persistent methane sinks *Sci Rep* **9** 16799

2.8) Supplementary Information.

2.8.1) Model governing equations.

Domain:

2D rectangle (width = 1 m, height = 0.3 m)

Domain divided into 3 layers (equal width) following available input data:

Layer 1: 0-5 cm

Layer 2: 5-15 cm

Layer 3: 15-30 cm

Boundary conditions:

No flux through either side or bottom boundaries.

Top boundary is in equilibrium with atmosphere, where $[\text{CH}_4]_g = [\text{CH}_4]_{\text{atm}} = 0.001217 \text{ g/m}^3 = 1.7 \text{ ppmv}$ (Earth Observatory NASA). $[\text{DOC}]_{\text{aq}} = 0$.

Key variables and constants:

ϕ = soil porosity (Coastal = 0.73, Desert = 0.47, Foothills = 0.71)

v_{wc} = soil volumetric water content [m^3/m^3] (time series input)

$1-v_{wc}$ = relative volume of air in pore space

$\phi * v_{wc}$ = relative volume of water in total volume

$\phi * (1-v_{wc})$ = relative volume of air in total volume

$[\text{CH}_4]_g$ = concentration of methane in gas phase

$[\text{CH}_4]_{\text{aq}}$ = concentration of methane in aqueous phase

$[\text{CH}_4]_{\text{aq}} = [\text{CH}_4]_g * H_C$; H_C = Henry's law constant or Bunsen solubility coefficient ($\beta=0.0035 \text{ ml/ml}$, used in Tian et al., 2010)

$[\text{DOC}]_{\text{aq}}$ = concentration of dissolved organic carbon in aqueous phase

$D_{\text{CH}_4,g} = 2.1\text{e-}5 \text{ m}^2/\text{s}$ (Engineering Toolbox, also Langenberg et al., 2020)

$D_{\text{CH}_4,\text{aq}} = 1.6\text{e-}9 \text{ m}^2/\text{s}$ (Engineering Toolbox)

$D_{\text{DOC},\text{aq}} = 1.9\text{e-}10 \text{ m}^2/\text{s}$ (Hendry et al., 2003)

$H = 0.3 \text{ m}$ = height of domain

Governing Equations

To solve for CH₄ and DOC concentrations, we employ reaction-diffusion equations:

Evolution of CH₄ in air:

$$\frac{\partial(\phi)}{\partial t} = \nabla(D_{CH_4,g}\phi\nabla[CH_4]_g)$$

Evolution of CH₄ in water:

$$\frac{\partial(vwc[CH_4]_{aq})}{\partial t} = \nabla(D_{CH_4,aq}vwc\nabla[CH_4]_{aq}) + vwcR_{production} - vwcR_{oxidation}$$

Combined Evolution of CH₄:

Since $D_{CH_4,aq} \ll D_{CH_4,g}$, we neglect diffusion in water

$$\frac{\partial((\phi + vwcHc)[CH_4]_g)}{\partial t} = \nabla(D_{CH_4,g}\phi\nabla[CH_4]_g) + vwcHc(R_{production} - R_{soil\ oxidation})$$

Evolution of DOC in water:

$$\frac{\partial(\phi[DOC]_{aq})}{\partial t} = \nabla(D_{DOC,aq}vwc\nabla[DOC]_{aq}) - vwcR_{production}$$

Reactions

Soil Methane Production (aqueous):

$$R_{production} = V_{max,prod} \frac{[DOC]_{aq}}{[DOC]_{aq} + K_{M,prod}} f(T) f_{prod}(vwc) [=] \text{g}/(\text{m}^3 \cdot \text{s})$$

Soil Methane Oxidation (aqueous):

$$R_{soil\ oxidation} = \min(V_{max,soil\ oxid} \frac{[CH_4]_{aq}}{[CH_4]_{aq} + K_{M,soil\ oxid}} f(T) f_{oxid}(vwc), [CH_4]_{aq}) [=] \text{g}/(\text{m}^3 \cdot \text{s})$$

Transport Fluxes

Atmospheric Methane Oxidation (gas):

$$F_{air\ oxidation} = (V_{max,air\ oxid} \frac{[CH_4]_{atm}}{[CH_4]_{atm} + K_{M,air\ oxid}} f(T) f_{oxid}(vwc)) [=] \text{g}/(\text{m}^2 \cdot \text{s})$$

Ebullition from water to atmosphere:

$$F_E = \max([CH_4]_{aq} - 6, 0) [=] \text{g}/(\text{m}^2 \cdot \text{s})$$

where:

6 is the threshold value above which dissolved CH₄ will form bubbles and leave water [g/m³].

Diffusion from water to atmosphere:

$$F_D = V_{exchange} ([CH_4]_{aq} - [CH_4]_{max}) [=] \text{g}/(\text{m}^2 \cdot \text{s})$$

where:

$V_{exchange} = 0.3 \frac{m}{d}$ = exchange coefficient of CH₄ through interface of soil pore water to air,

$[CH_4]_{max} = [CH_4]_{atm} * \beta$ = maximum concentration of CH₄ in soil solution [g/m³]

$\beta = 0.035 \frac{ml}{ml}$, Bunsen solubility coefficient.

Net Flux of Methane:

$$F_{CH_4} = F_D + F_E - (F_{air\ oxidation} * H) [=] \text{g}/(\text{m}^2 \cdot \text{s})$$

Environmental Dependencies (as in Tian et al., 2010)

$$f(T) = \begin{cases} 0, & T < -5 \\ Q_{10}^{\frac{T-30}{10}}, & 10 > T \geq -5 \\ 1, & T \geq 30 \end{cases}$$

$$f_{prod}(vwc) = \begin{cases} 0, & vwc \leq vwc_{fc} \\ \left(\frac{vwc - vwc_{fc}}{vwc_{sat} - vwc_{fc}} \right)^2 \times 0.368 \times e^{\left(\frac{vwc - vwc_{fc}}{vwc_{sat} - vwc_{fc}} \right)}, & vwc_{fc} < vwc < vwc_{sat} \\ 1, & vwc \geq vwc_{sat} \end{cases}$$

$$f_{oxid}(vwc) = 1 - f_{prod}(vwc)$$

Note: Soil VWC is given as time series input for each layer of soil. Data not available for middle soil layer—therefore values were derived by linearly interpolating between the top and bottom soil layers (using middle of soil depth for each layer).

Initial Values (Concentrations in g/m³):

Layer	CH ₄ (All Sites)*	DOC Coastal	DOC Desert	DOC Foothills
1 (0-5 cm)	0.001	1385	156	978
2 (5-15 cm)	0.0005	1108	125	487
3 (15-30 cm)	0.0003	423	93	240

*Initial CH₄ values approximated from Maier *et al* 2017.

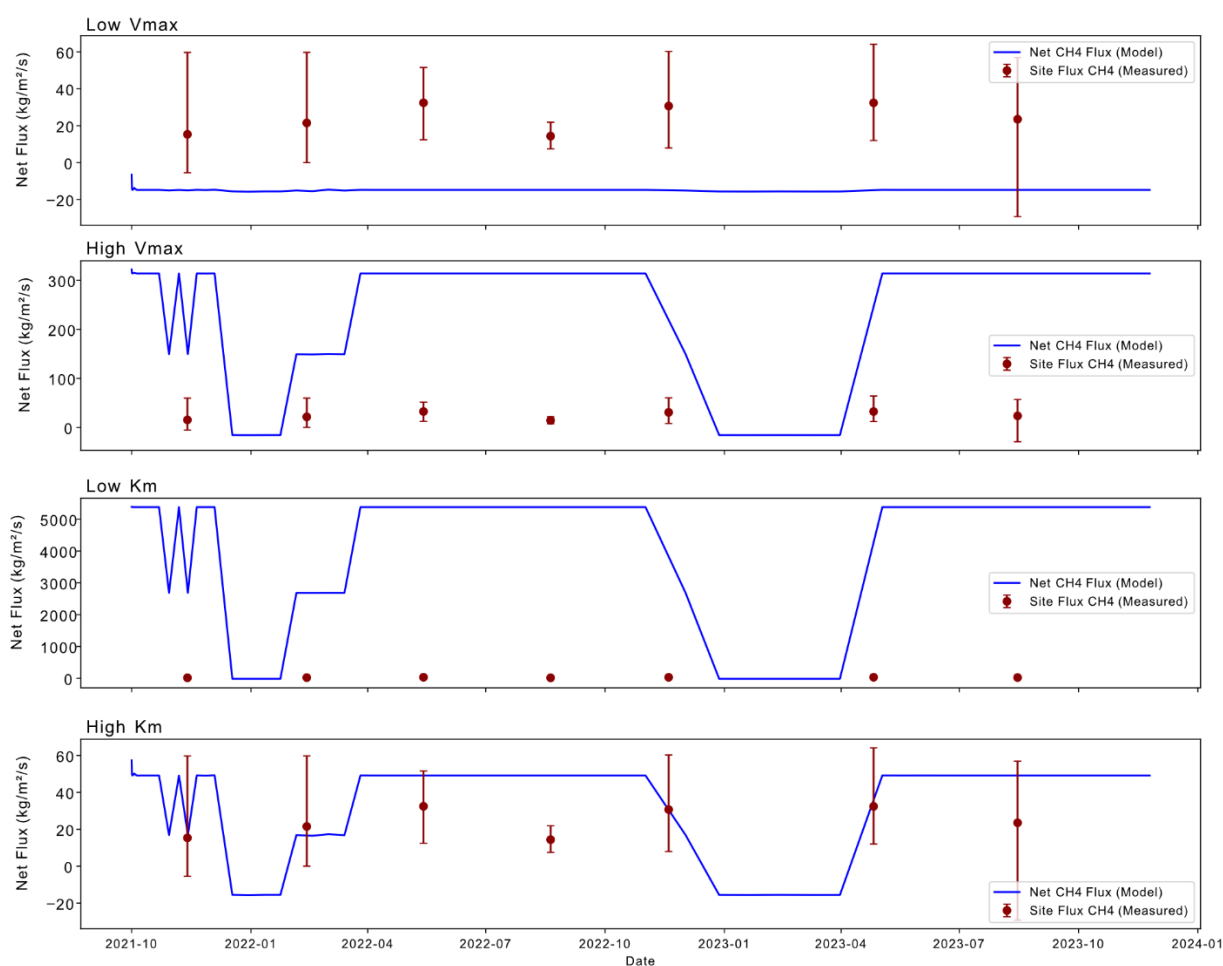
2.8.2) Model parameters

Supplementary Table 2.1: Parameters used for soil methane model.

Parameter	Site	Value	Source
Q10, methanotrophy	All	2.5	Song et al 2009
Q10, methanogenesis	All	2.5	Song et al 2009
VWC _{fc} , coastal	Coastal	0.21	Ratliff et al 1983 (sandy loam)
VWC _{fc} , foothills	Foothills	0.30	Ratliff et al 1983 (silt loam)
VWC _{fc} , desert	Desert	0.10	Ratliff et al 1983 (sand)
VWC _{sat} , coastal	Coastal	0.49	SoilGrids (Poggio et al 2021)
VWC _{sat} , foothills	Foothills	0.48	SoilGrids (Poggio et al 2021)
VWC _{sat} , desert	Desert	0.47	SoilGrids (Poggio et al 2021)
V _{exchange}	All	0.3 m d ⁻¹	Happell and Chanton, 1995
V _{soil, oxid, max}	All	0.457 g C m ⁻³ d ⁻¹	Dion-Kirschner et al 2024
V _{air, oxid, max}	All	0.457 g C m ⁻³ d ⁻¹	Dion-Kirschner et al 2024
K _{m, soil, oxid}	All	62.5 ppm	Dion-Kirschner et al 2024
K _{m, air, oxid}	All	62.5 ppm	Dion-Kirschner et al 2024
VCH ₄ , pro, max	Desert	0.25	Tian et al 2010
VCH ₄ , pro, max	Coastal and foothills	0.6	Tian et al 2010
K _m CH ₄ , pro	All	15	Tian et al 2010

2.8.3) Model sensitivity to kinetic parameters

To assess the sensitivity of modeled methane fluxes to kinetic parameters, we ran the model with low and high values of K_M (0.1 to 150 ppm) and V_{max} (0.001 to 1 g m⁻³ d⁻¹) of methanotrophy, reflecting the range of these values most commonly observed in soil samples from environments similar to the study sites (Dion-Kirschner *et al* 2024). Model results were highly sensitive to changes in both kinetic parameters (Figure 2.8).



Supplementary Figure 2.8) Model results for Foothills site under low and high K_M and V_{max} values, demonstrating the sensitivity to kinetic constants used as model parameters.

2.8.4) Supplementary references

Dion-Kirschner H, Nguyen N H, Frankenberg C and Fischer W W 2024 Evaluating the contribution of methanotrophy kinetics to uncertainty in the soil methane sink *Environ. Res. Lett.* **19** 064059

Happell J D, Chanton J P and Showers W J 1995 Methane transfer across the water-air interface in stagnant wooded swamps of Florida: Evaluation of mass-transfer coefficients and isotopic fractionation *Limnology and Oceanography* **40** 290–8

Poggio L, de Sousa L M, Batjes N H, Heuvelink G B M, Kempen B, Ribeiro E and Rossiter D 2021 SoilGrids 2.0: producing soil information for the globe with quantified spatial uncertainty *SOIL* **7** 217–40

Ratliff L F, Ritchie J T and Cassel D K 1983 Field-Measured Limits of Soil Water Availability as Related to Laboratory-Measured Properties *Soil Science Society of America Journal* **47** 770–5

Song C, Xu X, Tian H and Wang Y 2009 Ecosystem–atmosphere exchange of CH₄ and N₂O and ecosystem respiration in wetlands in the Sanjiang Plain, Northeastern China *Global Change Biology* **15** 692–705

Tian H, Xu X, Liu M, Ren W, Zhang C, Chen G and Lu C 2010 Spatial and temporal patterns of CH₄ and N₂O fluxes in terrestrial ecosystems of North America during 1979–2008: application of a global biogeochemistry model *Biogeosciences* **7** 2673–94

*Chapter 3***POSITION-SPECIFIC CARBON ISOTOPE ANALYSIS OF GLUCOSE AT
NATURAL ISOTOPE ABUNDANCE BY ORBITRAP MASS
SPECTROMETRY**

Hannah Dion-Kirschner, Celia Kong-Johnson, Kimberly R. Sharp, Nathan Dalleska, John Eiler, and Alex Sessions

3.1) Abstract

The isotopic composition of glucose carries the signature of the metabolic processes it undergoes, but conventional isotope analysis methods obscure its intramolecular structure. Here, we present a new method for position-specific isotope analysis (PSIA) of glucose using Electrospray Ionization-Orbitrap mass spectrometry (ESI-Orbitrap MS). This method measures $\delta^{13}\text{C}$ values at five unique intramolecular sites in glucose at natural isotope abundance and requires $< 50 \mu\text{g}$ per sample—over four orders of magnitude less than PSIA by NMR. By oxidizing glucose to gluconate and measuring with ESI-Orbitrap, we resolve the isotopic composition of the molecular ion and four fragment ions with analytical precision of 0.1–0.5%. Our method recapitulates intramolecular $\delta^{13}\text{C}$ patterns previously demonstrated for natural sugars formed through C3 and C4 photosynthetic pathways, while enabling substantially higher throughput and sensitivity. This is the first application of Orbitrap-PSIA to a carbohydrate, and it establishes a foundation for tracing metabolic fluxes in environmental, biomedical, and ecological systems. Future developments could extend the method to the ^{18}O and ^2H isotope systems, further enhancing its value for investigating glucose dynamics across many natural settings.

3.2) Introduction

Glucose is a universally relevant biomolecule, and its carbon isotopic composition in a given system carries traces of the metabolic processes it undergoes (Rossmann *et al* 1991, Tcherkez *et al* 2004). The isotopic signatures of metabolism as recorded by glucose have been used to elucidate nutrient flows in plant tissues (Rossmann *et al* 1991, Gilbert *et al* 2012), aquatic systems (Teece

and Fogel 2007), soils (Hobbie *et al* 2003, Dungait *et al* 2009), microbial mats (Gonzalez-Nayeck *et al* 2022), and host-parasite systems (Hesse *et al* 2023), as well as to test food authenticity (Guyon *et al* 2011, 2014, Cabañero *et al* 2006) and even to track human metabolism (Lefebvre *et al* 1975, Hawley *et al* 1992).

The stable carbon isotope composition ($\delta^{13}\text{C}$ value) of biomolecules, including glucose, primarily results from enzymatic reactions acting on those molecules (Hayes 2001). Many enzymatic reactions of glucose break and form bonds at specific atomic positions within the glucose monomer. The rate of bond breaking and formation is sensitive to isotopic substitutions: for example, bonds with ^{13}C are typically less kinetically favorable than bonds with ^{12}C . As a result of the difference in rate constants according to isotopic substitutions, enzymatic reactions often select for a higher proportion of ^{12}C in the product than in the reactant pool. The isotope effects imparted by these enzymatic reactions is concentrated at the atomic positions involved in bond breaking or formation. For example, during glycolysis the enzyme aldolase cleaves a 6-carbon sugar to two 3-carbon compounds, with strong isotopic selectivity at carbon positions 3 and 4 where a C-C bond is broken. As a result, the 3-carbon products of aldolase in the glycolysis pathway have a lower $\delta^{13}\text{C}$ value than the pool of 6-carbon reactant (Gleixner and Schmidt 1997). Due to the positional selectivity of enzymes like aldolase, previous studies of plant glucose have found that its intramolecular ^{13}C composition is typically heterogeneous (Rossmann *et al* 1991, Tcherkez *et al* 2004; Gilbert *et al* 2012), with different carbon isotopic composition at different atomic positions. Resolving positional differences in the isotopic composition of plant glucose (and likely glucose from other sources as well) can therefore reveal information about the enzymes with which it has interacted, helping to retrace metabolic fluxes.

Traditional methods for carbon isotope measurement destroy the spatial isotopic structure of biomolecules prior to measurement, making it impossible to resolve positional isotopic differences. EA-IRMS and GC-IRMS require conversion of the analyte to gaseous CO_2 , losing information about the positioning of isotopic substitutions. In contrast, methods for position-specific isotope analysis (PSIA) enable isotopic measurement of intact molecules, retaining more nuanced signals of metabolism recorded by the isotopic structure of biomolecules. Previous work

has demonstrated ^{13}C -PSIA of glucose using nuclear magnetic resonance (NMR) (Gilbert *et al* 2009). While PSIA via NMR is a powerful tool for resolving valuable isotopic information, it is limited by large sample size requirements (20-110 mg of glucose) (Wieloch *et al* 2018), long analysis times (23 to >100 hours per sample) (Thomas Wieloch, personal comm.), and substantial sensitivity to small (<0.5%) impurities (Gilbert *et al* 2009). Here, we present a new method for ^{13}C -PSIA of glucose using Orbitrap mass spectrometry that enables independent ^{13}C abundance measurements of five unique intramolecular sites while overcoming most limitations imposed by NMR-PSIA. This method employs Electrospray Ionization (ESI)-Orbitrap, an instrument with microgram-level sensitivity that can accommodate typical sample sizes in environmental and human health studies.

Orbitrap-PSIA is made possible through a combination of new sample introduction techniques, ultrahigh mass resolution, and tandem mass spectrometry (MS/MS) (Eiler *et al* 2017, Neubauer *et al* 2023). In the case of ESI-Orbitrap, samples are introduced by electrospray ionization, a soft ionization mode that does not induce fragmentation. For this application, we improve the efficiency of sample ionization by oxidizing glucose to gluconate prior to sample introduction. Once the intact analyte is ionized, a user can select the ion(s) of interest using the quadrupole, mitigating the impacts of minor sample impurities. The selected ion or ions are directed to the higher-energy collisional dissociation (HCD) cell, where molecular ions are broken into smaller fragments. These fragment ions, all descended from the analyte of interest, are subsequently introduced into the Orbitrap, where the $^{13}\text{C}/^{12}\text{C}$ ratio of every fragment can be observed simultaneously (Eiler *et al* 2017, Hilkert *et al* 2021). Because each fragment samples a different subset of atomic positions from the molecular ion (Figure 3), the isotopic composition at each position can be solved using matrix algebra (e.g., Wilkes *et al* 2022, discussed further in Sections 3.3.7 and 3.4.2).

PSIA via Orbitrap has previously been shown for amino acids (Neubauer *et al* 2018, Weiss *et al* 2023, Csernica *et al* 2023, Chimiak *et al* 2021), ethyltoluenes (Cesar *et al.*, 2019), and methylphosphonic acid (Csernica *et al* 2025). Here we present the first Orbitrap-based PSIA of a

carbohydrate compound at natural isotope abundance, opening the door for more nuanced understanding of glucose fluxes across many natural systems.

3.3) Experimental

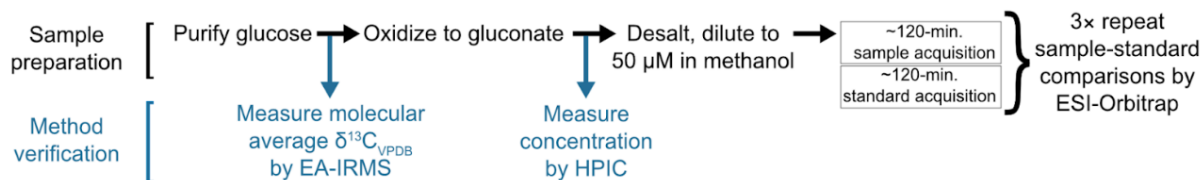


Figure 3.1. Schematic illustrating method steps for sample preparation and method verification.

3.3.1) Standard materials

We acquired two sodium gluconate standards from commercial suppliers, both >98% purity: standard “GlcA” from Sigma-Aldrich (Lot # SLBT7828), and standard “GlcB” from VWR Life Science (Lot # 21K1056318). These standards were used to produce working solutions with a concentration of 10 mM in 18 MΩ deionized water (Milli-Q IQ 7000 Purification) which were subsequently filtered to <0.22 μm. Working solutions were stored frozen and subsequent dilutions were freshly made for each analytical session.

We used two glucose standards in this work, both of >95% purity. Standard “MC4” was acquired from Mallinckrodt Chemicals (Lot # H17H08) and standard “SC3” from Sigma-Aldrich (Lot # BCCD9888). Glucose standards were used to produce working solutions with a concentration of 10 mM in 18 MΩ deionized water (Milli-Q IQ 7000 Purification), which were stored frozen. Fresh dilutions of glucose working solutions were made as needed for each experiment.

We additionally acquired six glucose standards with positional isotopic labels from Cambridge Isotope Laboratories, Inc. Each standard contained 98-99% ¹³C label at one atomic position (C1: Lot #PR-30074, 98-99%; C2: Lot #M-2128, 99%; C3: Lot #I-18488, 99%; C4: Lot #I-19624, 99%; C5: Lot #M-1633, 98%; C6: Lot #I-23305, 99%). Each standard was used to create a 10 mM working solution in 18 MΩ deionized water (Milli-Q IQ 7000 Purification) which was stored frozen.

3.3.2) Glucose oxidation

Glucose was oxidized to gluconate following a method modified from Bunzel and Mathews (1909). In brief, 1.1 equivalents of Br₂ and 2 equivalents of NaOH were added to 1 equivalent of glucose in aqueous solution. The solution was stirred at 300 rpm at room temperature for 5 hours. The yield of this reaction was 66±1% (n = 8), and reaction yield did not change after 4 hours (1σ = 2%, n = 20). The reaction was confirmed not to impart measurable ¹³C fractionation as described in results section 3.6.

The reaction product was desalted by passing through a 2.5 mL Dionex OnGuard II Ag/H cartridge. Each cartridge was washed with 15 mL of 18 MΩ deionized water prior to sample application. Sample was applied to the column and eluted at a rate of 1-2 mL/min. After the eluted sample was collected, an additional 1 mL of water was applied to the column and collected in order to flush out any remaining product. No gluconate was detected in cartridge backgrounds as verified by ion chromatography. Following desalting, gluconate yields were determined by ion chromatography.

3.3.3) Ion chromatography

The content of gluconate and residual salts in samples was measured with Dionex Integriion HPIC (Thermo Fischer) ion chromatography systems, with anion and cation columns operating in parallel. Samples were diluted to expected concentrations of 10-100 μM in 18 MΩ water and then loaded onto serial anion and cation columns and detectors via a Dionex AS-DV autosampler. The instrument was operated as previously described (Speth et al., 2022). The identity of gluconate and other anion peaks (Na⁺, Br⁻) was verified by comparison to the retention times of authentic standards. Chromatographic peaks were integrated using the Cobra algorithm in Chromeleon version 7.2.9 and peak area was correlated to concentration by generating 5-point calibration curves with authentic standards. The detection limit of gluconate on the instrument was < 1 μM.

3.3.4) Isotope measurements by Elemental Analyzer-Isotope Ratio Mass Spectrometer

Molecular average carbon isotope composition of glucose and gluconate standard materials was characterized by an EA IsoLink combustion elemental analyzer system interfaced to a Delta V Plus isotope ratio mass spectrometer (EA-IRMS, Thermo Fisher Scientific). Samples were weighed to ~20 µg carbon, encapsulated in tin, and combusted at 1020 °C, after which the resulting CO₂ was analyzed for its carbon isotope composition by electron impact mass spectrometry. Measured carbon isotope ratios were calibrated to the VPDB scale against in-house isotope standards and international reference materials. The standard deviation of repeat standard measurements was < 0.1‰.

3.3.5) Isotope measurements by Electrospray Ionization-Orbitrap

Position-specific isotope analysis was performed using a Q Exactive HF Orbitrap mass spectrometer (Thermo Fischer Scientific). Samples were introduced to the mass spectrometer via a Vanquish Horizon ultra-high performance liquid chromatography (UHPLC) system and Heated Electrospray Ionization (HESI-II) probe (Thermo-Fischer Scientific). The UHPLC system was used for its autosampling capability and stable continuous sample infusion; it was not equipped with a chromatography column and no online separation was performed. The HESI probe was fitted with a 34-gauge needle optimized for flow rates of 1-10 µL/minute. Instrument settings for the HESI probe and Q Exactive are described in Table 3.1.

Table 3.1. Instrument settings for Orbitrap position-specific carbon isotope analysis of glucose.

Condition	Value
<i>HESI probe</i>	
Polarity	Negative
Spray voltage	-3.0 kV
Capillary temperature	200 °C
Auxiliary gas heater temperature	100 °C
Auxiliary gas flow rate	3 (arbitrary units)
Sheath gas flow rate	1 (arbitrary units)
Sweep gas flow rate	0 (arbitrary units)
Spray current	0.00 µA
S-lens RF level	55 (arbitrary units)
<i>Quadrupole, HCD cell, C-trap, and Orbitrap</i>	
Scan type	Parallel Reaction Monitoring
Inclusion list	195.5±1.4
Microscans	1
Fragmentation type	Higher-energy collisional dissociation
Collision energy	17.0 keV CE
Resolution at 200 m/z ($\Delta M/M$)	60,000
Automatic Gain Control (AGC) target	3x10 ⁶
Maximum inject time	200 ms

3.3.6) Orbitrap method overview

Standard and sample compounds were prepared as 50 μM solutions in LC-MS-grade methanol (VWR Life Sciences). The UHPLC was used to autosample and infuse 100- μL injections of sample or standard solution into the Orbitrap at a constant flow rate, typically 4 $\mu\text{L min}^{-1}$. For a typical analysis, 6 successive injections were performed to produce a total sample or standard analysis time of >120 minutes, accounting for the required 3 minutes of dead time between injections for the ion signal to restabilize. Repeat injections were required because our Vanquish sample loop and injection module sizes were limited to 100 μL ; larger sizes are available. Following these successive injections of analyte, the system was rinsed with pure HPLC-grade methanol for 10 minutes at a flow rate of 20 $\mu\text{L min}^{-1}$. This routine was repeated for sample-standard brackets, with each sample typically measured in triplicate relative to a standard of equivalent ion signal intensity, for a total of 7 acquisitions.

3.3.7) Orbitrap data processing and isotope calculations

Each continuous Orbitrap measurement of a given sample or standard, termed an “acquisition,” is comprised of many unique scans of the image current recorded by the Orbitrap detector. Under the instrument conditions described in Section 3.3.5, scan rates are typically $\sim 5 \text{ s}^{-1}$ and an acquisition comprises $\sim 32\text{k}$ scans. For each scan, the instrument software converts the image current into the intensity of the ion signal across a user-specified range of masses via a Fourier transform. Several additional data processing steps are required to convert these measured ion signal intensities into final $\delta^{13}\text{C}$ values for each atomic position.

Ion signal intensities and other relevant acquisition data were retrieved from the .RAW file format generated by the instrument software using IsoX (Kantnerová *et al* 2024). Ion signal intensity was used to estimate the absolute number of ions entering the Orbitrap analyzer (hereafter “counts”) following Makarov and Denisov (2009) and Eiler *et al* (2017). Uncorrected isotope ratios (^{13}R values) for each fragment of interest in the mass spectrum were calculated for every scan by taking the ratio of the counts of ^{13}C -substituted and unsubstituted ion peaks. For example, for the molecular ion with nominal mass 195 and formula $\text{C}_6\text{H}_{11}\text{O}_7$:

$$^{13}\text{R}_{195} = (\text{Counts } ^{13}\text{C}^{12}\text{C}_5^1\text{H}_{11}^{16}\text{O}_7) / (\text{Counts } ^{12}\text{C}_6^1\text{H}_{11}^{16}\text{O}_7) \quad (3.1)$$

Intervals of dead time in between injections of sample were removed from each acquisition by dropping those scans from the dataset. Windows of injection times were then manually verified to ensure that small variations in instrument timing did not result in erroneous inclusion of dead time in acquisition data. Next, to avoid mass spectrometric artifacts (described in Eiler *et al* 2017) as well as artifacts of data extraction, a given scan was only included in isotope ratio calculations if: 1) both isotopologues were present for a given scan, 2) peak masses were within 0.3-0.4 mDa of the expected values and 10 standard deviations of the acquisition mean mass for that peak, and 3) the product of total ion count and injection time was within 3 standard deviations of the mean (Chimiak *et al* 2021). The final uncorrected ^{13}R value for each fragment peak was obtained by taking the mean of measured ^{13}R values remaining after the described data culling steps.

Next, the ^{13}R value for each measured fragment was converted to a $\delta^{13}\text{C}$ value on the basis of repeat sample-standard measurements:

$$\delta^{13}\text{C}_{\text{Sample-Standard}} = (^{13}\text{R}_{\text{Sample}} - ^{13}\text{R}_{\text{Standard}}) / ^{13}\text{R}_{\text{Standard}} \quad (3.2)$$

Calculating $\delta^{13}\text{C}$ values of sample-standard comparisons allows for consistent reporting of isotopic composition, correcting for any potential fractionation or drift imparted by the instrument.

$\delta^{13}\text{C}$ values are reported in permil (‰), where 1‰ indicates one part per thousand relative difference between the measured sample and standard ^{13}R value. Each reported $\delta^{13}\text{C}$ value is the average of triplicate sample-standard comparisons and error bars represent the standard deviation of replicate $\delta^{13}\text{C}$ measurements, unless otherwise noted.

While $\delta^{13}\text{C}$ values are typically reported on the VPDB scale, isotope ratios for ion fragments measured by ESI-Orbitrap can only be tied to VPDB by comparing to another standard for which position- or fragment-specific $\delta^{13}\text{C}_{\text{VPDB}}$ values have been externally determined. (This is because isotopic fractionations imparted during Orbitrap analysis can vary among instrument conditions and among fragment ions.) No glucose or gluconate reference materials with known position-

specific values are currently available. As a result, we report all $\delta^{13}\text{C}$ values measured by ESI-Orbitrap relative to the gluconate standard GlnA, and denote these values as $\delta^{13}\text{C}_{\text{GlnA}}$:

$$\delta^{13}\text{C}_{\text{GlnA}} = ({}^{13}\text{R}_{\text{Sample}} - {}^{13}\text{R}_{\text{GlnA}}) / {}^{13}\text{R}_{\text{GlnA}} \quad (3.3)$$

When reporting $\delta^{13}\text{C}$ values obtained by EA-IRMS and anchored to the VPDB scale, we denote these values as $\delta^{13}\text{C}_{\text{VPDB}}$:

$$\delta^{13}\text{C}_{\text{VPDB}} = ({}^{13}\text{R}_{\text{Sample}} - {}^{13}\text{R}_{\text{VPDB}}) / {}^{13}\text{R}_{\text{VPDB}} \quad (3.4)$$

When comparing measured isotopic composition between any other combinations of compounds, not using the GlnA standard or the VPDB scale, we report these measurements as $\Delta^{13}\text{C}$:

$$\Delta^{13}\text{C}_{\text{Sample 1-Sample 2}} = \delta^{13}\text{C}_{\text{Sample 1}} - \delta^{13}\text{C}_{\text{Sample 2}} \quad (3.5)$$

${}^{13}\text{R}$ or $\delta^{13}\text{C}$ values for each fragment ion measured in the Orbitrap represent the combination of 2-6 individual carbon atomic positions. To convert fragment measurements to position-specific ${}^{13}\text{R}$ or $\delta^{13}\text{C}$ values, we constructed a matrix of equations representing the carbon atomic positions present in each fragment and the fragment carbon isotope composition (Figure 3.7). The matrix was constructed as described in Wilkes et al., 2022. In short, 15,000 Monte Carlo simulations were performed based on the measured fragment $\delta^{13}\text{C}$ values and measurement error, and the optimal solution for the matrix was calculated for each simulation using the `linalg.lstsq` function in the ‘numpy’ python package. The $\delta^{13}\text{C}$ value and error for each position was reported as the average and standard deviation of solutions to the 15,000 simulations. The attribution of each fragment to its constituent atomic positions is further described in Section 3.4.2.

3.4) Results

3.4.1) Gluconate measurement sensitivity and stability

The useful ion yield of glucose was low: under the instrument conditions described in section 2.5, 0.0004% of molecules introduced into the instrument were ionized and counted in the mass spectrometer. Gluconate, an oxidation product of glucose, had higher useful ion yield: 0.002% of

introduced gluconate molecules counted in the mass spectrometer, a 5x improvement relative to glucose. Additionally, gluconate produced an interpretable fragmentation pattern where most fragment ions could be clearly related to particular atomic positions—unlike glucose, where the relationship between fragment ions and atomic positions was not straightforward. As a result of these differences in ionization and fragmentation, we proceeded with gluconate as the analyte for this project.

The useful ion yield of gluconate varied with sample concentration and flow rate. We examined ion yield at concentrations ranging from 5 to 100 μM . As expected, the highest total ion count (TIC) and highest ion counting rate were observed at the highest gluconate concentration (Figure 3.2B). However, because of limits on the maximum possible Orbitrap scan rate, useful ion yield was maximized at a gluconate concentration of 25 μM . Meanwhile, the relative TIC stability (assessed as the relative standard deviation of TIC across scans) was highest at concentrations of 70-100 μM . Accordingly, we performed measurements at a gluconate concentration of 50 μM in order to balance the need for signal stability and sample efficiency.

We tested the useful ion yield of gluconate for flow rates from 4-15 $\mu\text{L min}^{-1}$. We observed that the gluconate ion counting rate increased only by 1-5% with each 20-40% increase in sample flow rate (Figure 3.2B); thus, lower flow rates yield more efficient ionization. Meanwhile, ionization stability degraded at flow rates lower than 4 $\mu\text{L min}^{-1}$. Because our injector module was limited to 100 μL injections, we performed measurements at a flow rate of 4-5 $\mu\text{L min}^{-1}$ in order to minimize the total number of injections required for a ~120-minute measurement while maintaining a stable ion signal.

For our chosen gluconate concentration and flow rate, TIC for a 123-minute sample acquisition typically had a coefficient of variation of ~8-11% after removing intervals of dead time during injections. While TIC values throughout an individual acquisition were close to normally distributed, their distribution was typically slightly skewed toward higher values, with Fisher-Pearson skewness coefficients ranging from -0.3 to 1.1 (Figure 3.2A). ^{13}R values were typically closer to a normal distribution with skewness coefficients of -0.005 to 0.1. Measured ^{13}R values

showed no statistical correlation to TIC within a given acquisition ($r^2 \leq 0.01$) and there was no relationship between the skewness of TIC and the skewness of ^{13}R values.

In the above method, which infuses 50 μM gluconate solution at a flow rate of 4-5 $\mu\text{L min}^{-1}$ for 123 minutes, a single acquisition consumes 5-6 μg of gluconate. Triplicate analysis of each sample therefore consumes 15-18 μg of gluconate.

Because the acquisition duration is set by the desired precision (further detailed in Section 3.4.3), a less stringent requirement for measurement precision would enable shorter measurement durations and smaller sample sizes. For example, a 2x decrease in measurement precision could be achieved in a ~31-minute acquisition, and would consume only ~4 μg of gluconate per triplicate analysis. Meanwhile, a 2x increase in precision would require almost 500 minutes per acquisition. More substantial improvements in precision (without requiring unacceptably long measurement durations) might be possible through more stable infusion conditions that increase the rate of sample introduction, and/or with other Orbitrap interfaces that feature MS^n options or larger analyzers. Meanwhile, further improvements in sensitivity, and therefore sample consumption rates, may be possible through additional optimization of sample introduction parameters in the ESI source.

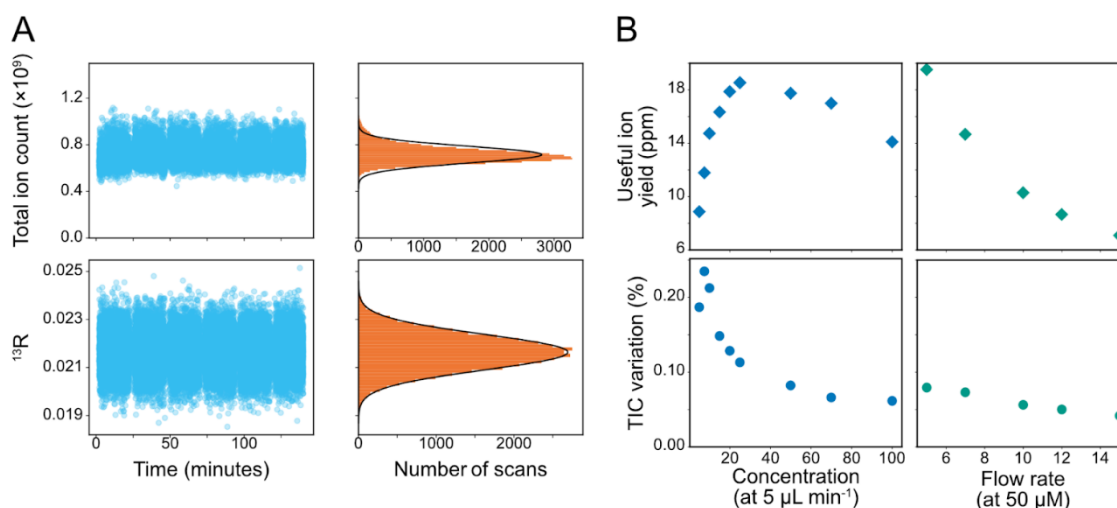


Figure 3.2: Metrics of measurement stability and sensitivity. A: Distribution of total ion count (TIC) and ^{13}R values across a 140-minute acquisition. B: Useful ion yield and TIC variation as a function of gluconate concentration (at 5 $\mu\text{L min}^{-1}$ flow rate) and flow rate (at 50 μM gluconate concentration).

3.4.2) Gluconate fragmentation pattern

The mass spectrum for gluconate under the instrument conditions described in section 2.5 contained the molecular ion and an additional 17 unique fragments, each with a detectable ^{13}C -substituted peak (Figure 3.3). In order to calculate position-specific $\delta^{13}\text{C}$ values from fragment $\delta^{13}\text{C}$ measurements, we sought fragments that met the following criteria: 1) could be clearly attributed to a specific set of atomic positions (e.g., a 5-carbon fragment descended from C1–C5 or C2–C6), and 2) represented unique combinations of atomic positions, where up to six unique fragments would allow us to mathematically solve for the six unknown positions.

For each fragment, we first calculated the molecular formula of each fragment ion (i.e., the number of unique C, H, and O atoms) from the ion's measured atomic mass. The difference between the exact mass for the predicted molecular formula and the measured mass was always < 0.6 mDa. Fourteen fragments contained between two and five C atoms, enabling the subsampling of different combinations of glucose atomic positions.

Once the molecular formula was known for each fragment ion, we confirmed the distribution of glucose atomic positions in each fragment using positionally labeled glucose standards. Each standard was diluted with the natural ^{13}C abundance standard GlnA to contain $\sim 10\%$ ^{13}C label at a single atomic position. The positionally labeled standards were oxidized to gluconate as described in section 3.3.2 and measured via the Orbitrap. Each labeled standard was measured relative to GlnA. The exact amount of ^{13}C label added was confirmed using the $\delta^{13}\text{C}_{\text{GlnA}}$ value of the gluconate molecular ion: for each positionally labeled standard, the label accounts for one of the six C atoms in the intact molecular ion, while the other five positions have identical ^{13}C values to GlnA. Therefore, the $\delta^{13}\text{C}_{\text{GlnA}}$ value at the labeled position can be calculated as six times the $\delta^{13}\text{C}_{\text{GlnA}}$ value of the molecular ion.

Once the $\delta^{13}\text{C}_{\text{GlnA}}$ value at the labeled atomic position was calculated, that value was used to determine the contribution of that atomic position to any given fragment. For example, if a positionally labeled gluconate standard is 50‰ enriched at the C1 position relative to GlnA, and it produces a two-carbon fragment that is 25‰ enriched, then 100% of that two-carbon fragment

contains the C1 atomic position. By performing this calculation for each positionally labeled standard and fragment, four fragments in addition to the molecular ion were found to descend from a single unique combination of gluconate atomic positions (Figure 3.3), meeting criterion 1 as described above; other fragments represented mixtures of two or more combinations of atomic positions.

For this study, only fragment ions representing a single set of atomic positions were used: four fragment ions with nominal masses of 75, 87, 99, and 129, as well as the molecular ion with a nominal mass of 195. These fragments enable the independent observation of atomic positions C-3, C-4, C-5, and C-6, according to criterion 2 (Figure 3.3). None of these fragments contained C1 without C2 or vice versa, so we report (C-1+C-2) as the fifth unique intramolecular site observed in this study. We used these five fragments and five intramolecular sites to construct a matrix as described in Section 3.3.7 (Figure 3.8).

In the future it may be possible to independently observe all six carbon atomic positions in glucose, because other fragments of gluconate that descend from mixed combinations of atomic positions do in some cases exclude C1. However, because different fragmentation pathways may induce different isotopic fractionations, further testing is first required to determine whether fragment ions descended from a mixture of fragmentation pathways can provide replicable isotope measurements.

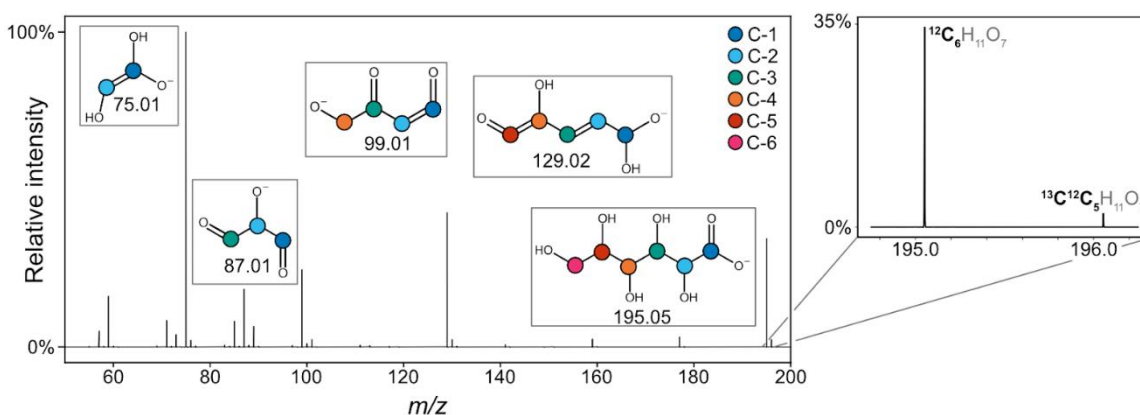


Figure 3.3: Orbitrap mass spectrum of gluconate, annotated with the molecular structure and atomic position makeup of 4 fragment ions and the molecular ion. The right panel shows a portion of the spectrum containing the isotopically unsubstituted molecular ion at $m/z = 195.05$ and the singly ^{13}C -substituted version at 196.05.

3.4.3) Intra-analysis precision

Each Orbitrap acquisition for a given standard or sample is comprised of many unique scans, typically ~30,000 individual scans for the instrument conditions described in Section 3.3.5. Each scan constitutes a single observation of the ^{13}R value for a given packet of fragment ions (mass spectral ‘peak’) or set of peaks. The ^{13}R value for a scan is calculated by dividing the number of ^{13}C -substituted ions counted by the number of isotopically unsubstituted ions counted. For a given peak, ~3,000–100,000 ions may be counted in a typical scan. We characterized the precision of these repeat observations of ^{13}R by comparing the relative standard error of the measured ^{13}R value across scans to the theoretical limit of precision imposed by counting statistics (i.e., the shot-noise limit). We consistently observed that the RSE across scans in an acquisition, termed “acquisition error”, decreased in inverse proportion to the square root of the number of ions counted, consistent with the behavior of counting statistics. Further, the acquisition error closely tracked the shot-noise limit as the number of ions counted increased: typical acquisition errors were within 20-30% above the corresponding (theoretical) shot noise error (Figure 3.4). This observation held true for all fragments of gluconate. As a result, the precision of ^{13}R measurements of all fragments is set by statistical limits rather than instrument stability, and by observing a larger number of ions (e.g., by performing a longer measurement), a user can achieve higher levels of intra-analysis precision. Further improvements in precision for a given measurement duration could be possible in instruments with higher count rates.

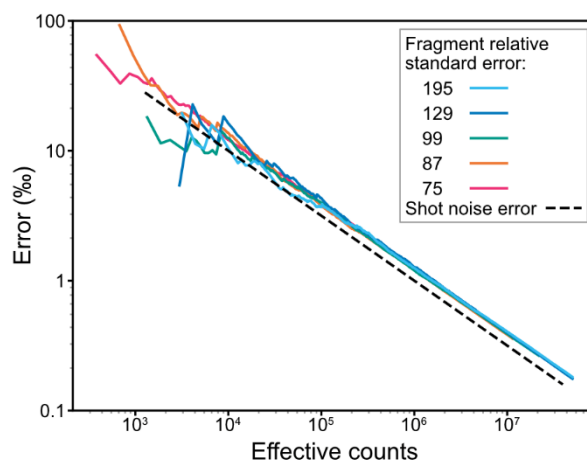


Figure 3.4: Cumulative precision of fragment ^{13}R values as ions are counted during an acquisition, assessed as the relative standard error of ^{13}R values. “Effective counts” is calculated by normalizing the total number of ions by adding isotopically substituted and unsubstituted counts in quadrature, following John and Adkins (2010). The shot noise error (i.e., the theoretical limit of precision imposed by counting statistics) is plotted as a dashed line.

3.4.4) Inter-analysis precision

Inter-analysis precision was assessed by calculating the standard deviation of $\delta^{13}\text{C}_{\text{GlcNA}}$ values produced through repeat bracketed measurements of GlcNA and GlcNB. It was separately determined that accurate values could be reached by making three successive sample-standard comparisons (see Section 3.4.5). Standard deviations of $\delta^{13}\text{C}_{\text{GlcNA}}$ values produced by triplicate measurements were typically similar to the propagated acquisition error (i.e., the RSEs for each individual acquisition among the replicate measurements added in quadrature) (Figure 3.5B). In a test of 8 repeated bracketed comparisons, the cumulative standard deviation of $\delta^{13}\text{C}_{\text{GlcNA}}$ did not appreciably improve between 3 and 8 replicates, consistently remaining between 0.4–0.5‰, indicating diminishing returns in measurement precision with further replicates.

3.4.5) Accuracy of molecular average measurement

Testing the accuracy of PSIA by ESI-Orbitrap is challenging because there are no glucose or gluconate reference materials with known position-specific $\delta^{13}\text{C}$ values. We therefore assessed measurement accuracy in two stages: first, we tested the accuracy of the molecular average measurement by comparing ESI-Orbitrap measurements of the molecular ion to externally measured values, described below. Second, we tested the accuracy of position-specific measurements using a positionally-labeled standard, described in section 3.4.6.

We externally determined the $\delta^{13}\text{C}_{\text{VPDB}}$ values for standards GlcNA and GlcNB using EA-IRMS, a method that converts the entire glucose molecule to CO_2 and measures the average $\delta^{13}\text{C}$ value for all six C atoms. We used these measured $\delta^{13}\text{C}_{\text{VPDB}}$ values to calculate the $\delta^{13}\text{C}$ value of GlcNB relative to GlcNA, notated as $\delta^{13}\text{C}_{\text{GlcNA}}$. The $\delta^{13}\text{C}_{\text{GlcNA}}$ value of GlcNB was found to be $0.64 \pm 0.08\%$ ($n = 5$ for each standard). We then used this externally verified value to benchmark the accuracy of ESI-Orbitrap measurements. The gluconate molecular ion (with nominal mass 195) present in the ESI-Orbitrap spectrum can be used to measure the $\delta^{13}\text{C}$ value for intact gluconate, analogous

to the molecular average value obtained by EA-IRMS. By comparing $\delta^{13}\text{C}_{\text{GlcNA}}$ values of GlcnB obtained by ESI-Orbitrap and EA-IRMS, we were able to assess the accuracy of the molecular ion measurement (Figure 3.5).

We first examined the effects of the instrument Automatic Gain Control (AGC) and resolution settings on the accuracy of our measurement. The AGC sets the number of ions that enter the Orbitrap for each scan, while resolution determines the length of time that the image current is observed during the scan. While a greater number of ions in the analyzer improves statistical uncertainty (via counting statistics), previous work has shown that a higher density of ions in the analyzer can also impart unwanted isotopic fractionations that might undermine measurement accuracy (Eiler *et al* 2017). Meanwhile, at a lower resolution, more frequent but shorter scans ensure that ions are counted more quickly (again improving uncertainty via counting statistics), but the failure to separate adjacent peaks can also cause systematic errors in measured isotope ratios. We found that $\delta^{13}\text{C}_{\text{GlcNA}}$ values were most accurate when the AGC target was set to its maximum value (i.e., the highest possible ion flux into the analyzer) (Figure 3.5A), and the resolution to a moderate value of 60,000. This finding suggests that for this measurement application, increased ion density does not decrease the accuracy of retrieved $\delta^{13}\text{C}$ values, and that an overlapping ^2H peak does not measurably bias ^{13}C measurements.

To further characterize measurement accuracy at the chosen AGC target and resolution, we performed repeat bracketed measurements of GlcnA and GlcnB by ESI-Orbitrap and calculated $\delta^{13}\text{C}_{\text{GlcNA}}$ of GlcnB for the molecular ion (Figure 3.5B). For a typical analytical session under stable instrument conditions, the average of any series of 3 or more bracketed measurements produced a $\delta^{13}\text{C}_{\text{GlcNA}}$ that was within error of the value obtained by EA-IRMS. Typical standard deviations for triplicate bracketed measurements of GlcnA vs. GlcnB were $<0.7\%$.

3.4.6) TIC-dependence of measurement accuracy

We found that measurement accuracy was highly sensitive to the ion signal intensity (total ion count, or TIC) delivered to the Orbitrap analyzer. TIC is a function of the concentration and flow rate of analyte introduced into the instrument (Figure 3.2B) as well as the presence of any

additional ions in solution (Kloepfer *et al* 2005) and the settings and stability of the ESI source (Leito *et al* 2008). As a result, differences in gluconate concentration produced biases in $\delta^{13}\text{C}$ values for all measured ions of up to 23‰ (Figure 3.5C; Figure 3.8). Accurate $\delta^{13}\text{C}$ values could only be recovered when the TICs of subsequent GlcnA standard measurements were identical within <15% relative difference.

Relative differences in the concentration and/or TIC of subsequent measurements might impart differences in measured $\delta^{13}\text{C}$ values through a number of possible mechanisms. First, interactions of ions in the ESI source may be a function of concentration, leading to concentration-dependent fractionations. For example, there may be a concentration-dependent formation of adduct ions with some isotopic preference, where adducts outside the AQS (Advanced Quadrupole Selector) mass window ($m/z = 195.5 \pm 1.4$ Da) are then excluded from the Orbitrap measurement. Second, fractionation due to nonuniform ion transmission through the AQS is thought to be dependent on TIC where TIC exceeds 10^8 (Eiler *et al* 2017); these measurements were made at TIC of $2.3 \times 10^8 - 1.6 \times 10^9$, exposing them to possible fractionation during quadrupole mass selection. Third, the AGC (automatic gain control) is a mechanism that controls the frequency and duration of ion injection (injection time, IT) from the C-trap into the Orbitrap following fragmentation in order to maintain a user-selected abundance of ions in the Orbitrap. At a set AGC, the IT will necessarily vary for different analyte concentrations, with shorter ITs for higher concentrations. Due to isotopic fractionations occurring in the C-trap and Orbitrap, longer ITs have been shown to result in higher δ values under otherwise identical conditions (Eiler *et al* 2017). Additional testing is required to determine whether one or more of these effects creates the observed TIC-dependency of $\delta^{13}\text{C}$ values measured for gluconate.

Regardless of the cause of this observed trend, a linear correction of observed $\delta^{13}\text{C}$ values based on relative differences in TIC may be possible. A linear regression of $\delta^{13}\text{C}_{\text{GlcNA}}$ for all measured ions of GlcnA vs. relative TIC difference produces a y-intercept of 0.1 ($r^2 = 0.9902$); this value is within analytical error of 0, consistent with the idea that measurements with no relative difference in TIC produce an accurate $\delta^{13}\text{C}$ value. By setting the intercept to 0, we obtain r^2 of 0.9901 and a slope of -40.8 (dotted line shown in Figure 3.5C). When each fragment is assessed separately,

slopes range from -41.5 to -40.4, indicating remarkable consistency in the effect of TIC on $\delta^{13}\text{C}$ values across fragments.

While a linear correction therefore seems like a promising approach to retrieving accurate $\delta^{13}\text{C}$ values across a moderate range of TIC differences, further testing is needed to determine whether the relationship between TIC difference and $\delta^{13}\text{C}$ is consistent over multiple analytical sessions for both molecular ion and fragment ion measurements. Additionally, since the effect may be specific to the abundance of other ions in the sample matrix (e.g., the gluconate counterion and other trace inorganic ions in the sample background) (Eiler *et al* 2017, Hofmann *et al* 2020), further tests are required to determine whether this correction for reagent-grade sodium gluconate standards can be applied to natural samples. As a result, the most reliable way to retrieve accurate $\delta^{13}\text{C}$ values is to carefully match the TIC of samples and standards within $\sim 15\%$ relative difference.

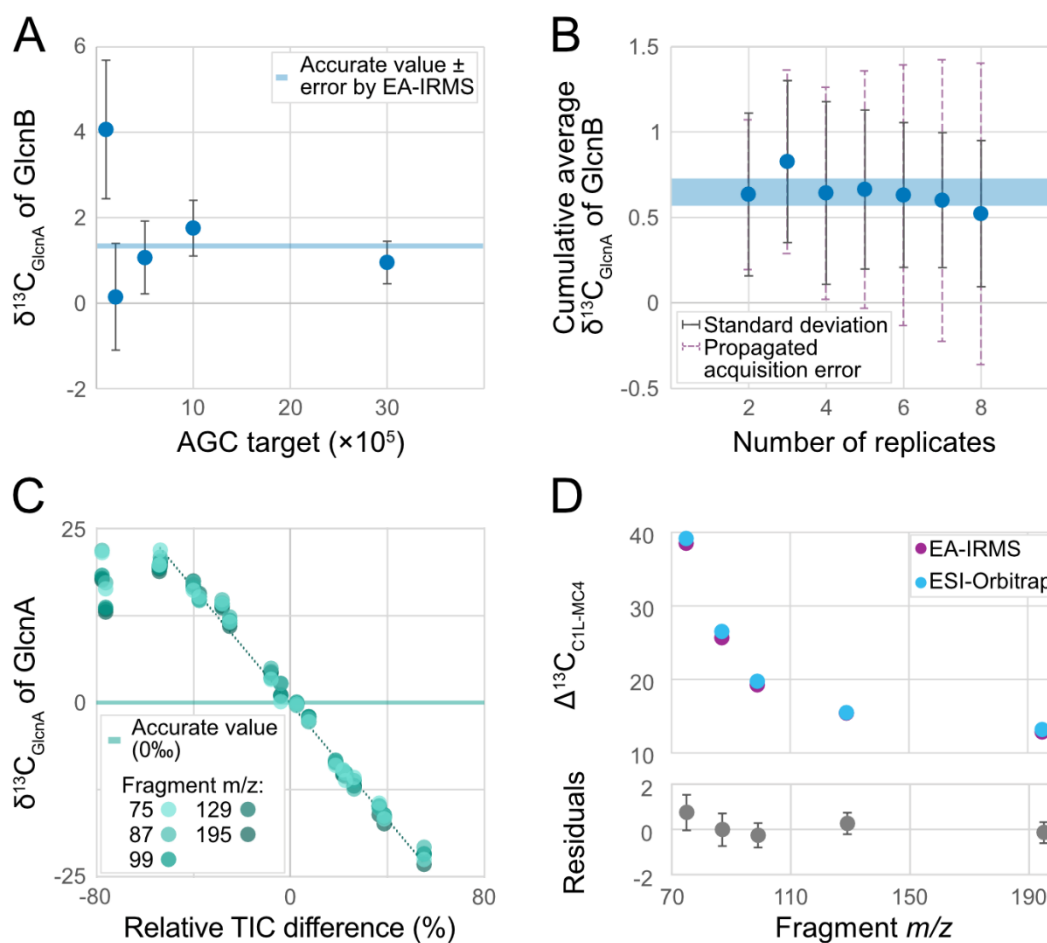


Figure 3.5: Metrics of measurement accuracy. A) Accuracy of $\delta^{13}\text{C}_{\text{GlcNA}}$ measurements of GlcnB with different Orbitrap AGC (Automatic Gain Control) targets. For A and B, blue shaded region indicates accurate value externally verified by EA-IRMS. B) Cumulative average $\delta^{13}\text{C}_{\text{GlcNA}}$ values obtained for GlcnB over 10 repeat bracketed measurements. C) Measurement accuracy for all five measured ions across different sample-standard TIC differences, assessed by repeat measurements of GlcnA against itself ($\delta^{13}\text{C}_{\text{GlcNA}}$ of GlcnA, accurate value = 0‰). Dotted line shows a linear regression with the y-intercept set to 0 ($r^2 = 0.99$), excluding measurements with relative difference >70%. D) Accuracy of fragment measurements comparing C-1 labeled (C1L) and unlabeled (MC4) standards on ESI-Orbitrap (blue) and EA-IRMS (magenta). Grey points show residuals, which are all within error of 0.

3.4.7) Accuracy of position-specific isotope measurements

After verifying the accuracy of the molecular average $\delta^{13}\text{C}$ values obtained by ESI-Orbitrap, we tested the accuracy for $\delta^{13}\text{C}$ measurements of fragment ions. To do so, we spiked glucose standard MC4 (a natural ^{13}C abundance glucose standard with a $\delta^{13}\text{C}$ value of -10.60‰) with ~0.01% glucose standard ^{13}C -labeled at the C-1 position, creating a new standard “C1L”. To verify the exact amount of added label, we measured MC4 and C1L by EA-IRMS. The molecular average $\delta^{13}\text{C}_{\text{VPDB}}$ of C1L was 2.22‰ VPDB resulting in a calculated $\Delta^{13}\text{C}_{\text{C1L-MC4}}$ of $12.83 \pm 0.37\text{‰}$ ($n = 5$). Since the added label is known to be located entirely at C-1, this implies a $\Delta^{13}\text{C}_{\text{C1L-MC4}}$ value for C-1 in C1L of 76.98‰.

We next oxidized MC4 and C1L to gluconate following the method described in section 2.2 to enable measurement by ESI-Orbitrap. Using the known contribution of C-1 to each fragment (described in Section 3.4.2) and the extent of C-1 labeling determined by EA-IRMS (above), we predicted the expected $\Delta^{13}\text{C}_{\text{C1L-MC4}}$ for each fragment, and compared them to the measured values. For these predictions, $\Delta^{13}\text{C}_{\text{C1L-MC4}}$ was assumed to be 0‰ at positions C-2 through C-6 (since no label was added at these positions). For example, the fragment with nominal m/z of 75, composed of 50% C-1 and 50% C-2, therefore had an expected $\Delta^{13}\text{C}_{\text{C1L-MC4}}$ of 38.49‰, and so on. The measured $\Delta^{13}\text{C}_{\text{C1L-MC4}}$ for each fragment by ESI-Orbitrap, using triplicate bracketed acquisitions, was within error of the predicted values (Figure 3.5D). Our developed method therefore achieves accurate $\Delta^{13}\text{C}$ values within error (± 0.5 – 0.7 permil) for both the molecular ion and fragment ions, without any additional bias introduced by our selected instrument parameters (including AGC target and resolution). This result further indicates that no meaningful ^{13}C fractionation occurs during preparatory chemistry, including glucose oxidation to gluconate.

3.4.8) ^{13}C -PSIA comparison of glucose standards from different plant sources by ESI-Orbitrap

To illustrate a real-world application of our method, we measured two glucose standards, SC3 and MC4, that are derived from C3 and C4 plants, respectively. The C3 and C4 photosynthetic pathways are named for the number of carbon atoms in their initial CO₂ fixation products, and the two pathways produce glucose with distinct $\delta^{13}\text{C}$ values (Bender 1968) due to differences in the strongly fractionating initial carboxylation reactions (O'Leary 1988). Accordingly, standard SC3 had a measured $\delta^{13}\text{C}_{\text{VPDB}}$ of $-26.43 \pm 0.07\text{‰}$ and MC4 of -10.99 ± 0.22 as measured by EA-IRMS. Previous work has shown that the carbon isotopic differences between C3 and C4 sugars are further distinguishable at the level of individual atomic positions (Rossmann *et al* 1991, Gilbert *et al* 2013), and these differences should be apparent using our PSIA method.

We oxidized both glucose standards to gluconate and measured each one relative to GlnA in triplicate bracketed acquisitions. GlnA was produced by microbial fermentation of corn glucose, a C4 product, and its molecular average $\delta^{13}\text{C}_{\text{VPDB}}$ value was externally measured on EA-IRMS to be $-11.92 \pm 0.03\text{‰}$. For MC4, triplicate $\delta^{13}\text{C}_{\text{GlnA}}$ measurements of the four measured fragments and the molecular ion produced standard deviations of 0.19–0.49‰ (Figure 3.6A). Standard deviations for triplicate $\delta^{13}\text{C}_{\text{GlnA}}$ measurements of SC3 ions ranged from 0.13–0.48‰.

Molecular average $\delta^{13}\text{C}_{\text{VPDB}}$ values for both standards were calculated from the $\delta^{13}\text{C}_{\text{GlnA}}$ of the molecular ion and the externally-determined $\delta^{13}\text{C}_{\text{VPDB}}$ of GlnA. The $\delta^{13}\text{C}_{\text{VPDB}}$ values for MC4 and SC3 as measured by ESI-Orbitrap were $-13.55 \pm 0.49\text{‰}$ and $-29.08 \pm 0.20\text{‰}$, respectively. These were offset from the values obtained via EA-IRMS by 2.56–2.65‰, outside of the error of the measurement. One possible explanation for the offset in measured $\delta^{13}\text{C}$ values between EA-IRMS and Orbitrap could be the effect of relative TIC difference on accuracy as described in Section 3.4.6. For SC3, the average relative sample-standard TIC difference was -17%, which may have contributed to a systematic offset in the $\delta^{13}\text{C}$ values retrieved. However, for MC4, the average relative difference was only 4%, well within the range where accurate values were measured in tests of standards. We showed in Section 3.4.7 that we retrieve accurate $\delta^{13}\text{C}$ values for each fragment after preparatory chemistry when both the standard and the sample have undergone glucose oxidation. However, here, we are comparing glucose standards SC3 and MC4, having undergone glucose oxidation, to the gluconate standard GlnA that did not undergo chemical

preparation. These results suggest that some fractionation occurs during glucose oxidation to gluconate: assuming a normal kinetic isotope effect at the C-1 position could occur with glucose oxidation, then incomplete reaction could result in a ^{13}C -depleted gluconate product relative to the starting glucose. This fractionation appears to affect all oxidized samples equally, as indicated by the results discussed in Section 3.4.7 (Figure 3.5D). Further testing is needed to verify the isotopic offset occurring with glucose oxidation and its relationship with reaction yield. However, because the offset is nearly identical for SC3 and MC4, we can compare the position-specific measurements for the two glucose sources with the expectation that any methodological fractionations would affect both equally.

Error for position-specific $\delta^{13}\text{C}$ values exceeds error in fragment values when more than one fragment is required to solve for a positional value (due to error propagation). For example, the $\delta^{13}\text{C}$ value of C-3 is calculated from the $\delta^{13}\text{C}$ values of fragments 75 and 87, so error from both fragment measurements is propagated to produce the error for C-3. As a result, the standard deviation of calculated $\delta^{13}\text{C}$ values for positions (C-1+C-2) and C-3–C-6 for MC4 were 0.42–3.10‰, and 0.21–2.33‰ for SC3 (Figure 3.6B).

Nevertheless, the ^{13}C -PSIA results for MC4 and SC3 show clear differences associated with their C4 and C3 plant origins. $\delta^{13}\text{C}_{\text{GlcNA}}$ for SC3 is lower at each intramolecular site by 12.1–31.8‰ than for MC4. To compare measurements of the two samples, we calculated the $\Delta\delta^{13}\text{C}$ for each atomic position:

$$\Delta\delta^{13}\text{C}_{\text{Position}} = \delta^{13}\text{C}_{\text{Position-GlcNA}} - \delta^{13}\text{C}_{\text{Molecular average-GlcNA}} \quad (3.6)$$

Although SC3 has more variable values among intramolecular sites than MC4, both glucose standards show broadly similar relative trends in $\Delta\delta^{13}\text{C}$ (Figure 3.6B). In both the C3 and C4 glucose standards, lower values of $\Delta\delta^{13}\text{C}$ were observed at (C-1+C-2) and higher values at C-3–C-4 and C-6. Meanwhile, in SC3 the $\Delta\delta^{13}\text{C}$ values at C-5 and C-6 have much larger amplitude than in MC4. C-6 has relatively low $\Delta\delta^{13}\text{C}$ values in both standards, but in SC3, it is -6.0‰, whereas it is only -0.7‰ in MC4. The relative depletion at C-6 has been previously observed in studies of C3 and C4 glucose (Rossmann *et al* 1991, Gilbert *et al* 2012). In contrast, the strong

difference in $\Delta\delta^{13}\text{C}$ at C-5 has not previously been identified in existing studies of intramolecular isotope composition of C3 and C4 glucose. The $\delta^{13}\text{C}$ signature at C-5 and C-6 of cellulose-derived glucose was recently hypothesized to descend from changes in metabolic flux downstream of phosphoenolpyruvate (PEP) (Wieloch *et al* 2025), which would be expected to affect both C-5 and C-6 similarly, and is supported by strong correlation of position-specific $\delta^{13}\text{C}$ signals at C-5 and C-6 in pine tree rings. This hypothesis is inconsistent with the divergent $\Delta\delta^{13}\text{C}$ values at C-5 and C-6 observed in SC3 here. Little information is available about the provenance of standards SC3 and MC4, so it is difficult to predict how plant growth or reagent processing conditions may have driven specific intramolecular signals. However, because these signals diverge from expectations of tree-ring cellulose-derived glucose, they may point to mechanisms affecting plant glucose pools but not cellulose.

Because the measurements presented here were made in reference to a laboratory standard GlcnA rather than on the VPDB scale, relative trends might also be influenced by the composition of GlcnA: for example, an unusually ^{13}C enriched value for (C-1+C-2) of GlcnA might lead to the lower values of $\delta^{13}\text{C}_{\text{GlcNA}}$ observed for MC4 and SC3 at those positions. Further work is planned to externally verify the $\delta^{13}\text{C}_{\text{VPDB}}$ of a glucose standard via NMR-PSIA, which will allow our Orbitrap analyses to be anchored to the VPDB scale in the future. Nevertheless, this preliminary analysis demonstrates the ability to distinguish molecular-average and intramolecular trends in $\delta^{13}\text{C}$ for natural glucose samples via ESI-Orbitrap PSIA. This method for measuring intramolecular $\delta^{13}\text{C}$ variations on μg - to mg -scale samples can enable a more nuanced study of glucose metabolism and provenance in many systems, from photosynthesis to food authenticity, microbial interactions, and human health.

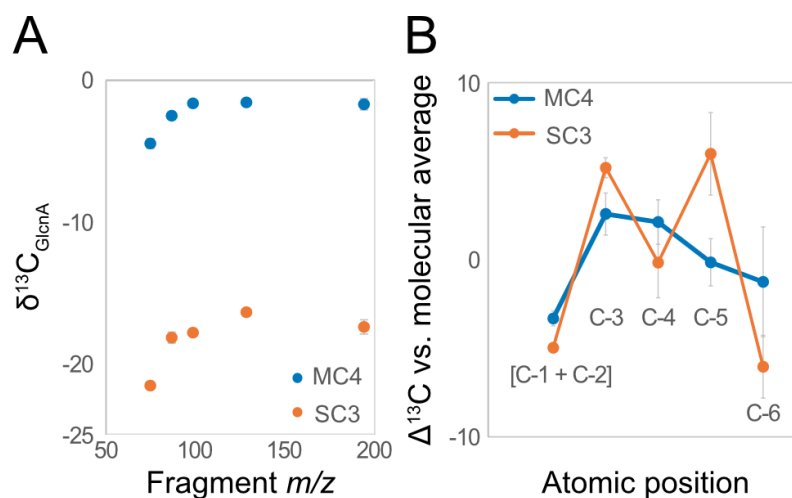


Figure 3.6: Measuring and comparing glucose standards MC4 and SC3 (as gluconate) via ESI-Orbitrap. A) $\delta^{13}\text{C}_{\text{GlcNA}}$ values of fragment ions and molecular ion for MC4 and SC3, reported relative to standard GlcnA. B) $\Delta^{13}\text{C}$ values of five unique atomic positions of glucose for MC4 and SC3, reported relative to the molecular average $\delta^{13}\text{C}_{\text{GlcNA}}$ value for each standard. Error bars indicate the standard deviation of triplicate measurements.

3.5) Conclusions

Here, we have demonstrated a new method for measuring the carbon isotopic composition of 5 intramolecular sites within glucose at natural isotope abundance. This method consumes $< 50 \mu\text{g}$ glucose for triplicate sample analysis, readily accommodating typical sample sizes for environmental and human health research. By measuring glucose as gluconate—an oxidation product of glucose produced by reaction with Br_2 and sodium hydroxide—we can accurately measure the $\delta^{13}\text{C}$ value of the molecular ion and four fragment ions, within analytical error of $\pm 0.1\text{--}0.5\%$. Using our new method, we can observe intramolecular trends in $\delta^{13}\text{C}$ values for natural sugars formed through two different photosynthetic pathways, recapitulating patterns observed in previous studies while decreasing sample consumption by more than four orders of magnitude (Gilbert *et al* 2009).

Several future improvements to this method are possible. For example, externally verifying the position-specific $\delta^{13}\text{C}_{\text{VPDB}}$ values of a glucose reference material will enable users to anchor Orbitrap measurements to the VPDB scale. Further work could also demonstrate the possibility for independently measuring $\delta^{13}\text{C}$ values for the C-1 and C-2 positions by testing the stability of isotope measurements for fragments with multiple formation pathways. Applying this method on

other Orbitrap analyzers may improve measurement precision without negatively impacting measurement duration or sample consumption. Finally, although this work has focused on ^{13}C , stable oxygen and hydrogen isotopes can also be measured by ESI-Orbitrap (e.g., Mueller *et al* 2022, Hilkert *et al* 2021), and we expect that further optimization and testing will allow measurements of position-specific $\delta^{18}\text{O}$ and $\delta^2\text{H}$ values in glucose. The position-specific isotope measurements we have shown, and the measurements that may soon be possible with further study, pave the way for more detailed investigations of sugar fluxes and provenance across a broad range of applications.

3.6) Acknowledgments

This project was supported by the NASA Astrobiology Institute. Elise Wilkes and Stuart Sessions helped develop the data processing script to calculate the matrix inversion. Tim Csernica provided extensive help with data processing. Thanks go to Simon Andren, Noam Lotem, Gabriella Weiss, and Elliott Mueller for helpful discussions of the technical aspects of Orbitrap analysis. Michael Mathuri assisted with EA-IRMS analyses and James Mullahoo with HPIC measurements. Juliann Panehal helped with methods testing. Youki Sato and Max Lloyd helped us to access standard materials that were essential in the completion of this work.

3.7) References

- Bender M M 1968 Mass Spectrometric Studies of Carbon 13 Variations in Corn and Other Grasses *Radiocarbon* **10** 468–72
- Bunzel H H and Mathews A P 1909 THE MECHANISM OF THE OXIDATION OF GLUCOSE BY BROMINE IN NEUTRAL AND ACID SOLUTIONS. *J. Am. Chem. Soc.* **31** 464–79
- Cabañero A I, Recio J L and Rupérez M 2006 Liquid Chromatography Coupled to Isotope Ratio Mass Spectrometry: A New Perspective on Honey Adulteration Detection *J. Agric. Food Chem.* **54** 9719–27
- Cesar J, Eiler J, Dallas B, Chimiak L and Grice K 2019 Isotope heterogeneity in ethyltoluenes from Australian condensates, and their stable carbon site-specific isotope analysis *Organic Geochemistry* **135** 32–7
- Chimiak L, Elsila J E, Dallas B, Dworkin J P, Aponte J C, Sessions A L and Eiler J M 2021 Carbon isotope evidence for the substrates and mechanisms of prebiotic synthesis in the early solar system *Geochimica et Cosmochimica Acta* **292** 188–202

- Csernica T, Bhattacharjee S and Eiler J 2023 Accuracy and precision of ESI-Orbitrap-IRMS observations of hours to tens of hours via reservoir injection *International Journal of Mass Spectrometry* **490** 117084
- Csernica T, Moran J J, Fraga C G and Eiler J M 2025 Simultaneous observation of 2H and ^{13}C enrichment of methyl phosphonic acid via Orbitrap-IRMS with applications to nerve agent forensics *Talanta* **281** 126802
- Dungait J A J, Bol R, Bull I D and Evershed R P 2009 Tracking the fate of dung-derived carbohydrates in a temperate grassland soil using compound-specific stable isotope analysis *Organic Geochemistry* **40** 1210–8
- Eiler J, Cesar J, Chimiak L, Dallas B, Grice K, Griep-Raming J, Juchelka D, Kitchen N, Lloyd M, Makarov A, Robins R and Schwieters J 2017 Analysis of molecular isotopic structures at high precision and accuracy by Orbitrap mass spectrometry *International Journal of Mass Spectrometry* **422** 126–42
- Gilbert A, Robins R J, Remaud G S and Tcherkez G G B 2012 Intramolecular ^{13}C pattern in hexoses from autotrophic and heterotrophic C_3 plant tissues *PNAS* **109** 18204–9
- Gilbert A, Silvestre V, Robins R J and Remaud G S 2009 Accurate Quantitative Isotopic ^{13}C NMR Spectroscopy for the Determination of the Intramolecular Distribution of ^{13}C in Glucose at Natural Abundance *Anal. Chem.* **81** 8978–85
- Gleixner G and Schmidt H-L 1997 Carbon Isotope Effects on the Fructose-1,6-bisphosphate Aldolase Reaction, Origin for Non-statistical ^{13}C Distributions in Carbohydrates * *Journal of Biological Chemistry* **272** 5382–7
- Gonzalez-Nayek A C, Mohr W, Tang T, Sattin S, Parenteau M N, Jahnke L L and Pearson A 2022 Absence of canonical trophic levels in a microbial mat *Geobiology* **20** 726–40
- Guyon F, Auberger P, Gaillard L, Loublanches C, Viateau M, Sabathié N, Salagoity M-H and Médina B 2014 $^{13}\text{C}/^{12}\text{C}$ isotope ratios of organic acids, glucose and fructose determined by HPLC-co-IRMS for lemon juices authenticity *Food Chemistry* **146** 36–40
- Guyon F, Gaillard L, Salagoity M-H and Médina B 2011 Intrinsic ratios of glucose, fructose, glycerol and ethanol $^{13}\text{C}/^{12}\text{C}$ isotopic ratio determined by HPLC-co-IRMS: toward determining constants for wine authentication *Anal Bioanal Chem* **401** 1551–8
- Hawley J A, Dennis S C and Noakes T D 1992 Oxidation of Carbohydrate Ingested During Prolonged Endurance Exercise: *Sports Medicine* **14** 27–42
- Hayes J M 2001 Fractionation of Carbon and Hydrogen Isotopes in Biosynthetic Processes* *Reviews in Mineralogy and Geochemistry* **43** 225–77
- Hesse T, Nachev M, Khaliq S, Jochmann M A, Franke F, Scharsack J P, Kurtz J, Sures B and Schmidt T C 2023 A new technique to study nutrient flow in host-parasite systems by carbon stable isotope analysis of amino acids and glucose *Sci Rep* **13** 1054
- Hilkert A, Böhlke J K, Mroczkowski S J, Fort K L, Aizikov K, Wang X T, Kopf S H and Neubauer C 2021 Exploring the Potential of Electrospray-Orbitrap for Stable Isotope Analysis Using Nitrate as a Model *Anal. Chem.* **93** 9139–48

- Hobbie E A, Watrud L S, Maggard S, Shiroyama T and Rygielwicz P T 2003 Carbohydrate use and assimilation by litter and soil fungi assessed by carbon isotopes and BIOLOG® assays *Soil Biology and Biochemistry* **35** 303–11
- Hofmann A E, Chimiak L, Dallas B, Griep-Raming J, Juchelka D, Makarov A, Schwieters J and Eiler J M 2020 Using Orbitrap mass spectrometry to assess the isotopic compositions of individual compounds in mixtures *International Journal of Mass Spectrometry* **457** 116410
- John S G and Adkins J F 2010 Analysis of dissolved iron isotopes in seawater *Marine Chemistry* **119** 65–76
- Kantnerová K, Kuhlbusch N, Juchelka D, Hilker A, Kopf S and Neubauer C 2024 A guide to precise measurements of isotope abundance by ESI-Orbitrap MS *Nat Protoc* 1–32
- Kloepfer A, Quintana J B and Reemtsma T 2005 Operational options to reduce matrix effects in liquid chromatography–electrospray ionisation–mass spectrometry analysis of aqueous environmental samples *Journal of Chromatography A* **1067** 153–60
- Lefebvre P, Mosora F, Lacroix M, Luyckx A, Lopez-Habib G and Duchesne J 1975 Naturally Labeled ¹³C-Glucose Metabolic Studies in Human Diabetes and Obesity *Diabetes* **24** 185–9
- Leito I, Herodes K, Huopolainen M, Virro K, Künnapas A, Kruve A and Tanner R 2008 Towards the electrospray ionization mass spectrometry ionization efficiency scale of organic compounds *Rapid Communications in Mass Spectrometry* **22** 379–84
- Makarov A and Denisov E 2009 Dynamics of ions of intact proteins in the Orbitrap mass analyzer *J. Am. Soc. Mass Spectrom.* **20** 1486–95
- Mueller E P, Sessions A L, Sauer P E, Weiss G M and Eiler J M 2022 Simultaneous, High-Precision Measurements of $\delta^2\text{H}$ and $\delta^{13}\text{C}$ in Nanomole Quantities of Acetate Using Electrospray Ionization-Quadrupole-Orbitrap Mass Spectrometry *Anal. Chem.* **94** 1092–100
- Neubauer C, Kantnerová K, Lamothe A, Savarino J, Hilker A, Juchelka D, Hinrichs K-U, Elvert M, Heuer V, Elsner M, Bakkour R, Julien M, Öztoprak M, Schouten S, Hattori S and Dittmar T 2023 Discovering Nature's Fingerprints: Isotope Ratio Analysis on Bioanalytical Mass Spectrometers *J. Am. Soc. Mass Spectrom.* **34** 525–37
- Neubauer C, Sweredoski M J, Moradian A, Newman D K, Robins R J and Eiler J M 2018 Scanning the isotopic structure of molecules by tandem mass spectrometry *International Journal of Mass Spectrometry* **434** 276–86
- O'Leary M H 1988 Carbon Isotopes in Photosynthesis *BioScience* **38** 328–36
- Rossmann A, Butzenlechner M and Schmidt H-L 1991 Evidence for a Nonstatistical Carbon Isotope Distribution in Natural Glucose *Plant Physiology* **96** 609–14
- Tcherkez G, Farquhar G, Badeck F and Ghashghaie J 2004 Theoretical considerations about carbon isotope distribution in glucose of C₃ plants *Functional Plant Biol.* **31** 857

- Teece M A and Fogel M L 2007 Stable carbon isotope biogeochemistry of monosaccharides in aquatic organisms and terrestrial plants *Organic Geochemistry* **38** 458–73
- Weiss G M, Sessions A L, Julien M, Csernica T, Yamada K, Gilbert A, Freeman K H and Eiler J M 2023 Analysis of intramolecular carbon isotope distributions in alanine by electrospray ionization Orbitrap mass spectrometry *International Journal of Mass Spectrometry* **493** 117128
- Wieloch T, Ehlers I, Yu J, Frank D, Grabner M, Gessler A and Schleucher J 2018 Intramolecular ¹³C analysis of tree rings provides multiple plant ecophysiology signals covering decades *Sci Rep* **8** 5048
- Wieloch T, Holloway-Phillips M, Yu J and Niittylä T 2025 New insights into the mechanisms of plant isotope fractionation from combined analysis of intramolecular ¹³C and deuterium abundances in *Pinus nigra* tree-ring glucose *New Phytologist* **245** 1000–17
- Wilkes E B, Sessions A L, Zeichner S S, Dallas B, Schubert B, Jahren A H and Eiler J M 2022 Position-specific carbon isotope analysis of serine by gas chromatography/Orbitrap mass spectrometry, and an application to plant metabolism *Rapid Comm Mass Spectrometry* **36** Online: <https://onlinelibrary.wiley.com/doi/10.1002/rcm.9347>

3.8) Supplementary information

Supplementary Table 3.2. Summary of all ions in the mass spectrum of gluconate when analyzed under the conditions described in Table 3.1: ion exact molecular mass, molecular formula, and the difference between measured and known mass immediately following Orbitrap mass calibration.

Exact mass	Formula	Δ mDa
195.05044	C ₆ H ₁₁ O ₇	0.51090
177.03977	C ₆ H ₉ O ₆	0.40618
159.02904	C ₆ H ₇ O ₅	0.24037
141.01841	C ₆ H ₅ O ₄	0.17581
129.01829	C ₅ H ₅ O ₄	0.05980
119.03399	C ₄ H ₇ O ₄	0.10543
111.00767	C ₅ H ₃ O ₃	-0.002255
101.02330	C ₄ H ₅ O ₃	-0.02116
99.00764	C ₄ H ₃ O ₃	-0.02759
89.02328	C ₃ H ₅ O ₃	-0.03812
87.00762	C ₃ H ₃ O ₃	-0.04886
85.02838	C ₄ H ₅ O ₂	-0.02764
75.00758	C ₂ H ₃ O ₃	-0.08837
73.02840	C ₃ H ₅ O ₂	-0.01003
72.99202	C ₂ HO ₃	-0.00088
71.01272	C ₃ H ₃ O ₂	-0.03744
59.01270	C ₂ H ₃ O ₂	-0.05706
57.03344	C ₃ H ₅ O	-0.05087

$$\begin{pmatrix} 2/6 & 1/6 & 1/6 & 1/6 & 1/6 \\ 2/5 & 1/5 & 1/5 & 1/5 & 0 \\ 2/4 & 1/4 & 1/4 & 0 & 0 \\ 2/3 & 1/3 & 0 & 0 & 0 \\ 1 & 0 & 0 & 0 & 0 \end{pmatrix} \begin{pmatrix} \delta^{13}\text{C}_{\text{C-1+C-2}} \\ \delta^{13}\text{C}_{\text{C-3}} \\ \delta^{13}\text{C}_{\text{C-4}} \\ \delta^{13}\text{C}_{\text{C-5}} \\ \delta^{13}\text{C}_{\text{C-6}} \end{pmatrix} = \begin{pmatrix} \delta^{13}\text{C}_{195} \\ \delta^{13}\text{C}_{129} \\ \delta^{13}\text{C}_{99} \\ \delta^{13}\text{C}_{87} \\ \delta^{13}\text{C}_{75} \end{pmatrix}$$

Figure 3.7: Matrix of equations used to calculate the $\delta^{13}\text{C}$ of five intramolecular positions: Left, fractional contributions of each position to each fragment; center, calculated $\delta^{13}\text{C}$ values for intramolecular positions; right, measured $\delta^{13}\text{C}$ values of molecular ion and fragment ions. The optimal solution for the $\delta^{13}\text{C}$ at each intramolecular position (center) is calculated through matrix inversion using the `linalg.lstsq` function in the 'numpy' python package.

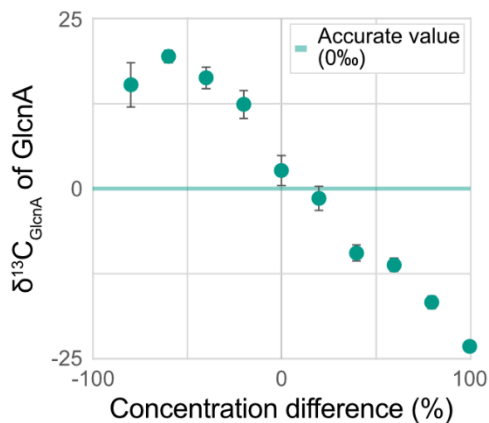


Figure 3.8: Measurement accuracy as a function of relative differences in sample-standard concentration, assessed by repeat measurements of GlcnA against itself ($\delta^{13}\text{C}_{\text{GlcNAc}}$ of GlcnA, accurate value = 0‰).

*Chapter 4***POSITION-SPECIFIC ^{13}C ANALYSIS OF CELLULOSE BY ORBITRAP UNCOVERS SPECIES-SPECIFIC ENVIRONMENTAL AND PHYSIOLOGICAL SIGNALS IN TREE RINGS**

Hannah Dion-Kirschner, Marco M. Lehmann, John Eiler, and Alex Sessions

4.1) Abstract

Tree-ring $\delta^{13}\text{C}$ records are a cornerstone of paleoclimate and ecophysiology research, but conventional compound-specific isotope analysis (CSIA) of tree-ring cellulose provides $\delta^{13}\text{C}$ values that average across multiple environmental and physiological signals. Position-specific isotope analysis (PSIA) offers the potential to deconvolve these co-occurring signals by measuring $\delta^{13}\text{C}$ values of individual atomic positions. However, existing methods for tree-ring PSIA rely on nuclear magnetic resonance (NMR), which requires sample sizes that are prohibitively large for most dendrochronological applications. Here, we present the first application of PSIA via Orbitrap mass spectrometry to tree-ring cellulose, enabling $\delta^{13}\text{C}$ analysis of individual atomic positions of cellulose-derived glucose using only 0.033 mg of cellulose per sample. We applied this method to 23 tree-ring samples from *Fagus sylvatica* and *Larix decidua* grown under varied temperature, vapor pressure deficit (VPD), and soil moisture. The method yields average position-specific $\delta^{13}\text{C}$ precision of 1.8‰, identifies intramolecular $\delta^{13}\text{C}$ differences up to 21.7‰, and accurately matches values obtained by traditional CSIA. $\delta^{13}\text{C}$ values at individual atomic positions, particularly C-3, recorded soil moisture and temperature changes more sensitively than did molecular-average $\delta^{13}\text{C}$ values, and provided evidence for species-specific differences in carbon allocation strategies. In light of these findings, PSIA by Orbitrap offers a high-sensitivity tool for more detailed reconstructions of past climates and investigations of plant physiology.

4.2) Introduction

Tree rings are an invaluable, time-resolved archive of past environmental conditions and their effects on plant physiology (Speer 2010). Although the carbon isotope compositions ($\delta^{13}\text{C}$ values)

of tree-ring cellulose are often interpreted as primarily reflecting plant water-use efficiency, in reality they convolve multiple forcings including vapor pressure deficit (VPD), precipitation amount, soil moisture, temperature, irradiance, and tree carbon allocation (Leavitt and Roden 2022 and references therein). Disentangling these signals from compound-specific cellulose $\delta^{13}\text{C}$ values has not been possible, but there is evidence that they can be separated by measuring $\delta^{13}\text{C}$ at specific molecular positions within the glucose monomers that comprise cellulose (i.e., position-specific isotope analysis, PSIA) (Wieloch *et al* 2018, 2022). To date the only analytical approach for doing so has been nuclear magnetic resonance (NMR), which has sample size requirements (20-100 mg cellulose per sample) incompatible with work on tree ring records. Here, we apply our recently-developed method for glucose PSIA to tree-ring cellulose samples at milligram-level sensitivity using Orbitrap mass spectrometry, and detail its first application to trees grown under varying combinations of vapor pressure deficit, temperature, and soil moisture.

For hundreds of years, researchers have made use of tree ring records' visually distinct annual increments of growth to learn about past climate (e.g., Du Hamel and De Buffon 1737). The application of stable isotope measurements to such records was firmly established via the late 20th-century development of theoretical models for carbon isotope fractionation during photosynthesis in leaves (Farquhar *et al* 1982, 1989). These models equipped researchers with a conceptual framework to interpret temporal shifts in tree-ring $\delta^{13}\text{C}$ values primarily as a function of plant water-use efficiency (WUE). The isotopic signature of WUE is imparted on fresh photosynthate as a result of the balance between CO_2 supply (diffusion) and demand (fixation), where the free diffusion of CO_2 under high WUE enables Rubisco to fully express its strong carbon isotope effect ($\alpha = 1.030$) (Roeske and O'Leary 1984), while low WUE limits its expression. As one relevant example among many, Frank *et al.* (2015) recently inferred a shift in plant WUE from tree-ring cellulose $\delta^{13}\text{C}$ values; this shift recorded the response of stomatal conductance to CO_2 fertilization since 1900.

Notwithstanding such successes, stable isotope dendroclimatologists have also recognized that signals of WUE in tree-ring $\delta^{13}\text{C}$ are convolved with other climatic and physiological signals affecting photosynthesis and post-photosynthetic tree metabolism (Gessler *et al* 2014, Leavitt and

Roden 2022 and references therein), including irradiance, temperature, and metabolic carbon allocation. To mitigate the effects of competing variables, most researchers limit their study sites to locations where the targeted climate signal is expected to strongly outweigh any competing effects (Frank *et al* 2022, Belmecheri *et al* 2022).

PSIA of cellulose offers an opportunity to deconvolve and measure many or all of the separate climate and physiological signals recorded in tree-ring $\delta^{13}\text{C}$ values. While post-photosynthetic processes can alter the climate-related $\delta^{13}\text{C}$ values of fresh photosynthate (Gessler *et al* 2014), they do so through enzymatic processes that impart isotopic fractionations at specific atomic positions where bonds are broken and formed. For example, drought can induce higher flux through the oxidative pentose phosphate pathway, where oxidation at C-1 is hypothesized to result in a stronger drought-related $\delta^{13}\text{C}$ signal at that position (Wieloch *et al* 2022, 2025). Meanwhile, the $\delta^{13}\text{C}$ value of C-4 is thought to be poorly correlated with climate variables because photosynthetic signals are overprinted by fractionation by the GAPDH enzyme (Wieloch *et al* 2018, 2025). One study of pooled *P. nigra* samples from Bierhäuselberg, Austria, in combination with a meta-analysis of plant physiological studies, indicated that individual atomic positions may independently record changes in vapor pressure deficit (VPD), precipitation, temperature, and irradiance (Wieloch *et al* 2025). By developing a method to interrogate these position-specific signals that accommodates ~mg-scale samples, we enable more detailed and nuanced reconstructions of climate variables from tree-ring records.

Conventional measurements of tree-ring cellulose are unable to resolve positional differences in $\delta^{13}\text{C}$ because these isotopic measurements are made on CO_2 : cellulose samples must be combusted prior to measurement, destroying any structural information. When every C position in the molecule is averaged prior to measurement, the method can be referred to as “molecular-average” or “compound-specific” isotope analysis (CSIA). In contrast, recently-developed methods for PSIA enable isotopic measurements on intact molecules. ^{13}C -PSIA of tree-ring glucose has been demonstrated via NMR, revealing the signals recorded at atomic positions C-1 and C-4 as described above (Wieloch *et al* 2018, 2022, 2025). These findings highlight how PSIA of tree-ring samples can improve the strength of climate reconstructions. However, PSIA via NMR has

demanding requirements for sample size (20-110 mg glucose) (Wieloch *et al* 2018), analysis time (23 to >100 hours per sample) (Thomas Wieloch, personal comm.), and sample purity (>99.5%) (Gilbert *et al* 2009). To reap the benefits of PSIA for more nuanced climate reconstructions while circumventing analytical challenges, we have developed a new method for PSIA via Electrospray Ionization (ESI)-Orbitrap (Chapter 3), and here we apply it to glucose derived from tree-ring cellulose for the first time.

Glucose ^{13}C -PSIA via Orbitrap is made possible by pairing the soft ionization capabilities of ESI with the tandem mass spectrometry and ultrahigh mass resolution of Orbitrap mass spectrometry (Eiler *et al* 2017, Neubauer *et al* 2023). Prior to analysis, we oxidize glucose to gluconate to optimize measurement sensitivity and the interpretability of the fragmentation pattern. We are then able to introduce gluconate into the mass spectrometer as an intact ion via ESI. Using the quadrupole, gluconate is then selected according to its m/z ratio to pass to the higher-energy collision dissociation (HCD) cell, while excluding any contaminant ions. In the HCD cell, gluconate is fragmented via interactions with nitrogen collision gas. When these fragment ions are introduced into the Orbitrap, the $^{13}\text{C}/^{12}\text{C}$ ratio of all relevant fragments can be simultaneously measured (e.g., Eiler *et al* 2017, Hilkert *et al* 2021). Each fragment contains a different combination of atomic positions all descended from gluconate, allowing us to solve for the isotopic composition at each position using matrix algebra (Wilkes *et al* 2022) (Figure 3.3, Figure 3.8).

Here, we present the first application of Orbitrap ^{13}C -PSIA to tree-ring cellulose. We analyzed 23 tree-ring samples from two tree species grown in a climate chamber under varied temperature, VPD, and soil moisture. We describe the preparatory chemistry we have developed to enable PSIA on natural wood samples, and demonstrate good agreement between whole-molecule $\delta^{13}\text{C}$ values obtained from traditional compound-specific analysis versus those obtained from Orbitrap analysis. We show that PSIA produces good precision of $\delta^{13}\text{C}$ values among biological replicates, and that different intramolecular positions exhibit different sensitivity to the VPD and moisture conditions the trees experienced during their growing season. Finally, we discuss avenues for future methodological improvements and opportunities to extend our method to other isotope

systems. Our results highlight the promise of Orbitrap PSIA for gaining new insights from tree-ring records about how plants respond to environmental change.

4.3) Methods

4.3.1) Standard materials

The glucose standard used in this work, called “SC3”, is of >95% purity and was obtained from Sigma-Aldrich (Lot # BCCD9888). Standard SC3 was derived from wheat, a C3 plant, and has a molecular-average $\delta^{13}\text{C}$ value of $-26.43 \pm 0.07\%$. Cellulose hydrolysis was tested using an α -cellulose standard from Sigma-Aldrich (Lot # SLCN2412).

4.3.2) Tree sample description and climate chamber treatment

To assess the independent effects of tree physiology, temperature, and hydroclimate on position-specific carbon isotope distribution in cellulose, we obtained tree-ring samples from two laboratory-grown tree species subject to different climate chamber treatments. The two tree species studied here were selected to capture both functional and phylogenetic diversity. The angiosperm *Fagus sylvatica* L. (European beech) is adapted to maritime and temperate climate regions, while the gymnosperm *Larix decidua* Mill. (European larch) is typically found in subalpine or montane environments. Both species have ecological and economic importance in European and North American forests.

During the climate chamber experiment, 3-year-old trees of both species were grown at the Phytotron facility at ETH Zürich from May to November 2020. Trees were planted in 3-liter containers with a water-retentive soil mixture and distributed across four climate chambers (PGV36, Conviron, Canada). After a 5-week acclimation phase, the trees were subject to climate manipulation from June to November 2020, which exposed the samples to varied combinations of temperature, VPD, and soil moisture (Table 4.1). Chambers were set to a 16-hour daytime temperature of 25 °C or 30 °C (nighttime temperatures were 15 °C and 20 °C, respectively). For the chambers at 30 °C, one was set to a low daytime VPD of 1.0 ± 0.3 kPa, and the other to a high VPD of 2.2 ± 0.3 kPa. For the chambers at 25°C, trees of both species were exposed to either high

or low soil moisture (30% or 5% volumetric water content, respectively). Additional experimental details are provided in Schönbeck *et al* (2022).

Table 4.1. Summary of experimental conditions, tree species, and sample number for climate chamber experiment.

Climate variable	Temp = 25 °C	Temp = 30 °C
VPD = 1.0 kPa	<i>L. decidua</i> (n = 3)	<i>L. decidua</i> (n = 3)
Moist soil	<i>F. sylvatica</i> (n = 2)	<i>F. sylvatica</i> (n = 3)
VPD = 1.0 kPa	<i>L. decidua</i> (n = 3)	-
Dry soil	<i>F. sylvatica</i> (n = 3)	-
VPD = 2.2 kPa	-	<i>L. decidua</i> (n = 3)
Moist soil	-	<i>F. sylvatica</i> (n = 3)

Approximately every five weeks during the climate chamber manipulation treatments, tree physiological measurements were performed and samples were collected for isotope analysis. Air CO₂ was collected for measurements of concentration and carbon isotope composition, averaging 467 ± 12.4 ppm and -10.9 ± 0.4 ‰ across all timepoints and chambers, respectively. At the end of the five-month climate chamber manipulations, stem tree-ring samples were collected, transferred to paper bags, and dried at 60 °C. To ensure samples represented only the growth that occurred during the climate chamber experiment, the youngest ring was separated from the tree stem samples prior to cellulose extraction. Tree-ring width was determined with visual examination and with scans of wood in thin section (Peters *et al* 2020) (Peters et al., 2020, Tree Physiology).

In addition to the analyses described in this work, many other measurements were performed on samples from the climate chamber study, including the $\delta^2\text{H}$, $\delta^{13}\text{C}$, and $\delta^{18}\text{O}$ of leaf and stem starch and sugars. We compare those measured properties to the results of PSIA in Section 4.4.5; full details of starch and sugar measurements were previously described in Lehmann et al. (2023).

4.3.3) Cellulose purification

Cellulose was extracted from tree-ring samples at the Swiss Federal Research Institute WSL as described in Schuler et al., 2023 and 2024. In brief, cut wood material was transferred and sealed in F57 fibre filter bags (Ankom Technology, Macedon, NY, USA). Sample lipids were removed by Soxhlet extraction in 2:1 toluene:ethanol for 8 hours or until solvent extract was colorless, then

for another 8 hours in pure ethanol. After drying overnight, samples were placed in an Erlenmeyer flask and boiled in deionized water for 3-4 hours to remove sugars. Next, sample holocellulose was isolated by bleaching in 7% sodium chlorite (adjusted to pH 4-5 with glacial acetic acid) at 60 °C for 30 hours, refreshing the solution every 10 hours. Samples were rinsed three times with boiling water and dried. Holocellulose samples were then incubated in 17% w/v sodium hydroxide at room temperature for one hour, repeating this step a total of two times before rinsing three times with boiling water. Finally, samples were incubated for one hour at room temperature in a 10% acetic acid solution and rinsed three more times with boiling water to yield purified α -cellulose. The cellulose product was removed from the filters, soaked in deionized water, homogenized with ultrasonication (UP200St, Hielscher, Teltow, Germany), and freeze-dried. The reaction yielded ~10% α -cellulose.

4.3.4) Cellulose hydrolysis

To prepare samples for analysis by ESI-Orbitrap, cellulose was first hydrolyzed to its constituent glucose monomers in sulfuric acid following standard protocols (Saeman *et al* 1945, Betson *et al* 2006). For each 5 mg of cellulose, 50 μ L of 72% (w/w) H_2SO_4 , chilled to 5 °C, was added. Samples were vortexed and then briefly spun in a benchtop mini centrifuge to maximize cellulose exposure to acid. Samples in screw-top conical polypropylene tubes were incubated in a water bath at 30 °C for one hour, vortexing every 15 minutes to mix. Following the one hour incubation, samples were diluted by adding 850 μ L of water per 5 mg cellulose and then autoclaved at 121 °C for 1 hour. As soon as the autoclave cycle was completed, sample tubes were submerged in an ice bath. Solid $CaCO_3$ was gradually added to each sample to bring the pH to ~5 (~60 mg per 5 mg cellulose). Neutralized samples were vacuum filtered through glass fiber filters. When tested on pure cellulose standards, the reaction proceeded with 70-80% yield and produced no discernible ^{13}C fractionation between the starting cellulose and the final glucose solution (Supplementary Figure 4.5). Glucose yields were determined by high performance liquid chromatography using refractive index detection (HPLC-RID) (Section 4.3.5).

Dissolved inorganic ions, including Ca^{2+} and SO_4^{2-} , were removed from the filtrate prior to glucose oxidation in order to avoid precipitation of evolved gluconate. SO_4^{2-} was first removed by

precipitation as solid BaSO₄: 15 mg of BaCl were added to each sample per 50 μL H₂SO₄.

After a 30 minute incubation at room temperature, samples were passed through a 0.22 μm PES filter to remove BaSO₄ crystals. The filtrate was further desalted to remove Ca²⁺, Cl⁻, and trace remaining SO₄²⁻ by passing through a 2.5 mL Dionex OnGuard II Ba/Ag/H cartridge. Each cartridge was washed with 15 mL of 18 MΩ deionized water prior to sample application. Sample was applied to the column and eluted at a rate of 1-2 mL/min. Following sample elution, an additional 1 mL of water was applied to the column and collected in order to flush out any remaining product.

4.3.5) Glucose quantification

To quantify glucose yield, samples were measured via an Agilent 1100 high-performance liquid chromatography (HPLC) system with a refractive index detector (RID). The HPLC was equipped with an Aminex HPX-87H column (300 x 7.8 mm) and sample compounds were separated with an isocratic method using 0.6 mL min⁻¹ of 4 mM sulfuric acid. Glucose concentrations were determined from sample peak areas by comparison to a 4-point calibration curve. The standard deviation of repeat measurements was <0.6% of peak area.

4.3.6) Glucose oxidation and desalting

Glucose was oxidized to gluconate following (Bunzel and Mathews 1909), as described in Chapter 3. In brief, the glucose solution produced by cellulose hydrolysis was combined with 1.1 equivalents of Br₂ and 2 equivalents of NaOH and stirred at room temperature for 5 hours. The product was desalted using a Dionex OnGuard II Ag/H column, following the same steps as described in Section 4.3.4. Gluconate yields were determined by ion chromatography and the oxidation method was found to impart no discernible ¹³C fractionation, as detailed in Chapter 3.

4.3.7) Compound-specific δ¹³C measurements

Compound-specific δ¹³C values of standards and samples were measured by elemental analyzer-isotope ratio mass spectrometry (EA-IRMS). Measurements were performed on an EA IsoLink combustion elemental analyzer system interfaced to a Delta V Plus IRMS (Thermo Fischer

Scientific). Samples were weighed to ~20 µg carbon in tin capsules and combusted at 1020 °C, and the evolved CO₂ was quantified and analyzed for its carbon isotope composition. Measured isotope ratios were calibrated to the VPDB scale using in-house isotope standards and international reference materials, and the standard deviation of repeat standard measurements was <0.1‰.

4.3.8) Orbitrap measurements

Aqueous gluconate samples were filtered to 0.22 µm with a syringe and PES filter (Tisch Scientific, Cleves, OH, USA) and then diluted to 50 µM in LC-MS grade methanol for analysis by ESI-Orbitrap. Full details of the Orbitrap measurement are found in Chapter 3. Briefly, samples were introduced onto a Q Exactive HF Orbitrap mass spectrometer (Thermo Fischer Scientific) using a Vanquish Horizon ultrahigh-performance liquid chromatography (UHPLC) system and a Heated Electrospray Ionization (HESI-II) probe (Thermo-Fischer Scientific). The UHPLC was not equipped with a column and no online separation occurred. Rather, the UHPLC was used to autosample and stably infuse 100-µL injections of sample or standard solution into the Orbitrap at a constant flow rate of 4 µL/min. For a typical analysis, 6 successive sample or standard injections were performed to produce a total analysis time of >120 minutes. This ~120-minute measurement is termed an “acquisition”. This routine was repeated for sample-standard brackets, and each sample was measured in triplicate relative to a standard with matching ion signal intensity. These parameters were shown in Chapter 3 to maximize measurement precision and accuracy while minimizing sample consumption. Settings for the HESI-II source and the Orbitrap are detailed in Chapter 3.

4.3.9) Data processing

Several steps of data processing are required to convert Orbitrap .RAW files into molecular-average and compound-specific $\delta^{13}\text{C}$ values, outlined in full in Chapter 3. Briefly, ion signal intensities first were retrieved from .RAW files using IsoX (Kantnerova *et al* 2024) and used to estimate ion counts following Makarov and Denisov (2009) and Eiler *et al* (2017). Ion counts were used to calculate uncorrected isotope ratios (¹³R values) for each relevant ion in the mass spectrum in each scan, where ~30k scans are collected at a rate of ~5 s⁻¹ during a single acquisition. Scans

were dropped from the dataset if they were collected during intervals of dead time between injections, or if they did not meet data quality thresholds established for mass accuracy and expected Automatic Gain Control behavior (Chapter 3; Eiler *et al* 2017; Chimiak *et al* 2021). In a typical measurement, >99% of scans met these data quality thresholds. The uncorrected ^{13}R value for a sample acquisition was calculated as the mean of ^{13}R values measured across all remaining unculled scans.

4.3.10) Isotope calculations

The uncorrected ^{13}R value for each measured fragment in a given acquisition was converted to a $\delta^{13}\text{C}$ value on the basis of repeat sample-standard measurements:

$$\delta^{13}\text{C}_{\text{Sample-Standard}} = \frac{{}^{13}\text{R}_{\text{Sample}} - {}^{13}\text{R}_{\text{Standard}}}{{}^{13}\text{R}_{\text{Standard}}} \quad (4.1)$$

$\delta^{13}\text{C}$ values are reported in permil (‰), indicating parts per thousand relative difference between measured sample and standard ^{13}R values. The $\delta^{13}\text{C}$ values reported here are the average of three sample-standard comparisons, and the error bars represent the standard deviation of these comparisons, unless otherwise noted.

While studies usually report $\delta^{13}\text{C}$ values on the VPDB scale, ESI-Orbitrap measurements can only be tied to VPDB by comparing to another standard for which position- or fragment-specific $\delta^{13}\text{C}_{\text{VPDB}}$ values have been externally determined. No glucose or gluconate reference materials with known position-specific values are currently available. As a result, we report all $\delta^{13}\text{C}$ values measured by ESI-Orbitrap relative to the standard SC3, and denote these values as $\delta^{13}\text{C}_{\text{SC3}}$:

$$\delta^{13}\text{C}_{\text{SC3}} = \frac{{}^{13}\text{R}_{\text{Sample}} - {}^{13}\text{R}_{\text{SC3}}}{{}^{13}\text{R}_{\text{SC3}}} \quad (4.2)$$

When we report $\delta^{13}\text{C}$ values anchored to the VPDB scale (i.e., those obtained by EA-IRMS), we denote these values as $\delta^{13}\text{C}_{\text{VPDB}}$.

We converted measured $\delta^{13}\text{C}$ values for fragment ions to position-specific $\delta^{13}\text{C}$ values using a matrix of equations constructed as previously described (Chapter 3; Wilkes *et al* 2022). Fragments

were attributed to their constituent atomic positions using positionally ^{13}C -labeled standards. For each sample, 15,000 Monte Carlo simulations of the matrix of equations were constructed based on the measured fragment $\delta^{13}\text{C}$ values and measurement error, and the optimal solution for the matrix was calculated for each simulation using the `linalg.lstsq` function in the ‘NumPy’ Python package. The $\delta^{13}\text{C}$ value and error for each intramolecular position was reported as the average and standard deviation of solutions across the Monte Carlo simulations. However, because measurement error is relatively well-correlated among fragments, the error propagated through the Monte Carlo simulations likely overestimates the true measurement uncertainty. Measurement precision and uncertainty are further discussed in Sections 4.4.3 and 4.4.4.

4.3.11) Data analysis

To identify significant correlations among measured variables, we calculated linear regressions by ordinary least squares (OLS). Regression p-values were corrected for multiple hypothesis testing using the Benjamini-Hochberg false discovery rate correction using the ‘`fdrcorrection`’ function in the Python package ‘statsmodels’. When performing t-tests between different conditions, we applied Welch’s t-test to accommodate instances of unequal variance, using the ‘`ttest_ind`’ function from the Python library ‘SciPy’. T-test p-values were similarly adjusted with the Benjamini-Hochberg correction.

4.4) Results and discussion

4.4.1) Sample consumption

For each measurement, samples were diluted to 50 μM based on the gluconate concentration determined by ion chromatography (Section 4.3.6), and 6 100- μL sample injections of 100 μL were made for each acquisition. To measure one sample in triplicate therefore consumed a total of ~ 18 μg gluconate. According to the yields observed for the preparatory chemistry methods, total sample consumption amounts to ~ 0.033 mg α -cellulose. This compares favorably to the α -cellulose consumption reported for traditional (i.e., molecular-average) cellulose ^{13}C analyses, which ranges from 0.04 mg to over 1 mg among 285 studies from 2009–2019 (Belmecheri *et al* 2022), not to

mention those for PSIA by NMR (> 100 mg). The sample efficiency of Orbitrap-based PSIA highlights its utility for measuring environmental samples, where material is often limited.

We expect that it is possible to further reduce sample consumption during Orbitrap ^{13}C -PSIA of gluconate by lowering analyte concentrations. As shown in Chapter 3, decreasing the analyte concentration from 50 to 25 μM causes only a minor loss in signal stability while improving the useful ion yield. While we have not yet verified the limits of measurement precision and accuracy at lower sample concentration, these early results show promise for further decreasing sample requirements for PSIA.

4.4.2) Accuracy effects of signal intensity

In Section 3.4, we showed that Orbitrap measurements of gluconate standards can retrieve accurate $\delta^{13}\text{C}$ values for the molecular average and for each fragment ion, enabling accurate calculation of position-specific values. However, the $\delta^{13}\text{C}$ values retrieved for comparisons of subsequent acquisitions were strongly dependent on the relative difference in total ion count (TIC) between those acquisitions. The TIC-dependent effect we observe is analogous to nonlinearities in isotope ratios observed in sector mass spectrometers across a range of signal intensities (e.g., Merritt and Hayes 1994), sometimes called a “linearity effect” (e.g., Brand 1998). However, the cause of this effect in Orbitrap analyses is not yet known. Several hypotheses could explain the observed TIC-dependence: possible mechanisms might include sample-matrix interactions in the source or nonlinearities in AQS (advanced quadrupole selector) ion transfer at very high ion abundance. Because the samples measured here differ from the gluconate standards measured in Chapter 3 in both matrix composition and ion abundance, we tested whether the effect observed in gluconate standards was replicable for cellulose standards and samples.

Size effects on $\delta^{13}\text{C}$ were tested using standard SC3, a reagent-grade glucose standard that we oxidized to gluconate and desalted following the protocols outlined in Section 4.3.6. As a result, any minor side products and residual salts introduced during glucose oxidation would be present in SC3 as in the natural cellulose samples. These include a minor component at nominal mass 193 with molecular formula $\text{C}_6\text{H}_9\text{O}_7$ (relative peak height = < 5%) and any Na^+ and Br^- not fully

removed during desalting. SC3 was measured repeatedly relative to itself ($\delta^{13}\text{C}_{\text{SC3}}$ of SC3, accurate value = 0‰), diluted to different concentrations in order to induce TIC differences. Like in tests of sodium gluconate standards (see Section 3.4.6), this test produced a TIC dependence of $\delta^{13}\text{C}$ values; however, the relationship between relative TIC difference and the bias in $\delta^{13}\text{C}$ values was much more muted and with an opposite sign (slope = 4.7) compared to the relationship we found for gluconate standards (slope = -40.8) (Figure 4.1). It is not currently known whether this substantial difference in TIC-dependent behavior between standards and samples is related to a matrix effect, a TIC effect, or some other mechanism.

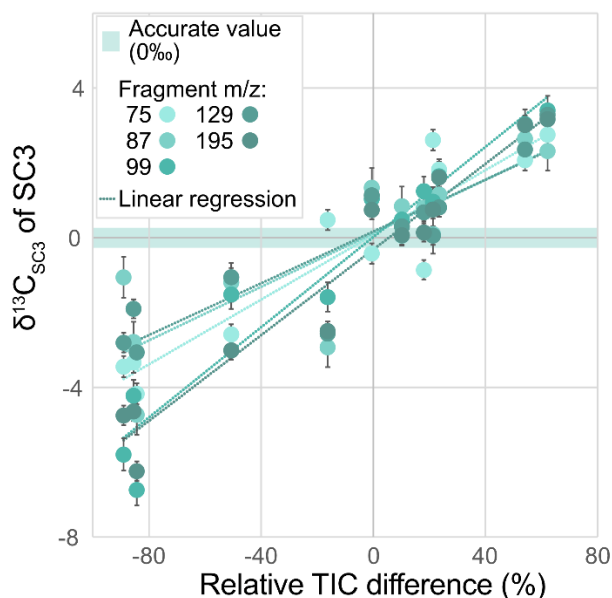


Figure 4.1: Measurement accuracy for all five measured ions across a range of relative TIC differences, assessed by repeat measurements of SC3 against itself ($\delta^{13}\text{C}_{\text{SC3}}$ of SC3, accurate value = 0‰). Each point represents a comparison of two acquisitions for a given ion; error bars show the relative standard error of ^{13}R among scans propagated from both acquisitions. Dotted lines show a linear regression between relative TIC difference and $\delta^{13}\text{C}$ value for each ion.

For the molecular ion and all 4 fragments of SC3 measured across 12 different relative differences in TIC, the y-intercept of a linear regression between relative TIC difference and $\delta^{13}\text{C}$ value was within or nearly within one relative standard error of zero (-0.31 ± 0.25 to 0.37 ± 0.72 ; average y-intercept = 0.07) (Figure 4.1). This finding suggests that an accurate $\delta^{13}\text{C}$ value of sample-standard comparisons can be retrieved by estimating the y-intercept of a linear regression between relative TIC difference and measured $\delta^{13}\text{C}$.

Based on these results, we corrected measured sample $\delta^{13}\text{C}$ values for each fragment according to signal intensity. Standards were prepared to match each sample's expected TIC (using short test measurements to select appropriate standard dilutions); nevertheless, because of unpredictable run-to-run variability in TIC, the relative sample-standard TIC differences among all 24 measured samples ranged from -65% to +94%. To correct for size-dependent errors, measured $\delta^{13}\text{C}$ values were extrapolated back to the y-intercept by linear regression between relative TIC difference and $\delta^{13}\text{C}$ value. The average correction across all 120 fragment ion $\delta^{13}\text{C}$ measurements was +0.69‰. We report uncertainty for each fragment's $\delta^{13}\text{C}$ value as the 90% confidence interval of the calculated y-intercept.

Of twenty-three measured samples, four had an average correction larger than 2.5‰ across all five measured ions. These samples were not distinguished by unusual TIC values, TIC variability, sample-standard TIC differences, or abundance of contaminant ions in the sample matrix. Nevertheless, each of these four samples exhibited an unusually high TIC dependence of measured $\delta^{13}\text{C}$ values (slope = 12.8–22.9‰ per 100% relative difference) relative to other samples (average slope among other samples = 2.4). These slopes were also markedly higher than the slope of 4.7 observed for the glucose standard SC3. Although the reason for this trend is not yet known, the four samples with unusually large $\delta^{13}\text{C}$ corrections were flagged as a possible source of error in data analysis, discussed further in Section 4.4.3.

4.4.3) Accuracy of molecular-average $\delta^{13}\text{C}$ values

To further assess the accuracy of our measurements on natural samples, we compared the $\delta^{13}\text{C}_{\text{VPDB}}$ values measured for the gluconate molecular ion to the molecular-average $\delta^{13}\text{C}_{\text{VPDB}}$ value of cellulose obtained by EA-IRMS. ($\delta^{13}\text{C}_{\text{VPDB}}$ of the molecular ion could be determined by Orbitrap because the molecular-average $\delta^{13}\text{C}_{\text{VPDB}}$ of the standard, SC3, was externally determined by EA-IRMS.) Both of these methods report the average $\delta^{13}\text{C}_{\text{VPDB}}$ value across all six carbon atomic positions in the glucose monomer of cellulose. A pairwise comparison of the $\delta^{13}\text{C}$ values retrieved from the two methods showed strong agreement, with an average offset of only -0.6‰ (Figure 4.2). In all, 22 out of 23 molecular-average values measured by Orbitrap were accurate within error of values measured by EA-IRMS (1σ).

The four samples with the largest TIC correction (Section 4.4.2) also had the largest offset between $\delta^{13}\text{C}$ values measured by EA-IRMS and by Orbitrap. These four samples had an average offset of -4.1‰ , while the rest of the dataset averaged 0.1‰ (Figure 4.2). A linear regression of the Orbitrap and EA-IRMS $\delta^{13}\text{C}$ values measured for all 23 samples produced a slope of 0.82 and an r^2 value of 0.30; removing the four flagged samples improves the slope to 0.94 and the r^2 value to 0.78. This finding suggests that, by identifying and controlling for the factors that induce TIC sensitivity in measured $\delta^{13}\text{C}$ values, measurement accuracy can be further improved.

Where an offset is observed between molecular-average $\delta^{13}\text{C}_{\text{VPDB}}$ values measured by Orbitrap and by EA-IRMS, several explanations are possible. EA-IRMS measurements were performed on whole α -cellulose, while Orbitrap measurements were made on cellulose-derived gluconate. Isotopic fractionation during preparatory chemistry is therefore a candidate to explain the disagreement between measured $\delta^{13}\text{C}$ values of cellulose and gluconate. We showed in Chapter 3 that any fractionation occurring during the oxidation of glucose to gluconate affects samples and standards equally (Figure 3.5D). Similarly, in tests of cellulose hydrolysis using reagent-grade α -cellulose standards, EA-IRMS measurements of the cellulose reactant and the glucose product produced $\delta^{13}\text{C}_{\text{VPDB}}$ values that were identical within error (1σ , Supplementary Table 4.2). These tests support that preparatory chemistry is not a significant source of fractionation for reagent-grade materials. Nevertheless, some samples may have behaved differently from reagent-grade materials due to differences in cellulose particle size, sample matrix components, or other properties.

To further investigate potential sources of isotopic fractionation during sample preparation, we measured the molecular-average $\delta^{13}\text{C}$ of the cellulose hydrolysis product for each natural cellulose sample by EA-IRMS. In contrast to the test of reagent-grade cellulose, this test revealed a systematic offset between cellulose and glucose $\delta^{13}\text{C}$, where glucose was enriched by an average of 0.77‰ relative to cellulose (range: -0.01 to 1.74‰) (Supplementary Figure 4.6). Several mechanisms might explain this trend. First, incomplete hydrolysis of α -cellulose to glucose could impart an isotopic fractionation. However, an inverse kinetic isotope effect would be required in order to create the observed enrichment of the glucose product relative to the cellulose reactant

pool. Inverse isotope effects are uncommon, and hydrolysis of glycosidic bonds was previously reported to induce a normal—not inverse—carbon isotope effect (Bennet and Sinnott 1986), making incomplete cellulose hydrolysis an unlikely explanation for the ^{13}C enrichment of glucose. A second possibility is that the α -cellulose preparation protocol did not fully remove all other components of the wood. If the cellulose samples measured by EA-IRMS also contained some other component not hydrolyzable to glucose, and that component was ^{13}C -depleted relative to α -cellulose, this could explain the relative ^{13}C -enrichment of the glucose product we observe here. By mass balance calculation, the non-cellulose component of the samples would need to be as much as 6.9‰ more ^{13}C -depleted than the colocated cellulose. While previous studies have shown that tree-ring lignin and fatty acids are typically 2–4‰ depleted in ^{13}C relative to cellulose (Helle *et al* 2022), a 7‰ offset between components even after thorough α -cellulose purification seems unlikely. Additionally, while we would expect the proportion of non-cellulose components like resin and lignin to differ substantially between our angiosperm and gymnosperm tree samples (Sjöström 1993), a t-test found no statistically significant difference in the $\delta^{13}\text{C}$ offsets between tree species ($p = 0.78$). A third possible mechanism is that the glucose evolved from cellulose hydrolysis might partially degrade under hot and acidic reaction conditions before the reaction is quenched, imparting a normal kinetic isotope effect. When we examined the relationship between measured hydrolysis yield and the $\delta^{13}\text{C}$ offset between cellulose and glucose for natural samples, we found a weak but statistically significant positive correlation ($r^2=0.25$, $p=0.014$) (Supplementary Figure 4.6). Additionally, samples were hydrolyzed in batches of 6; comparisons of the $\delta^{13}\text{C}$ offset between batches were statistically significant in 5 of 6 possible pairs ($p \leq 0.05$). In an initial test subjecting reagent-grade glucose to the conditions of our cellulose hydrolysis method, no glucose loss was apparent (yield = 100% glucose, $n = 2$). Nevertheless, the evidence for carbon isotopic fractionation of samples due to glucose degradation is otherwise strong, and offers the best explanation for the $\delta^{13}\text{C}$ offset observed between sample cellulose and glucose.

Previous work has shown that glucose degradation at high temperature and low pH forms 5-hydroxymethylfurfural, which further degrades to levulinic acid and formic acid (Saeman *et al* 1945). While 5-HMF was not detected in sample cellulose hydrolysates by LC-RI or MS, levulinic acid was detected at substantial abundance by MS ($[\text{C}_5\text{H}_8\text{O}_3 - \text{H}^+]$, $m/z = 115.039$). The proposed

degradation pathway involves oxidation and reduction of functional groups at the C-1 and C-2 positions (Kang *et al* 2019) that could impart fractionation against ^{13}C , leaving the remaining glucose pool with higher $\delta^{13}\text{C}$ values. If the isotopic fractionation equally affected the C-1 and C-2 positions, then a difference of 0.77‰ in the molecular average $\delta^{13}\text{C}$ value would result in a bias at each of those positions of 2.31‰. However, no statistical relationship was found between the relative intramolecular enrichment of positions C-1 and C-2 and the hydrolysis yield for a given sample ($r^2 = 0.03$, $p = 0.40$). This result supports that despite possible ^{13}C fractionation during cellulose hydrolysis, no strong or systematic bias was imparted in measured position-specific $\delta^{13}\text{C}$ values.

To further verify the effect of cellulose hydrolysis on position-specific $\delta^{13}\text{C}$ values, we will expose a glucose standard with a known ^{13}C enrichment at C-1 to the conditions of cellulose hydrolysis, and compare the product to an unaltered glucose standard by EA-IRMS and Orbitrap. Until the results of this test are available, we can interpret the initial PSIA results while keeping in mind that the $\delta^{13}\text{C}$ values measured at C-1 and C-2 might be artificially high in some samples, although no systematic difference is present.

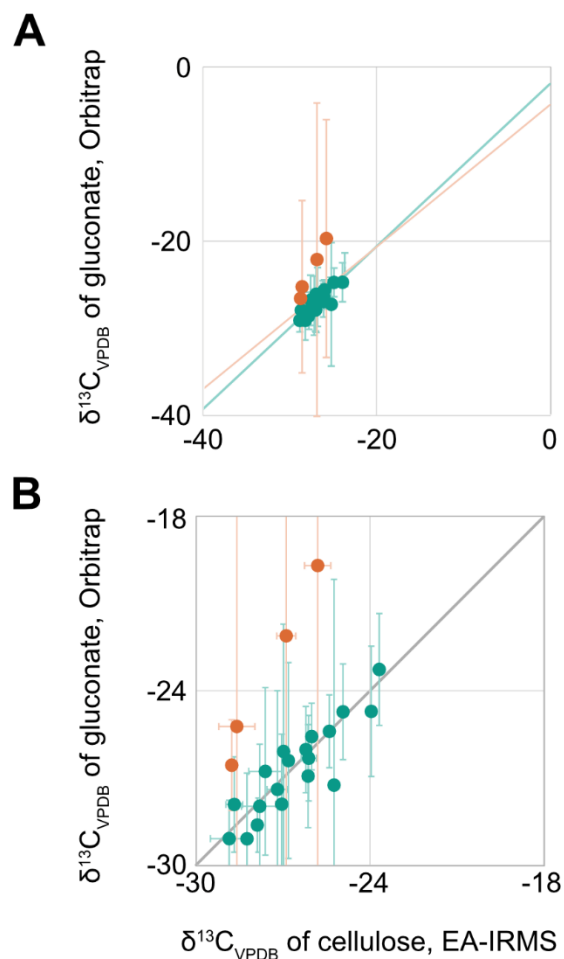


Figure 4.2: A: Comparison of molecular-average $\delta^{13}\text{C}$ values as measured by EA-IRMS (x-axis) and Orbitrap (y-axis). Error bars show one standard deviation of $\delta^{13}\text{C}$ values measured for that sample. Orange points are those for which the TIC correction of the $\delta^{13}\text{C}$ value measured by Orbitrap was $> 2.5\%$ (Section 4.4.2). Orange line shows a linear regression including those values; green line shows a linear regression excluding those values. B: Detail of panel A. Gray line is 1:1 line. 22 of 23 samples are within error of 1:1 line (1σ).

4.4.4) Precision of position-specific values

For each fragment measurement in each sample, precision was assessed as the 90% confidence interval of the y-intercept of a regression between TIC and $\delta^{13}\text{C}$, as described in Section 4.4.2. Since position-specific $\delta^{13}\text{C}$ values are calculated using more than one fragment measurement, the uncertainty from each measured fragment is propagated, producing larger error bars. For example, one sample had uncertainties in fragment $\delta^{13}\text{C}$ values ranging from 0.09–0.68‰, while the uncertainty for atomic position $\delta^{13}\text{C}$ values ranged from 0.18–3.06‰. Uncertainty was often highest for the C-5 and C-6 positions: these positions are measured only in the one or two ions

with highest mass (195 and 129), where the signal is diluted by the signal from the four to five co-occurring carbon atoms.

The uncertainties estimated by comparing biological replicates were consistently much smaller than those derived from error propagation of the fragment uncertainties. The standard errors of position-specific $\delta^{13}\text{C}$ values among biological triplicates averaged 1.8‰, ranging from 0.1–7.2‰. This closely approaches the precision observed for PSIA of glucose standards, which averaged 1.4‰ (range: 0.21–3.10‰). In other words, sample measurements generally match the limits of precision achieved with reagent-grade standards. Meanwhile, the error propagated through our Monte Carlo simulations was never better than 3.0‰ and typically exceeded 10‰. The good agreement of position-specific values among biological triplicates suggests that propagation of fragment uncertainties substantially overestimates the true uncertainty of the measurement. The method of error propagation we apply to calculate position-specific $\delta^{13}\text{C}$ values assumes that each source of error is independent of the others. In contrast, errors in $\delta^{13}\text{C}$ values across fragments are likely to be correlated, because they arise from similar effects. For example, we have shown that the TIC-dependence of $\delta^{13}\text{C}$ produces similar trends in all fragments (Figure 4.1). As Orbitrap-PSIA is further developed, future work should investigate how to accurately characterize measurement uncertainty, identifying correlated and uncorrelated sources of error for fragment measurements. Here, we report uncertainty on PSIA results as the standard error of biological triplicates.

Overall, our position-specific analyses of tree-ring cellulose samples approach the precision achieved by NMR (0.7–1.4‰; Wieloch *et al* 2018) while consuming over 650 times less sample and requiring up to 6-fold less measurement time. While this exceeds the typical uncertainty of molecular average $\delta^{13}\text{C}$ values measured by EA-IRMS, observing the same signal size in a molecular-average measurement would in effect require 6x better precision due to dilution by the other 5 C atoms—so, for example, 1‰ precision for a single atomic position is analogous to 0.17‰ precision for the whole molecule. PSIA additionally offers the substantial advantage of independently observing atomic positions, where opposing $\delta^{13}\text{C}$ trends would counteract each other in a molecular-average measurement. Since only one record of position-specific $\delta^{13}\text{C}$ in tree

rings currently exists, it is difficult to anticipate the magnitude of climate signals that can be observed by ^{13}C -PSIA in comparison to the precision we achieve here. However, the existing record recovers up to 3.37‰ variance in positional $\delta^{13}\text{C}$ over 34 years (Wieloch *et al* 2018), which already exceeds the typical uncertainty of our position-specific measurements.

4.4.5) Intramolecular trends in $\delta^{13}\text{C}$

Clear intramolecular trends in $\delta^{13}\text{C}$ values are visible across our dataset (Figures 4.3 and 4.4). For example, the $\delta^{13}\text{C}$ of C-1+C-2 is consistently more negative than $\delta^{13}\text{C}$ of C-3, with the difference averaging 6.6‰. We measure intramolecular differences in $\delta^{13}\text{C}$ of up to 21.7‰, with an average spread of 11.6‰ within a given experimental condition. These intramolecular differences far exceed the uncertainty of our measurement, demonstrating the sensitivity of Orbitrap PSIA for detecting intramolecular heterogeneity in natural carbohydrates. Meanwhile, position-specific $\delta^{13}\text{C}$ values were uncorrelated with one another ($p > 0.05$) except for C-4 and C-6 ($p = 0.0001$), suggesting that each position generally records different signals.

Because the $\delta^{13}\text{C}$ values for each atomic position were measured relative to standard SC3—a natural glucose standard from a C3 plant, with its own intramolecular pattern—the intramolecular differences we detect here are the sum of the patterns in SC3 and in the tree-ring samples, which may combine to enhance or diminish the true intramolecular variability in the samples. We can estimate samples' true intramolecular patterns by assuming that SC3 is similar to another glucose standard from the same product number that was measured by NMR (Youki Sato, pers. comm.; Supplementary Figure 4.7). Under this assumption, we estimate the true intramolecular variability to be on average ~13‰. This result closely matches our measured variability of 11.6‰, supporting that our measurements accurately represent the true amplitude of intramolecular signals.

To assess the value added by performing PSIA rather than CSIA alone, we compared the $\delta^{13}\text{C}$ values measured for each position to the molecular-average values obtained by EA-IRMS. Of the five measured positions, only C-3 had a significant linear correlation with molecular-average values ($p = 0.001$). (For C-1+C-2, $p = 0.090$, and for C-4–C-6, $p > 0.2$.) This indicates that any trends observed at positions other than C-3 in this dataset would not likely be observed by

traditional compound-specific $\delta^{13}\text{C}$ measurements. Further, the regression of C-3 $\delta^{13}\text{C}$ values as a function of the molecular average produces a slope of 1.75. This suggests that isotopic signals are more strongly recorded at C-3 than in the molecular average, where other atomic positions can dilute the signal.

We also compared positional $\delta^{13}\text{C}$ values to compound-specific $\delta^2\text{H}$, $\delta^{13}\text{C}$, and $\delta^{18}\text{O}$ values measured for leaf and stem starch and sugars (Section 4.3.2). C-3 had statistically significant correlations with the $\delta^{13}\text{C}$ of stem starch and sugars and the $\delta^2\text{H}$ of stem sugars, while C-6 was significantly correlated with the $\delta^2\text{H}$ of leaf and stem sugars ($p = 0.01$ for all). No other positions correlated with any of the starch or sugar measurements, including the $\delta^{13}\text{C}$ of starch and sugar, despite the fact that cellulose is synthesized from glucose-6-phosphate, which is closely linked to plant starch and sugar pools. This finding suggests that the $\delta^{13}\text{C}$ at positions other than C-3 may be altered by metabolic fractionations acting on starch and sugars. For example, C-1 and C-2 of cytosolic glucose is predicted to experience ^{13}C fractionation during fluxes through glucose-6-phosphate isomerase (GPI) and glucose-6-phosphate dehydrogenase (G6PDH) (Wieloch *et al* 2025), including at metabolic branchpoints associated with starch synthesis. Variation in carbon allocation among metabolic pathways like starch production would therefore be expected to change the relationship between the $\delta^{13}\text{C}$ of sugar, starch, and cellulose pools at atomic positions where fractionations occur. Meanwhile, C-3 is not thought to be strongly fractionated by most enzymes in plant metabolism (Wieloch *et al* 2025), which aligns with our observation that its $\delta^{13}\text{C}$ signature is closely related among starch, sugar, and cellulose ($r^2 = 0.50$ for cellulose vs. starch and for cellulose vs. sugar).

4.4.6) Response of position-specific $\delta^{13}\text{C}$ values in tree-ring cellulose to moisture and temperature

Using tree-ring samples from the climate chamber experiment, we were able to assess the independent effects of air moisture (via vapor pressure deficit, VPD), soil moisture (via soil volumetric water content, VWC), and temperature on the position-specific $\delta^{13}\text{C}$ values of cellulose. Each condition produced distinct position-specific signatures, and the two studied tree species (*F. sylvatica*, European beech; and *L. decidua*, European larch) also exhibited different patterns of sensitivity to climate perturbations.

In the soil moisture experiment, trees grown at 25 °C and 1 kPa VPD were grown in soil with either 5% (low) or 30% (high) volumetric water content. The $\delta^{13}\text{C}$ value of C-3 was significantly correlated with soil moisture ($p = 0.004$), driven most strongly by ^{13}C enrichment at low soil moisture in larch samples (Figure 4.3C and F). Previous work has indicated that the carbon isotopic composition of C-3 is imparted primarily during CO_2 diffusion and fixation by Rubisco (Wieloch *et al* 2025), where the extent of fractionation is controlled by the balance of stomatal conductance and photosynthetic rate (Farquhar *et al* 1982, 1989). Because all plants in the soil moisture experiment grew at equal temperature and illumination, stomatal conductance is expected to be the primary control on fractionation during photosynthesis. The relationship we observe between C-3 and soil moisture is therefore likely to reflect higher stomatal conductance when more soil moisture is available, consistent with plant hydraulic control of leaf gas exchange (Sadras and Milroy 1996, Martínez-Vilalta *et al* 2014). Soil moisture was also significantly correlated with molecular-average $\delta^{13}\text{C}$ of cellulose ($p = 0.002$), and with the $\delta^{13}\text{C}$ of stem starch and sugars ($p = 0.001$). However, C-3 was roughly twice as sensitive to soil moisture than any molecular-average measurement (slope = -0.22 for C-3 vs. -0.10–0.13 for molecular-average measurements), again supporting the enhanced sensitivity of PSIA over CSIA for detecting climatic signals.

Beech and larch samples grown at low soil moisture also exhibited species-specific trends in $\delta^{13}\text{C}$ values: in beech, C-4 was 7.9‰ higher, while in larch, C-3 and C-5 were elevated by 5.7‰ and 6.3‰, respectively (Figure 4.3C and F). While our results suggest that C-3 records differences in stomatal conductance (driven by soil moisture) across all conditions, species-specific signals at C-4 and C-5 could represent metabolic adjustments each taxon makes in response to soil drought, such as fluxes to glycolysis via glyceraldehyde-3-phosphate dehydrogenase (GAPDH) at C-4 (Canellas and Cleland 1991) or to the tricarboxylic acid cycle or methylerythritol phosphate (MEP) pathway at C-5 (Wieloch *et al* 2025).

In the air moisture experiment, trees grown at 30 °C and 30% VWC were exposed to VPD of either 1 or 2.2 kPa. Unlike the soil moisture experiment, here there was no statistically significant effect at any intramolecular position (Figure 4.3B and E). Linear regression of VPD against each position and against the molecular average produced p values ranging from 0.14–0.91. Similarly, Welch's

t-test showed no significant difference between low and high VPD treatments at any position or for the molecular average ($p = 0.28\text{--}0.90$). In the larch samples, C-4 and C-6 have higher $\delta^{13}\text{C}$ values under higher VPD, but the values are within error of the low VPD treatment. These findings contrast with a previous study that reported that VPD strongly correlated with C-1, C-2, and molecular-average $\delta^{13}\text{C}$ values (Wieloch *et al* 2018) at VPD values between 0.35 and 0.75 kPa. It is possible that with plentiful soil moisture ($\text{VWC} = 30\%$), the plants did not decrease their stomatal conductance even under low-humidity conditions. While another study of these climate chamber samples showed minor loss of stomatal conductance with VPD increase (Schoenbeck *et al* 2022), these tests of stomatal conductance were performed at elevated irradiance compared to climate chamber conditions. Without further study, we cannot conclude why no clear VPD signal was observed, but adequate soil moisture availability provides a reasonable explanation.

In the temperature treatment, trees grown at 1 kPa VPD and 30% soil moisture were exposed to daytime temperatures of either 25 or 30 °C (nighttime temperatures were 15 °C and 20 °C, respectively). This treatment induced distinct responses in beech and larch samples: beech showed a large difference in $\delta^{13}\text{C}$ of C-3 vs. C-4 at 25 °C that was almost completely muted at 30 °C (Figure 4.3 A and D). Meanwhile, larch showed a significantly higher $\delta^{13}\text{C}$ value at C-6 at 30 °C than at 25 °C. C-3 in beech samples was consistently negatively correlated with temperature across all experimental treatments ($p = 0.005$), with a slope of -0.97‰ per degree C. The opposing trend in C-3 and C-4 at lower temperature may derive from flux through aldolase, which exerts a normal kinetic isotope effect at C-3 and an inverse isotope effect at C-4 in the direction of bond formation. This trend imparted by aldolase on the cytosolic sugar pool is muted with increased glycolytic flux through GAPDH (Canellas and Cleland 1991). Thus, if beech samples upregulate glycolysis in response to increased temperature, that could explain the isotopic trends we observe at C-3 and C-4. Meanwhile, no compound-specific $\delta^{13}\text{C}$, $\delta^2\text{H}$, or $\delta^{18}\text{O}$ measurements of cellulose, starch, or sugar were correlated with temperature. It may thus be possible to reconstruct temperature changes from a tree-ring cellulose record by comparing the $\delta^{13}\text{C}$ of C-3 to compound-specific measurements. In larch, the positive correlation of C-6 $\delta^{13}\text{C}$ with temperature is consistent with previous predictions, and may relate to temperature-sensitive fluxes to the tricarboxylic acid cycle and/or the MEP pathway (Wieloch *et al* 2025). Increased flux to isoprenoid synthesis via the MEP

pathway, which could explain elevated $\delta^{13}\text{C}$ values at C-6, would be consistent with previous observations of high plant isoprenoid emissions at high temperature (Rennenberg *et al* 2006, Sharkey *et al* 1996, Sharkey and Yeh 2001), including in *Larix* (Yu and Blande 2021).

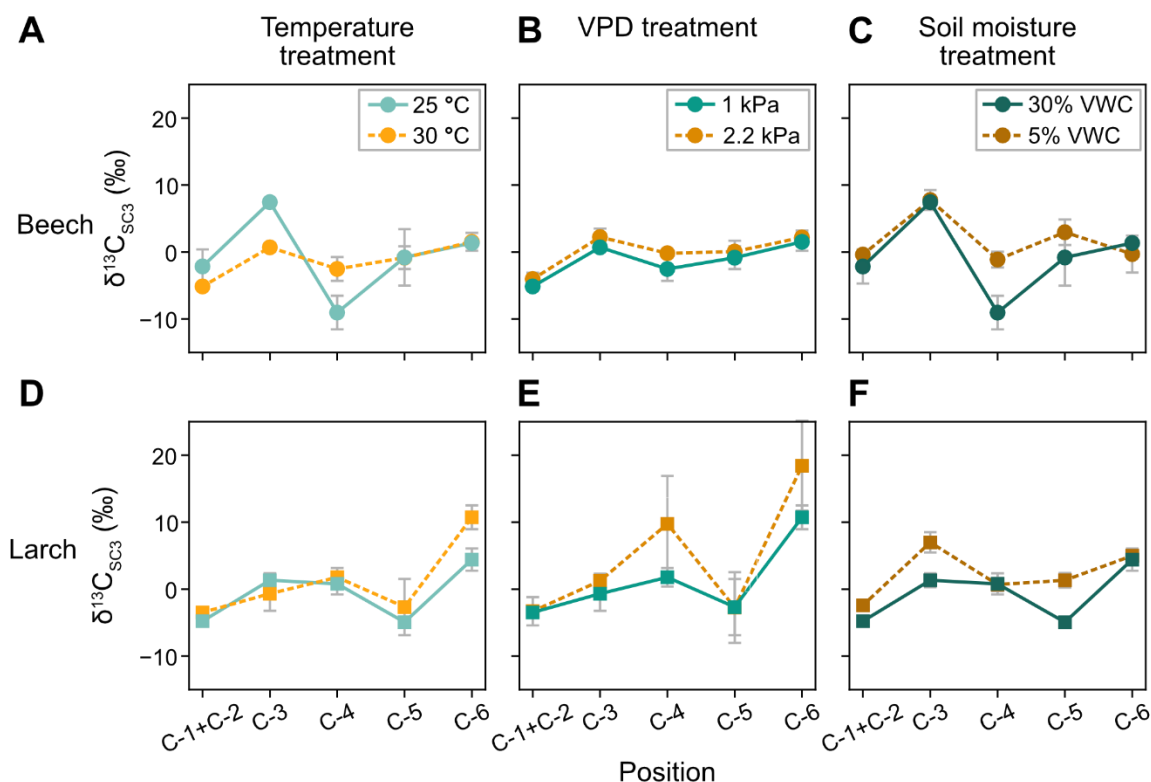


Figure 4.3: Position-specific $\delta^{13}\text{C}_{\text{GlcNA}}$ values measured for *F. sylvatica* (beech: A–C, circle) and *L. decidua* (larch: D–F, square) tree-ring cellulose samples, plotted by climate chamber treatment. A and D, temperature treatment (25 °C vs. 30 °C, VPD = 1 kPa, soil moisture = 30% VWC); B and E, VPD (vapor pressure deficit) treatment (1 vs. 2.2 kPa, temperature = 30 °C, soil moisture = 30% VWC); C and F, soil moisture treatment (30% vs. 5% VWC, temperature = 25 °C, VPD = 1 kPa). Error bars show one standard error of $\delta^{13}\text{C}_{\text{GlcNA}}$ values measured among biological replicates.

4.4.7) Trends in position-specific $\delta^{13}\text{C}$ between gymnosperm and angiosperm samples

In addition to the species-specific responses to climate perturbations at C-4–C-6 discussed above, the gymnosperm (*L. decidua*, larch) and angiosperm (*F. sylvatica*, beech) samples showed unique intramolecular trends in $\delta^{13}\text{C}$ under the same environmental conditions (Figure 4.4). For example, C-4 and C-6 in larch samples were ^{13}C -enriched relative to these positions in beech samples (C-4, $p = 0.045$; C-6, 0.018), with a significant difference across all treatments except for low soil moisture. Differences at these positions may reflect differences in carbon allocation according to growth strategy: for example, a previous study revealed ~2-fold differences in aboveground wood

and belowground root growth between gymnosperm and angiosperm species (Rog *et al* 2021).

Future work can ascertain what specific metabolic pathways (and their associated ^{13}C fractionations) contribute to distinct position-specific isotope distributions among tree taxa.

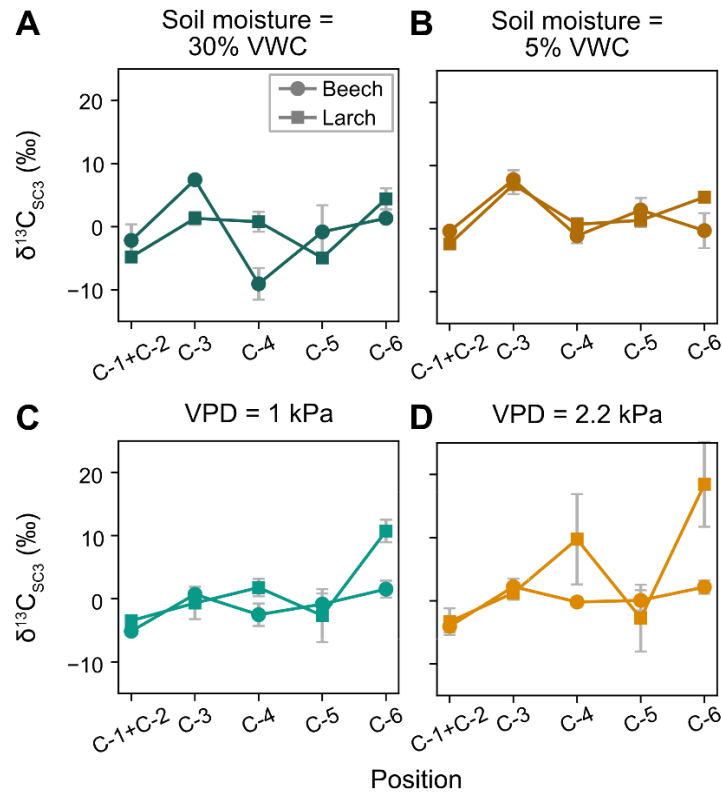


Figure 4.4: Position-specific $\delta^{13}\text{C}_{\text{GlcNA}}$ values measured for *F. sylvatica* (beech: circle) and *L. decidua* (larch: square) tree-ring cellulose samples. A-B show soil moisture treatments: A, 30% VWC; B, 5% VWC (temperature = 25 °C, VPD = 1 kPa). C-D show vapor pressure deficit (VPD) treatments: C, 1 kPa; D, 2.2 kPa (temperature = 30 °C, soil moisture = 30% VWC). Error bars show one standard error of $\delta^{13}\text{C}_{\text{GlcNA}}$ values measured among biological replicates.

Across treatments, position-specific $\delta^{13}\text{C}$ values in beech samples at C-1–C-3 were more significantly correlated with temperature and soil moisture ($r^2 = 0.38\text{--}0.78$) than in larch ($r^2 = 0.00\text{--}0.55$). This indicates that carbon isotope fractionation via stomatal conductance is more climate-sensitive in *F. sylvatica* than in *L. decidua*. Because *F. sylvatica* is a temperate and maritime-adapted species, while *L. decidua* inhabits subalpine to alpine environments, *L. decidua* is more likely to experience strong seasonal temperature shifts and rapid soil moisture changes (Silvestri *et al* 2025). Differences in the sensitivity of position-specific $\delta^{13}\text{C}$ values may therefore reflect these species' climate adaptations: for example, the narrow, waxy needles of *L. decidua*

impart greater desiccation resistance than the broad, soft leaves of *F. sylvatica*. Meanwhile, the $\delta^{13}\text{C}$ values at C-4–C-6 were more strongly correlated with climate perturbations in *L. decidua* ($r^2 = 0.01\text{--}0.42$) than in *F. sylvatica* ($r^2 = 0.07\text{--}0.22$). *L. decidua* may therefore have adapted a more flexible metabolic response to climate perturbation than *F. sylvatica*—for example, through the thermoprotective emissions of isoprenoids. Studies across a wider range of tree species can further investigate how adaptive strategies manifest in position-specific ^{13}C signatures of cellulose.

4.5) Conclusions and outlook

Here, we have demonstrated position-specific carbon isotope analysis of tree-ring cellulose by Orbitrap, consuming only 0.033 mg of cellulose for triplicate sample analysis. Our method achieves an average precision of 1.8‰ for position-specific values, approaching the precision achieved by NMR while improving analytical time by up to 6-fold and sensitivity by 650-fold. In the first application of this method, we are able to observe intramolecular differences in $\delta^{13}\text{C}$ of up to 21.7‰. PSIA recovers distinct patterns in response to soil moisture, air moisture, and temperature changes, with the potential to offer a nuanced picture of carbon assimilation and allocation in gymnosperm and angiosperm records in response to different environmental perturbations. Across the dataset, changes in soil moisture and temperature are most consistently recorded by the $\delta^{13}\text{C}$ of C-3; the soil moisture response at C-3 is more than twice as sensitive as in the molecular average, while molecular average values have no correlation with temperature, demonstrating the utility of PSIA for recovering clearer climate signals from cellulose $\delta^{13}\text{C}$ measurements. Meanwhile, the gymnosperm (*L. decidua*, larch) and angiosperm (*F. sylvatica*, beech) samples show distinct responses to moisture and temperature at positions C-4–C-6 that may indicate species-specific changes in carbon allocation to tasks like glycolysis or isoprenoid synthesis. Consistent differences between position-specific $\delta^{13}\text{C}$ patterns of larch and beech samples across treatments may reflect fundamental differences in these species' strategies for growth and adaptation. As a result, comparing position-specific $\delta^{13}\text{C}$ records from co-located trees of different species could produce more detailed climate reconstructions. These findings highlight the value of ^{13}C -PSIA for reconstructing more nuanced information about both climate and tree physiology from tree-ring records.

Several routes are available to further refine the method we present here. The largest source of bias in uncorrected $\delta^{13}\text{C}$ values measured by Orbitrap is the dependence of these values on TIC differences between sample and standard, and samples with the smallest TIC correction also produced the most accurate and precise $\delta^{13}\text{C}$ values. Future efforts may refine our method for correcting $\delta^{13}\text{C}$ values based on relative TIC differences, or may develop new approaches to minimize TIC variation or its effect on measured values. We have additionally shown that cellulose hydrolysis may impart a minor ^{13}C fractionation, likely concentrated at C-1 and C-2. The hydrolysis method should be modified to prevent degradative fractionation of glucose: for example, tests can determine whether shorter exposure times to high temperature could reduce isotopic fractionation while maintaining glucose yields. Finally, the method we employ here does not enable independent measurement of C-1 and C-2; we have previously described how future tests might determine the possibility for independent measurements of these positions (Chapter 3).

Using the method described here, 24 samples can readily be prepared in a 5-day work week. Meanwhile, measuring the same number of samples in triplicate would require 16 days, not including instrument setup time. Because the time required for Orbitrap analysis creates a bottleneck, additional efforts should focus on improving the time-efficiency of measurements. For example, adjustments to the injection system to increase sample flow rate and decrease the dead time between injections could shorten measurement times by ~10-20%.

Alongside these proposed improvements to our existing method, there are opportunities to expand the method to new isotope systems and measurement approaches. The Orbitrap mass spectrometer can simultaneously retrieve isotope ratios of multiple elements— ^{13}C , ^{18}O , and ^2H , in the case of glucose. While this work has focused only on ^{13}C -PSIA, we expect that future work will be able to establish optimal instrument conditions to enable ^{18}O PSIA and ^2H of tree-ring samples as well. Further, gluconate measurements by Orbitrap may offer an opportunity to make molecular-average $\delta^{13}\text{C}$ measurements with yet smaller cellulose samples. The Orbitrap enables measurement of the intact gluconate molecule without fragmentation, and can thus obtain molecular-average $\delta^{13}\text{C}$ measurements; in bypassing fragmentation, the ion count rates increase by a factor of ~10, allowing a user to reach precise values more quickly. This approach could help users measure

molecular-average values of $\delta^{13}\text{C}$ while consuming under 0.01 mg of cellulose. In view of the results presented here, as well as the numerous opportunities to improve and expand on our method, PSIA by Orbitrap presents a promising frontier for stable isotope dendrochronology.

4.6) Acknowledgments

This project was supported by the NASA Astrobiology Institute. Thanks go to Kimberly Sharp, Thomas Wieloch, Celia Kong-Johnson, and Sarah Vierling for help optimizing preparatory chemistry methods. Michael Mathuri assisted with EA-IRMS measurements, Nathan Dalleska with HPLC-RI measurements, and James Mullahoo with HPIC measurements. Thank you to Noam Lotem, Simon Andren, and Amy Hofmann for helpful discussions of TIC sensitivity, and to Brett Davidheiser and Caj Neubauer for their generous help with instrumentation. Elise Wilkes, Elliott Mueller, Sarah Zeichner, and Tim Csernica provided assistance with data processing. Yeonsoo Park provided instrumental help with interpreting intramolecular signals. Trees were grown and cellulose samples prepared by Marco Lehmann and his collaborators, including Oliver Rehmann, Leonie Schoenbeck, Philipp Schuler, Charlotte Grossiord, Haoyu Diao, and Valentina Vitali.

4.7) References

- Belmecheri S, Wright W E and Szejner P 2022 Sample Collection and Preparation for Annual and Intra-annual Tree-Ring Isotope Chronologies *Stable Isotopes in Tree Rings: Inferring Physiological, Climatic and Environmental Responses* ed R T W Siegwolf, J R Brooks, J Roden and M Saurer (Cham: Springer International Publishing) pp 103–34 Online: https://doi.org/10.1007/978-3-030-92698-4_4
- Bennet A J and Sinnott M L 1986 Complete kinetic isotope effect description of transition states for acid-catalyzed hydrolyses of methyl .alpha.- and .beta.-glucopyranosides *J. Am. Chem. Soc.* **108** 7287–94
- Betson T R, Augusti A and Schleucher J 2006 Quantification of Deuterium Isotopomers of Tree-Ring Cellulose Using Nuclear Magnetic Resonance *Anal. Chem.* **78** 8406–11
- Bunzel H H and Mathews A P 1909 THE MECHANISM OF THE OXIDATION OF GLUCOSE BY BROMINE IN NEUTRAL AND ACID SOLUTIONS. *J. Am. Chem. Soc.* **31** 464–79
- Canellas P F and Cleland W W 1991 Carbon-13 and deuterium isotope effects on the reaction catalyzed by glyceraldehyde-3-phosphate dehydrogenase *Biochemistry* **30** 8871–6

- Chimiak L, Elsila J E, Dallas B, Dworkin J P, Aponte J C, Sessions A L and Eiler J M 2021 Carbon isotope evidence for the substrates and mechanisms of prebiotic synthesis in the early solar system *Geochimica et Cosmochimica Acta* **292** 188–202
- Du Hamel and De Buffon 1737 Observations des différents effets que produisent sur les végétaux les grandes gelées d' hiver et les petites gelées du printemps *Académie royale des sciences* 273
- Eiler J, Cesar J, Chimiak L, Dallas B, Grice K, Griep-Raming J, Juchelka D, Kitchen N, Lloyd M, Makarov A, Robins R and Schwieters J 2017 Analysis of molecular isotopic structures at high precision and accuracy by Orbitrap mass spectrometry *International Journal of Mass Spectrometry* **422** 126–42
- Farquhar G D, Ehleringer I J R, and Hubick, K T 1989 CARBON ISOTOPE DISCRIMINATION AND PHOTOSYNTHESIS *Annu. Rev. Plant Physiol. Plant Mol. Biol.* **40** 503–37
- Farquhar G, O'Leary M and Berry J 1982 On the Relationship Between Carbon Isotope Discrimination and the Intercellular Carbon Dioxide Concentration in Leaves *Functional Plant Biol.* **9** 121
- Frank D C, Poulter B, Saurer M, Esper J, Huntingford C, Helle G, Treydte K, Zimmermann N E, Schleser G H, Ahlström A, Ciais P, Friedlingstein P, Levis S, Lomas M, Sitch S, Viovy N, Andreu-Hayles L, Bednarz Z, Berninger F, Boettger T, D'Alessandro C M, Daux V, Filot M, Grabner M, Gutierrez E, Haupt M, Hilasvuori E, Jungner H, Kalela-Brundin M, Krapiec M, Leuenberger M, Loader N J, Marah H, Masson-Delmotte V, Pazdur A, Pawelczyk S, Pierre M, Planells O, Pukiene R, Reynolds-Henne C E, Rinne K T, Saracino A, Sonninen E, Stievenard M, Switsur V R, Szczepanek M, Szychowska-Krapiec E, Todaro L, Waterhouse J S and Weigl M 2015 Water-use efficiency and transpiration across European forests during the Anthropocene *Nature Clim Change* **5** 579–83
- Frank D, Fang K and Fonti P 2022 Dendrochronology: Fundamentals and Innovations *Stable Isotopes in Tree Rings: Inferring Physiological, Climatic and Environmental Responses* ed R T W Siegwolf, J R Brooks, J Roden and M Saurer (Cham: Springer International Publishing) pp 21–59 Online: https://doi.org/10.1007/978-3-030-92698-4_2
- Gessler A, Ferrio J P, Hommel R, Treydte K, Werner R A and Monson R K 2014 Stable isotopes in tree rings: towards a mechanistic understanding of isotope fractionation and mixing processes from the leaves to the wood *Tree Physiology* **34** 796–818
- Gilbert A, Silvestre V, Robins R J and Remaud G S 2009 Accurate Quantitative Isotopic ¹³C NMR Spectroscopy for the Determination of the Intramolecular Distribution of ¹³C in Glucose at Natural Abundance *Anal. Chem.* **81** 8978–85
- Helle G, Pauly M, Heinrich I, Schollän K, Balanzategui D and Schürheck L 2022 Stable Isotope Signatures of Wood, its Constituents and Methods of Cellulose Extraction *Stable Isotopes in Tree Rings: Inferring Physiological, Climatic and Environmental Responses* Tree Physiology ed R T W Siegwolf, J R Brooks, J Roden and M Saurer (Cham: Springer

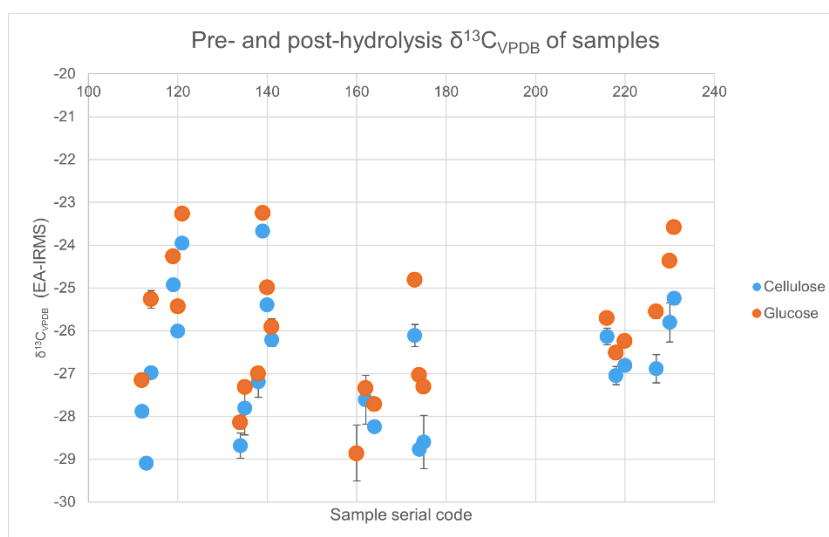
- International Publishing) pp 135–90 Online: https://doi.org/10.1007/978-3-030-92698-4_5
- Hilkert A, Böhlke J K, Mroczkowski S J, Fort K L, Aizikov K, Wang X T, Kopf S H and Neubauer C 2021 Exploring the Potential of Electrospray-Orbitrap for Stable Isotope Analysis Using Nitrate as a Model *Anal. Chem.* **93** 9139–48
- James H. Speer 2010 *Fundamentals of Tree-Ring Research* (University of Arizona Press)
- Kang P-L, Shang C and Liu Z-P 2019 Glucose to 5-Hydroxymethylfurfural: Origin of Site-Selectivity Resolved by Machine Learning Based Reaction Sampling *J. Am. Chem. Soc.* **141** 20525–36
- Kantnerova K, Kuhlbusch N, Juchelka D, Hilkert A, Kopf S H and Neubauer C 2024 A guide to precise measurements of isotope abundance by ESI-Orbitrap MS *Nature Protocols* 1–32
- Leavitt S W and Roden J 2022 Isotope Dendrochronology: Historical Perspective *Stable Isotopes in Tree Rings: Inferring Physiological, Climatic and Environmental Responses* ed R T W Siegwolf, J R Brooks, J Roden and M Saurer (Cham: Springer International Publishing) pp 3–20 Online: https://doi.org/10.1007/978-3-030-92698-4_1
- Lehmann M M, Schuler P, Schönbeck L, Rehmann O, Diao H, Vitali V and Grossiord C 2023 Effects of vapour pressure deficit, temperature and soil drought on triple isotope patterns of assimilates and tree-ring cellulose *EGU General Assembly Conference Abstracts* p EGU-6353 Online: <https://ui.adsabs.harvard.edu/abs/2023EGUGA..25.6353L/abstract>
- Makarov A and Denisov E 2009 Dynamics of ions of intact proteins in the Orbitrap mass analyzer *J. Am. Soc. Mass Spectrom.* **20** 1486–95
- Martínez-Vilalta J, Poyatos R, Aguadé D, Retana J and Mencuccini M 2014 A new look at water transport regulation in plants *New Phytologist* **204** 105–15
- Merritt D A and Hayes J M 1994 Factors Controlling Precision and Accuracy in Isotope-Ratio-Monitoring Mass Spectrometry *Anal. Chem.* **66** 2336–47
- Neubauer C, Kantnerová K, Lamothe A, Savarino J, Hilkert A, Juchelka D, Hinrichs K-U, Elvert M, Heuer V, Elsner M, Bakkour R, Julien M, Öztoprak M, Schouten S, Hattori S and Dittmar T 2023 Discovering Nature’s Fingerprints: Isotope Ratio Analysis on Bioanalytical Mass Spectrometers *J. Am. Soc. Mass Spectrom.* **34** 525–37
- Peters R L, von Arx G, Nievergelt D, Ibrom A, Stillhard J, Trotsiuk V, Mazurkiewicz A and Babst F 2020 Axial changes in wood functional traits have limited net effects on stem biomass increment in European beech (*Fagus sylvatica*) *Tree Physiology* **40** 498–510
- Rennenberg H, Loreto F, Polle A, Brilli F, Fares S, Beniwal R S and Gessler A 2006 Physiological Responses of Forest Trees to Heat and Drought *Plant Biology* **8** 556–71
- Roeske C A and O’Leary M H 1984 Carbon isotope effects on enzyme-catalyzed carboxylation of ribulose biphosphate *Biochemistry* **23** 6275–84

- Rog I, Jakoby G and Klein T 2021 Carbon allocation dynamics in conifers and broadleaved tree species revealed by pulse labeling and mass balance *Forest Ecology and Management* **493** 119258
- Sadras V O and Milroy S P 1996 Soil-water thresholds for the responses of leaf expansion and gas exchange: A review *Field Crops Research* **47** 253–66
- Saeman J F, Bubl J L and Harris E E 1945 Quantitative Saccharification of Wood and Cellulose *Ind. Eng. Chem. Anal. Ed.* **17** 35–7
- Schönbeck L C, Schuler P, Lehmann M M, Mas E, Mekarni L, Pivovarov A L, Turberg P and Grossiord C 2022 Increasing temperature and vapour pressure deficit lead to hydraulic damages in the absence of soil drought *Plant, Cell & Environment* **45** 3275–89
- Sharkey T D, Singsaas E L, Vanderveer P J and Geron C 1996 Field measurements of isoprene emission from trees in response to temperature and light *Tree Physiology* **16** 649–54
- Sharkey T D and Yeh S 2001 Isoprene emissions from plants *Annual Review of Plant Biology* **52** 407–36
- Silvestri L, Saraceni M, Brunone B, Meniconi S, Passadore G and Bongioannini Cerlini P 2025 Assessment of seasonal soil moisture forecasts over the Central Mediterranean *Hydrology and Earth System Sciences* **29** 925–46
- Sjöström E 1993 *Wood Chemistry: Fundamentals and Applications* (San Diego, CA: Academic Press)
- Wieloch T, Ehlers I, Yu J, Frank D, Grabner M, Gessler A and Schleucher J 2018 Intramolecular ¹³C analysis of tree rings provides multiple plant ecophysiology signals covering decades *Sci Rep* **8** 5048
- Wieloch T, Holloway-Phillips M, Yu J and Niittylä T 2025 New insights into the mechanisms of plant isotope fractionation from combined analysis of intramolecular ¹³C and deuterium abundances in *Pinus nigra* tree-ring glucose *New Phytologist* **245** 1000–17
- Wieloch T, Sharkey T D, Werner R A and Schleucher J 2022 Intramolecular carbon isotope signals reflect metabolite allocation in plants ed A Rogers *Journal of Experimental Botany* **73** 2558–75
- Wilkes E B, Sessions A L, Zeichner S S, Dallas B, Schubert B, Jahren A H and Eiler J M 2022 Position-specific carbon isotope analysis of serine by gas chromatography/Orbitrap mass spectrometry, and an application to plant metabolism *Rapid Comm Mass Spectrometry* **36** Online: <https://onlinelibrary.wiley.com/doi/10.1002/rcm.9347>
- Willi A. Brand 1998 Isotope Ratio Mass Spectrometry: Precision from Transient Signals *Advances in Mass Spectrometry* vol 14, ed Karjalainen, E. J., Hesso, A. E., Jalonen, J. E., and Karjalainen, U. P. pp 661–86
- Yu H and Blande J D 2021 Diurnal variation in BVOC emission and CO₂ gas exchange from above- and belowground parts of two coniferous species and their responses to elevated O₃ *Environmental Pollution* **278** 116830

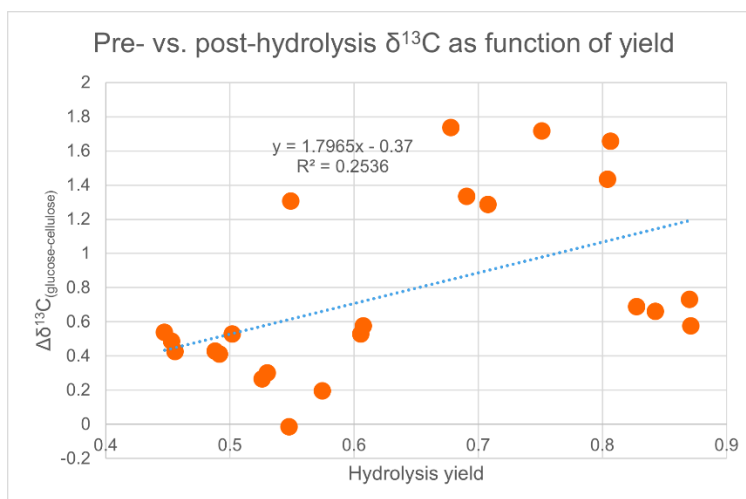
4.8) Supplementary Information

Supplementary Table 4.1. $\delta^{13}\text{C}_{\text{VPDB}}$ of α -cellulose standard and glucose product of hydrolysis by EA-IRMS, showing no discernable offset between the reactant and product. (Glucose appears possibly slightly enriched, but the offset is not statistically significant.)

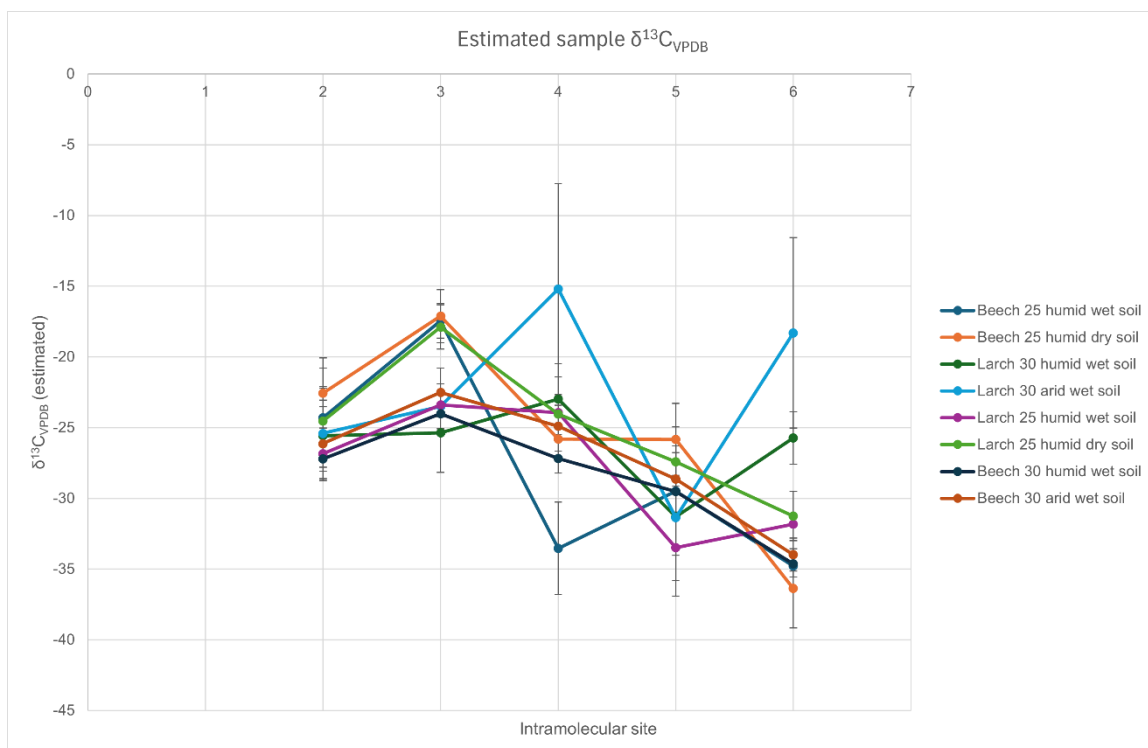
Material	Average $\delta^{13}\text{C}$ value (‰)	Standard deviation (‰)
α -cellulose (pre-hydrolysis)	-26.5	0.08
Glucose (post-hydrolysis)	-26.3	0.23



Supplementary Figure 4.5 $\delta^{13}\text{C}_{\text{VPDB}}$ of cellulose samples (blue) and the product of sample hydrolysis (orange) by EA-IRMS, showing a systematic enrichment of glucose relative to sample cellulose.



Supplementary Figure 4.6) Measured $\Delta\delta^{13}\text{C}$ of post-hydrolysis glucose product vs. pre-hydrolysis sample cellulose, showing a weak but significant correlation between hydrolysis yield and isotopic offset.



Supplementary Figure 4.7) Estimated $\delta^{13}\text{C}_{\text{VPDB}}$ of climate chamber tree-ring samples, calculated based on $\delta^{13}\text{C}_{\text{VPDB}}$ values of a glucose standard from the same product number (but different batch) as standard SC3. Values measured by Alexis Gilbert and provided by Youki Sato.

*Appendix I***POREWATER METHANE CONCENTRATION MEASUREMENTS BY
PORTABLE SPECTROSCOPY ANALYZER****5.1) Benefits of field-portable methane concentration measurement**

Porewater methane concentration is a commonly measured characteristic in studies of microbial activity and biogeochemistry across diverse sedimentary settings. Measurements of methane in sedimentary porewater have been used to predict the dynamics of methane release with Arctic warming (Emerson *et al* 2021), understand microbial biogeography at hydrothermal vents (Orphan *et al* 2004), and investigate transformations of organic carbon in coastal marine environments (Euler *et al* 2024), among many other applications. Samples for porewater methane measurement are typically collected at field sites or even shipboard, with samples then requiring transport prior to laboratory-based analysis. Careful sample handling during transportation is required to prevent sample alteration, including diffusive methane loss as well as further methane production and/or consumption during storage.

The ability to perform porewater methane measurements with field-portable instrumentation circumvents many of the pitfalls of sample storage and transport. Additionally, for multi-day field sampling campaigns or cruises, portable porewater concentration analysis introduces the possibility for iterative sampling, where researchers can use porewater methane data collected in the field to make decisions about additional sample collection. We have developed a method to measure porewater methane concentrations using field-portable instrumentation, and used the method to collect porewater methane data on the same day that samples were retrieved. The preliminary data we collected indicates that our method produces results that are consistent with traditional lab-based analyses.

5.2) Method**5.2.1) Instrumentation**

Measurements for this study were performed using the Picarro G4302 portable cavity-ringdown spectroscopy (CRDS) analyzer (Picarro, Santa Clara, CA, USA), which simultaneously measures concentrations of methane, ethane, and water vapor. We equipped the analyzer for headspace methane measurement by constructing a sample loop connected to the instrument inlet and outlet via Colder coupling bodies, which convert from the instrument's built-in quick-disconnect ports to NPT fittings (Colder Products Company, Arden Hills, MN, USA). The sample loop was constructed from copper tubing and an injection port where headspace samples could be introduced into the measurement flow path. Flow rate through the sample loop and instrument during measurement was 2 slpm (standard liters per minute). Because a measurement of the internal volume of the analyzer was not available, the total internal volume of the system was determined by calibration (see Section 5.2.6 for details).

5.2.2) Sampling

All cores for this project were retrieved from Station 6 in Mono Lake, Mono County, CA (37.95739 N, -119.0316 W), a representative site in the deepest section of Mono Lake's south basin. Cores were sampled by gravity coring into core barrels with pre-drilled holes spaced throughout the length of the barrel, which were secured with electrical tape prior to core collection.

Sampling campaign 1 occurred on 5/10/22. During campaign 1, half of all samples were collected to be measured using our method for porewater methane measurement by field-portable CRDS, and the other half were sent to David Valentine and Frank Kinnaman at the University of California Santa Barbara (UCSB) for measurement by gas chromatography–flame ionization detection (GC-FID). For this campaign, delays between the times of core recovery, sediment subsampling, and sample measurement caused some ambiguity in interpreting the dataset. As a result, we undertook an additional sampling campaign (campaign 2) on 10/3/2022, where we were able to correct for the difficulties encountered during campaign 1.

5.2.3) Sampling campaign 1

At 11 am on 5/10/22, an 89-cm sediment core was recovered in a core barrel with pre-drilled holes every ~5 cm. Sediment subsamples were collected from the core at 2 pm on the same day, by which time the core had expanded to a length of 93 cm, partially due to gases exsolving from solution. One subsample was collected through each hole in the core barrel, retrieving 3 mL of sediment with a syringe. Each collected subsample was immediately submerged in 3 mL supersaturated sodium chloride solution in nanopure water in a preweighed serum bottle and capped with a butyl rubber stopper and crimp cap. Nine samples were collected to be measured via CRDS and nine to be measured via GC-FID, with alternating depths assigned to each method (i.e., samples from 2.5 and 12.6 cm depth were prepared for measurement by CRDS; samples from 7.5 and 17.7 by GC-FID, etc.).

Because of a malfunction of the portable CRDS analyzer, headspace methane concentration measurements by CRDS were performed on 5/16/22, 6 days after sample collection. Samples were stored frozen between collection and measurement. Prior to measurement, samples were warmed to ~30 °C in a water bath and 0.5 mL of nanopure water was added to increase headspace pressure. 0.5 mL of headspace gas was then sampled with a gas-tight gas syringe (Restek, Bellefonte, PA, USA) and needle and injected into the sample loop. For campaign 1, the sample injection port was constructed from a quick-turn–NPT coupling compatible with Luer style syringes (McMaster-Carr, Santa Fe Springs, CA) and plumbed into the sample loop via an NPT tee fitting secured with teflon tape.

After sample injection, methane concentrations were observed for ~5–10 minutes. Following each measurement, the sample loop was disconnected from the instrument for at least one minute to enable gas concentrations to re-equilibrate with ambient air.

Sample measurements by GC-FID were performed at UCSB on 5/13/2022 using a Shimadzu GC-14a (Shimadzu, Kyoto, Japan). Measured methane concentrations were compared to an 18/point calibration curve ($r^2 = 0.99$). The relative standard deviation (RSD) of methane concentration for replicate sample measurements was 0.02–4.51%.

5.2.4) Sampling campaign 2

At 12:15 pm on 10/3/22, a 104-cm sediment core was recovered into a core barrel with pre-drilled holes every 3 cm. To avoid the evolution of bubbles by core degassing at ambient pressure, subsamples were immediately collected from the core onboard the sampling boat, working from top to bottom. ~3 mL subsamples were collected and immediately submerged in supersaturated sodium chloride solution in nanopure water in a preweighed 20 mL VOA vial. A total of 16 sediment subsamples were collected at 6-cm intervals throughout the core, all within 30 minutes of core retrieval.

Sample processing and headspace methane measurement was performed beginning at 4pm on 10/3/22. Samples were warmed to ~30 °C in a water bath. Prior to sample measurement, 2 mL of nanopure water was injected into each sample by syringe and needle through the cap septum. 2 mL of headspace gas was then retrieved with a gas-tight gas syringe and needle and injected into the spectroscopy analyzer sample loop. During campaign 2, a Swagelok Ultra-Torr vacuum fitting with a rubber septum was used as the injection port (Swagelok, Solon, OH, USA) and connected to the sample loop with a smaller Swagelok tee. This fitting was selected because of its shorter length: as a result, headspace samples were injected closer to the sample loop flow path and entrained more quickly in the circulating air, enabling faster measurements relative to campaign 1.

After sample injection, methane and ethane concentrations were observed for ~5-10 minutes. The sample loop was disconnected from the instrument for a minimum of 30 seconds in between measurements to equilibrate internal methane concentration with ambient air.

5.2.5) Data processing

The time and volume of each methane injection during standard and sample measurements was recorded. At the recorded time of each injection, the local maximum value of methane concentration (dry air basis) measured by the CRDS analyzer was detected using the 'idxmax' function in pandas version 2.2.3 in python. It was manually verified that the detected local maximum aligned with the peak of the methane concentration trace following injection (allowing a short time for the injected sample to be entrained into the sample loop airflow). The measured

methane concentration was averaged over the 30 seconds following the detected local maximum. The methane concentration for that injection time was recorded as the average \pm the standard deviation of measured concentration over the 30-second window. The background methane concentration was reported as the average methane concentration over 5–15 seconds preceding the injection, so the methane increase associated with each injection was calculated as the difference between background and sample (or standard) methane concentration.

The increase in methane concentration from each injection was converted to moles of methane using the calibrated internal volume of the measurement system (see Section 5.2.6) and the ideal gas law, accounting for sample temperature and ambient atmospheric pressure (~ 0.96 atm in Pasadena; ~ 0.76 atm in Mammoth Lakes). Porewater methane concentration was calculated from moles of methane based on the sample volume and porosity. Porosity was not measured on the collected samples, but based on previous measurements of Mono lake sediments, a porosity of 90% was assumed. In sampling campaign 2, the core bottom contained more consolidated gray-colored sediment, which has previously been determined in other Mono Lake samples to have an approximate porosity of 75%; this porosity value was applied to samples from this sedimentary horizon.

5.2.6) Calibration

Measurement linearity was confirmed and the internal volume of the measurement apparatus was estimated by calibration via injections of 1.998% methane in nitrogen (Air Liquide, Houston, TX, USA) at known volume. Repeat injections of between 100 and 800 μL 2% methane produced a linear trend in measured methane concentration with $r^2 = 0.99$ (Figure 5.1). The relative standard deviation of measured concentrations at each injection volume was 3-5%, with uncertainty deriving in large part from the imprecision in the exact volume of injected standard as assessed by markings on the by gastight syringe (the relative standard deviation calculated for individual injections was on average 1%).

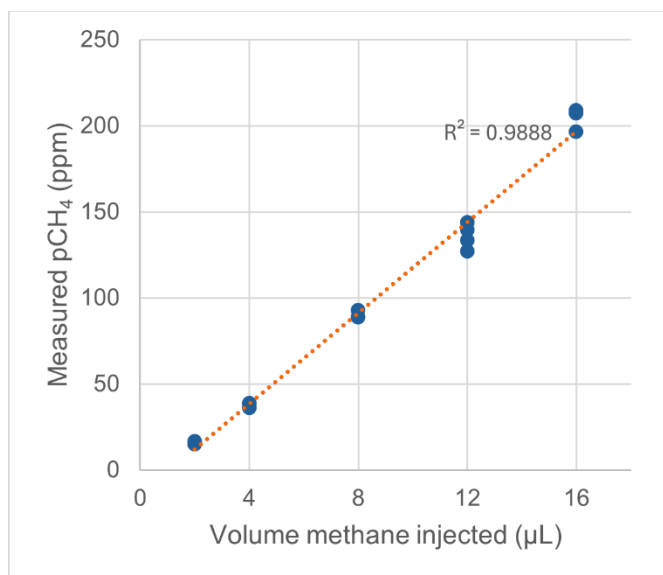


Figure 5.1. Measured concentration of methane (in ppm) across 20 injections of a 2% methane standard at known volume (blue points). Linear fit between volume of sample injected and measured concentration is shown in orange ($r^2 = 0.9888$).

As described in Sections 5.2.3 and 5.2.4, the sample loop construction differed slightly between sampling campaigns 1 and 2. For each campaign, calculations of the measured concentration as a factor of the known amount of injected methane were used to estimate the effective internal volume of the sample loop–instrument system. For campaign 1, the effective internal volume of the sample loop and instrument together was determined to be 89 ± 10 mL. For campaign 2, the effective internal volume was determined to be 103 ± 8 mL.

5.3) Results

5.3.1) Campaign 1: Comparison to GC-FID

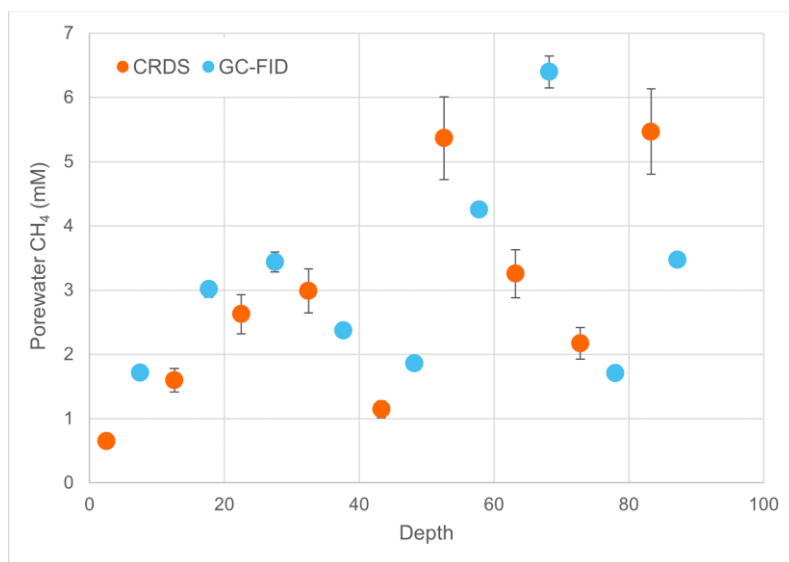


Figure 5.2: Porewater methane concentrations from sampling campaign 1 measured by field-portable cavity ringdown spectroscopy (CRDS, blue) and by gas chromatography-flame ionization detection (GC-FID, orange). Error bars show the propagated analytical uncertainty and replicate error.

Porewater methane concentration measurements by field-portable CRDS analyzer and by GC-FID yielded very similar trends (Figure 5.2). Both methods showed an increase in methane concentration from the core top to a depth of 32.5 cm ranging from minimum values of 0.6–1.7 mM to maximum values of 3.0–3.4 mM. In this region of the core, concentrations measured by CRDS were slightly below, but within error of, the values measured by GC-FID for the most proximal samples. From 32.5 to 57.2 cm, both methods found a decrease in porewater methane concentration; and at depths below 57.2 cm, both measured high and variable concentration. The decrease in calculated porewater methane concentration between 32.5 and 57.2 cm may be due to the assumption of constant porosity; the deeper sediments may be more compressed, leading to artificially low calculated porewater concentrations. The elevated and variable porewater methane concentrations measured in the deepest sediments may be attributable to the sampling of exsolved methane bubbles when core subsamples were collected; the presence of exsolved gas bubbles was physically confirmed when the core was retrieved. No ethane was detected at any depth in the core.

5.3.2) Campaign 2: Same-day measurements

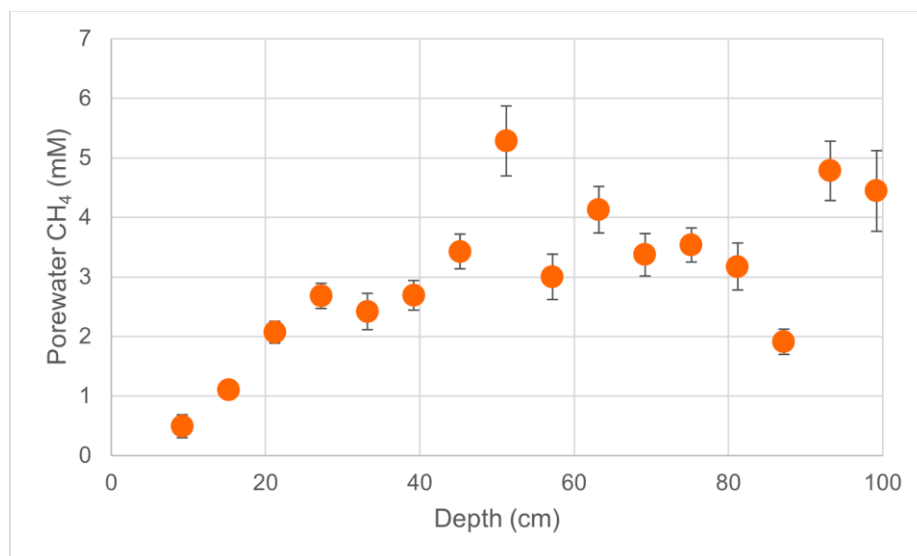


Figure 5.3: Porewater methane concentrations from sampling campaign 2 measured by field-portable cavity ringdown spectroscopy (CRDS). Error bars show the propagated analytical uncertainty and error of 2–3 replicate measurements.

During sampling campaign 2, sediment subsamples were collected immediately after core retrieval (onboard the boat) in order to minimize bubble exsolution. Additionally, porewater headspace was measured on the same day, resolving any possible concerns about sample alteration during storage. The measured porewater methane concentrations from campaign 2 yielded similar results to campaign 1. In particular, a clear rise in methane concentration was observed with depth in the core, increasing from 0.5 mM at 0 cm to 2.7 mM (Figure 5.3). This increase matched the trends observed from sampling campaign 1, and is likely a result of autochthonous biological methane production, diffusing from the area of production at or below 27.2 cm up into the water column. A further increase was detected from 33.2 to 51.2 cm with a concave up curvature, suggesting this may be a zone of active methane production. Alternately, it is possible that the methane concentration measured at 51.2 cm was artificially high due to sampling inconsistencies; disregarding this point shows a more steady, concave-down increase in methane concentration throughout the core. Measured porewater methane concentrations were more variable between 57.2 and 99.2 cm depth, although the average concentration measured in this zone, 3.5 mM, matches closely to the observed concentration at 45.2 cm of 3.4 mM. Again, no ethane was detected at any depth, suggesting that the methane is likely to be primarily biological rather than thermogenic in origin.

5.3.3) Comparison of timepoints

A comparison of CRDS measurements of sediment cores from sampling campaigns 1 (spring) and 2 (fall) reveals several points of agreement (Figure 4). As discussed above, both cores show a steady increase in methane concentration near the core top from 0 to 35 cm, and close agreement in absolute methane concentrations, ranging from 0.5 to 4 mM in the porewater. The decrease in methane concentration observed at from 32 to 42 cm during campaign 1 was not replicated in campaign 2. However, interestingly, both campaigns produced a clear maximum concentration of 5.3–5.4 mM at 51.2–52.6 cm. The origin of this local maximum value is unclear, but may be identified by comparison to biological and geochemical characterization of other cores from Mono Lake station 6. At depths below 53 cm, values measured during campaign 2 are much less variable than those measured during campaign 1, clearly illustrating the benefit of immediate core subsampling before significant bubble exsolution can occur. Overall, the strong agreement of measurements (despite both seasonal changes and different sample retrieval methods) indicates that field-portable CRDS enables the user to rapidly and accurately measure porewater methane concentrations.

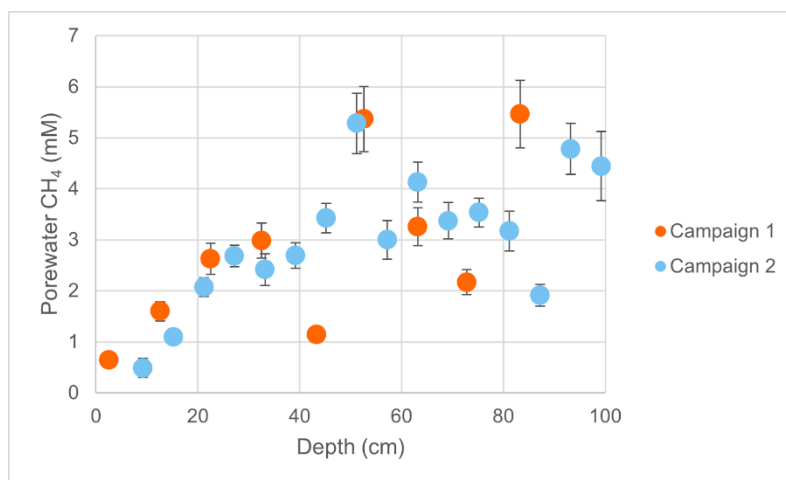


Figure 5.4: Comparison of porewater methane concentrations measured by field-portable cavity ringdown spectroscopy (CRDS) during campaigns 1 (orange) and 2 (blue).

5.3.4) Limit of detection

We estimated the limit of detection for our developed method based on the noise in $p\text{CH}_4$ measured by the CRDS analyzer (~ 45 ppb at ambient methane concentration). In order to achieve $S/N > 2$, an injection would need to contain at least $\sim 4.1 \times 10^{-10}$ mol methane for a 100-mL system volume. Given a 1-mL injection from a 3-mL porewater sample with 10 mL of headspace, the porewater methane concentration would need to be at least $\sim 1.4 \mu\text{M}$, 500x higher than the aqueous methane concentration in equilibrium with the atmosphere. Lower methane concentrations might be detected by decreasing the system volume (e.g., by using tubing with lower ID) or by increasing the ratio of porewater to headspace volume.

5.4.) Outlook

The preliminary results reported here indicate that accurate porewater methane concentration measurements can be performed with field-portable equipment. This method holds promise for researchers wishing to avoid the logistics associated with gas sample storage, or to make same-day measurements from samples collected at remote locations.

Some remaining analyses are required to more accurately calibrate methane abundance values retrieved by this method, and therefore to accurately estimate the effective internal volume of the measurement apparatus (on which the absolute values reported for porewater methane concentration depend). In particular, due to the compressibility of gas, when injections of 2% methane are sampled and introduced by gas-tight syringe, the syringe's internal pressure may not be exactly equivalent to atmospheric pressure. This can result in inaccurate estimations of the total amount of methane introduced into the sample loop. For example, if the syringe indicates a volume of 800 μL , but the internal pressure of the syringe is lower than 1 atm, the amount of methane injected will be overestimated. To accurately record the amount of methane injected to the system during calibration, the methane standard should be present at a known, constant concentration and pressure. This can be achieved by storing gas standards in Teflon film bags, which maintain a pressure of 1 atm (John Crouse, pers. comm.).

The method as reported here depends on measuring an increase in methane abundance in the sample loop relative to what is present at atmospheric background. However, the sensitivity of

the method to lower methane concentrations may be improved by flushing sample vials and the sample loop with a methane-free gas such as zero air. With this adjustment, the method might be sensitive to headspace methane concentrations as low as 1 ppm.

5.5) References

- Emerson J B, Varner R K, Wik M, Parks D H, Neumann R B, Johnson J E, Singleton C M, Woodcroft B J, Tollerson R, Owusu-Dommey A, Binder M, Freitas N L, Crill P M, Saleska S R, Tyson G W and Rich V I 2021 Diverse sediment microbiota shape methane emission temperature sensitivity in Arctic lakes *Nat Commun* **12** 5815
- Euler S, Jeffrey L C, Maher D T, Johnston S G, Sugimoto R and Tait D R 2024 Microbiome mediating methane and nitrogen transformations in a subterranean estuary *Environmental Microbiology* **26** e16558
- Orphan V J, Ussler W, Naehr T H, House C H, Hinrichs K-U and Paull C K 2004 Geological, geochemical, and microbiological heterogeneity of the seafloor around methane vents in the Eel River Basin, offshore California *Chemical Geology* **205** 265–89

TOWARDS FIELD-BASED MEASUREMENTS OF METHANOTROPHY KINETICS

6.1) Current state of the field

Aerobic methanotrophy, the bacterial oxidation of methane, plays a key role in determining the methane budget of terrestrial ecosystems (Saunio *et al* 2020). Most models of terrestrial methane cycling rely on a linear (or Michaelis-Menten) constant describing the kinetic response of methanotrophy rates to methane availability in order to simulate methane fluxes (Xu *et al* 2016). However, I have shown that the kinetics of methanotrophy in natural soils vary over many orders of magnitude (Dion-Kirschner *et al* 2024), and that this variability may contribute to uncertainty in global models. The total number of measurements of methanotrophy kinetics in natural soils is limited; my compilation of reported Michaelis-Menten kinetic constants in soils identified only 542 measurements published between 1987 and 2023, and over 35% of these measurements were from landfill soils, limiting their relevance to global land area. The sparsity of data makes it difficult to justify the selection of kinetic parameters for existing global models. More thorough characterization of kinetic variability in methanotrophy—and the biological controls on this variability across environments—will contribute to more accurate models of methane cycling.

The limited number of measurements of methanotrophy kinetics is understandable in light of the effort required to make these measurements. Because Michaelis-Menten kinetics describe a nonlinear relationship between substrate concentration and biological rate, these curves are typically constructed from more than five points, but not infrequently twenty or more. Here, each point is an observed methane uptake rate at a given initial methane concentration. Because each point on a kinetic curve is a measurement of uptake rate, it actually represents multiple timepoints of methane concentration observed over hours or days after an initial injection of elevated methane into the sample headspace. As a result, the full kinetic characterization of a

single soil sample can easily amount to five or more timepoints of soil samples incubated at six or more distinct methane headspace concentrations, for a total of thirty timepoints or more, each measured by gas chromatography-flame ionization detection (GC-FID) or GC-thermal conductivity detection (GC-TCD).

Among published studies, no standard practice for soil sample treatment before and during kinetic characterization is evident. For example, measurements are variably made on field-moist, air-dried, or wetted samples (e.g., Bender and Conrad 1992, 1993, Megraw and Knowles 1987); with or without prior incubation at high methane concentration (e.g., Bradford *et al* 2001); and with or without the addition of amendments like nitrate and ammonium (e.g., Chan *et al* 2005).

Given the importance of further measurements to our understanding of global methane cycling and its likely response to ongoing environmental change, there is strong justification for an easier and more standardized method for characterizing the kinetics of soil methanotrophy. To address this need, here I present the first efforts to develop a method for field-based characterization of methanotrophy kinetics using a portable cavity ringdown spectroscopy (CRDS) analyzer. As developed, the method enables the user to characterize soil methane uptake rates across a range of headspace methane concentrations in under one hour, while introducing minimal disruption to the soil between sampling and characterization. Further method development is needed to circumvent methodological problems encountered in early testing, especially the inability of the field-portable analyzer to maintain above-ambient methane concentration without diffusive methane loss. Nevertheless, initial results indicate the promise of this method, which would greatly improve researchers' capability for high-throughput methanotrophy kinetic measurements across a wide range of terrestrial environments.

6.2) Measurement design

6.2.1) Instrumentation and materials

Methane concentrations were measured using a Picarro GasScouter G4302 field-portable cavity ringdown spectroscopy (CRDS) analyzer (Picarro, Santa Clara, CA, USA). A leak-tight chamber

was constructed in order to contain a soil sample and facilitate injections of methane into the headspace while circulating air from the chamber through the CRDS analyzer (Figure 6.1A). Materials were selected to be impermeable and unreactive to methane. The chamber top was constructed from polycarbonate, with an internal volume of 8.2 L and a footprint of 0.0307 m². The top formed an airtight seal with the chamber base, which was constructed from a ~4-cm deep neoprene ring fixed to an acrylic sheet with butyl rubber adhesive, into which the chamber top could be fitted (Figure 6.1B). The chamber top was sealed with a butyl rubber stopper, through which two lengths of tubing were passed to allow the chamber headspace to flow into and out of the CRDS analyzer. During measurements, the analyzer operated at a flow rate of 2 slpm (standard liters per minute).



Figure 6.1: Components of kinetics measurement system. A: Measurement system during a kinetics measurement. Chamber is fitted into the chamber base, with a neoprene skirt covering the juncture between chamber and chamber base. Chamber is connected to the field-portable CRDS analyzer inlet and outlet via two lengths of tubing and an inline water trap. B: Detail of chamber base, a Neoprene collar fixed to an acrylic sheet with butyl rubber adhesive.

To test the response of soil methane uptake rate to ambient methane availability, we injected a standard composed of 1.998% methane in nitrogen (Air Liquide, Houston, TX, USA) into the chamber headspace. The measurement process is further described in Section 6.2.2.

6.2.2) Measurement method

To prepare for kinetic characterization, ~100-200 g soil was sampled, integrating the top 10 cm of the soil profile after the removal of aboveground vegetation. Soil sampling was performed with an isopropanol-sterilized trowel, taking care to maintain soil structure as much as possible (e.g., not disrupting soil aggregates, root material, etc). The soil sample was transferred from the trowel directly into the chamber base. The chamber top was then placed on the chamber base.

For at least two minutes, the headspace methane concentration in the chamber was observed under ambient conditions. After this time, increasingly large volumes of the 1.998% methane standard were introduced by injection with a gas-tight syringe and needle through the chamber's butyl rubber stopper. After each injection, the headspace methane concentration was observed for at least six minutes. A typical measurement series comprised successive injections of 0.5, 1, 2, 5, and 10 mL of 2% methane standard.

After kinetic characterization, the soil sample was collected for laboratory characterization. Soil samples were dried at 105 C for at least 24 hours until complete dryness and then weighed. The recorded sample dry weights were used to report V_{max} values on the basis of soil dry weight.

6.2.3) Data processing

The headspace methane concentrations measured by the CRDS analyzer in the minutes following each injection were used to calculate the rate of methane drawdown. Data were selected by manually identifying peaks in measured methane concentration resulting from each injection, and a linear fit was calculated for measured methane abundance (dry air basis) over the ~5-minute period following each injection. Outlier values (typically an instrument artefact) were identified as those that deviated from the detrended mean of a measurement by more than three times the interquartile range. The uptake rate for each value of $pCH_{4,initial}$ was recorded as the

slope of the linear fit (Figure 6.2), and uncertainty as the 90% confidence interval of the slope. Slopes measured in ppm min^{-1} were converted to uptake rates in $\text{nmol methane min}^{-1}$ as in Chapter 2. K_M and V_{max} values were calculated from the set of measured methane uptake rates across 5-6 values of $p\text{CH}_{4,\text{initial}}$ using the `curve_fit` function in the Python library SciPy.

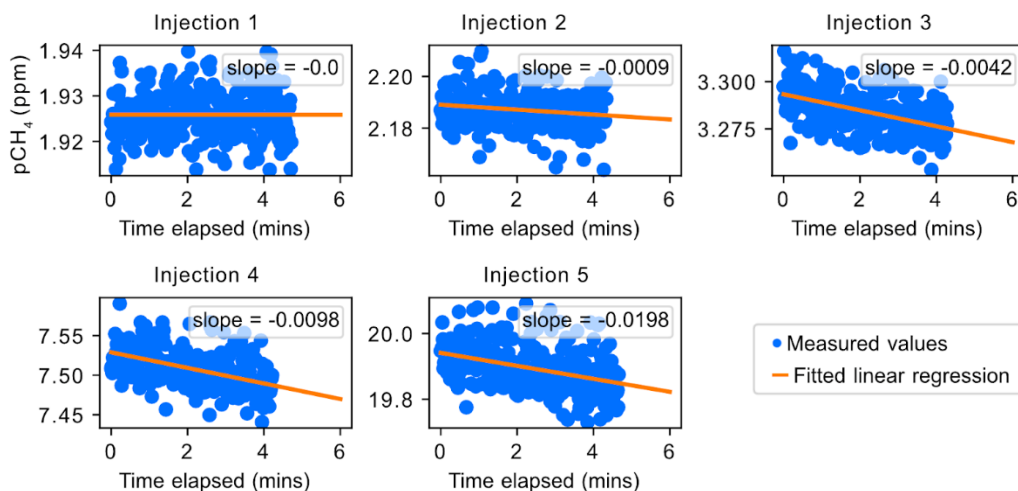


Figure 6.2: Example of one kinetic measurement series, showing $p\text{CH}_4$ values measured by the CRDS analyzer following each of five methane injections into the chamber headspace (blue points). Methane uptake is calculated from the slope of a linear fit of $p\text{CH}_4$ over time (orange line).

6.3) Method testing results and preliminary measurements

6.3.1) Blank measurement and leak characterization

Extended observation of the closed measurement system with no sample or methane injections produced a stable measurement of constant $p\text{CH}_4$ value over the course of hours. This result indicated that no component of the measurement system was a significant source of offgassed methane.

System leak rates were characterized by injecting the 1.998% methane standard into the closed system without any sample in the system and recording changes in the system's internal $p\text{CH}_4$. Under these conditions, minor loss of internal methane was observed, with an average leak rate of 3.9×10^{-4} percent min^{-1} . The slope of $p\text{CH}_4$ over time was linear with respect to $\Delta p\text{CH}_4_{\text{chamber-ambient}}$ ($r^2 = 0.9944$) (Figure 6.3), in line with expectations for diffusive methane loss. To identify the source of the leak, the chamber was removed from the measurement flow path and

the inlet tubing and outlet tubing were connected to form a loop. Under these conditions, the observed leak rate was on average 1.5×10^{-2} percent min^{-1} . In other words, the observed leak rate increased significantly as a higher percentage of the measurement system volume comprised the instrument itself. This finding suggests that leaks within the measurement system were the predominant source of diffusive methane loss. Observed methane loss persisted even after all internal instrument fittings were confirmed to be tightly sealed. To further determine the location of leaking within the instrument, methane was injected near specific locations on the instrument body: the inlet, outlet, fan, solenoid valve, and pump. A large spike in measured $p\text{CH}_4$ was observed when methane was injected near the pump. This result suggests that diffusive methane exchange occurs between the pump and the surrounding air.

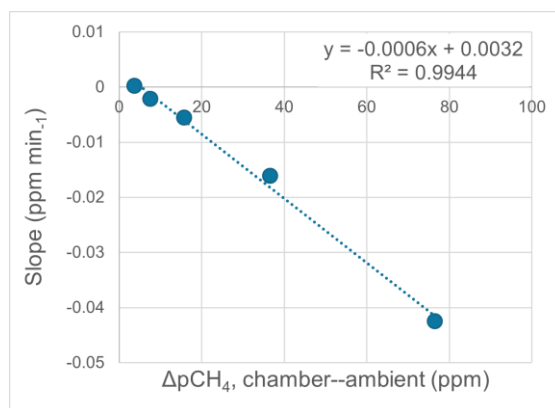


Figure 6.3: Measured methane loss rate (in ppm min^{-1}) from the chamber-analyzer system when no soil sample was present, plotted against the methane gradient between the chamber interior and the ambient atmosphere ($\Delta p\text{CH}_4$, ppm). Dotted line represents a linear regression of the x and y variables, and the slope and r^2 value of the linear fit are shown at top right. An r^2 value of 0.9944 indicates a strong linear relationship between methane concentration gradient and loss rate, supporting that loss is occurring by diffusion.

On different days of testing, we observed that the leak rate for a given condition (i.e., with or without the chamber in the flow path) varied. This is consistent with the pump as the primary source of the leak, since pump function varies with variables including ambient pressure and temperature. Because the leak rate was not predictable over time, we were unable to apply a generalized correction to remove the influence of methane leaking from measurement data.

6.3.2) Preliminary sample measurements

We performed preliminary kinetic characterization of soil samples to determine whether the signals from sample measurements significantly exceeded the influence of methane leaks. Of 24 kinetic measurements across three field sites, 8 were indistinguishable from a linear trend between methane loss rate and $p\text{CH}_4$. A linear trend could be observed either because of diffusive methane loss, or because measurements were performed at $p\text{CH}_4$ values far below the K_M value (or some combination of both). Typical methane loss rates observed for these samples were only $\sim 2\times$ the typical leak rates measured from the chamber when empty (described in section 6.3.1), indicating that diffusive loss contributed substantially to the measured decrease in methane. Further, because linear trends were observed most commonly for samples where methane uptake under ambient conditions was lowest, a leak is a likelier explanation than high values of K_M . Nonetheless, future measurements using a measurement system that is secured against leaking may reveal a wide range of K_M values across field sites, including values well above the max $p\text{CH}_4$ value of 60 ppm to which samples in this study were exposed; while K_M values in natural well-oxygenated soils are typically $\sim 10\text{--}100$ ppm, values above 10,000 ppm have sometimes been observed (Dion-Kirschner *et al* 2024).

Figure 6.4 shows three example measurements where a Michaelis-Menten-like relationship between $p\text{CH}_4$ and methane loss rate was observed. The fitted curves fell outside the confidence interval of measured rates at low values of $p\text{CH}_4$; the failure of curve fitting may be due to an increasing contribution of diffusive methane loss to measured rates at higher values of $p\text{CH}_4$ as V of methanotrophy approaches the community value of V_{max} . Nevertheless, these three measurements produced reasonable values of both parameters: calculated K_M values ranged from 21.8–43.8 ppm, and V_{max} values from 80.5–305.2 nmol methane g dry soil⁻¹ hr⁻¹, all within the typical range of values measured in natural soils (Dion-Kirschner *et al* 2024), suggesting that the measurement method may achieve accurate values if leaking is prevented.

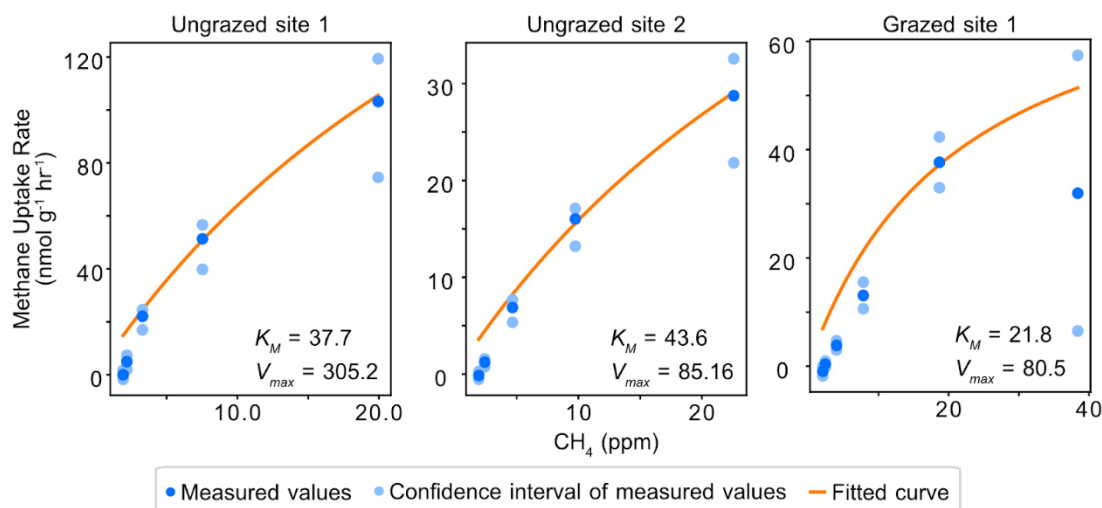


Figure 6.4: Kinetic characterization of three soil samples. Dark blue points show measured methane uptake (and/or loss) rate for a given methane abundance (in ppm). Light blue points show the 90% confidence interval of the uptake rates, which were estimated by linear fit. Orange line shows the curve fitted to these values using the `curve_fit` function from the Python library SciPy. K_M and V_{max} values calculated from the fitted curve are noted in the bottom right of each panel.

6.4) Outlook

While instrumentation difficulties still need to be resolved, early results suggest that realistic Michaelis-Menten parameters of methane uptake can be recovered from field-based measurements of natural soils with less than 60 minutes of total measurement time. With further refinement, this method holds great promise in enabling higher-throughput kinetic characterization of methanotrophy in soils while simultaneously minimizing disruption to soil samples prior to measurement. Better characterizing the range of kinetic variability in natural settings will help to improve the accuracy of soil methane models and further illuminate the ecophysiology of an important natural greenhouse gas sink.

6.5) References

- Bender M and Conrad R 1992 Kinetics of CH_4 oxidation in oxic soils exposed to ambient air or high CH_4 mixing ratios *FEMS Microbiology Ecology* **10** 261–9
- Bender M and Conrad R 1993 Kinetics of methane oxidation in oxic soils *Chemosphere* **26** 687–96
- Bradford M A, Ineson P, Wookey P A and Lappin-Scott H M 2001 The effects of acid nitrogen and acid sulphur deposition on CH_4 oxidation in a forest soil: a laboratory study *Soil Biology and Biochemistry* **33** 1695–702

- Chan A S K, Steudler P A, Bowden R D, Gullede J and Cavanaugh C M 2005 Consequences of nitrogen fertilization on soil methane consumption in a productive temperate deciduous forest *Biol Fertil Soils* **41** 182–9
- Dion-Kirschner H, Nguyen N H, Frankenberg C and Fischer W W 2024 Evaluating the contribution of methanotrophy kinetics to uncertainty in the soil methane sink *Environ. Res. Lett.* **19** 064059
- Megraw S R and Knowles R 1987 Methane production and consumption in a cultivated humisol *Biol Fert Soils* **5** 56–60
- Saunois M, Stavert A R, Poulter B, Bousquet P, Canadell J G, Jackson R B, Raymond P A, Dlugokencky E J, Houweling S, Patra P K, Ciais P, Arora V K, Bastviken D, Bergamaschi P, Blake D R, Brailsford G, Bruhwiler L, Carlson K M, Carrol M, Castaldi S, Chandra N, Crevoisier C, Crill P M, Covey K, Curry C L, Etiope G, Frankenberg C, Gedney N, Hegglin M I, Höglund-Isaksson L, Hugelius G, Ishizawa M, Ito A, Janssens-Maenhout G, Jensen K M, Joos F, Kleinen T, Krummel P B, Langenfelds R L, Laruelle G, Liu L, Machida T, Maksyutov S, McDonald K C, McNorton J, Miller P A, Melton J R, Morino I, Müller J, Murguía-Flores F, Naik V, Niwa Y, Noce S, O’Doherty S, Parker R J, Peng C, Peng S, Peters G P, Prigent C, Prinn R, Ramonet M, Regnier P, Riley W J, Rosentreter J A, Segers A, Simpson I J, Shi H, Smith S J, Steele L P, Thornton B F, Tian H, Tohjima Y, Tubiello F N, Tsuruta A, Viovy N, Voulgarakis A, Weber T S, van Weele M, van der Werf G R, Weiss R F, Worthy D, Wunch D, Yin Y, Yoshida Y, Zhang W, Zhang Z, Zhao Y, Zheng B, Zhu Q, Zhu Q and Zhuang Q 2020 The Global Methane Budget 2000–2017 *Earth Syst. Sci. Data* **12** 1561–623
- Xu X, Yuan F, Hanson P J, Wullschleger S D, Thornton P E, Riley W J, Song X, Graham D E, Song C and Tian H 2016 Reviews and syntheses: Four decades of modeling methane cycling in terrestrial ecosystems *Biogeosciences* **13** 3735–5